Influence of Thermal Post-Processing on the Microstructure and Mechanical Behavior of the Additively Manufactured Inconel 718 Superalloy using the Laser Powder Bed Fusion Process

By

Eslam Mohamed Fayed

A Thesis

In the Department

of

Mechanical, Industrial and Aerospace Engineering

Presented in Partial Fulfilment of the Requirements for the Degree of

Doctor of Philosophy (Mechanical Engineering)

at

Concordia University

Montreal, Quebec, Canada

December 2020

CONCORDIA UNIVERSITY

School of Graduate Studies

This is to certify that the thesis prepared

By: Eslam M. Fayed

Entitled: Influence of Thermal Post-Processing on the Microstructure and Mechanical Behavior of the Additively Manufactured Inconel 718 Superalloy using the Laser Powder Bed Fusion Process

and submitted in partial fulfillment of the requirements for the degree of

DOCTOR OF PHILOSOPHY (Mechanical Engineering)

complies with the regulations of the University and meets the accepted standards with respect to originality and quality.

Signed by the final examining committee:

_____ Chair
Dr. Catherine Mulligan

_____ External Examiner
Dr. Olanrewaju Ojo

_____ External to Program
Dr. Sana Jananshahi-Anbuhi

_____ Examiner
Dr. Robin Drew

_____ Examiner
Dr. Mehdi Hojjati

_____ Thesis Supervisor
Dr. Mamoun Medraj

Approved by _____
Dr. Wei-Ping Zhu, Graduate Program Director

December 10th, 2020 _____
Dr. Mourad Debbabi, Interim Dean
Gina Cody School of Engineering and Computer Science

Abstract

Influence of Thermal Post-Processing on the Microstructure and Mechanical Behavior of the Additively Manufactured Inconel 718 Superalloy using the Laser Powder Bed Fusion Process

Eslam M. Fayed, PhD
Concordia University, 2020

In an attempt to improve the performance of the additively manufactured (AM) Inconel 718 (IN718) superalloy, a typical material widely used for turbine engine components in the aerospace and energy industries, the current work studies the effect of thermal post-processing on the microstructure and mechanical behavior of the AM IN718. Additive manufacturing and, in particular, the laser powder bed fusion (LPBF) of IN718 offers several advantages over the conventionally manufactured IN718 (cast and wrought). However, the existence of some inherited manufacturing defects in the as-printed parts presents an obstacle to produce components with specifications that meet the design requirements. Thus, post-heat treatment of LPBF printed IN718 is an essential and integral part of the industrial operations to mitigate these drawbacks.

For this purpose, in the present study, a heat treatment time window, including a wide time range of homogenization (at 1080°C; 1 to 7h) and solution (at 980°C; 15 to 60 min) treatments, is established to study the effects of the treatments time on the microstructure and mechanical properties at room temperature (RT) and at 650°C of the LPBF printed IN718 parts. The results demonstrate that the 1h homogenization treatment is not enough to significantly change the as-printed grain structure, the strong crystallographic texture and to annihilate the primary dislocation tangles. However, a completely recrystallized IN718 material with non-distinct texture and stress relived grains are obtained after 4h. A further increase in the homogenization time to 7h results in grain growth as well as greater and coarser MC carbides. Therefore, the increase in the homogenization time from 1 up to 7h results in a progressive decrease in the mechanical properties

at RT and at 650°C. For the solution treatment, the treatment time does not cause a noticeable change in the grain structure and material texture but significantly affects the precipitation amount of δ-phase. The role of the solution time in the improvement of the mechanical properties at 650°C is crucial due to the increase in the grain boundary strength through the pinning effect of δ-phase.

Based on the results obtained at different treatment time, a multi-objective optimization is employed to tune homogenization and solution time and achieve the optimum heat treatments that can fulfill the required mechanical properties and material texture. The results show that, after the conditions which include 2.5 and 4h homogenization treatment at 1080°C followed by 1h solution at 980°C and standard aging treatments (2.5H/1S and 4H/1S), a significant improvement in the mechanical properties at RT and 650°C is observed, compared with the wrought IN718. Furthermore, after the 4H/1S condition, a good balance between the strength and ductility is obtained at RT.

To assess the thermal stability of the obtained optimum heat treatments during the in-service conditions, the as-printed, 2.5H/1S and 4H/1S conditions are subjected to thermal cycling similar to what is encountered in the aircraft turbine engines for long periods up to 3000h. The results reveal that the 4H/1S condition possesses higher thermal stability over the in-service exposure than the as-printed and 2.5H/1S conditions, as a relatively lower strength loss of 3.3% is counted for the 4H/1S condition after 3000h thermal exposure, while for the as printed and 2.5H/1S conditions, strength loss of 7.4 and 5.3%, respectively, are counted. Furthermore, the 4H/1S treatment results in delaying the deterioration of material strength for longer thermal exposure time (after 2000h), whereas the 2.5H/1S treatment results in deterioration of the material strength after only 1000h thermal exposure due to the retarded phase transformation of the metastable γ″ into more stable δ-phase within grains interior in the former treatment.

Acknowledgements

First and foremost, I would like to express my sincere and earnest gratitude to my supervisor, Professor Mamoun Medraj, for all of his valuable guidance, patience, endless support, and encouragement to reach the significant achievements during my PhD program at Concordia University. I would also like to thank him for his constructive suggestions and criticisms along my path to completing this thesis.

My sincere thanks go to Professors Mohammad Jahazi and Vladimir Brailovski (École de technologie supérieure) for their support and contributions during the course of my PhD program. Also, my gratitude goes to Dr. Mohammad Saadati and Dr. Davood Shahriari for their technical advice throughout this work. Mazen Samara is also gratefully acknowledged for his good administrative work in the TMG lab. To my wonderful TMG group members, Abdullahi Gujba, Mohamed Elhadi, Fatile Babajide, Mostafa Elyoussef, Khaled Alhammad, Rizwan Ahmed, Xinzhao Mu, Ming Jing, and Ashkan Arab, thank you very much for your support.

My family members and all my relatives supported and prayed for my success in this task. Their efforts are gratefully acknowledged. I deeply thank my dear parents, brothers and sister for their unconditional trust, timely encouragement, and patience. They gave me their great effort, care, and support to build what has brought me this far. I would like to express my sincere thanks and gratitude to my wife (Menna Samy) for her continuous support and motivation to reach that success. I would like to extend a hearty thanks to my beautiful daughters (Login and Lara) and brave son (Hady). They were the energy source which motivated me to reach this success.

Finally, I would like to express my gratitude to the Egyptian Armed Forces to give me their trust and to give me this Ph.D. scholarship at Concordia University.

Contents

List of Figures

List of Tables

List of Abbreviations

TET	Turbine Entry Temperature
IN718	Inconel 718
LPBF	Laser Powder Bed Fusion
FCC	Face Centered Cubic
AMS	Aerospace Material Specification
SHT	Standard Heat Treatment
RT	Room Temperature
AM	Additive Manufacturing
ASTM	American Society for Testing and Material
RP	Rapid Prototyping
DED	Direct Energy Deposition
BJ	Direct Energy Deposition
SL	Sheet Lamination
PBF	Powder Bed Fusion
CNC	Computer Numerical Control
DMD	Direct Metal Deposition
LENS	Laser Engineered Net Shaping
DLF	Directed Light Fabrication
SLM	Selective Laser Melting
SLS	Selective Laser Sintering
CAD	Computer-Aided Design
LSP	Laser Shock Peening
GA	Gas Atomization
HIP	Hot Isostatic press
DA	Direct Aging
BCT	Body Centered Tetragonal
OM	Optical Macrographs
SEM	Scanning Electron Microscopy (Micrographs)
EBSD	Electron Backscatter Diffraction

XRD	X-Ray Diffraction
EDS	Energy Dispersive Spectroscopy
EOS	Electro-Optical System
WEDM	wire Electro-Discharge Machining
TTT	Time-Temperature-Transformation
IPF	Invers Pole Figure
WSF	Weighted Schmid Factor
OIM	Orientation Imaging Microscopy
SF	Schmid Factor
KAM	Kernel Average Misorientation
MAs	Misorientation Angles
HAGBs	High Angle Grain Boundaries
LAGBs	Low Angle Grain Boundaries
CSL	Coincidence Site Lattice
DRX	Dynamic Recrystallization

Chapter 1 : Introduction

This chapter introduces a brief background about the challenges facing the manufacturing of Inconel 718 parts using conventional methods. The laser powder bed fusion process, an additive manufacturing technique, is emerging as one of the promising manufacturing methods for Inconel 718 parts. Also, the potentials and drawbacks associated with this technique are discussed. Finally, the layout of this thesis is presented.

1.1 Problem statement

In the aerospace and power generation industries, the thermodynamic efficiency of the turbine engines is an important issue and directly dependent on the turbine entry temperature (TET) [1]. TET is the temperature of the gases exhausted from the combustion chamber in turbine engines as shown in Figure 1-1. The higher the TET, the higher the thermodynamic efficiency of the turbine engine [1]. Such a temperature rise requires robust materials for turbine components (blades and disks) to withstand extreme stresses in such a harsh environment. As can be seen in Figure 1-1, turbine components are located in the hottest zone inside the turbine engine. Inconel 718 (IN718), a nickel-based superalloy, has been designed to meet these requirements. However, further improvements in the material properties and modifications in the design of IN718 parts are required to cope with the fast performance development of the advanced turbine engine generations. For instance, in the turbine blades, more internal cooling channels and design features were added to increase the part capability to withstand such high temperatures [1,2]. Figure 1-2 shows the historic development of the blade material capabilities in relation to TET while factoring the use of cooling systems and thermal barrier coatings. As can be seen from this figure, initially, there was no cooling system used since the temperature was under the capability limit, whereas with the development of the turbine engines (increase in TET), cooling systems became necessary.

From 1950 to date, the IN718 components used in the elevated-temperature applications are in the form of cast and wrought products [3]. However, as a requirement of more cooling to increase the performance of turbine engines, more complex geometry of turbine blades is needed in contrast with the old designs. Such design changes become increasingly difficult and costly to be fabricated using conventional routes. Besides, other numerous challenges have been faced during the manufacturing of IN718 parts using casting and forging processes (further details are discussed in the literature review, chapter 2). Accordingly, significant attention is paid towards the possibility to produce these components directly using additive manufacturing. Among additive manufacturing techniques, the laser powder bed fusion (LPBF) process has received considerable interest in aerospace and energy applications due to its attractive advantages over the conventional techniques. More details about the LPBF process and its potentials are provided in chapter 2.

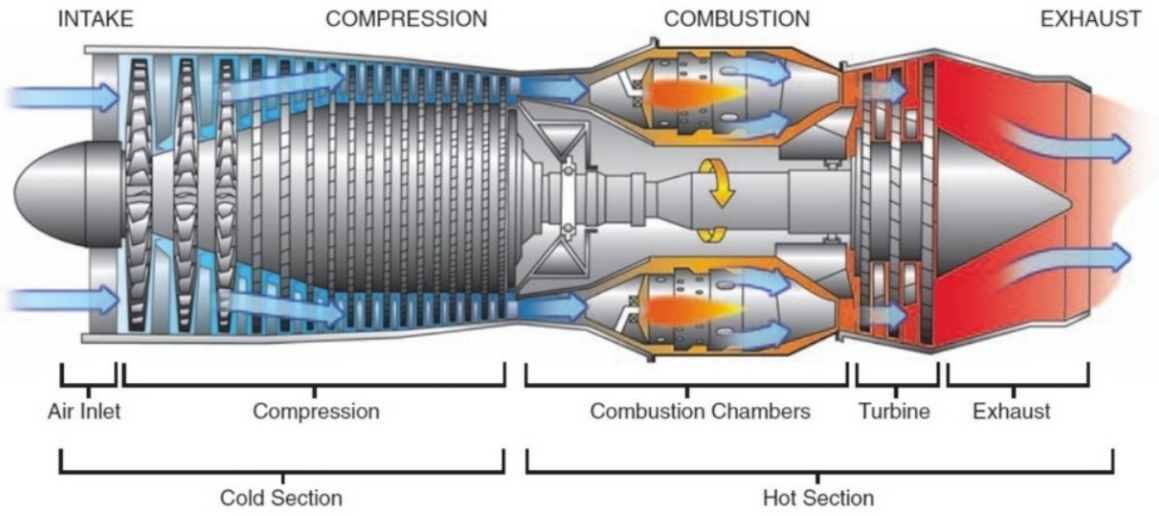

Figure 1-1: Diagram of the gas turbine engine with the basic components [4].

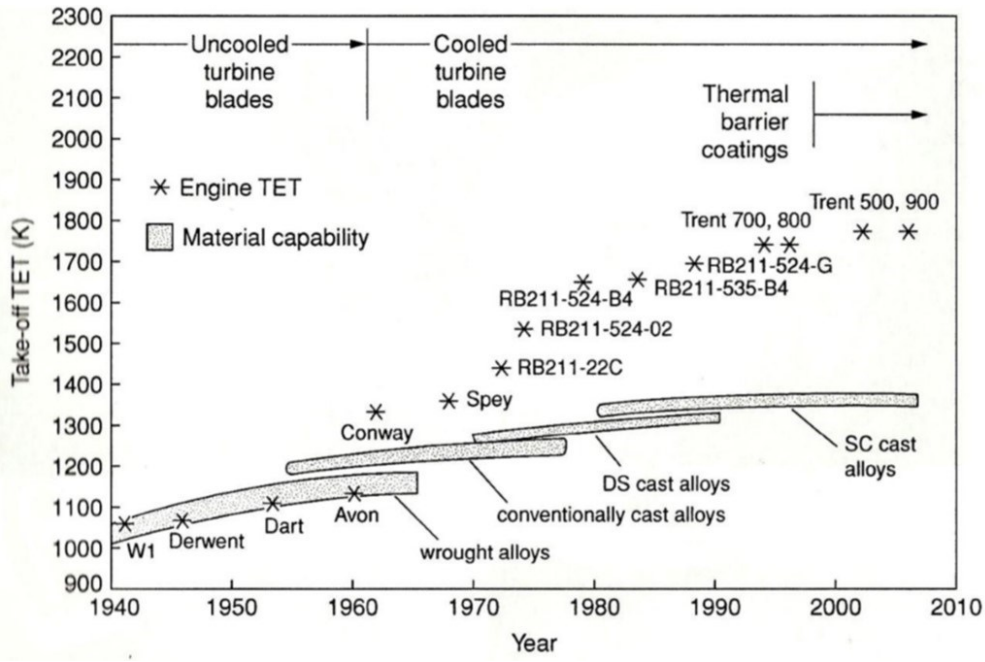

Figure 1-2: The historic development of the turbine blade with the TET [1].

Despite the great promises that the LPBF process has clearly exhibited, there is a number of drawbacks such as a high level of induced residual stresses, elemental segregation, heterogeneous microstructure, and anisotropic mechanical properties which have become obstacles for the industry to implement this technique in real production. Several studies were conducted to mitigate these drawbacks and maximize the potential of the LPBF process in industrial applications. It has been concluded that the post-heat treatment of the LPBF IN718 is required to combat such downsides and obtain the desired properties to meet the application requirements. However, so far, there are no standard specifications for the heat treatment of the LPBF IN718 parts similar to those existed for cast and wrought IN718. Most of the conducted research has been using the industrial standard heat treatment of the conventionally fabricated (cast and wrought) IN718 to improve the microstructure and mechanical properties of the LPBF IN718. All these attempts end up with non-encouraging results since each of these manufacturing techniques produces a completely different starting microstructure. Furthermore, the lack of information about the behavior of the additively

manufactured IN718 parts when exposed to service conditions for a long time keeps the LPBF process far from implementation in the real production of the critical components in the aerospace and energy industries. This shows that more investigations are still needed to identify the optimum heat treatment conditions that can be employed to mitigate such drawbacks.

1.2 Thesis outline

In this section, the thesis layout is outlined. Based on the approach followed in this research, the entire body of this dissertation consists of seven chapters. It is worth noting that the present dissertation is in a manuscript-based format containing four journal papers. Chapter 1 introduces the challenges encountered during the conventional fabrication of IN718 components demonstrating the importance of additive manufacturing as an alternative fabrication route. This chapter also discusses the associated problems with additive manufacturing of IN718 components using the LPBF process which still require further studies. Chapter 2 reviews in detail the potentials and drawbacks of the LPBF process to manufacture IN718 components. In the same chapter, previous efforts on the influence of different post-heat treatments on the microstructure and mechanical properties aiming to mitigate the drawbacks of LPBF IN718 are reviewed. On the basis of the literature findings, the research motivations and objectives are highlighted in this chapter. Chapter 3 presents the first article on the influence of the homogenization and solution treatments time on the precipitates, crystallographic texture, grain structure and room temperature mechanical properties of LPBF printed IN718. In Chapter 4, the second article on the evolution of the elevated-temperature mechanical behavior and fracture mechanisms of LPBF IN718 as a function of the homogenization and solution treatments time is presented. Based on the results obtained in Chapters 3 and 4, Chapter 5 presents the third article which addresses the optimization of the soaking time of both homogenization and solution treatments with an aim to develop a

suitable/standard heat treatment conditions of LPBF IN718 alloy. In Chapter 6, the fourth article investigates the impact of the in-service thermal cycle exposure of the aircraft turbine engines for a long time on the microstructure and elevated-temperature mechanical properties of the as-printed and optimum heat-treated LPBF IN718 alloy. Finally, Chapter 7 contains overall conclusions and contributions in the present study as well as recommendations for future studies.

Chapter 2 : Literature Review and Research Motivations

This chapter provides a review on the metallurgy of Inconel 718 (IN718), as one of the most important superalloys, and the role of its phases and alloying elements within the matrix along with a description of its cast and wrought form. The fundamentals and descriptions of the metallic-based additive manufacturing techniques are presented with a focus on the laser powder bed fusion (LPBF) process. The microstructure of the IN718 alloys fabricated by the LPBF process is reviewed along with the description of the main associated manufacturing drawbacks. The potentials of thermal post-processing studied in the literature to improve the microstructure and mechanical properties of LPBF IN718 are highlighted. Based on the literature findings, the need for more research is emphasized.

2.1 Superalloys

Superalloy is a term refers to a class of metallic materials that are designed to be employed in severe elevated-temperatures that can reach up to 0.7 of their absolute melting temperature while maintaining high mechanical properties and resistance to surface deterioration [5]. In the 1940s, superalloys were developed as an extension of stainless steel technology due to the frequent failure of stainless steels in gas turbine engines [6]. Inside typical gas turbine engines, the basic components can be divided into two sections: cold and hot sections [1]. The cold section consists of the intake and compression components where the experienced temperature is relatively low, thus titanium alloy is used to fabricate these components [1]. On the other hand, the hot section consists of a combustion chamber, turbine and exhaust components that require materials with high capabilities such as superalloys to withstand such a harsh working environment.

Superalloys can be traditionally classified into three main categories based on the dominant present metals in the alloy such as cobalt-based superalloy, iron-based superalloy and nickel-based

superalloy [5,6]. It is important to notice that the face-centered cubic (FCC) structure is the common crystal structure for all superalloys since the material with FCC structure is distinguished by its toughness and ability to attain high mechanical properties at elevated temperatures [6]. In the cobalt-based superalloys, the material strengthening depends on the solid solution strengthening mechanism and precipitation of the intermetallic phase (Co_3M) which is equivalent to the γ′ phases in the nickel-based superalloy. However, it is not as hard as nickel-based superalloys [5]. Extreme high-temperature components are usually fabricated from the cobalt-based superalloys due to their ability to maintain stable mechanical properties at a very high temperature such as 1100°C [5].

In the Iron-based superalloys, the strengthening mechanism is similar to the nickel-based superalloy, solid solution and precipitation hardening strengthening mechanisms [7]. However, it is less expensive than nickel and cobalt-based superalloys [1]. Iron-based superalloys are often used as a wrought material rather than cast. Nickel-based superalloys are the most widely used superalloy in high-temperature applications, as up to 50 % of the weight of the modern aircraft engine is manufactured from this alloy [5]. Depending on the application, it can be used as a wrought or cast material. Nickel-based superalloys can be subcategorized into several alloys by changing the chemical composition and microstructure such as Inconel 600 (76Ni-15Cr-8Fe), alloy 601 (lower nickel content (61%) with aluminum and silicon additions), Nimonic 75 (80/20 nickel-chromium alloy with addition of titanium and carbon), alloy X750, alloy X (48Ni-22Cr-18Fe-9Mo) and Inconel 718 (55Ni-21Cr-5Nb-3Mo) [5].

2.2 Inconel 718 superalloy

Inconel 718 (IN718) is a nickel-based superalloy developed by the International Nickel Company in 1959 [8]. Initially, in 1960, the major applications of the IN718 alloy were in the

military engines. For instance, it was used for the manufacturing of engine parts in the surveillance and reconnaissance aircraft (SR-71 Blackbird) [8]. Then, in the late of sixties, IN718 was extensively used in numerous commercial engines especially in gas turbine engines. It has been reported that, among the Inconel family, around 35 % of all superalloy production is counted for IN718 alloy [8]. This due to its competitive price, since it contains low cobalt and high iron contents, in addition to its superior strength, fatigue and creep properties at elevate temperatures [8]. Also, it possesses a high resistance to oxidation, wear and corrosion at high temperatures.

IN718 is a multicomponent superalloy composed mainly of Ni, Fe, Cr, Nb, Ti, Al and Mo with a wide range of chemical composition as shown in Table 2-1. Each alloying element is added to provide favorable properties and precipitate particular phases. In Table 2-1, the role of each element with the matrix of IN718 superalloy is listed.

Table 2-1: The effect of alloying elements in the Inconel 718 superalloy [5,9–11].

Element	Weight %	Effect
Ni	50 ~ 55	Solid solution base
Cr	17 ~ 21	Solid solution strengther, improve hot corrosion and oxidation resistance, $M_{23}C_6$ carbides former
Nb	4.75 ~ 5.5	Strengthening phase former γ″ (Ni_3Nb), M_6C and MC carbides former
Ti	0.65 ~ 1.15	Strengthening phase former γ′ ($Ni_3(Al,Ti)$), MC carbides former
Al	0.2 ~ 0.8	Strengthening phase γ′ ($Ni_3(Al,Ti)$) former, improve hot corrosion and oxidation resistance
Mo	2.8 ~ 3.3	Solid solution strengthener, M_6C, $M_{23}C_6$ and MC carbides former, improves the tribological properties and wet corrosion resistance
Co	< 1.0	Solid solution strengthener, increases the solvus temperature of γ′ phase
Cu	< 0.3	Solid solution strengther
B	< 0.006	Grain boundary strengthener, enhances rupture strength and creep properties
C	< 0.08	Grain boundary strengthener
Fe	Balance	Solid solution strengther

2.2.1 Phases and their properties in IN718

IN718 is a multiphase superalloy with a γ-matrix as the primary phase and a variety of secondary phases such as γ′ and γ″ strengthening phases, δ, Laves and carbides [12]. Controlling the type, content, distribution, and size of these precipitations optimizes the microstructure and mechanical properties of IN718 superalloy [13]. The chemical composition and crystal structure of these phases are shown in Table 2-2. In the following sections, further details of primary and secondary phases are discussed.

Table 2-2: Crystal structure and chemical formula of secondary phases in the IN718 superalloy [14].

Phase	Chemical formula	Crystal structure	Space group
γ	Ni,Cr,Fe – Based	FCC	Fm-3m
γ′	$Ni_3(Al,Ti)$	FCC (ordered $L1_2$)	Pm-3m
γ″	Ni_3Nb	BCT (ordered $D0_{22}$)	I4/ mmm
δ	Ni_3Nb	Orthorhombic	Pmmn
Laves	$(Ni,Fe,Cr)_2(Nb,Mo,Ti)$	Hexagonal	P63/ mmc
MC carbide	(Nb,Ti)C	Cubic	Fm-3m
$M_{23}C_6$ carbide	$(Cr,Fe)_{23}C_6$	Cubic	Fm-3m

2.2.1.1 Gamma phase (γ)

The gamma phase (γ) is the primary phase that represents the matrix of the IN718 superalloy. It is a solid solution with the following constituent elements: Ni, Fe, Cr, Nb, Ti, Al and Mo [10]. The addition of these alloying elements to the host nickel alloy forms a variety of secondary phases that significantly affects the microstructure and mechanical properties of IN718 alloy.

2.2.1.2 Gamma prime phase (γ')

Gamma prime (γ′) is an intermetallic phase with an ordered FCC $L1_2$ structure. Figure 2-1a shows the unit cell structure of the γ′ phase that consists of Al and Ti atoms at the corners of the

unit cell and Ni atoms at the center of the unit cell faces [10]. γ′ coherently grows within γ-matrix in a spherical morphology which precipitates as a result of aging treatment [15]. The precipitation temperature of γ′ begins at 649°C and the solvus temperature is between 843 and 871°C [10]. The maximum precipitation rate of the γ′ is within a temperature range of 732 to 760°C [10]. γ′ plays a considerable role in the hardening of the IN718 alloy, but not more than the gamma double prime (γ″) which is discussed in the next section. The contribution of the γ′ phase to the strengthening of the IN718 alloy represents 10 to 20 % [10].

2.2.1.3 Gamma double prime phase (γ")

Gamma double prime (γ″) is a metastable phase with an ordered body-centered tetragonal (BCT) $D0_{22}$ structure as shown in Figure 2-1b [15]. As can be seen in this figure, Nb atoms are located at the corners and the center of a tetragonal cell that consists of two FCC cells one on the top of the other, whereas the Ni atoms are located at the center of the unit cell faces. γ″ is the primary strengthening phase of the IN718 superalloy which precipitates during aging treatment. The lattice mismatch between the coherent interfaces of γ″/ γ is the main strengthening mechanism of γ″ to strengthen the γ-matrix but it is also the main cause of its transformation to δ-phase [11]. γ″ is susceptible to transform into the equilibrium δ-phase during the in-service operation or heat treatments (temperatures above 816°C) [10]. This transformation phenomenon can be retarded by increasing the content of the Al+Ti and/or Al/Ti ratio in the IN718 superalloy [11]. By increasing the content of Al+Ti and/or Al/Ti ratio in IN718, the lattice mismatch between the metastable γ″ and γ-matrix reduces as well as the size of γ″ that consequently reduces the driving force for δ-phase formation [11]. The morphology of the γ″-phase is a disc-shape which grows coherently within the γ-matrix. γ″ begins to form under the normal exposure at temperatures between 649 to 760°C. By comparison with γ′, γ″ contributes more to the strength of IN718.

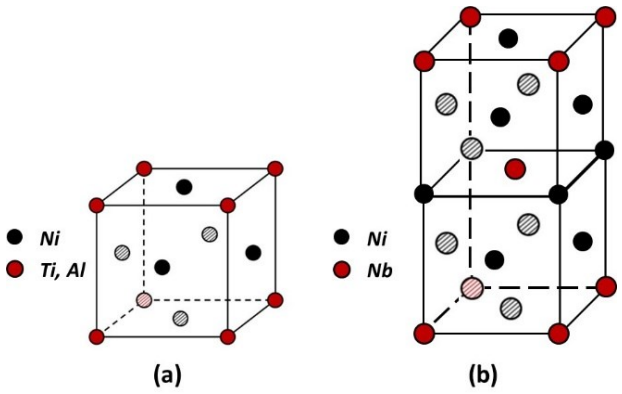

Figure 2-1: Crystal structure of: (a) γ′ [15], and (b) γ″ [10].

2.2.1.4 Delta phase (δ)

Delta (δ) is a compound with an orthorhombic crystal structure [10]. Despite δ is considered as a stable phase, it grows incoherently with the γ-matrix in the IN718 superalloy [10,11]. Thus, its contribution to the strength of IN718 alloy is insignificant [10]. The precipitation temperature range of δ-phase is between (700 – 1000°C) with a maximum precipitation rate at 900°C, while the solvus temperature is 1038°C [13]. In the literature, there are discrepancies around the kinetics of δ-phase formation. According to Eiselstein [16], five hours at a temperature of 927°C is required to form δ-phase. However, Keiser *et al*. [10] reported that δ-phase starts to form after only 15 to 20 minutes at the same temperature. There are two common morphologies of δ-phase, needle-like and spherical shape. The morphology stability of the δ-phase is dependent on the temperature [17,18]. At temperatures below 930°C, the needle-like shape is the more stable, whereas above 1010°C, the stable morphology is spherical shape [18]. At the temperatures between 930 and 1010°C, both morphologies of δ-phase, needle-like and spherical, are stable [18].

The size and content of the δ-phase play a significant role in the microstructure evolution and mechanical properties of the IN718 superalloy. Under certain circumstances, δ-phase has favorable influences on the microstructure and mechanical properties of IN718. According to the study of Dunyong [11], the presence of 4 % of δ-phase at the grain boundaries can effectively prevent grain

growth during the in-service exposure and heat treatments. Besides, improving the grain boundary strength and restricting the grain boundary sliding are other beneficial effects of the δ-phase. Li *et al.* [19] reported that the presence of spherical δ-phase along the grain boundaries enhances the creep and stress rupture properties [19]. They attributed this behavior to the retarding effect of the δ-phase against the inter-granular crack propagation which is the dominant failure mechanism [19]. Despite these benefits, the non-optimum amount and size of δ-phase would harm the microstructure and the mechanical properties of the IN718 superalloy.

2.2.1.5 Laves phase

Laves is a brittle intermetallic phase with a chemical composition of $(Ni,Fe,Cr)_2(Nb,Mo,Ti)$ which precipitates as a result of Nb, Mo and Ti segregation during the solidification stage [11]. Laves phase forms at the areas where these elements are rejected from the dendrites to the inter-dendrites zone as well as grain boundaries [11]. Microscopically, Laves phase appears a bright white particle [10]. It is well-recognized that the precipitation of Laves phase is detrimental to the mechanical behavior of the IN718 superalloy because of its brittle nature. Thus, areas occupied by Laves phase act as preferred sites of voids formation and cracks propagation [11]. Besides, Laves phase consumes a lot of Nb from the matrix which is the principal element for the precipitation of the strengthening phase γ″ [10,11].

2.2.1.6 Carbides

There are four common forms of carbides in the nickel-based superalloys: MC, $M_{23}C_6$, M_6C and M_7C_3 [3]. Further details of each form are provided below.

- **MC carbide**

MC-type carbide refers to the (Ni,Ti) C which is denoted as the primary carbide phase in IN718 superalloy that forms at high temperatures [1,11]. The Nb-rich MC carbide is the dominant carbide

phase in the IN718 due to the relatively high amount of Nb. Being beneficial or detrimental to the mechanical properties, it mainly depends on its size and distribution. Under a microscope, MC carbide appears as gray irregular-shaped particles (blocky shape) that distribute randomly within the grains as well as the grain boundaries [11].

The presence of fine MC-type carbide within the matrix (intra-granular MC carbide) strengthens the material through impeding the dislocation movements but its contribution to the strength of IN718 is very little when compared with the γ″-phase [11]. Moreover, these carbides can be oxidized and/or be cracked under the thermal stresses if they are at the surface of the components resulting in the formation of an undesired surface notch that adversely affects the fatigue properties [20].

On the other hand, the precipitation of inter-granular MC carbide may result in the transition of the fracture mode from intra-granular to inter-granular mode [11,21]. During plastic deformation, the inter-granular MC carbide particles imped the dislocation movements that concentrate at the interface between the matrix and MC carbide causing micro-voids and micro-cracks to release the stress concertation which consequently result in inter-granular fracture [11]. However, it has been reported that its presence at grain boundaries (when properly formed) has some beneficial effect in strengthening the grain boundaries by restricting its sliding and improving the rupture life [1,3,11].

- **$M_{23}C_6$ carbide**

In $M_{23}C_6$ carbide, M usually refers to Fe, Mo, Cr and W [3]. $M_{23}C_6$ has several morphologies such as films, globules and platelets, and mostly precipitates at the grain boundaries at lower temperatures during service conditions or aging treatment [1,3]. It has been reported that its precipitation in films form along the grain boundaries harms the material ductility at low and high

temperatures [1,3,22]. Also, it might form due to the breakdown of large size MC-type carbide at the grain boundary through the movement of metal atoms from carbides to γ-matrix according to the following reaction.

$$\gamma + MC \rightarrow M_{23}C_6 + \gamma' \text{ [1,22]}$$

- **M_6C carbide**

M usually refers to Mo and W in M_6C-type carbide [3]. It is a randomly distributed carbide and appears as blocky-shape particles with pinkish color under the microscope [3].

- **M_7C_3 carbide**

M usually refers to Cr in M_7C_3 and it is not a stable carbide type which transforms into $M_{23}C_6$ [3]. It is usually observed at the grain boundaries in a blocky irregular-shape.

2.3 Conventionally-manufactured IN718 and its standard heat treatment

2.3.1 Cast IN718 superalloy

The casting of the IN718 superalloy was developed due to the demand for fabricating complex components in different applications such as the aerospace and energy industries. These complex shaped-parts are often produced by investment casting of IN718 cylindrical bars produced by vacuum induction melting [23,24]. Figure 2-2 shows the procedure of the investment casting process. As can be seen from this figure, a disposable model of the component to be cast is fabricated using wax material [3]. Then, this model is covered using ceramic slurry to build a mold cavity of the component [3]. The wax model is then melted and disposed of using a steam autoclave to evacuate the ceramic mold cavity [3]. The molten metal is poured into the ceramic mold cavity. After solidification, the ceramic mold is destroyed to remove the cast component to be cleaned and surface finished.

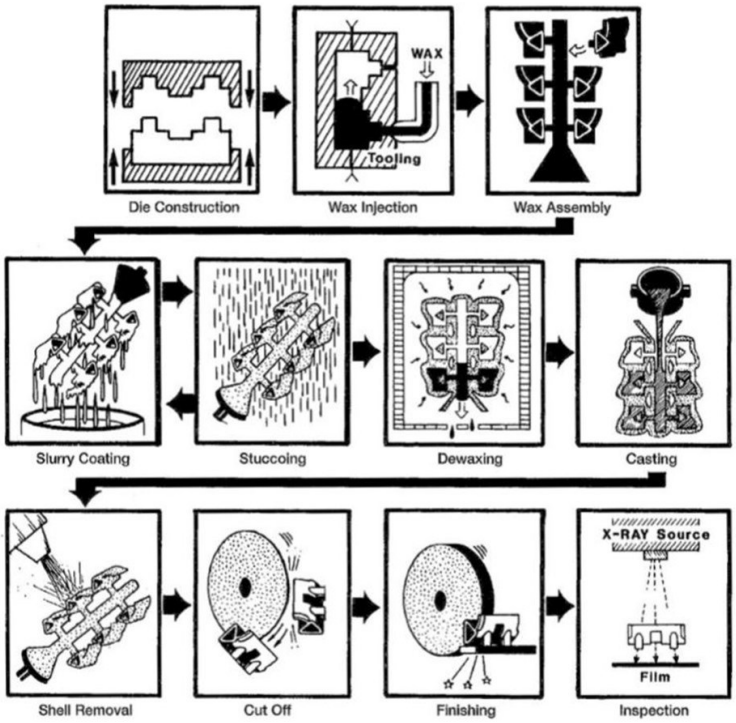

Figure 2-2: Schematic diagram showing the procedures of the investment casting process [20].

Although the present cast IN718 parts have some microstructural defects such as coarse grains and macrosegregation which lead to poor mechanical properties, cast IN718 is still used in the manufacturing of combustor cases, fuel nozzle rings, compressor and turbine frames, and other hot engine structures in the aircraft engines [11,25]. This is after applying the standard heat treatment (SHT) of the cast IN718 according to the aerospace material specification (AMS 5383) as listed in Table 2-3. In cast IN718, the presence of Laves and inter-dendritic macrosegregation requires a homogenization treatment at high temperature to completely dissolve these detrimental phases and segregated elements. However, the high temperature of the homogenization treatment would dissolve that grain boundary δ-phase. The dissolution of δ-phase would deteriorate the grain boundary strength and decrease the mechanical properties of the IN718 during in-service thermal exposure. Thus, solution heat treatment after the homogenization treatment is required to re-precipitate the δ-phase.

Table 2-3: Industrial standard heat treatment of cast IN718 superalloy according to AMS 5383 [11,26].

ASM specifications	Homogenization heat treatment	Solution heat treatment	Aging treatment
AMS 5383	1080°C for 1h followed by air cooling	980°C for 1h, followed by air cooling	720°C for 8h, furnace cooling to 620°C with 55°C/h, holding at 620°C for 8h, followed by air cooling

2.3.2 Wrought IN718 superalloy

Wrought is a word that takes the meaning of the past or the past participate of the verb "work", so "wrought IN718" means "worked IN718" [27]. Wrought IN718 is a process of mechanical working of a cast billet or ingot IN718 at high temperature to obtain the desired final IN718 components [11]. Figure 2-3 shows the common forms of the wrought working process. The microstructure of the wrought IN718 tends to be more homogenous than that of the cast, as the macrosegregation precipitated during the casting process is dissolved and dispersed after the repeated heating during the working processes [3]. Moreover, the grain structure in wrought material is finer than the coarse cast microstructure due to the plastic deformation during the working processes [3]. Through working processes, a wide range of mechanical properties can be obtained from a single alloy composition by controlling the introduced deformation parameters (temperature, strain rate and amount of work energy) [3].

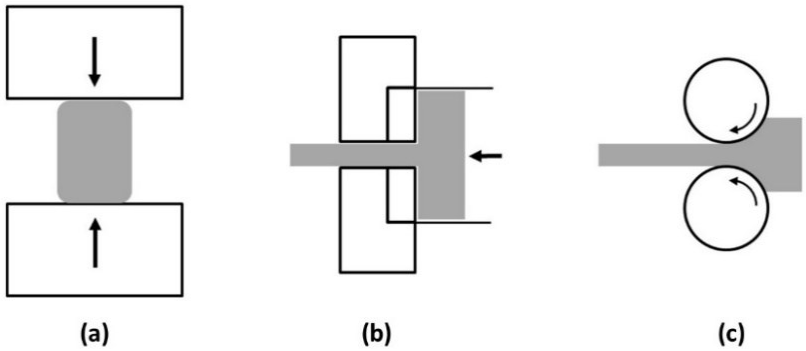

Figure 2-3: The common forms of wrought processes: (a) forging, (b) extrusion, and (c) rolling [20].

Wrought is the dominant form of IN718 components in most industrial applications [11]. This is because of its fine and homogeneous microstructure. According to the AMS, there are several SHTs for wrought IN718 as shown in Table 2-4. Such a variety in the treatment conditions comes from the variation in the required properties for different applications. For instance, in gas turbine disks, high tensile strength, high fatigue and rupture strength are required, so SHT1 is used to obtain such required properties [11]. It is interesting to note that the solution treatment in SHT1 is carried out at lower than the solvus temperature of δ-phase (≈ 1038°C) to precipitate δ-phase because it is known that the presence of a proper amount of δ-phase at the grain boundaries improves the rupture and tensile strength [11]. For some other applications, SHT2 is used to produce components with high ductility and impact strength [11]. In SHT2, the solution temperature is above the dissolution temperature of δ-phase to prevent it from precipitation due to its harmful impact on the material ductility [11]. Finally, it can be concluded that the selection of suitable SHT is dependent on the required properties of the IN718 components.

Table 2-4: Industrial standard heat treatment of wrought IN718 superalloy AMS [11,26]

	ASM specification	**Solution heat treatment**	**Aging heat treatment**
SHT1	AMS 5596 AMS 5589 AMS 5662 AMS 5562	927 ~ 1010°C for 1~2h, followed by water cooling	719°C for 8h, furnace cooling to 621°C, holding at 621°C for a total aging time of 18h, followed by air cooling
SHT2	AMS 5597 AMS 5590 AMS 5663 AMS 5564	1038 ~ 1066°C for 1~2h, followed by water cooling	760°C for 10h, furnace cooling to 649°C, holding at 649°C for a total aging time of 20h, followed by air cooling
DA	-	-	719°C for 8h, furnace cool to 621°C, holding at 621°C for a total aging time of 18h, followed by air cooling

2.3.3 Challenges of conventional manufacturing of IN718 alloys

To date, IN718 components, which are extensively used in a wide range of elevated-temperature applications in turbocharger rotors, aircraft, liquid-fueled rockets and nuclear reactors, are in the form of wrought, cast and powder metallurgy products [20,28]. However, the high hardness, poor machinability, low thermal conductivity and inferior high-temperature ductility of IN718 alloy possess dramatic difficulties during forming and conventional machining [28]. Also, IN718 components are becoming ever more complex along with the acceleration of engine performance improvement which consequently adversely affected the fabrication cost, and in some cases, are even impossible to incorporate in the manufacturing process using existing traditional methods. Most importantly, using conventional manufacturing methods, the high buy-to-fly ratio of IN718 components can reach up to 20 [29].

Due to these challenges, a new and effective manufacturing method is required to avoid the encountered difficulties and cope with such fast development in the application design. Additive manufacturing is one of the promising alternatives for producing IN718 parts and growing interests in various industrial applications.

2.4 Additive manufacturing

Additive manufacturing (AM) is a group of manufacturing processes that use the layer-by-layer concept to fabricate near net-shape 3D components from a digital 3D model [11]. According to the American Society for Testing and Materials (ASTM), AM is defined as “a process of joining materials to make objects from 3D model data, usually layer upon layer, as opposed to subtractive manufacturing methodologies” [30]. Initially, in 1987, AM emerged as a rapid prototyping (RP) technique [31]. Then, in recent years, the functionality of AM is shifted from RP to be used in rapid manufacturing (RM) of near net shape products and rapid tooling (RT) [32]. This is due to

its distinct advantages over traditional manufacturing such as its freedom to manufacture complex components without the need for specific tooling which are either impossible or more expensive to be fabricated using subtractive processes [25]. Besides, a reduction in manufacturing time, low production cost and low buy-to-fly ratio are other advantages of AM [25,33–35]. Therefore, AM has gained significant attention in various industries such as aerospace, automotive and medical applications.

2.4.1 Metallic-based AM

According to the (ASTM F42) standard, AM is classified into 7 categories [36]. Each category differs depending on the material used, heating source, the deposition technique, or the way by which the material is fused or solidified [36]. Among the AM categories, powder bed fusion (PBF), direct energy deposition (DED), binder jetting (BJ) and sheet lamination (SL) are the only manufacturing processes used to fabricate metallic. In the BJ process, metallic powder is used as a raw material which is selectively joined using a jet of a liquid bonding agent. However, its applications are very limited due to the structure of the produced parts that includes a binder material which is not suitable for most of the industrial applications. Whereas in the SL process, metallic sheets are bonded together using ultrasonic welding to form 3D objects. After SL printing, post-processing is required such as CNC to remove the unbonded sheets and finalize the end-use product. For the DED process, a metallic material, in a form of powder or wire, is melted using a laser or electron beam source and coaxially deposited onto the specific surface where it solidifies. It can be used for repairing of existing components and/or manufacturing of near net shape components. This technique is distinguished by its high deposition rate (≈ 2 layers/minute) and the potential to fabricate large-scale components [37]. However, its high manufacturing speed is at the expense of product accuracy and surface quality. Thus, a balance between the fabrication speed

and product quality is required. DED has several different synonyms such as direct metal deposition (DMD), laser engineered net shaping (LENS), directed light fabrication (DLF) and 3D cladding [37]. In the PBF process, the metallic powder is selectively melted and fused using either a high-intensity laser beam or electron beam to form three-dimensional (3D) objects. The laser-based powder bed fusion (LPBF) process includes some processes which share the same feedstock AM methods such as selective laser melting (SLM) and selective laser sintering (SLS) [37,38]. Each process exhibits distinct microstructure and mechanical properties due to the various metallurgical mechanisms such as partial melting and complete melting during the SLS and SLM, respectively [38]. However, some manufacturers of AM machines recently use both terminologies for the same process concept, which is SLM, for a marketing and advertising purpose. The LPBF process is distinguished by a higher cooling rate (10^5°C/s) and better surface finishing in relation to DED processes [26]. As a result of this, finer microstructure and higher mechanical properties can be obtained when compared to those obtained using DED processes. Thus, more interests are directed towards the LPBF process to fabricated critical components in different industrial sectors. The LPBF is the process used in this research, thus it is discussed further below.

2.4.2 Laser powder bed fusion process (LPBF)

The LPBF operation is schematically shown in Figure 2-4. Before the printing process, a CAD model of the component is prepared. Then, the volume of the CAD model is sliced into cross-sections with even thickness equal to the layer thickness used in the LPBF process parameters. The powder on the building platform is pre-heated to mitigate the thermal gradient and minimize the thermal stresses during the printing process. Also, the building chamber is evacuated and filled with argon gas to minimize oxidation effects. The printing process starts with a deposition of a thin layer of metallic powder with a thickness of 20 – 30 mm on the top of the building platform

using a rotating powder-leveling roller [6]. The two powder feed cartridges on both sides are responsible for feeding the powder bed by the metallic powder needed for each layer. A focused laser beam is then directed to the deposited layer to melt and fuse the metallic powder according to the cross-section of the 3D model. The surrounded powder remains loose and acts as a support for the subsequent layers. After finalizing this layer, the building platform moves down with displacement equal to the layer thickness. Then, one of these side cartridges moves up to provide the required powder for the new layer which is spread upon the powder bed using the rotating powder-leveling roller. The focused beam scans the new layer that corresponds to the subsequent cross-section. This process is frequently repeated until the 3D component is built. Finally, the built component is removed from the powder bed after the temperature of the building chamber cool-down to low temperature and then the loose powder is cleaned off the component.

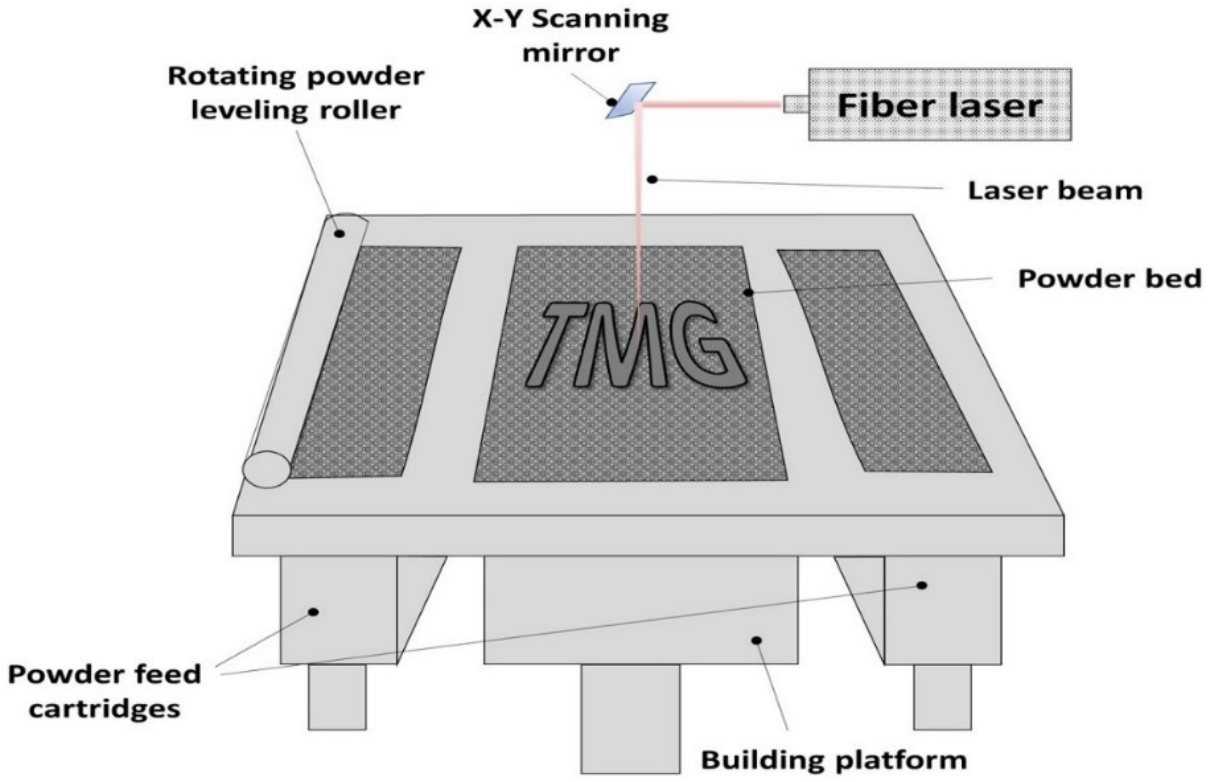

Figure 2-4. Schematic drawing of the laser powder bed fusion process (redrawn from [39]).

2.4.2.1 LPBF process parameters

The LPBF process parameters can be divided into four main categories: laser beam parameters, laser scanning parameters, powder-related parameters, and temperature-related parameters, as shown in Figure 2-5 [40]. Numerous studies were conducted to investigate the influence of these parameters on the microstructure and mechanical properties of LPBF parts. Choi *et al*. [41] studied the effect of changing laser scanning speed (100 mm/s to 1600 mm/s) at a constant laser power of 90W on the microstructure of IN718 superalloy. Their [41] results show that the porosity percentage was reduced by decreasing the laser scanning speed. The lowest porosity (0.35%) and highest hardness (320HV) were obtained at 800 mm/s scanning speed which corresponds to a laser energy density of 110 J/m [41]. Yap *et al*. [42] investigated the effect of laser energy on the LPBF

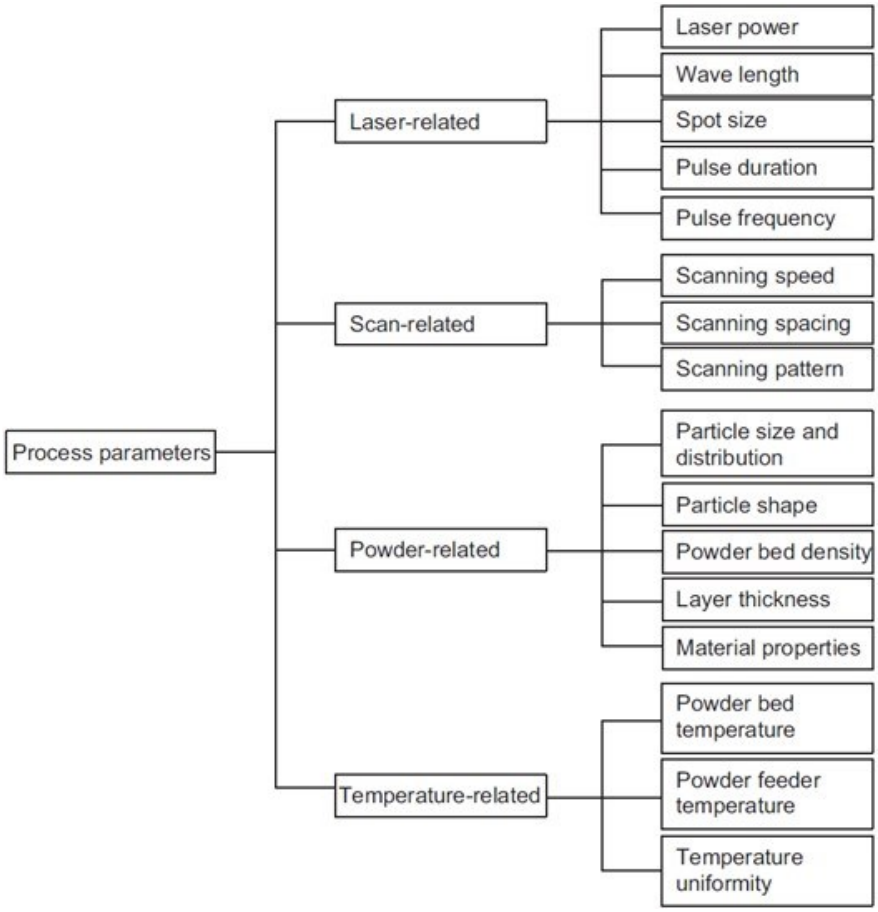

Figure 2-5: The principle process parameters of the laser powder bed fusion process [40].

parts quality. Their [42] results demonstrate that the insufficient laser energy (low laser power and/or high scanning speed) resulted in a balling effect and un-melted powder inside the LPBF components which deteriorated the process quality. However, very high laser energy (very low scanning speed) has been reported to bring about keyhole effect and evaporation which diminishes the component density [42]. Therefore, it is required to optimize laser energy density in order to obtain dense products.

Furthermore, an improper hatch angle has also been reported to have a significant effect on the mechanical properties of as-fabricated components. Guan *et al*. [43] investigated the effect of hatch angle variation on the mechanical properties of LPBF printed 304 stainless steel. Their [43] results show that the tensile strength and elongation percentage were enhanced by increasing the interval number (N). N is the number of layers necessary to return to the original scanning direction as shown in Figure 2-6. The authors [43] attributed this behavior to the larger relief of stress concentration and the lower degree of anisotropic properties that were obtained at a maximum interval number. Moreover, Shiom *et al*. [44] studied the effect of powder bed temperature and re-scanning of the laser beam on the distribution of residual stress within LPBF printed chromium-molybdenum steel (SCM440). Their [44] results reveal that the residual stress at the top surface of the manufactured steel was reduced by 40% when heating the base plate to 160°C. Besides, residual stress was reduced by 55% through laser beam re-scanning with the same laser process parameters that were used to manufacture SCM440 components [44].

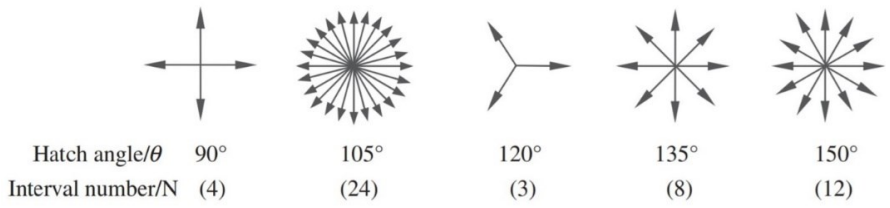

Figure 2-6: Schematic drawing illustrates the interval number corresponding to different hatch angles [43].

2.4.3 LPBF of IN718 superalloy

Among all metallic-based AM processes, the LPBF process has received significant attention to fabricating critical metallic parts in various applications especially in the aerospace industry [45]. This is due to its great potential to produce dense metallic components with a high relative density that can reach up to 99.7% and high dimensional precision using the optimum laser process parameters [46]. Moreover, a large range of metallic engineering materials are successfully processed using the LPBF such as aluminide, stainless steel (e.g. PH 17-4) titanium alloys (e.g. Ti-6Al-4V) and nickel-based alloys (e.g. Inconel 625, Inconel 718, etc.) [6,47]. IN718 has been frequently processed using the LPBF, as IN718 possesses good resistance to hot strain-age cracking due to the sluggish precipitation kinetics of the strengthening phases (γ'' and γ') [11].

Compared to the cast IN718, the LPBF of IN718 superalloy exhibits microstructure and mechanical properties that outperform that of cast components and even reach the wrought standard properties after proper heat treatment [24,35]. Zhang *et al*. [24] investigated the differences in the microstructure and mechanical properties encountered during the LPBF and casting processes of IN718 superalloy. Their [24] results reveal that the microstructure of the LPBF IN718 was significantly finer with an average grain size of 52 μm and fine precipitates when compared to the cast IN718 with an average grain size of 1300 μm and coarse precipitates. Moreover, after heat treatment, the mechanical properties of the LPBF IN718 far exceeded the cast samples. They [24] attributed this difference to the higher cooling rate of the LPBF process in relation to the casting process. Similarly, Trosch *et al*. [35] studied the microstructure and mechanical properties of the heat-treated IN718 which was produced by three different techniques: LPBF, casting and forging. Their [35] results show that the room temperature tensile strength (TS) of the LPBF fabricated components, 1430 MPa, was higher than the cast and forged materials, 950

MPa and 1380 MPa, respectively. Furthermore, the elevated-temperature TS of forged and LPBF IN718 was very close. Therefore, the LPBF process is considered as a promising alternative that can be used to manufacture IN718 components for current aerospace industries.

2.4.4 LPBF IN718 drawbacks

Despite the great promises and improvement in the microstructure and mechanical properties of the LPBF IN718, there are still a number of drawbacks encountered during the manufacturing process that should be overcome to fully realize and maximize the potentials of the LPBF process. The LPBF process has a complex thermal cycle during its processing which is distinguished by: (1) high heating rate due to the localized intense laser energy; (2) rapid cooling and solidification rate due to heat source movement and the steep thermal gradient between the platform and molten pool temperatures; and (3) re-melting of the previously solidified layers simultaneous with melting of newly deposited one [48]. Such complex heating history results in producing IN718 with non-homogeneous microstructure and anisotropic mechanical properties, in addition to the high level of residual stresses that are induced in the manufactured components. In the following section, the LPBF drawbacks are investigated in detail.

2.4.4.1 Anisotropy

- **Microstructural anisotropy**

Microstructural anisotropy is a widely recognized phenomenon for the laser-based additively manufactured components which originates from the layer by layer and line by line scanning strategy of the laser beam [49]. In order to avoid the lack of fusion of the metallic powder during the laser beam scanning, overlaps between the adjacent laser tracks/passes in the horizontal (xy) plane as well as between the consecutive solidified layers in the vertical (xz) plane are usually performed as shown in Figure 2-7. Thus, changes in the microstructure among the overlapping

zones and the central bulk material, in terms of sub-structure size and direction, are observed. As can be seen from the xy-plane in Figure 2-7a, the overlapping zones (between two adjacent laser tracks) contain a coarser cellular/columnar substructure compared to the central areas since the overlapping zones experience double laser passes and more heat input.

Concerning the substructure direction, only cellular substructure is observed in the central zones, whereas in the overlapping zone, both cellular and columnar substructures are observed. This is because, during the laser beam scanning of the adjacent un-melted track, high thermal gradient and heat dissipation towards the previously solidified tracks exist as indicated by the red arrows in Figure 2-7a. This thermal gradient governs the substructure orientation along the direction of the heat flow to form such a columnar substructure in the laser track edge (overlapping zone). The same behavior is also observed in the overlapping zones between consecutive layers in xz-plane. Mostafa *et al*. [45] analyzed the morphological difference between the center zone (I) and edge zone (II) of the laser track areas of IN718 samples which were processed by LPBF. Their [45] results show that at zone (I), small grains size of 30 μm with fine dendritic arm spacing of 0.6 μm were formed, while zone (II) had a larger grain size of 50 μm with 1.25 μm dendritic arm spacing as shown in Figure 2-7b. The authors [45] attributed this difference to the overlapping laser passes in zone (II).

Moreover, the differences in the heat input between the first and last deposited layers along the building directions result in gradual changes in the microstructures of these layers. It has been reported by Tucho *et al*. [12] and Seede *et al*. [50] that the microstructure analysis of the top and bottom layers of vertically built samples revealed the precipitation of small γ′ and γ″ in the bottom microstructure only. This is because the bottom layers (first deposited layers) experience a repetitive heating process more than the top layers (last deposited layers) during the printing

process [12,50]. These further heating cycles act as an aging treatment to precipitate the strengthening phases γ′ and γ″ [12,50].

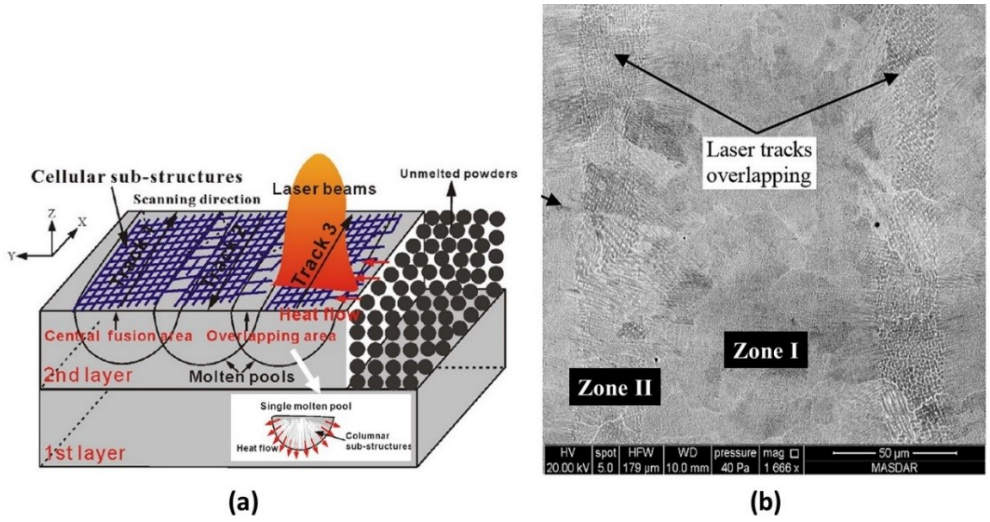

Figure 2-7. (a) Schematic drawing shows the heterogenous microstructure in xy-plane [13], and (b) real LPBF IN718 showing the overlapping zones in xy-plane [45].

- **Mechanical anisotropy**

Mechanical anisotropy of additively manufactured parts is strongly linked with the microstructural anisotropy. Several investigations have marked the existing of inconsistent mechanical properties of the LPBF printed parts. For instance, Tucho *et al*. [12] reported that such differences observed in the microstructure between the first deposited layer (bottom) and the last deposited one (top) caused the variation in hardness values from 301 ± 6 HV at bottom and 288 ± 7 HV at top [12]. Similar behavior is reported by Seede *et al.* [50].

Furthermore, the existence of columnar grain structure, which is the typical microstructure of the AM parts, is one of the root causes of high degree anisotropy in mechanical properties [51,52]. The presence of such elongated grains is attributed to the high thermal gradient along the building direction. This thermal gradient results from the high-temperature difference between the upper level of the powder bed, where the intense laser beam focuses, and the building platform. It has been reported that the ratio between the thermal gradient (G) and solidification rate (R), which is

influenced by the laser process parameters, governs the grain morphology [51]. Low G/R ratio results in equiaxed grains, whereas high ratio results in columnar morphology [51]. Such a columnar grain morphology results in a high dependence of as-printed mechanical properties on the printing orientation as shown in Figure 2-8a and b.

Chlebus *et al*. [46] used LPBF to fabricate IN718 samples in three different orientations (vertical, horizontal and 45°) to investigate the dependency of mechanical properties on the printing orientation. Their results demonstrate that as-printed tensile strength at room temperature of these orientations were 904, 991 and 954 MPa, and the elongation to failure were 19, 13 and 20 %, respectively [46]. The authors [46] attributed this behavior to the effect of columnar grain microstructure in the as-fabricated condition which was oriented parallel to the building direction. Besides, the preferred crystallographic orientation of the FCC crystal structure, <001>, resulted in a clear dependence of mechanical properties on the building orientation [35,46,52]. Similar behavior was observed by [34,46,52,53].

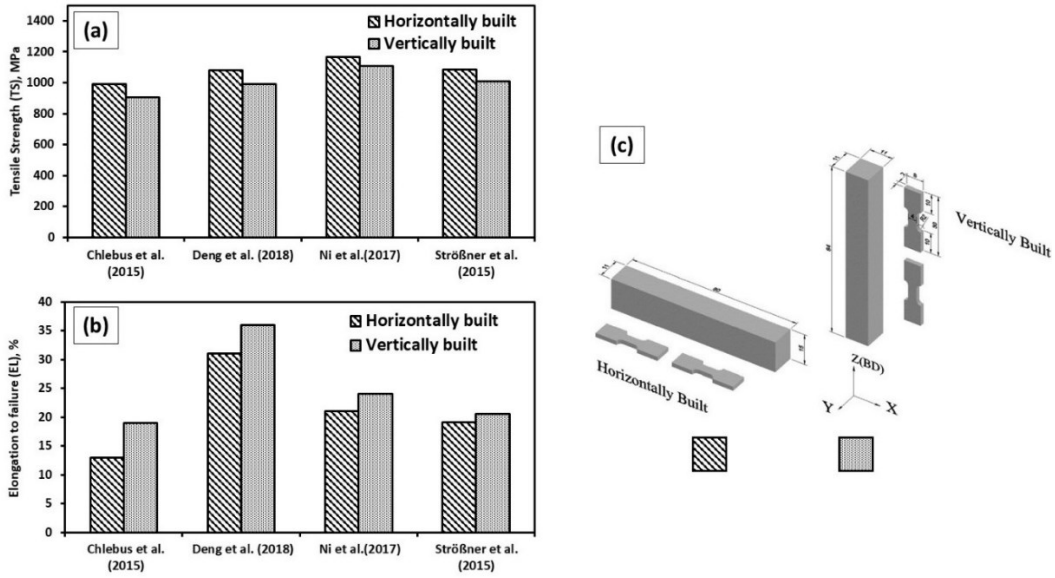

Figure 2-8. Differences in the tensile properties of the horizontally and vertically built LPBF IN718 in the as-printed condition as reported in [34,46,52,53]: (a) TS, (b) elongation to failure, (c) schematic drawing shows the orientation of the vertically and horizontally as-printed samples with respect to the building direction [53].

It is interesting to note from Figure 2-8 that the horizontally built samples often exhibit higher mechanical strength than those of vertically built samples, whereas the ductility has an opposite trend. This is attributed to the dependence of the material strength on the angle between the tensile loading direction and the slip direction of the FCC crystal structure of the IN718 that can be accounted for Schmid factor (μ), where the yield stress of the FCC can be calculated as follows:

$$\sigma_y \geq \frac{\tau_c}{\mu}, \quad \mu = \frac{1}{2}\sin 2\varphi \quad [52]$$

where σ_y is the yield stress, τ_c is the critical resolved shear stress and φ is the angle between the loading direction and the normal to the slip plane. According to this equation, the larger the Schmid factor, the lower the yield strength. Also, it is well-known that the slip system of the FCC crystal structure is $\{111\} < 110 >$ and the crystallographic orientation of (100) is the typical and preferred fiber texture (parallel to the building direction) of the AM IN718 (FCC) superalloy as illustrated in Figure 2-9a [52]. Thus, in the vertically built samples, the loading direction is parallel to the Z-axis, while in the horizontal ones, the loading direction is parallel to X/Y-axis. On the basis of these given data, the calculation shows that the Schmid factor in vertically built samples (≈ 0.47) is higher than that of the horizontally built samples (≈ 0.32) as reported by Mang *et al*. [52]. Therefore, lower strength is encountered for the vertically built samples relative to that of the horizontal samples.

Moreover, such anisotropy in the material ductility is attributable to the dependence of the cracking mechanism on the angle between the stress direction and the orientation of the columnar grains [52]. In the horizontal samples, the stress loading is perpendicular to the longest axis of the columnar grain boundary (Figure 2-9c) resulting in the Mode-I opening mechanism [52]. Thus, the pile of dislocations on the columnar grain boundaries results in stress concentration and, consequently, micro-cracks formation [52]. For the vertical samples, the stress direction is

perpendicular to the short axis of the columnar grain boundary (Figure 2-9b) which means more difficult for opening failure, thus higher ductility is obtained [52].

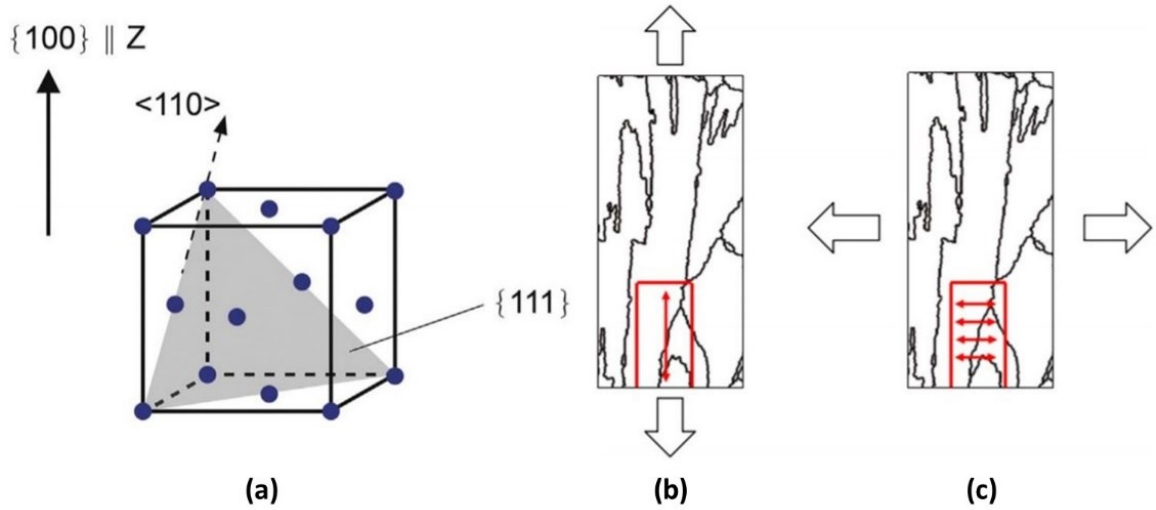

Figure 2-9: (a) The softest slip system in FCC crystal structure with respect to the strong fiber texture (100) in AM IN718 alloy, (b) and (c) schematic drawing shows the orientation of the tensile loading relative to the columnar grains in vertically and horizontally, respectively, build samples [52].

Furthermore, it has been reported that the accumulated residual stress and dislocation density in the LPBF fabricated samples play an important role in the dependence of the mechanical properties on the printing orientation [53]. Deng *et al.* [53] reported that the tensile strength and yield strength of LPBF IN718 samples produced horizontally were higher than that built vertically, while the elongation exhibited the opposite trend. They [53] concluded that the difference in mechanical behavior was not only due to the crystallographic orientation, but residual stress also contributed to this difference. In the horizontally printed samples, residual stress had its higher component parallel to the scanning direction, X direction, and increased by increasing the scanning vector length which is the total length of the distance traveled by the laser beam along the scanning direction [53]. Thus, higher mechanical properties along this direction were observed in relation to those vertically built due to the effect of the residual stress which caused strain hardening [53].

2.4.4.2 Elemental segregation

Segregation is an ubiquitous phenomenon during the LPBF processing of many engineering alloys due to solute rejection and redistribution during the solidification stage [54]. Figure 2-10 shows the stages of the elemental segregation along with the formation of columnar dendrites. As can be seen from this figure, initially, when the focused laser beam hits the paved metallic powder during the beam scanning, the upper layer starts to melt forming a planar liquid/solid interface. Then, protrusion forms, ahead of the solidification stage, in a direction parallel to the direction of the thermal gradient along with the building direction as shown in the second stage in Figure 2-10. The protrusion formation is associated with a lateral rejection of the solute elements from the matrix to concentrate at the root of the formed protrusion. The enrichment of these solutes results in a decrease of the equilibrium solidification temperature that consequently triggers the formation of other protrusions along the thermal gradient with also solute rejection at their roots [13]. Finally, the areas among the formed protrusions (inter-dendritic regions) enriched with the rejected solutes. For the LPBF of IN718 superalloy, it has been reported that Nb, Ti and Mo have high susceptibility to be rejected in the inter-dendritic and grain boundary regions [13].

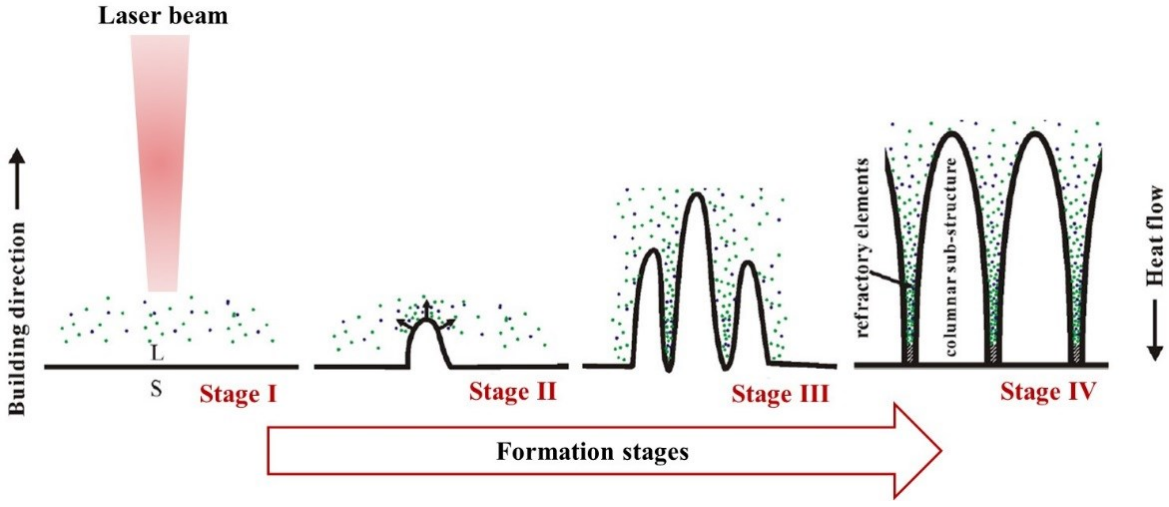

Figure 2-10: Schematic drawing illustrates the stages of solutes rejection along with the formation of dendritic substructure [13].

As a consequence of this phenomenon, changes in the local composition of IN718 alloy are observed to be outside the permissible limits range which consequently changes the physical and mechanical properties of the alloy [54]. In addition, the segregated refractory elements in the inter-dendritic and grain boundaries provide nucleation sites for the formation of undesired phases, such as Laves phase which adversely affects the mechanical properties of IN718 as reported by Li *et al*. [13]. They [13] investigated the microstructure evolution of the as-built IN718 samples fabricated by the LPBF. Their [13] results show that Nb and Ti tended to cluster near the inter-dendritic region at the end of the solidification stage. They [13] reported that the presence of this microsegregation resulted in the formation of the brittle Laves phase that consequently caused cracks formation at the areas where Laves phase formed.

2.4.4.3 Residual stress and distortion

Residual stresses and distortion in additively manufactured parts are common and occur due to the combined effects of the encountered complex thermal cycle during the printing process (localized and repetitive rapid heating followed by rapid cooling) and the high thermal gradient inside the building chamber [55]. Residual stresses in the material can be categorized into three different scales, type I, II and III [48]. Type I residual stress is in a macroscale level, in which the stresses continuously vary over a length scale comparable to the sample size. Type II and III are in microscale (length scale comparable to the grain size, misfit strain) and nanoscale (dislocations level), respectively [3,48]. Residual stresses of type II and III confer a limited effect on the mechanical properties of the AM processed material, whereas, type I has a dramatic effect on the bulk properties of the LPBF printed material [3]. In the LPBF process, there are two main mechanisms of formation of type I residual stress [56]. The first mechanism is caused by the Gaussian distribution of the laser beam energy along the horizontal direction that results in the

thermal gradient within the layer and non-uniform deformation during the cooling stage [56]. On the other hand, the second one occurs due to the thermal gradient along the building direction.

Figure 2-11 shows the second mechanism of residual stress formation. During the laser beam scanning, the top layer is heated rapidly, and the heated material tends to expand against the surrounding lower temperature medium. As a consequence, compressive stress is induced in the heated area as shown in Figure 2-11a. When the laser beam moves away, the heated layer begins to cool rapidly and contract. However, the top layer contraction is partially hindered by the substrate or the previously deposited layers due to the variation in the cooling rate and contraction level among consecutive deposited layers [48]. Thus, tensile residual stress in the solidified layers is generated which results in part distortion, loss of geometric tolerance and a dramatic deterioration in the part functionality as shown in Figure 2-11b [48]. Moreover, crack propagation along the grain boundary and delamination between the consecutive layers could be observed if the tensile residual stress surpasses the strength of the solidified metal [42,55].

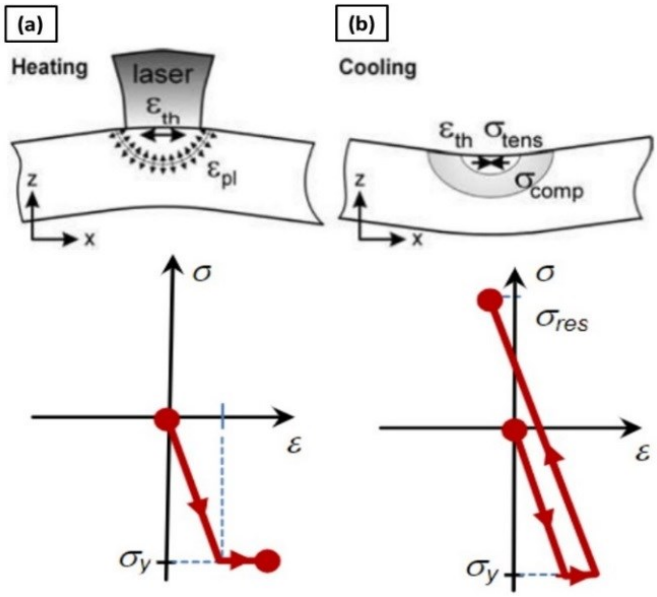

Figure 2-11: Schematic drawing shows the formation of residual stresses due to the thermal gradient: (a) during the heating phase, and (b) during the cooling phase [48].

2.4.4.4 Porosity and lack of fusion

Pores in the volume of LPBF fabricated parts, which have an adverse effect on the density and mechanical properties, stem from three main mechanisms: inadequate laser energy density, entrapped gas inside the raw powder particles during the gas atomization process (GA), and lack of fusion during solidification [47,55]. Utilizing a very high laser energy density (low scanning speed) results in forming unstable keyhole in the molten pool, leaving voids inside the solidified metal [55]. However, at a very high scanning speed (low laser energy density), the high viscosity of the molten metal prevented the liquid from spreading out smoothly which consequently resulted in open pores formation as reported by Jia *et al*. [57]. Thus, laser energy density should be optimized in order to obtain parts free from pores.

Furthermore, during the gas atomization process of metallic powder, atomizing gas could be entrapped inside the metallic particles forming spherical pores during the solidification stage [47,55]. Similarly, gas voids can be formed as a result of the entrapment of shielding gas that is used during the LPBF printing process. For the lack of fusion voids, the ratio between the molten pool depth and the layer thickness should be high enough to ensure proper metallurgical bonding between consecutively deposited layers and avoid the formation of this kind of voids [55]. Such pores act as stress raisers and crack initiation sites which cause premature failure. These defects cannot be totally avoided but can be minimized using contamination free powder, fine GA powder and proper laser energy density [47].

2.5 Thermal post-processing of LPBF IN718

The drawbacks of the LPBF process can be mitigated by a combination of a proper selection of laser process parameters, such as laser energy density and scanning strategy, and thermal post-processing in order to achieve the properties that fulfill the industrial requirements [9]. Over the

past few years, understanding the relationship between the process parameters, microstructure and mechanical properties of LPBF has attracted great interest. Abundant studies were conducted to optimize the laser process parameters and to tailor the microstructure and mechanical properties. However, some of the LPBF drawbacks such as residual stresses, directional grain growth and microsegregation are not totally overcome by only adjusting the process parameters. Therefore, more attention should be directed towards obtaining more information on the suitable thermal post-processing procedures to enhance the performance of IN718 parts fabricated by the LPBF process.

Thermal post-processing of LPBF parts serves diverse functions regarding the microstructural evolution and mechanical properties improvement. Residual stress relief, microstructure homogenization, strengthening phase precipitation, dissolving detrimental phases and recrystallization of the matrix are the most common beneficial effects of post-thermal treatments [58]. Generally, there are common thermal post-processing techniques that can be applied to IN718 superalloy such as HIP, homogenization, solution treatment and aging treatment [59]. The HIP is used for a twofold purpose – to close the internal pores in the AM parts by applying a high pressure under elevated-temperature and to homogenize the as-printed microstructure [59]. However, significant undesired change to grain structure may occur, in addition to a reduction in the fabricated part dimensional accuracy [60].

Homogenization treatment is applied to homogenize the as-printed microstructure, diffuse the segregated elements and dissolve the detrimental phases [11]. Thus, for the IN718 superalloy, a high temperature (1080°C) is used in the homogenization treatment to be close to the solvus temperature of the detrimental phases, Laves phase. The material is held at this temperature for a while to completely dissolve the Laves phase and diffuse the segregated elements in the matrix to release as much as possible the necessary elements for the precipitation of the strengthening

phases. Then, the material is rapidly cooled to room temperature to create a supersaturated matrix [61].

In the solution heat treatment, the material is heated to a temperature (980°C) slightly less than the solvus temperature of δ-phase and held until the proper amount of δ precipitates [11,59]. It is worth mentioning that to precipitate only inter-granular δ and avoid its presence within the matrix, the solution heat treatment should be preceded by a homogenization treatment step.

Aging heat treatment is applied in two stages to precipitate γ″ and γ′ phases. In the first stage, the IN718 material is heated to an intermediate temperature (≈ 720°C) and held for 8 hours, then followed by furnace cooling to 620°C with a 55°C/hour cooling rate to start the second stage. In the second stage, the material is held at 620°C for 8 hours followed by air cooling to room temperature.

The selection of the heat treatments and their parameters (temperature and soaking time) is mainly dependent on the manufacturing method since the thermal history during the conventional (cast and forging) and LPBF processes of IN718 is not the same, thus requiring different post-heat treatment conditions. Various studies have investigated the effect of thermal post-processing using different treatment conditions on the microstructure and mechanical properties of IN718 alloy fabricated by LPBF. However, to date, there is no standard AMS for the LPBF IN718 superalloy since the manufacturing process (LPBF) is still not well understood, and its microstructure is very complex and completely different from that of the conventionally manufactured alloy. In contrast, for wrought and cast IN718, the heat treatment conditions are well defined since these manufacturing methods are extensively studied and have become well established. Therefore, the majority of past research studied the effect of standard AMS heat treatment conditions used for cast and wrought IN718 (AMS 5383 and AMS 5662, respectively) on the microstructure and

mechanical properties of LPBF printed IN718 parts. In the following section, examples of some research conducted in this area are discussed.

Figure 2-12 and Figure 2-13 show the impact of the AMS standard heat treatment of wrought IN718 (AMS 5662) on the mechanical properties (TS, YS and EL) at RT and at 650°C, respectively, of the LPBF IN718 parts as reported by [26,34,35,62,63]. For comparison, the tensile properties of fully heat-treated wrought IN718 reported in [35,62] are included in these charts. As can be seen in these figures, after applying the standard heat treatments, the LPBF IN718 exhibited comparable tensile and yield strengths to those of the wrought alloy, whereas its ductility significantly deteriorated. Such a deterioration in the material ductility of LPBF IN718 could be attributed to the improper selection of the heat treatment conditions to meet the requirements of the room and high-temperature applications.

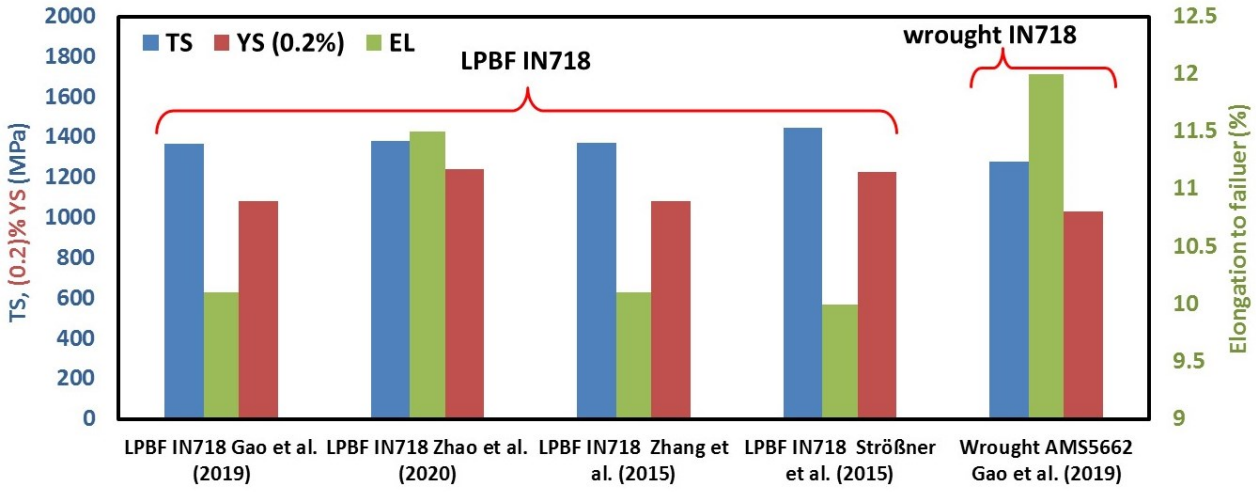

Figure 2-12: Room temperature (RT) tensile strength, yield strength and elongation to failure of heat-treated LPBF IN718 superalloy, using standard AMS heat treatments of the wrought IN718, in comparison with those of heat-treated wrought alloys at RT as reported in [26,34,62,63].

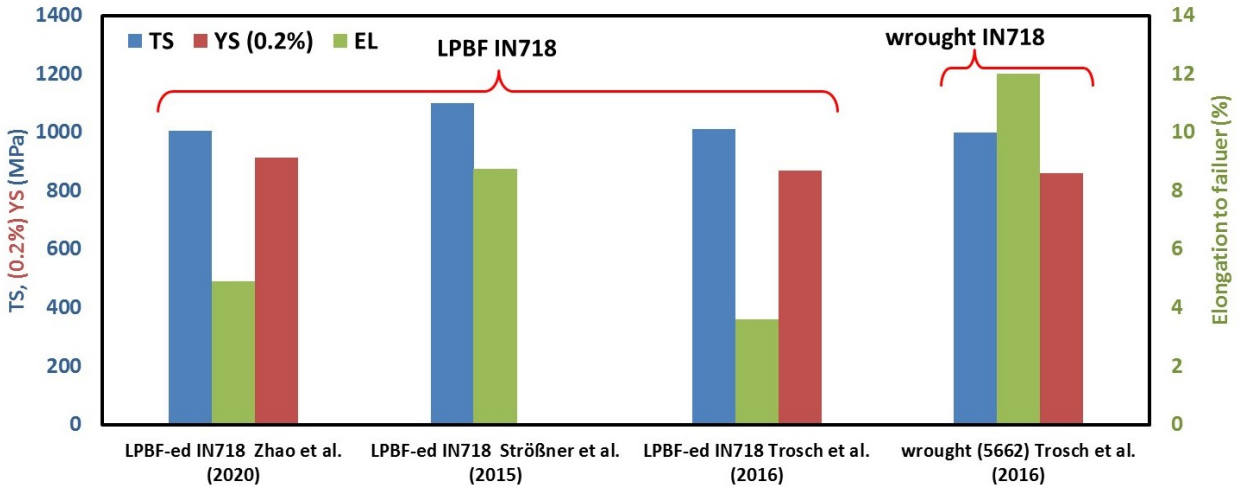

Figure 2-13: Tensile strength, yield strength and elongation to failure at 650°C of heat-treated IN718 superalloy, using standard AMS heat treatments of the wrought IN718, in comparison with those of heat-treated the wrought alloys at 650°C as reported in [34,35,63].

Furthermore, Chlebus *et al.* [46] investigated the effect of wrought heat treatments on the microstructure of the LPBF IN718. The details of their heat treatments are as follows: (i) direct aging treatment (DA) (720°C/8h/furnace cooling at 100°C/h to 620°C/10h/ air cooling), (ii) and solution treatment (1100°C/1h/water cooling) + DA treatment, which designated by SA [46]. Their [46] results show that the as-printed microstructure, in the xz-plane (vertical cross-section and parallel to building direction), has a strong texture along the building direction with a very fine columnar dendritic substructure. Differently, in the xy-plane (horizontal cross-section and normal to the building direction), the microstructure consists of an equiaxed grain structure with a cellular dendritic substructure that corresponds to the transverse cross-section of the columnar grains of the xz-plane [46]. After DA heat treatment, no noticeable changes in the as-printed microstructure in terms of grain structure and dendritic substructure across both xy and xz-planes were observed as shown in Figure 2-14. This is attributed to the lower temperature of the DA treatment to homogenize and refine the dendritic microstructure of the as-printed conditions [46].

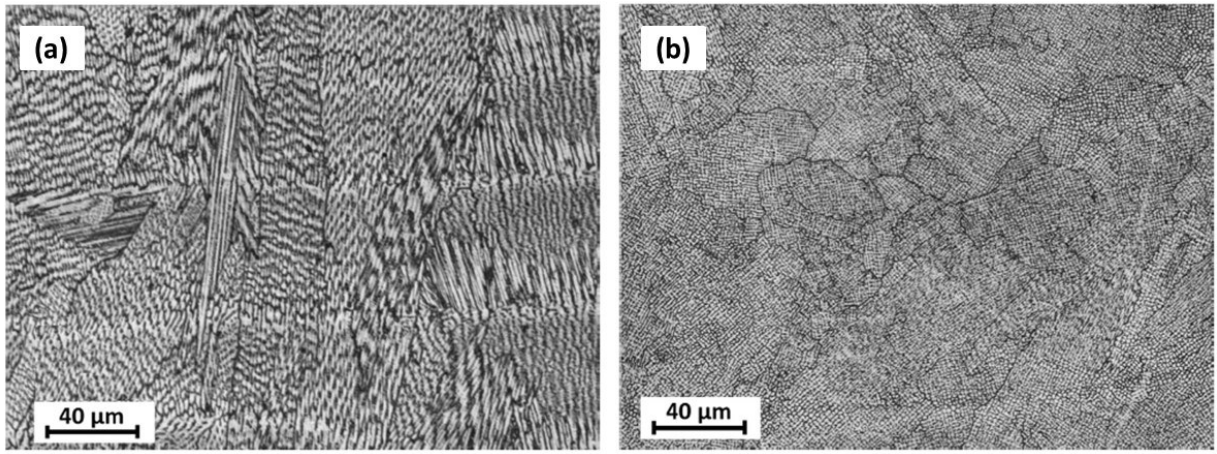

Figure 2-14: Optical microscopic microstructure of LPBF-fabricated IN718 after direct aging treatment in: (a) xz-plane, and (b) xy-plane [46].

In contrast, the application of SA treatment resulted in dissolving the dendritic substructure and produced a more homogeneous microstructure as shown in Figure 2-15. However, this treatment did not completely eliminate the textured microstructure and change the elongated grains as shown in Figure 2-15a [46]. The existence of such anisotropic microstructure in the xz and xz-planes even after heat treatment is expected to lead to undesired anisotropic mechanical properties confirming that the standard treatment conditions of wrought IN718 are not effective to produce IN718 components with specifications that meet the design requirements.

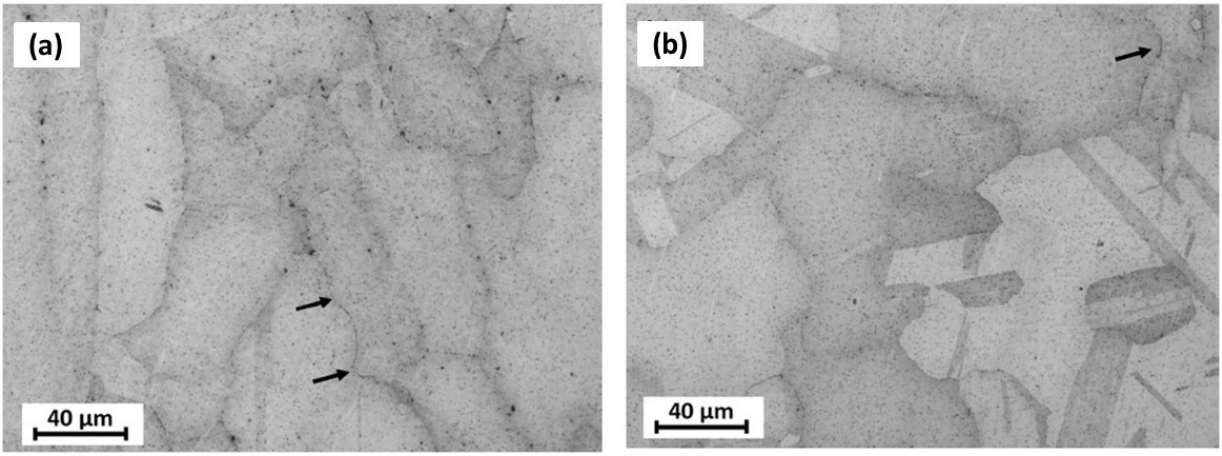

Figure 2-15: Optical microscopic microstructure of the heat-treated sample at 1100°C/1h followed by aging in: (a) xz-plane, and (b) xy-plane [46].

As noticed, the main findings in the existing literature show that using the AMS standard treatments of the conventionally manufactured IN718 to heat treat the LPBF IN718 ended up with non-consistent microstructure and inferior mechanical properties at both room and elevated temperatures. Thus, the current study focuses on tuning the heat treatment parameters to obtain the optimum post-treatment conditions of the LPBF IN718 alloy.

2.6 Motivation and research objective

The main objective of this study is to improve the performance of the additively manufactured IN718 components fabricated by the laser powder bed fusion process. Thermal post-processing of the as-printed IN718 is required to effectively eliminate the manufacturing drawbacks and obtain components with functional properties that meet the design requirements of the aerospace industries. Despite the abundant research available in the literature on the thermal post-processing of the LPBF IN718 superalloy during the last few years, obtention the optimum heat treatment conditions that can address these drawbacks has not been established yet. Therefore, based on the main literature findings, the objectives of the present study can be specifically identified as follows:

1- Studying the effect of soaking time of both homogenization and solution treatments on the grains structure, crystallographic texture, precipitates formation/dissolution, diffusion of microsegregations and material hardness. This is done by establishing a heat treatment time window with a wide range of soaking time for homogenization treatment (at 1080°C; 1 to 7h) and solution treatment (at 980°C; 15 to 60 min). Detailed microstructural characterization of the as-printed and heat-treated conditions is carried out using scanning electron microscopy (SEM), energy dispersive X-ray spectrometer (EDS), electron backscattered diffraction (EBSD) and X-ray diffraction (XRD).

2- Investigating the elevated-temperature (650°C) tensile properties and the corresponding fracture mechanisms as a function of homogenization and solution treatments time. A thermal post-processing map is provided to assist in tailoring the mechanical properties of LPBF IN718 based on the design requirements.

3- Optimizing the soaking time of both homogenization and solution treatments to obtain homogeneous microstructure, recrystallized material with non-distinct texture and high mechanical properties at room and elevated temperature.

4- Studying the effect of the in-service exposure of the aircraft turbine engines for long period (up to 3000h) on the microstructure and mechanical properties of LPBF IN718 in the as-printed and optimum heat-treated conditions. The evolution of the microstructure and high-temperature (650°C) mechanical properties at intervals of 0, 500, 1000, 2000 and 3000h are examined.

Chapter 3 : Influence of Homogenization and Solution Treatments Time on the Microstructure and Hardness of Inconel 718 Fabricated by Laser Powder Bed Fusion Process

Eslam M. Fayed [1], Davood Shahriari [2], Mohammad Saadati [2], Vladimir Brailovski [2], Mohammad Jahazi [2] and Mamoun Medraj [1,*]

[1] Department of Mechanical, Industrial and Aerospace Engineering, Concordia University, 1515 Rue Sainte Catherine west, Montreal, QC H3G 2W1, Canada; e_fayed@encs.concordia.ca (E.F.)
[2] Department of Mechanical Engineering, École de Technologie Supérieure, 1100, Notre-Dame Street West, Montreal, QC H3C 1K3, Canada; davood.shahriari@etsmtl.ca (D.S.); mohammad.saadati.1@ens.etsmtl.ca (M.S.); vladimir.brailovski@etsmtl.ca (V.B.); mohammad.jahazi@etsmtl.ca (M.J.)
* Correspondence: mmedraj@encs.concordia.ca; Tel.: +1-514-848-2424

This paper has been published in *Materials* 2020, *13*(11), 2574; https://doi.org/10.3390/ma13112574

Abstract

In the present study, Inconel 718 (IN718) superalloy fabricated by laser powder bed fusion (LPBF) has been characterized focusing on the effect of both homogenization and solution treatment time on grains structure, crystallographic texture, precipitates formation/dissolution and material hardness. For this purpose, a heat treatment time window with a wide range of soaking times for both treatments was established aiming to develop the optimal post-treatment conditions for laser powder bed fused IN718. It was found that the as-printed IN718 is characterized by very fine columnar/cellular dendrites with Laves phase precipitating at the grain boundaries as well as inter-dendritic regions, which differs from the microstructure of wrought and cast materials and requires special heat treatment conditions different from the standard treatments. The results reveal that the relatively short homogenization treatment at 1080°C for 1h was not enough to significantly change the as-printed grain structure and completely dissolve the segregates and Laves phase. However, a completely recrystallized IN718 material and more Laves phase dissolution were obtained after homogenization treatment for 4h. A further increase in time of the homogenization

treatment (7h) resulted in grain growth and coarsening of carbides precipitates. The solution treatment time at 980°C did not cause noticeable changes in the crystallographic texture and grain structure. Nevertheless, the amount of δ-phase precipitation was significantly affected by the solution treatment time. After applying the heat treatment time window, the hardness increased by 51–72% of the as-printed condition depending on the treatment time due to the formation of γ′ and γ″ in the γ-matrix. The highest material hardness was obtained after 1h homogenization, whereas the prolonged time treatments reduced the hardness. This study provides a comprehensive investigation of the post-heat treatments of the laser powder bed fused IN718 that can result in an optimized microstructure and mechanical behavior for particular applications.

Keywords: additive manufacturing; laser powder bed fusion; metal 3D printing; nickel-based superalloy; IN718; microstructure; heat treatment

3.1 Introduction

Inconel 718 is a nickel-based superalloy which was developed by the International Nickel Company in 1959 [11]. Over the past decades, IN718 superalloy experienced outspread evolution in different industrial applications such as aerospace and energy industries [53]. This is due to its outstanding properties such as high strength, high resistance to corrosion, wear and oxidation at both low and elevated temperatures up to 650°C [47,57]. Hence, IN718 has been implemented in several high-temperature applications such as the production of a majority (50 wt.%) of turbine engine components: rotor disc and turbine blades [62]. Solid solution strengthening and precipitation hardening are the principle strengthening mechanisms for IN718 superalloys [7]. IN718 is a multiphase superalloy that consists of primary face-centered-cubic (FCC) γ-phase matrix along with other secondary phases such as FCC γ′ ($Ni_3(Al,Ti)$), body-centered-tetragonal (BCT) γ″ (Ni_3Nb), orthorhombic δ-phase (Ni_3Nb), hexagonal Laves phase $(Ni,Fe,Cr)_2(Nb,Mo,Ti)$ and (MC, $M_{23}C_6$, M_6C) carbides [12]. Both γ′ and γ″ are the primary strengthening phases of the

γ-matrix, whereas δ and Laves phases are known to degrade the mechanical properties in this alloy [12]. It is important to note, however, that the presence of an appropriate amount of δ-phase along the grain boundaries prevents undesired grain growth and improves the strength of the grain boundaries [53]. The microstructure and mechanical properties of IN718 superalloy are sensitive to the types, contents, distribution, and size of these precipitates [13]. Therefore, studying post-printing heat treatments thoroughly is very important.

To date, IN718 components are usually fabricated using conventional manufacturing methods. However, several challenges face the manufacturing industries, such as excessive tool wear, high material waste, high production cost and long manufacturing time, because of the high hardness and poor machinability of IN718 superalloy [47,64]. Moreover, the extreme complexity of most of the IN718 components, such as turbine blades with internal cooling channels, requires long processing time and high manufacturing cost using the conventional techniques. Also, some of the existing manufacturing techniques, such as casting, require high temperature during the processing of IN718 parts which consequently results in macrosegregation of the Nb and Mo as reported by Hosseini *et al*. [28]. These challenges have become the motivation to look for new, more effective, manufacturing techniques for the IN718 superalloys. Additive manufacturing is one of the proposed and promising techniques to fabricate IN718 parts.

The laser powder bed fusion (LPBF) process is one of the additive manufacturing (AM) techniques that utilizes a layer-by-layer fabrication method to produce three dimensional (3D) metallic components using a high-intensity laser beam [62]. LPBF has attracted significant attention in the processing of advanced engineering materials such as aluminide, titanium alloys and nickel-based alloys [47]. This is due to its high potential to fabricate complex shape components without the need for specific tooling. Furthermore, the LPBF process offers several

advantages compared to conventional subtractive manufacturing methods such as a reduction in manufacturing time, lower buy-to-fly ratio and lower production cost [33–35]. Moreover, dense metallic components, with a high relative density, up to 99.7%, can be achieved using LPBF at the optimal laser process parameters [46]. Thus, the LPBF process is fast becoming an attractive process for the fabrication of high-valued and critical IN718 components in various industries. Despite the great promises that the LPBF process has clearly exhibited, some inherent manufacturing drawbacks remain, such as high-level of residual stresses, elemental segregation, microstructure heterogeneity and anisotropic mechanical properties that should be overcome to fully realize and maximize the LPBF process's potential [13,47,49,54,55]. To achieve the required microstructure and mechanical properties, thermal post-processing is required to obtain homogenous microstructure and defect-free components [12].

Numerous studies have been conducted to investigate the effect of thermal post-processing treatments on the microstructure and mechanical properties of 3D printed IN718 parts. Nevertheless, producing laser powder bed fused IN718 components with acceptable mechanical properties and cracking resistance considering the harsh in-service conditions has not been achieved yet [24,26,53]. According to the Aerospace Material Specification (AMS) of IN718, there are two industrial standard heat treatments, AMS 5662 for wrought IN718 and AMS 5383 for cast IN718 [65,66]. The AMS 5662 treatment cycle includes solution anneal (980°C for 1h, air cooling) followed by aging treatment (720°C for 8h, furnace cooling at 55°C/h to 620°C, 8h, air cooling) which is designated as SA [26,65], whereas AMS 5383 treatment includes homogenization treatment (1080°C for 1.5h, air cooling) followed by solution treatment (980°C for 1h, air cooling) + aging treatment (720°C for 8h, furnace cooling at 55°C/h to 620°C for 8h, air cooling) which is designated as HSA [26,66]. Through literature, the majority of conducted

researches on the thermal post-processing of laser powder bed fused IN718 were focusing on studying the effects of these standard treatments on the microstructure and mechanical properties. However, the microstructure, precipitates and texture of IN718 printed by LPDF are considerably different from those of the conventionally manufactured by forging and casting. This is because of the rapid solidification process associated with the LPBF process [12]. Therefore, these standard heat treatments are expected to require some changes to become suitable for IN718 components fabricated by LPBF. The present work is aimed at helping to achieve this objective.

Zhang *et al.* [26] investigated the effect of the standard SA treatment of the wrought IN718 (AMS 5662) on the microstructure and mechanical behavior of the laser powder bed fused IN718 alloy. Their results show that the strength of as-printed specimens was lower than that of the wrought IN718 [26]. After SA treatment, the strength became comparable to that of the wrought alloy, but the ductility dramatically decreased in contrast with the ductility of wrought IN718. They attributed this behavior to a larger amount of δ-phase precipitates inside the grains and at the grain boundaries [26]. It was observed that the time scale of the δ-phase precipitation in nickel-based superalloy fabricated through LPBF is much shorter than in the wrought alloy (minutes versus tens to hundreds of hours) as reported by Fan *et al.* [54]. The faster precipitation of δ-phase in the laser powder bed fused IN718 was attributed to the non-uniform distribution of Nb in the as-printed state, since δ-phase usually precipitates in Nb-enriched areas [12,26,54]. Thus, the standard treatments of wrought IN718 alloy should not be expected to result in the optimum conditions and improve the microstructure and mechanical properties of IN718 processed by LPDF.

Furthermore, Deng *et al.* [53] studied the effect of a standard HSA treatment for cast IN718 (AMS 5383) on the microstructure and mechanical properties of IN718 samples fabricated by

LPBF. Their results show that the HSA-treated microstructure still had brittle intermetallic Laves phase which resulted in the formation of microvoids during tensile testing and consequently deteriorated the mechanical behavior [53]. In addition, larger size and volume fraction of the δ-phase precipitated after the HSA conditions which resulted in lower ductility. The authors [53] concluded that homogenization treatment at 1080°C for 1h was not enough to completely dissolve the Nb and Ti-rich segregates and Laves phase. Also, they mentioned that the 1h holding time of the solution treatment at 980°C resulted in the precipitation of a larger amount and coarser size of δ-phase, which consequently consumed more Nb at the expense of precipitation of the strengthening γ″ phase [53]. However, some beneficial effects of the presence of δ-phase particles at the grain boundaries can be noted, including dislocation pinning and grain growth inhibition, when the amount and size of δ-phase particles are controlled [24,53]. In this context, Deng [11] reported that the presence of approximately 4% of δ-phase at the grain boundaries could effectively inhibit the grain growth during the in-service conditions. Therefore, it is desirable that the sought after heat treatments result in grain boundary δ-phase and avoid its precipitation inside the grains.

Similarly, Dongyun *et al.* [24] applied the standard HSA and HA (1080°C for 1.5h, air cooling + 720°C for 8h, furnace cooling at 55°C/h to 620°C for 8h, air cooling) heat treatments to LPBF-processed IN718 alloy in order to analyze the effect of δ-phase on the mechanical behavior. Their results reveal that after the HSA treatment, the dendritic microstructure transformed to recrystallized grains in addition to precipitating fine δ-phase and MC carbides along the grain boundaries [24]. Also, they confirmed that δ-phase did not form in the matrix after the HA treatment [24]. Thus, the HA-treated samples exhibited improved mechanical behavior as compared to the HSA-treated samples [24]. The authors [24] attributed this trend to the fact that the Nb is the principle element necessary for the formation of both γ″ strengthening phase and δ-

phase. Therefore, at a certain concentration of Nb in the matrix, δ-phase is formed at the expense of γ″-phase during the HSA heat treatment, thus reducing the mechanical properties [24].

On the basis of the aforementioned findings, applying the industrial standard heat treatment conditions of the cast IN718 superalloy (ASM5383) has some beneficial effects on the microstructure and mechanical behavior of the as-printed IN718. However, the times of the homogenization and solution treatments still need to be optimized further to obtain more homogeneous microstructure and improve the combination of strength and ductility in laser powder bed fused IN718 parts. Therefore, in the present study, a window of heat treatment time has been established to optimize the post-treatment conditions for the printed IN718 by homogenizing the microstructure, dissolving the segregated elements and the brittle precipitates, and to improve the mechanical behavior.

This window covers a range of soaking times of both homogenization and solution treatments to investigate their effects on the microstructure, phase formation/dissolution, texture evolution and mechanical behavior of the 3D printed IN718. The soaking time of the homogenization treatment at 1080°C was varied from 1 to 7h, whereas for the solution heat treatment at 980°C, it was from 15 to 60 min. In addition, a mid-point condition, at 4h of the homogenization and 37.5 min of the solution heat treatment times, was selected to follow the microstructure and mechanical properties changes within this window. This approach could help to achieve the industrial standard conditions of the laser powder bed fused IN718 that have not been reported in the literature. It also provides a thermal post-processing map to control the precipitation of Laves, δ-phase and carbides which is essential for optimizing the printed IN718 mechanical behavior. The microstructure, compositional analysis, texture analysis and phase identification are studied using optical microscopy (OM), scanning electron microscopy (SEM), energy-dispersive spectroscopy (EDS),

electron backscatter diffraction (EBSD) and X-ray diffraction (XRD) techniques. As for the mechanical behavior evaluation, Vickers microhardness measurements of the as-printed and post-treated specimens were carried out.

3.2 Experimental procedure and materials

3.2.1 Material and manufacturing methods

Gas-atomized IN718 powder, supplied by EOS-GmbH (Krailling, Germany), with a particle size distribution of D10 (18.2 μm), D50 (32.4 μm) and D90 (54.2 μm) was used as raw material to fabricate IN718 test samples via the LPBF process. The nominal chemical composition of the as-received powder is given in Table 3-1 and the SEM micrographs of the as-received powder are shown in Figure 3-1. As can be seen in Figure 3-1a, IN718 powder particles are dominantly spherical and some particles have a deviation from the spherical shape that is caused by smaller satellite particles. In the high-magnification SEM image in Figure 3-1b, a dendritic microstructure is observed on the surface of the particles which could be attributed to the rapid solidification during the gas atomization process [45].

Table 3-1: Nominal chemical composition of gas atomized IN718 powder.

Element	**Ni**	**Cr**	**Nb**	**Mo**	**Ti**	**Al**	**Fe + Traces**
wt.%	49.19	19.04	4.92	2.70	1.08	0.33	Bal.

An EOS M280 (EOS, Krailling, Germany) LPBF system equipped with Yb:YAG 400 W fiber laser system was utilized to fabricate IN718 test samples using the EOS Original Parameter Set IN718_Surface 1.0 (285 W laser with 100 μm beam diameter, 1000 mm/s scanning speed, 110 μm hatching space with 67° hatching angle, and 40 μm layer thickness). The building platform was pre-heated to 80°C to reduce the thermal gradient along the building direction, thus reducing thermal stresses in the produced parts. For this research, a set of cuboid specimens with a size of 22 × 17 × 10 mm^3 were printed to investigate the microstructure evolution and for phase

identification, as shown in Figure 3-2 a and b. Figure 3-2c shows the laser beam scanning strategy used in this study. A controlled argon atmosphere was used to minimize the possibility of metal oxidation during the printing process. After the printing, all samples were removed from the building platform using wire electro-discharge machining (WEDM) in the as-built conditions without stress relief.

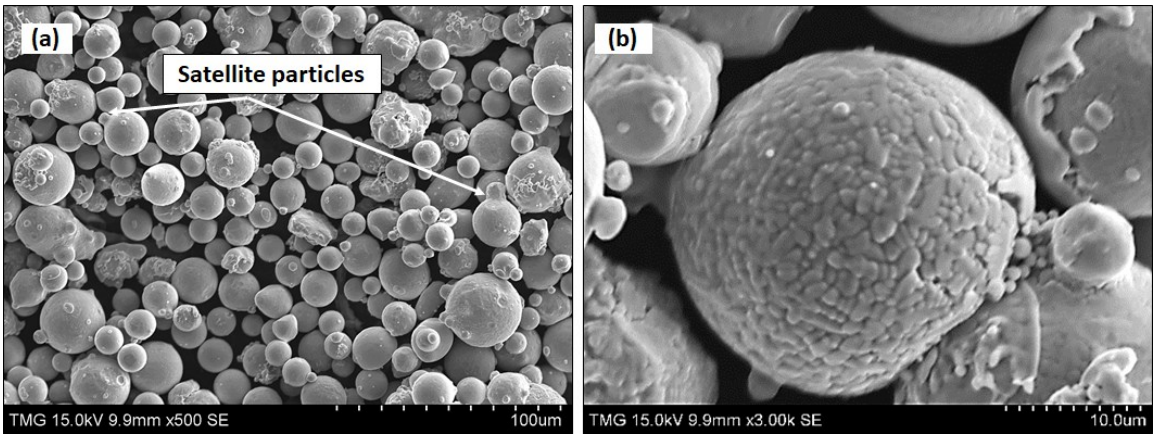

Figure 3-1: (a, b) Secondary electron scanning electron microscopy (SEM) micrograph of Inconel 718 (IN718) powder.

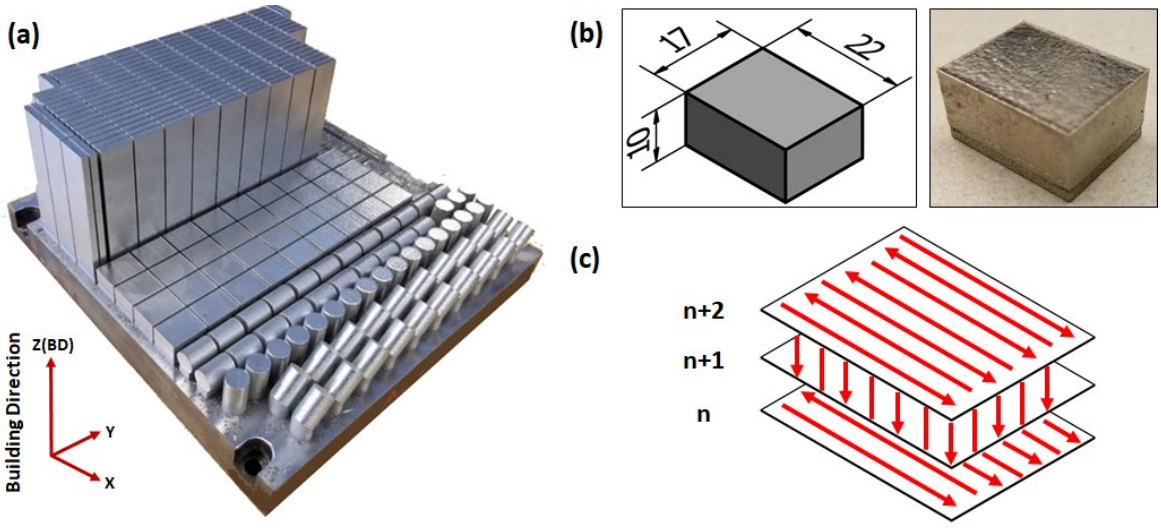

Figure 3-2: (a) LPBF building platform of IN718 displaying the building orientation; (b) schematic drawing and real as-printed IN718 test samples after WEDM removal; (c) schematic illustration of the laser scanning strategy in this study.

3.2.2 Thermal post-treatments

Thermal post-processing was applied to the as-printed IN718 samples to homogenize the microstructure and control the dissolution and precipitation of IN718 phases. To this end, a thermal post-treatment time window has been established to obtain the suitable treatment conditions for the laser powder bed fused IN718 superalloy. This post-treatment time window combines a wide range of soaking times of both homogenization and solution heat treatments. The ranges of the homogenization and solution treatments soaking times were selected based on the transformation-time–temperature (TTT) diagram of the IN718 welds [45] and after studying the several heat treatment studies in the literature.

Figure 3-3a and b shows the heat treatment cycle and the window of the treatment time, respectively. As can be seen in this figure, the homogenization heat treatment was performed at 1080°C with soaking times of 1, 4 and 7h, followed by air cooling in order to effectively homogenize the segregated elements and dissolve Laves phase. Then, the solution heat treatment was carried out at 980°C with soaking times of 15, 37.5 and 60 min, followed by air cooling, to control the size and amount of δ-phase precipitates. So, a total of five treatment conditions have been applied to the as-printed LPBF IN718 as listed in Table 3-2. The details of the five treatment conditions are as follows: among the five treatment conditions, two samples were homogenized at 1080°C for 1h and one of them was followed by solution treatment at 980°C for 15 min, while the other was followed by solution treatment for 60 min at the same temperature, HS1 and HS2, respectively. Similarly, two other samples were homogenized at 1080°C for 7h and one of them was followed by solution treatment at 980°C for 15 min, while the other, was for 60 min, HS4 and HS5, respectively. In addition, a mid-point for both the homogenization and solution soaking times was selected at 4h of homogenization and 37.5 min of solution treatment, HS3.

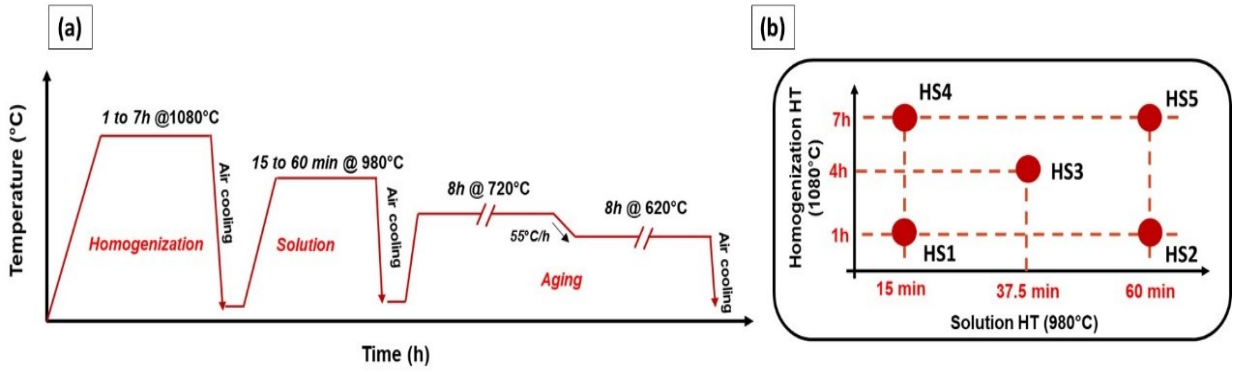

Figure 3-3: (a) Schematic representation of the entire heat treatment cycle of the laser powder bed fused IN718 in the present study; (b) schematic drawing illustrates the position of the homogenization and solution treatment conditions inside the post-treatment time window.

Table 3-2: Designations of specimens and the details of the corresponding post-treatment conditions.

Designation	Homogenization Heat Treatment (H)	Solution Heat Treatment (S)	Aging Heat Treatment (A)
As-printed	None	None	None
HSA1	1080°C for 1 h/AC*	980°C for 15 min/AC	720°C/8 h/FC** at 55°C/h to 620°C + 620°C/8 h/AC
HSA2	1080°C for 1 h/AC	980°C for 1 h/AC	
HSA3	1080°C for 4 h/AC	980°C for 37.5 min/AC	
HSA4	1080°C for 7 h/AC	980°C for 15 min/AC	
HSA5	1080°C for 7 h/AC	980°C for 1 h/AC	

*AC: air cooling, **FC: furnace cooling.

Then, the five post-treated samples were aged under the same conditions of 720°C for 8h, furnace cooled by 55°C/h to 620°C, then held for 8h at 620°C, followed by air cooling—in order to study the effect of the preceded homogenization and solution heat treatments on the precipitation of the strengthening phases and the mechanical properties of laser powder bed fused IN718. All heat treatment conditions were performed using an electric-resistance furnace using a set of K-type thermocouples for monitoring the temperature of the IN718 samples during the treatments where the temperature difference was controlled within ± 5°C.

3.2.3 Characterization methods

Microstructure examinations of the IN718 in the as-printed and heat-treated conditions were carried out using a MEIJI TECHNO optical microscope (OM, San Jose, California, USA) equipped with a 3.0 MP camera and scanning electron microscope, SEM (HITACHI S-3400N, Minato, Tokyo, Japan) equipped with an energy dispersive X-ray spectrometer, EDS at 15 kV. The chemical analysis of all primary and secondary phases was carried out using semi-quantitative EDS. Phase analysis of the as-printed and heat-treated samples was performed using XRD, (PANAnalytical X'pert Pro X-ray diffractometer, Lelyweg 1, Almelo, The Netherlands) with a CuKα radiation at 45 kV and 35 mA. The scanning range (2θ) from 30° to 100° was selected to include the maximum number of possible diffraction peaks. It is worth mentioning that all the XRD analysis was performed on the xy-plane (perpendicular to the building direction) of the as-printed and heat-treated samples.

For the metallographic analysis, the as-printed and heat-treated samples were sectioned in both xy-plane and xz-plane (parallel to the building direction) using a slow cutter (Buehler, Lake Bluff, Illinois, USA) with a mineral oil bath to prevent heat generation. The cut samples were mounted using conductive hot epoxy resin which then were mechanically ground gradually from 320 to 1200 grit using SiC abrasive papers and polished down to 0.5 μm using alcohol-based diamond suspension. To reveal the precipitated phases and dendritic microstructure, the polished samples were etched using a solution of 10 mL hydrochloric acid + 1.5 mL 30% hydrogen peroxide [2]. Electron backscatter diffraction analysis (EBSD, SU-8230 Hitachi SEM equipped with Bruker e-Flash HR EBSD detector, Minato, Tokyo, Japan) was used to analyze the microstructure texture evolution, grain size and grain shape distributions in as-printed and after different post-treatment conditions. For the EBSD analysis, the specimens were polished manually down to 0.5 μm grit

size, then a vibromet polishing with a 0.05 grit size colloidal silica for 24h. An IM4000Plus Hitachi ion milling was used to eliminate the residual scratches and deformed surfaces using process parameters: 6 kV accelerating voltage and 1.5 kV discharge voltage for 40 min. For consistency, all EBSD maps were acquired at the center of the cuboid IN718 samples. In the EBSD analysis, the IN718 test samples were scanned at 20 kV and the pixel size of 1.62 μm. It is worth mentioning that the total map size for each condition was 1298×973.4 μm^2 surface area to cover the maximum number of grains (>1500).

3.2.4 Room temperature mechanical testing

Room temperature mechanical properties of the as-printed and heat-treated conditions were evaluated using the Mitutoyo, MNK-H1 Vickers microhardness tester (Aurora, Illinois, USA) under a load of 500 gf and a dwell time of 15 s. All tested samples were ground and polished as required for the microhardness test [53]. Microhardness testing was conducted in two stages of before and after aging treatment. At least 15 evenly distributed measurements for each condition were performed to obtain accurate results. All indentations were performed on the xy-plane of the cuboid samples.

3.3 Results and discussion

3.3.1 Microstructure of the as-printed condition

The microstructure of the vertical (xz) and horizontal (xy) planes in the as-printed condition were analyzed as shown in Figure 3-4a and b, respectively. The examined surface, with respect to the building direction, was indicated in the lower right corner of each SEM micrograph. As can be seen on the xz-plane in Figure 3-4a, the morphologies of the grains appear relatively elongated and the longitudinal axes of these grains are approximately parallel to the building direction. This microstructure is attributed to the high dependence of the grain size and morphologies on the

intensity and direction of the thermal gradient during the printing process. The temperature difference between the upper level of the powder bed, where the local laser heating is at its maximum, and the lower level which is close to the building platform results in high heat dissipation and thermal gradient along the building direction. Besides, the thermal conductivity of the dense material (previously solidified layers) is roughly 100 times higher than that of the powder material (adjacent to laser track) which results in higher heat dissipation in the -z direction [24]. Thus, during the solidification stage, the grains grow along the heat dissipation direction and form such a columnar grain structure. By contrast, in the xy-plane, equiaxed grains morphology are observed which corresponds to the transverse cross-section of the elongated grain structure, as shown in Figure 3-4b. Moreover, very fine precipitates, a few hundred nm in size, embedded inside the grains and along the grain boundaries are seen in the magnified inset of Figure 3-4b.

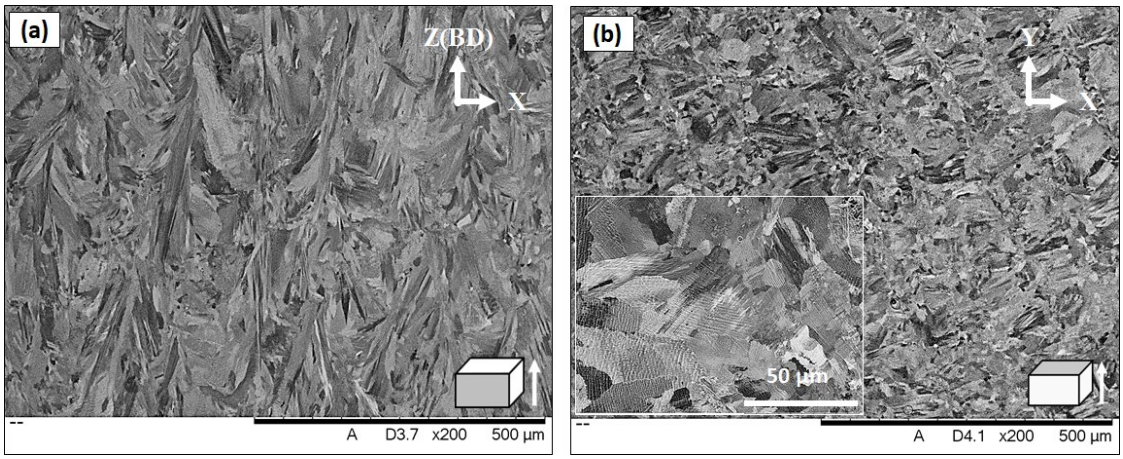

Figure 3-4: SEM micrograph of the non-etched as-printed laser powder bed fused IN718 superalloy: (a) vertical plane (xz); (b) horizontal plane (xy).

To characterize the dendritic microstructure and obtain further details about the as-printed substructure, both the xz and xy-planes were etched and examined as shown in Figure 3-5 and 3-6, respectively. After etching, the melt pool boundaries can be clearly seen in the OM micrograph of the xz-plane in Figure 3-5a. The shape of the molten pool appears as arc-shaped contours facing

upwards along the building direction, which reflects the Gaussian distribution shape of the laser beam intensity. This is the typical microstructure of the laser powder bed fused IN718 superalloy as also reported in [12,67,68]. The microstructure of each individual melt pool consists of very fine columnar dendrites as shown in Figure 3-5b to d. The growth direction and size of the dendrites in the molten pool depend on the direction of the local thermal flux and the cooling rate, respectively [69]. Moreover, the <100> texture is the preferred crystallographic orientation for the FCC structure [53]. This strong texture was observed to be preferential for many FCC engineering materials, built using the laser and electron beam powder bed fusion (PBF) processes [70,71]. Therefore, anisotropic mechanical properties are expected for the as-printed IN718 superalloy. Also, as shown in Figure 3-5b, some of these columnar dendrites extend across several melt pools, suggesting that the epitaxial growth of new dendrites occurred upon the preexisting dendrite colonies of the solidified grains along the building direction. This is because, during the laser beam scanning, the laser radiation causes extremely fast melting of the current powder layer and also partial melting of the previously solidified layer. After the laser beam leaves the melt pool, rapid cooling of the molten pool and rapid solidification occur with epitaxial growth. Such epitaxial growth crossing over several melt pool boundaries is widely reported in the literature [53,69,72]. This kind of growth indicates a strong bonding between the solidified layers due to the lower lattice mismatch that consequently reduces the risk of the inter-layer delamination [69]. However, such elongated grain morphology along the building direction results in strong anisotropic mechanical properties.

The microstructure inside the melt pool (Figure 3-5c) is inhomogeneous, as the fine dendritic microstructure is observed at the bottom of the melt pool that gradually changes to be coarser dendrites towards the top of the molten pool. This confirms the microstructure inhomogeneity that

consequently leads to anisotropic mechanical properties as reported by Seede *et al.* [50]. The change in the size of the dendrites can be attributed to the change in the cooling rate across the melt pools during the solidification stage [69] and also the fact that some dendrites have been engulfed by those which are better aligned crystallographically opposite to the heat flux direction. This provides a wider area for each dendrite to grow and develop the arms [73]. Furthermore, at the beginning of the solidification process, the cooling rate of the bottom part of the melt pools, in contact with the solid substrate, is relatively high but gradually decreases towards the top side which promotes the constitutional undercooling respectively. Therefore, the bottom part experiences an earlier solidification leading to the formation of fine and narrow dendrites that slightly increases in size towards the top border. Such an inhomogeneous microstructure was also reported by Calandri *et al.* [69].

In the xy-plane shown in Figure 3-6a, traces of the laser beam passes are observed to have 67° between two adjacent layers that reflect the laser scanning strategy. The width of each laser track is found to be approximately near the diameter of the laser beam (≈100 μm). As shown in Figure 3-6b to e, the microstructure of the overlapping zone is different from that in the center of the laser track. In the center of the laser tracks (zone 1), the growth direction of the cellular dendrites does not change as it stays oriented along the building direction as shown in Figure 3-6d. But at the laser track edges (zone 2), dendrites tend to even up to rotate 90° with respect to the building direction as shown in Figure 3-6e. Such a microstructure change between the center and the edge of the laser tracks is also observed in the xz-plane, as shown in Figure 3-5d. This is because of the local variations in the direction of the thermal gradient and heat flux towards the center of the melt pool. At the boundaries of the laser tracks, the thermal flux towards the center of the molten pool is greater than along the building direction due to the Gaussian shape of the laser beam intensity.

Such a change in the dendrites growth direction at the laser tracks boundaries has also been reported by Mostafa *et al.* [45] and Calandri *et al.* [69].

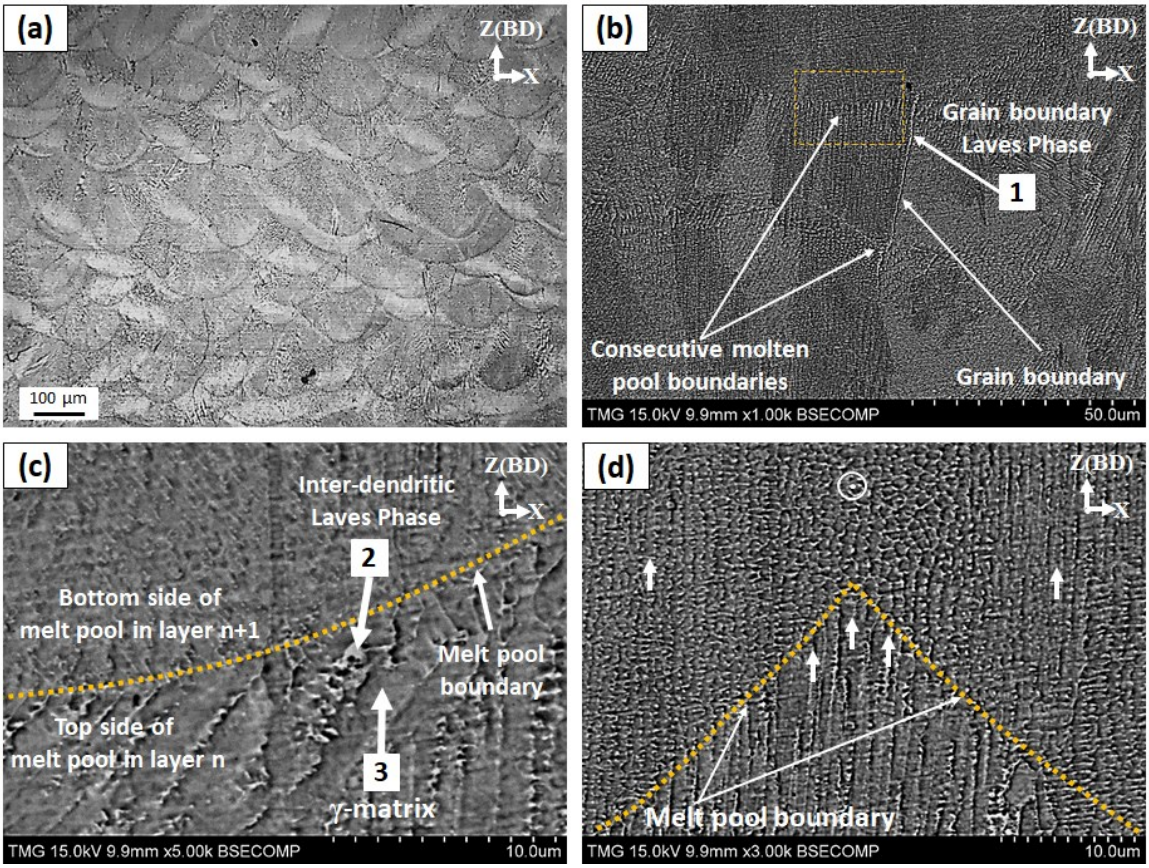

Figure 3-5: (a) Optical microscope (OM) micrograph of the vertical plane with arc-shape melt pool boundaries; SEM micrograph of the etched as-printed IN718 in the vertical plane showing: (b) columnar grains with epitaxial growth across several layers; (c) dendrite size at the melt pool boundaries; (d) changes in the dendrite direction in the overlapping zone. Arrows 1, 2 and 3 indicate the EDS spot analysis of grain boundaries Laves phase, inter-dendritic Laves and γ-matrix, respectively, as listed in Table 3-3.

Table 3-3: EDS spot analysis results of the as-printed condition in Figure 3-5 (wt.%).

Spectrum	Phase	Fe	Ni	Cr	Nb	Ti	Mo	Al
1, 2	Laves	Bal.	43.55 ± 3.9	15.83 ± 1.25	14.45 ± 6.53	1.85 ± 0.71	3.62 ± 0.01	0.44 ± 0.08
3	Matrix	Bal.	50.03 ± 0.46	18.51 ± 0.19	3.88 ± 0.01	0.79 ± 0.03	3.22 ± 0.07	0.56 ± 0.11

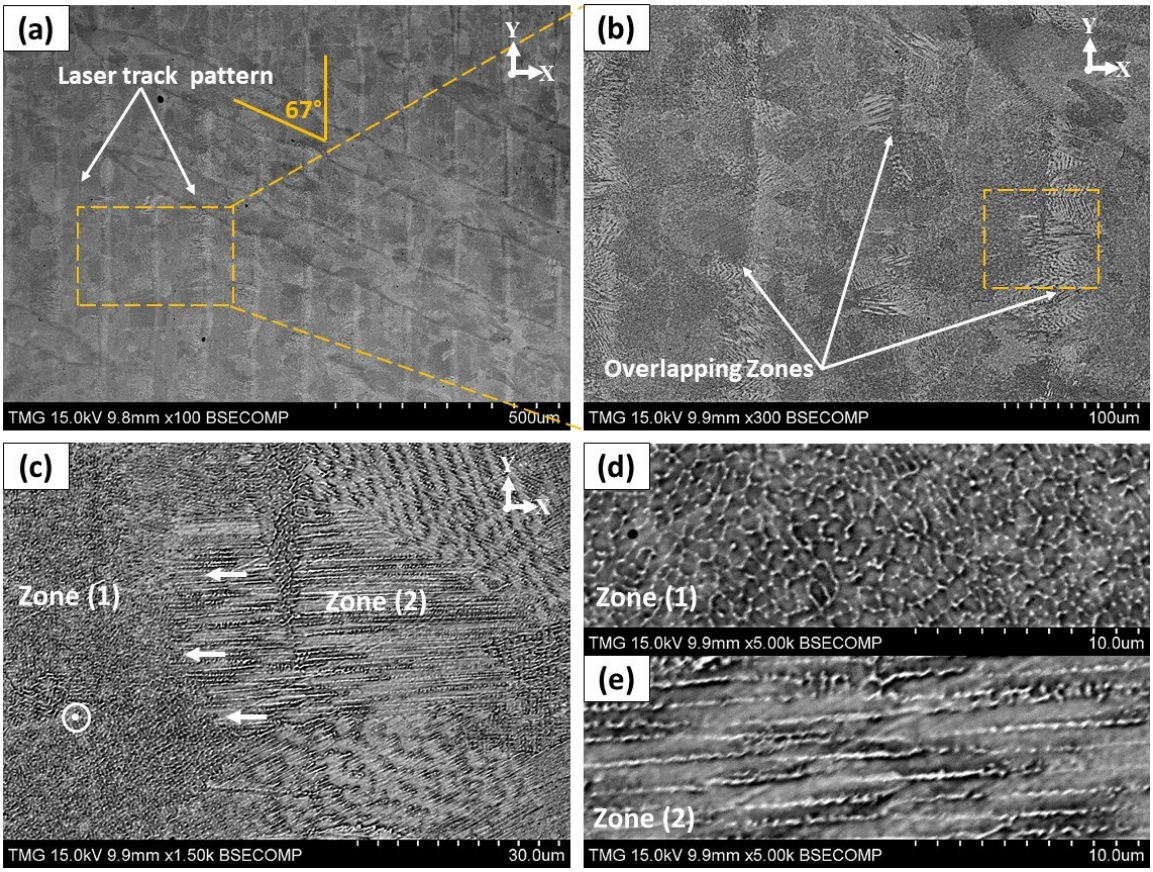

Figure 3-6: SEM micrograph of the etched as-printed IN718 in the horizontal plane showing: (a) the laser beam track and scanning strategy; (b) high magnification view for the area marked in (a); (c, d, e) changes in the dendrite directions in the horizontal overlapping zone as indicated in (b).

Figure 3-7 illustrates the elemental mapping of the as-printed IN718 using the EDS analysis to determine the chemical composition of the inter-dendritic (white phase) and the dendritic (dark phase) zones. As can be seen in Figure 3-7c, high concentrations of Nb, Ti and Mo are observed in the inter-dendritic regions in comparison with the primary dendrites along with depletion in Ni, Fe and Cr. The concentration of Nb, Ti and Mo at these precipitates reached up to 5.4, 3.2 and 1.1 times, respectively, higher than that of the dendrites, but they are depleted in Ni, Fe and Cr with respect to the nominal composition of the matrix as can be inferred from Table 3-3. This is attributed to the solute rejection and element redistributions during the solidification process. During the solidification process of IN718, segregation of Nb in the inter-dendritic region occurs

due to its partitioning behavior, and the solidification sequence is well established as follows: Liquid → γ → γ + NbC → γ + NbC + Laves [53]. However, the amount and size of these Nb-precipitates in the laser powder bed fused IN718 superalloy are much lower and smaller than those in the cast IN718 as reported by Zhang *et al.* [24]. This is because the amount and the size of precipitates are significantly minimized by increasing the cooling rate [24,53]. Such microsegregation of Nb, Ti and Mo results in the formation of brittle intermetallic Laves phase along the grain boundaries and in the inter-dendritic regions. According to the work of Tucho *et al.* [12], Laves phase formation requires, approximately, 10 wt.% Nb. Therefore, the formation of brittle intermetallic Laves phases consumes most of the segregated Nb and therefore depletes it from the matrix, which is confirmed by the current EDS analysis. The presence of such large amounts of Laves phases in the inter-dendritic regions and at the grain boundaries is detrimental to the mechanical properties. Thus, further heat treatments are required to dissolve these precipitates and microsegregates. Besides, the precipitation of the strengthening phases (γ′ and γ″) and δ-phase is not observed in the as-printed microstructure, which is in agreement with the results obtained by Gao *et al.* [62]. This is attributed to the extremely high cooling rates of the LPBF process.

To assess the material textures, grain orientations and morphologies of the laser powder bed fused IN718 in the as-printed condition, EBSD mappings were acquired from both the xz and xy-planes. Also, inverse pole figure (IPF) and grain maps were constructed from the EBSD data to illustrate the microstructural anisotropy of both the xy and xz-planes, in the as-printed condition, as shown in Figure 3-8. For simplicity, the examined surface, relative to the building direction, is indicated in the upper right corner of each EBSD map in Figure 3-8. From the IPF in the xz-plane (Figure 3-8a), the as-printed LPBF IN718 exhibits strong texture (red area) along <100>, whereas

in the xy-plane (Figure 3-8b), a non-distinct/weak texture is observed. Also, it can be confirmed that the microstructure of the as-printed condition in the xz-plane contains mainly elongated grains oriented parallel to the building direction as shown in Figure 3-8c. By contrast, the xy-plane mapping reveals a pattern of chessboard-like shape which can be related to the laser beam scanning strategy as shown in Figure 3-8d. Such as-printed features and grain morphologies are consistent with those obtained by Deng *et al.* [53].

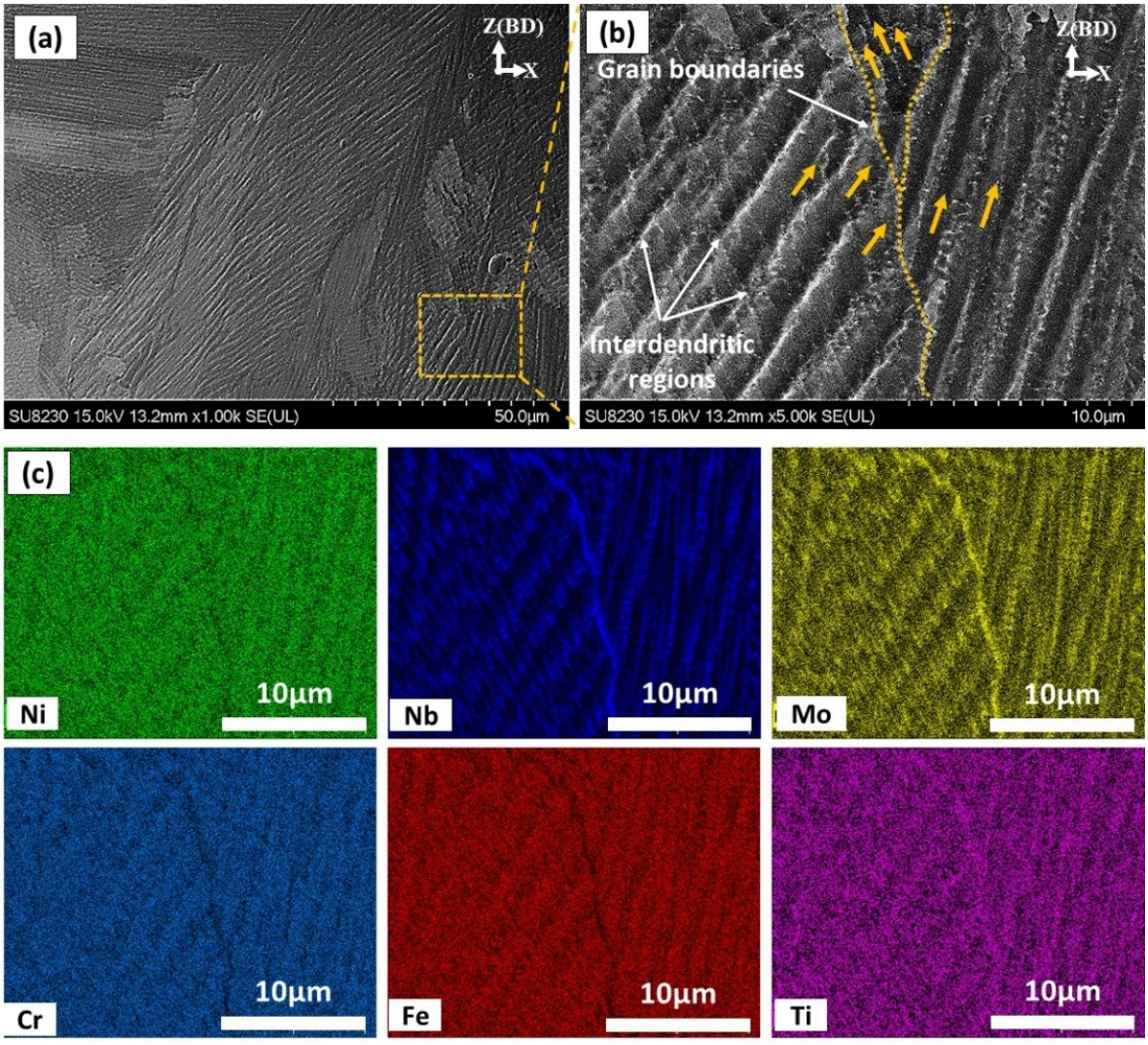

Figure 3-7: (a, b) SEM micrograph of the as-printed condition illustrating the segregates in the inter-dendritic and grain boundary regions; (c) EDS elemental distribution in the areas indicated in (b).

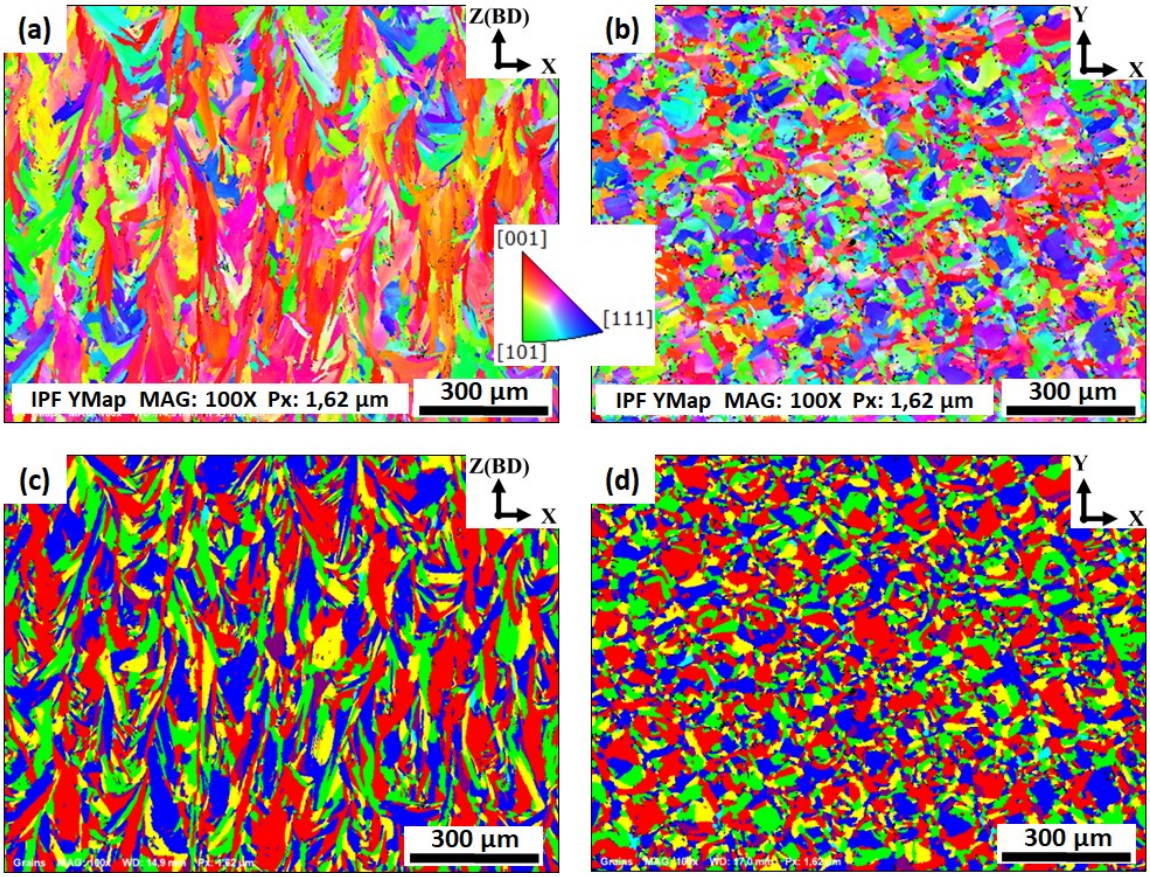

Figure 3-8: Inverse pole figures (IPF) (a, b) and grain maps (c, d) of the as-printed laser powder bed fused IN718: (a, c) xz-plane; (b, d) xy-plane. The EBSD mappings of the as-printed samples were plotted using the y-based projected IPF.

3.3.2 Microstructural evolutions with heat treatment time

As illustrated in Figure 3-5 and 3-6, the as-printed microstructure contains elongated grains with large amounts of segregations and Laves phase at the grain boundaries and inter-dendritic regions which is detrimental to the mechanical behavior of the IN718 alloy. Applying the post-treatment time window in this study aims to optimize the homogenization and solution treatment time for laser powder bed fused IN718. Figure 3-9 shows the grain structure evolution after applying the five heat treatment conditions with variations in the homogenization and solution treatments times. The as-printed micrograph is included in this figure for comparison. All microstructure analyses of the heat-treated conditions were carried out on the xz-plane before the

aging step for better comparison. All heat treatments before the aging step are designated by HS referring to the homogenization treatment (H) followed by the solution treatment (S). As can be seen in Figure 3-9b and c, after the homogenization treatment at 1080°C for 1h in both HS1 and HS2 conditions, the grain morphology did not significantly change from that in the as-printed condition and the microstructure still consisted of elongated grains oriented parallel to the building direction.

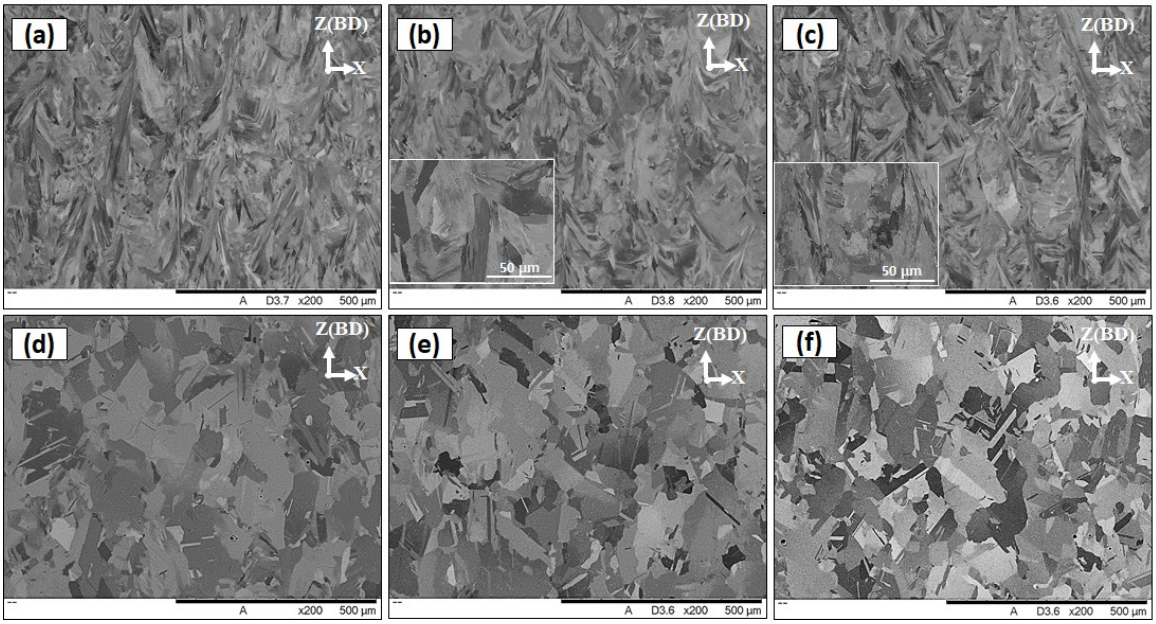

Figure 3-9: SEM micrograph of non-etched laser powder bed fused IN718 in conditions: (a) as-printed; (b) HS1; (c) HS2; (d) HS3; (e) HS4; (f) HS5.

The EBSD-based grain structure aspect ratio measurements were performed in the as-printed and heat-treated conditions as shown in Figure 3-10. As seen in Figure 3-10a and b, the aspect ratio measurements demonstrate that the relatively short (1h) homogenization time retains the elongated grain structure of the as-printed specimens, which is consistent with SEM and EBSD results. This finding indicates that the heat input during the 1h homogenization treatment at 1080°C is not sufficient for complete recrystallization which is driven by the residual stresses induced during the LPBF of IN718. It is worth mentioning that the recrystallization temperature of the

(30%–50%) cold-worked Inconel 718 is above 885°C [74], while the results obtained in the present study reveal a significantly higher recrystallization temperature. This suggests that the level of induced residual stresses during the printing process is lower than that in the cold-worked condition in [74].

Figure 3-9c shows an illustrative microstructure of the sample after 4h homogenization at 1080°C in HS3. More equiaxed grains with an average grain size of 66 µm are observed in comparison with the as-printed and 1h homogenized conditions suggesting that this treatment promoted a near complete static recrystallization. Moreover, a relatively higher aspect ratio was measured as compared with the 1h homogenization time as shown in Figure 3-10c. This further confirms that the 4h homogenization treatment at 1080°C, in HS3, provides sufficient activation energy to break the interatomic bonds and improve the diffusion which finally results in noticeable recrystallization in relation to other conditions with shorter holding times. The transformation of grain structure from columnar to equiaxed grains is necessary to achieve isotropic mechanical properties.

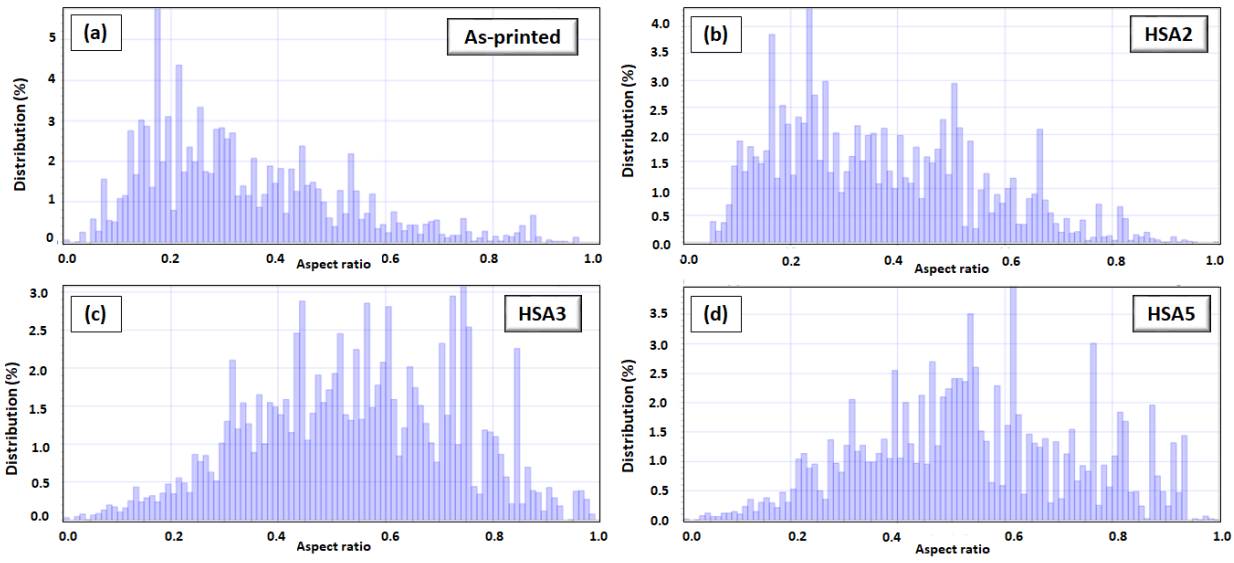

Figure 3-10: Grain morphology distribution displaying the change in grains aspect ratio as a function of heat treatment conditions: (a) as-printed; (b) HSA2; (c) HSA3; (d) HSA5.

For the prolonged homogenization treatment (7h), equiaxed grain structure with an average size of 75 μm were obtained, as shown in Figure 3-9e and f. This finding indicates that the recrystallization process has been completed and followed by a grain growth which is consistent with the aspect ratio analysis in Figure 3-10d. The comparison between the grains structure in both HS1 and HS2 conditions in Figure 3-9b and c reveals that the solution time at 980°C did not significantly affect the grain morphologies. The same behavior is observed in the HS4 and HS5 conditions, as shown in Figure 3-9e and f.

Figure 3-11 shows the microstructure evolution, in terms of segregated elements and phases dissolution and/or precipitation, as a function of the soaking time of both homogenization and solution treatments. Generally, as can be seen in this figure, the arc-shaped contours present in the as-printed condition (Figure 3-5a), that corresponds to the melt pool boundaries, completely disappeared after applying any of the five heat treatment conditions. For the HS1 condition, Laves phase was partially dissolved in comparison with the as-printed condition. However, the cellular-dendritic microstructure in condition HS1 is still observed as shown in Figure 3-11a and b. The EDS point analysis for these dendrites shows the occurrence of Nb and Ti enrichment and depletion in Ni, Fe and Cr at the edge of the dendrites, compared with the γ-matrix (spectrum 1 and 2 in Table 3-4). This could be attributed to the fact that the 1h homogenization time of the HS1 condition is not enough to completely dissolve the segregated elements and Laves phase. Furthermore, limited amounts of δ-phase precipitated during the solution treatment at 980°C for 15 min after the HS1 condition.

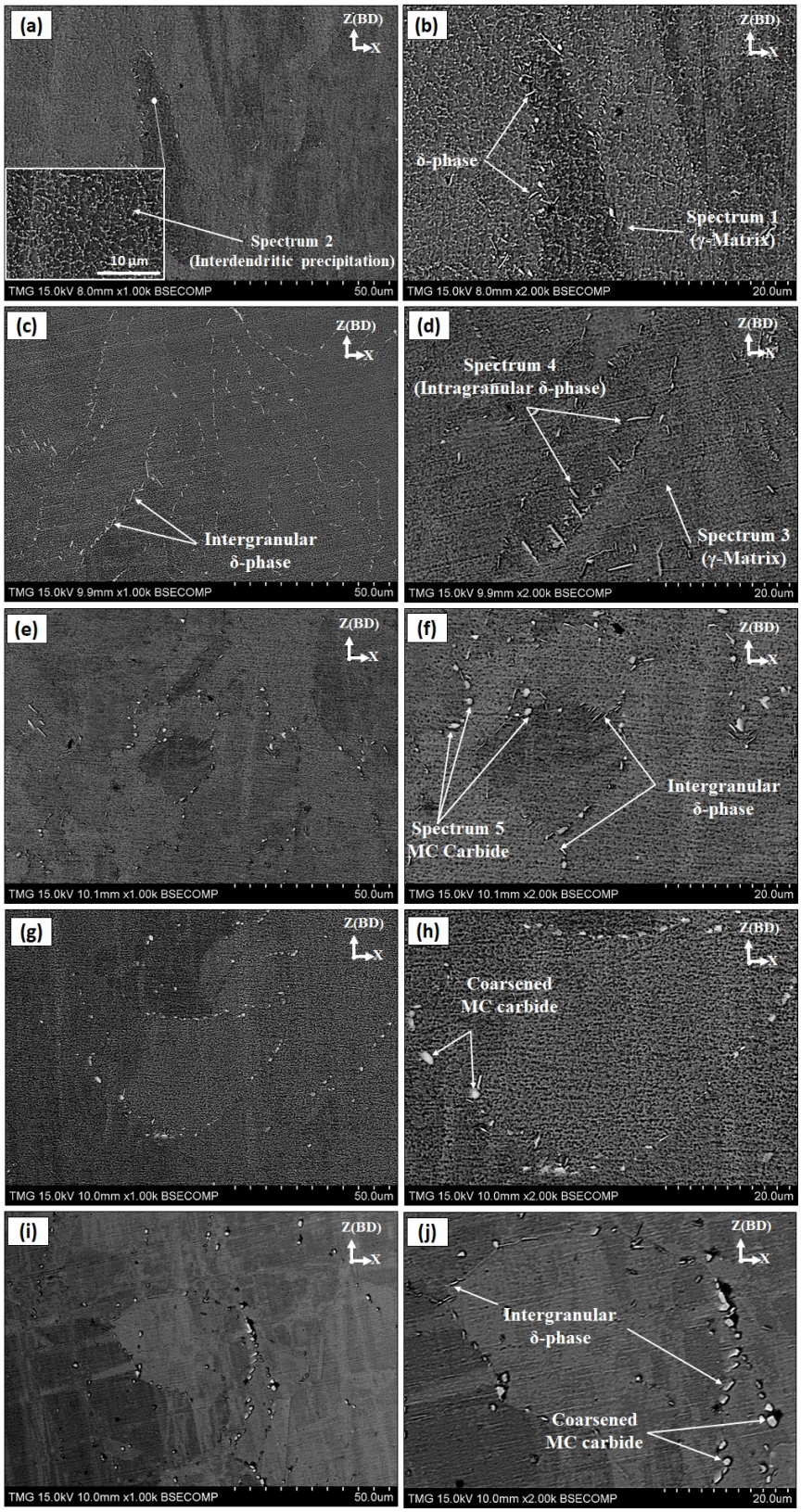

Figure 3-11: Microstructure of etched LPBF IN718 samples on vertical (xz) plane in heat-treated conditions: (a,b) HS1; (c,d) HS2; (e,f) HS3; (g,h) HS4; (i,j) HS5 treatments.

Table 3-4: EDS spot analysis results of the heat-treated conditions in Figure 3-11(wt.%).

Spectrum	Phase	Fe	Ni	Cr	Nb	Ti	Mo	Al
1	Matrix	Bal.	50.02 ± 0.43	18.25 ± 0.21	5.59 ± 0.15	0.98 ± 0.08	3.38 ± 0.11	0.48 ± 0.03
2	Laves	Bal.	44.82	13.77	14.32	1.68	2.72	0.43
3	Matrix	Bal.	49.70 ± 0.47	18.28 ± 0.19	5.46 ± 0.31	0.96 ± 0.05	3.36 ± 0.17	0.50 ± 0.02
4	δ- phase	Bal.	53.70	10.94	15.44	1.57	2.40	0.30
5	Carbides	Bal.	14.52	6.44	52.17	5.80	-	-

In the HS2 condition, the network of the cellular-dendritic substructure completely disappeared as shown in Figure 3-11c and d. Moreover, a large amount of needle-like δ-phase precipitated close to and along the grain boundaries as shown in Figure 3-11d. Since the homogenization treatment at 1080°C for 1h is not enough to completely dissolve the microsegregates of Nb and Ti in the inter-dendritic region (cellular substructure), intra-granular nucleation and growth of the δ-phase are observed close to the grain boundaries. It is well-known that the δ-phase preferentially precipitates at regions of Nb-enrichment [53]. This suggests that the concentration of the segregated Nb in the inter-dendritic region and along the grain boundaries was high enough to drive the formation of δ-phase through the subsequent solution heat treatment process. This is in good agreement with Tucho *et al.* [12] who reported that δ-phase requires a localized concentration of at least 6–8 wt.% of Nb to precipitate. The absence of the cellular microstructure inside the grains, which were enriched by Nb, after HS2 in comparison with HS1 suggests that the segregated Nb is consumed to precipitate the intra-granular needle-like δ-phase during the 1h solution heat treatment at 980°C. The precipitation of the intra-granular δ-phase has a detrimental impact on the mechanical behavior as reported by Trosch *et al.* [35]. Also, more precipitation of δ-phase consumes more Nb, which is an essential alloying element for the precipitation of γ″ strengthening

phase. Therefore, the extent of the δ-phase precipitation has a direct impact on the mechanical behavior of the laser powder bed fused IN718.

EDS analysis was performed to identify the precipitated phases and follow the back diffusion of the segregated elements into the γ-matrix after HS1 and HS2 treatments. The average of at least five EDS spot analyses in the γ-matrix at different locations is reported in Table 3-4. As can be seen from Table 3-4, the concentrations of Nb, Ti and Mo in the γ-matrix of both HS1 and HS2 conditions increased in relation to the as-printed IN718 listed in Table 3-3. The relatively lower concentration of Nb in the HS2 with respect to the HS1 condition is attributed to the higher precipitation of δ-phase (Ni_3Nb) after HS2.

The results reported in Figure 3-11e and f reveal that after the HS3 treatment, more Laves phase dissolution and complete dissolution of cellular-dendritic microstructure occurred in contrast to HS1. This indicates that with longer homogenization times (4h), enough energy is provided to significantly diffuse elemental segregates and the Laves phase. However, more irregular-shaped precipitations along the grain boundaries are observed as shown in Figure 3-11e and f. According to the EDS analysis, these precipitates are highly enriched with Nb (≈52 wt.%), Ti (≈6 wt.%) and C and, therefore, indexed as carbides, as shown in Table 3-4. Although carbon content in these precipitates was found to be significantly higher than that in the matrix, specific values are not reported here due to the low accuracy of the EDS in measuring carbon, especially for such small precipitates. The presence of such coarse carbides along the grain boundaries has a detrimental effect on the mechanical behavior of the IN718 superalloy, especially at elevated temperatures. Furthermore, a moderate amount of needle-like δ-phase precipitated mainly along the grain boundaries as can be seen in Figure 3-11. By comparison, the amount and the size of the δ-phase were less than that precipitated in HS2 treatment. This again confirms that the amount and

size of the δ-phase are directly proportional to solution treatment time. Also, it can be seen from Figure 3-11f that only inter-granular δ-phase precipitated in the HS3 condition reflecting the fact that the homogenization at 1080°C for 4h completely dissolved the Nb-rich precipitates in the inter-dendritic regions [12].

Coarse irregular-shaped precipitates along the grain boundaries are observed after applying the prolonged (7h) homogenization treatment at 1080°C as shown in Figure 3-11g to j. According to the EDS analysis of these particles, enrichment in Nb, Ti and C is observed and identified as carbides according to Tucho *et al.* [12]. Despite that both the HS5 and HS2 treatments include the same solution time, 1h, at 980°C, the amount of δ-phase in the HS5 condition is less than that in the HS2 condition as shown in Figure 3-11c and i. This could be attributed to the long homogenization treatment in the HS5 condition that preceded the solution treatment. This significantly dissolved the segregated Nb along with Laves phase in the inter-dendritic regions and grain boundaries, resulting in a relatively uniform distribution of Nb in the matrix. Accordingly, the concentration of Nb at the grain boundaries after HS5 is not enough to precipitate the same amount of δ-phase after HS2 since the precipitation of δ-phase requires at least 6–8 wt.% of Nb as reported by Tucho *et al.* [12].

3.3.3 Structure, texture and phase evolution

3.3.3.1 Structure and phase evolution using XRD analysis

The XRD patterns of the as-received IN718 powder, as-printed and heat-treated IN718 samples (before and after aging treatment) from the xy-plane are illustrated in Figure 3-12. The diffraction pattern of the as-received IN718 powder shows the main five peaks at diffraction angles of: 43.39° (111), 50.49° (200), 74.39° (220), 90.29° (311), and 95.57° (222) that correspond to the γ-matrix [91]. Compared to the IN718 powder, the as-printed condition shows a higher peak intensity of

(200) than (111) which is consistent with the commonly recognized texture for the laser powder bed fused IN718 superalloy. This is attributed to the preferred <001> crystallographic growth orientation of the γ (FCC) crystals and the presence of a large thermal gradient along the building direction [67].

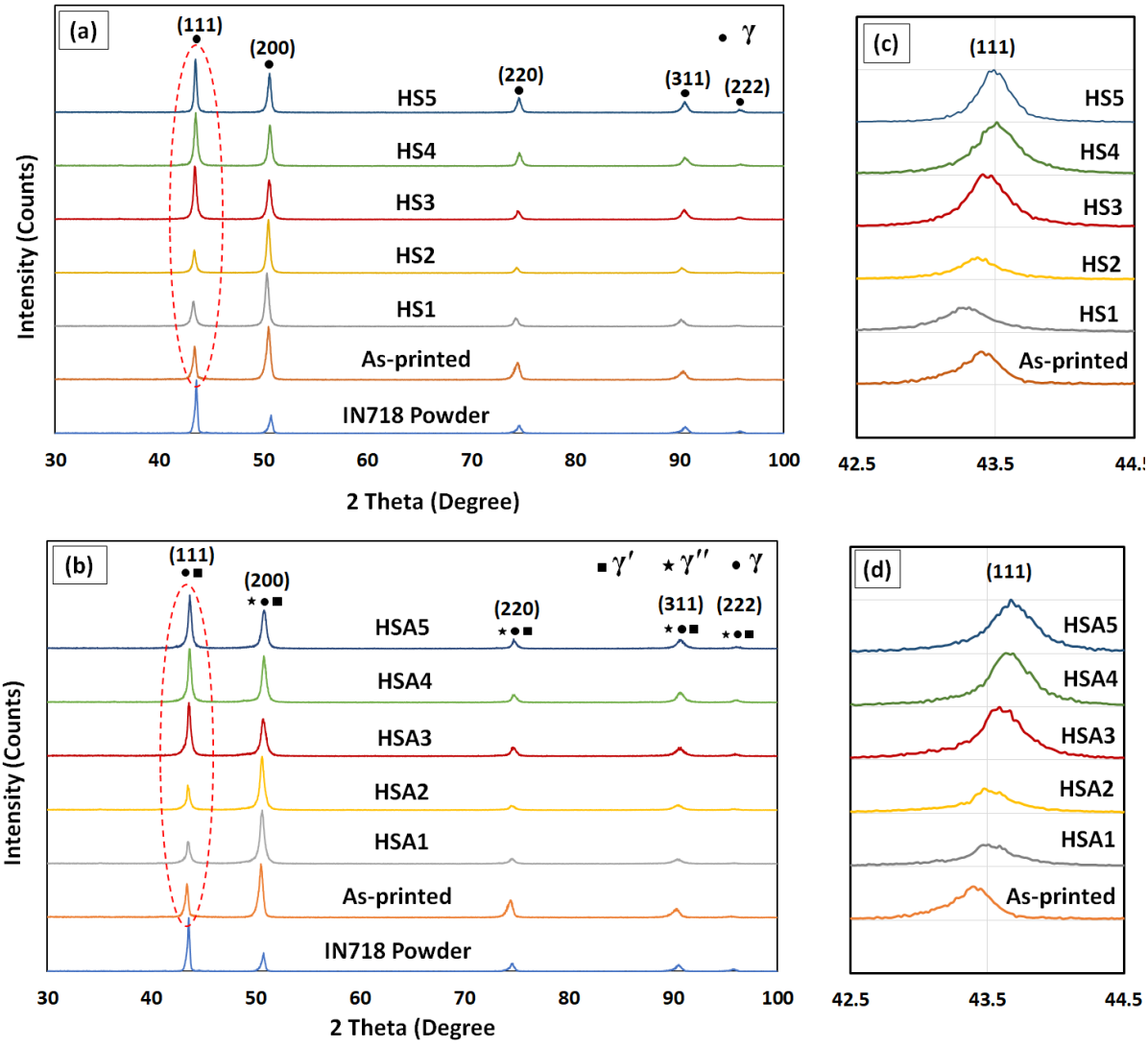

Figure 3-12: XRD patterns of the IN718 powder, as-printed LPBF and heat-treated conditions: (a) before aging; (b) after aging; (c, d) focus on 2θ = 43.3 in both (a, b).

Generally, after applying the five heat treatments, changes in the peak intensities and peak positions are observed suggesting microstructural evolution in terms of texture and secondary phase dissolution and/or precipitation. Before aging treatment, the XRD patterns of the HS1 and

HS2 conditions exhibited also higher peak intensity of γ (200) than of γ (111) suggesting that homogenization treatment for 1h was not enough to change the as-printed strong texture along γ (200) as shown in Figure 3-12a. After the HS3, HS4 and HS5 treatments, the XRD patterns exhibited a different peaks intensity compared to the as-printed, HS1 and HS2 conditions. The intensity of the γ (111) peak became higher than that of the γ (200), indicating that significant change in the as-printed texture occurred after the HS3, HS4 and HS5 treatments. This suggests that homogenization treatment at 1080°C for 4h or more is sufficient to significantly change the as-printed texture. Figure 3-12b shows the diffraction pattern of the heat-treated conditions after aging. It can be observed that the XRD patterns of the post-processed conditions before and after aging appear identical in terms of texture, implying that the aging treatment did not cause noticeable changes in the material texture, which is in agreement with Wakshum *et al.* [75].

According to Bragg's law, changes in the peak positions (2θ) are explained by variations in lattice spacing, which consequently refer to change in material composition [76]. Also, it is well recognized that the atomic size of Nb, Ti and Mo, which are the dominant segregated elements in the as-printed condition, are 33%, 18% and 27.5% larger than that of Ni, respectively [77]. This indicates that noticeable changes in lattice parameters are expected to occur during the diffusion and/or rejection of these solute elements. Thus, following the changes in the peak positions helps to follow the precipitation/dissolution of Nb, Ti and Mo during the heat treatments [76]. Figure 3-12c and d shows the peak position of the γ (111) plane before and after aging treatment. Before aging treatment, the HS1 and HS2 conditions revealed a peak shift to smaller 2θ values in relation to the as-printed sample as shown in Figure 3-12c. This could be attributed to the back diffusion of the segregated alloying elements into the matrix during the 1h homogenization treatment. While after HS3, HS4 and HS5 treatments, peaks shifted to the higher 2θ values that could be explained

by the depletion of the Nb, Ti and Mo in the γ-matrix. This behavior is consistent with the current microstructure and EDS results of the HS3, HS4 and HS5 treatments since after the application of these conditions, more precipitation of carbides is observed which consequently consumed more Nb and Ti from the γ-matrix. While after aging treatment, γ (111) of the γ-matrix in the five treatments conditions shifted to higher diffraction angles because of the precipitation of the strengthening phases, γ′ (Ni_3 (Ti, Al)) and γ″ (Ni_3Nb), that consumed Ti and Nb from the matrix.

To analyze this further, the lattice parameter of the γ-matrix was calculated from the main five diffracted peaks in the as-printed and post-processed specimens before aging, and then the average value for each condition was calculated. Figure 3-13 shows the calculated lattice parameter of the γ-matrix and the grain structure evolution as a function of the heat treatment conditions. After the HS1 and HS2 treatments, the lattice parameter of the γ-matrix increased from (3.5999 ± 0.0034 Å) in the as-printed condition to (3.6070 ± 0.0017 Å) and (3.6039 ± 0.0016 Å), respectively. This behavior is attributed to the back diffusion of the Nb and Ti into the γ-matrix during the 1h homogenization treatment in both HS1 and HS2 conditions that consequently resulted in an expansion of the lattice parameters. Among the HS1- and HS2-treated conditions, HS2 exhibited a relatively smaller lattice parameter. This is due to a larger amount of δ-precipitates (Ni_3Nb) after HS2 treatment that depleted Nb from the γ-matrix. On the other hand, after the HS3, HS4 and HS5 treatments, reduction in the lattice parameter value with respect to the other conditions is observed and the lattice parameter stays relatively constant after these treatments due to the precipitation of Ti and Nb carbides, which is consistent with the microstructure and EDS analyses.

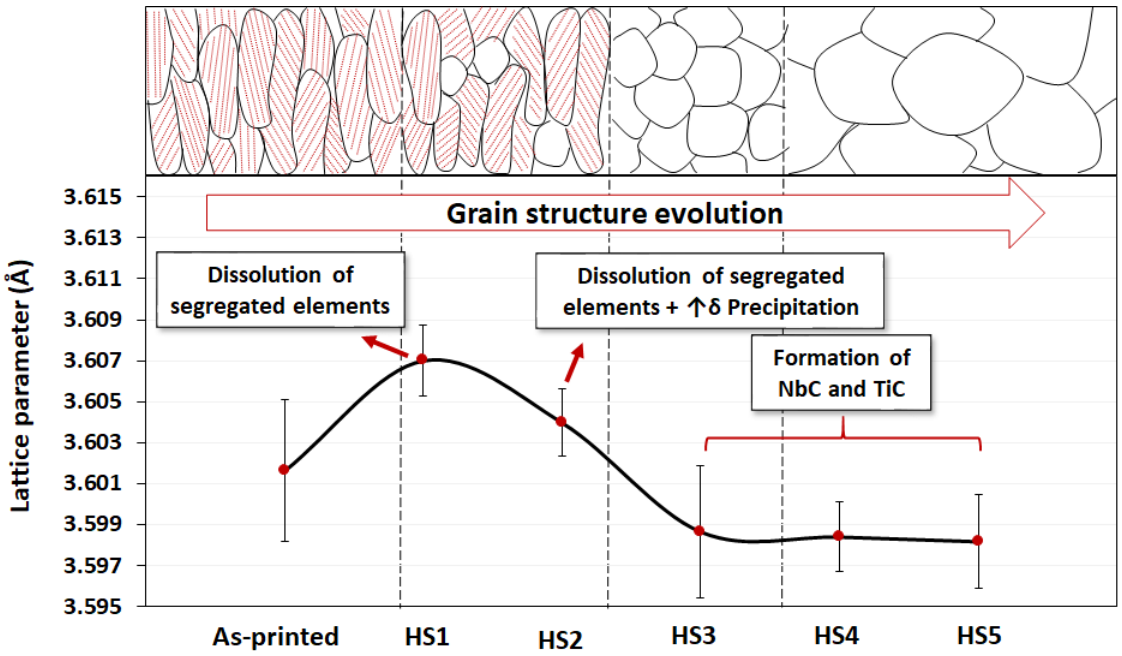

Figure 3-13: Evolution of the γ-matrix's lattice parameter and grain structure as a function of the post-treatment conditions.

3.3.3.2 Texture evolution and grain structure analysis

Since producing materials with strong texture and anisotropic mechanical properties are considered to be one of the main drawbacks of the LPBF process of Inconel 718, crystallographic orientations of IN718 as a function of the homogenization and solution treatment times were examined aiming to obtain the treatment conditions that result in a weak material texture and isotropic mechanical properties. For that, EBSD analysis was carried out to evaluate the material textures, grain orientations and grain morphologies of the post-treated laser powder bed fused IN718 superalloy. According to the XRD results, it is found that the homogenization holding time significantly affects the crystallographic orientation of the as-printed IN718. Thus, the three levels of the homogenization time 1, 4 and 7h, which corresponded to HSA2, HSA3 and HSA5 heat treatments, were examined using EBSD mapping. All EBSD maps were acquired from the xz-plane, since the crystallographic orientation along the building direction is of main interest. It can be confirmed from Figure 3-14a that the HSA2 treatment in the present study did not significantly

alter the crystallographic structure and orientations as the grains remained columnar and oriented parallel to the building direction which is consistent with the current microstructure and XRD results. This indicates that anisotropic mechanical properties are expected for the HSA2-treated samples.

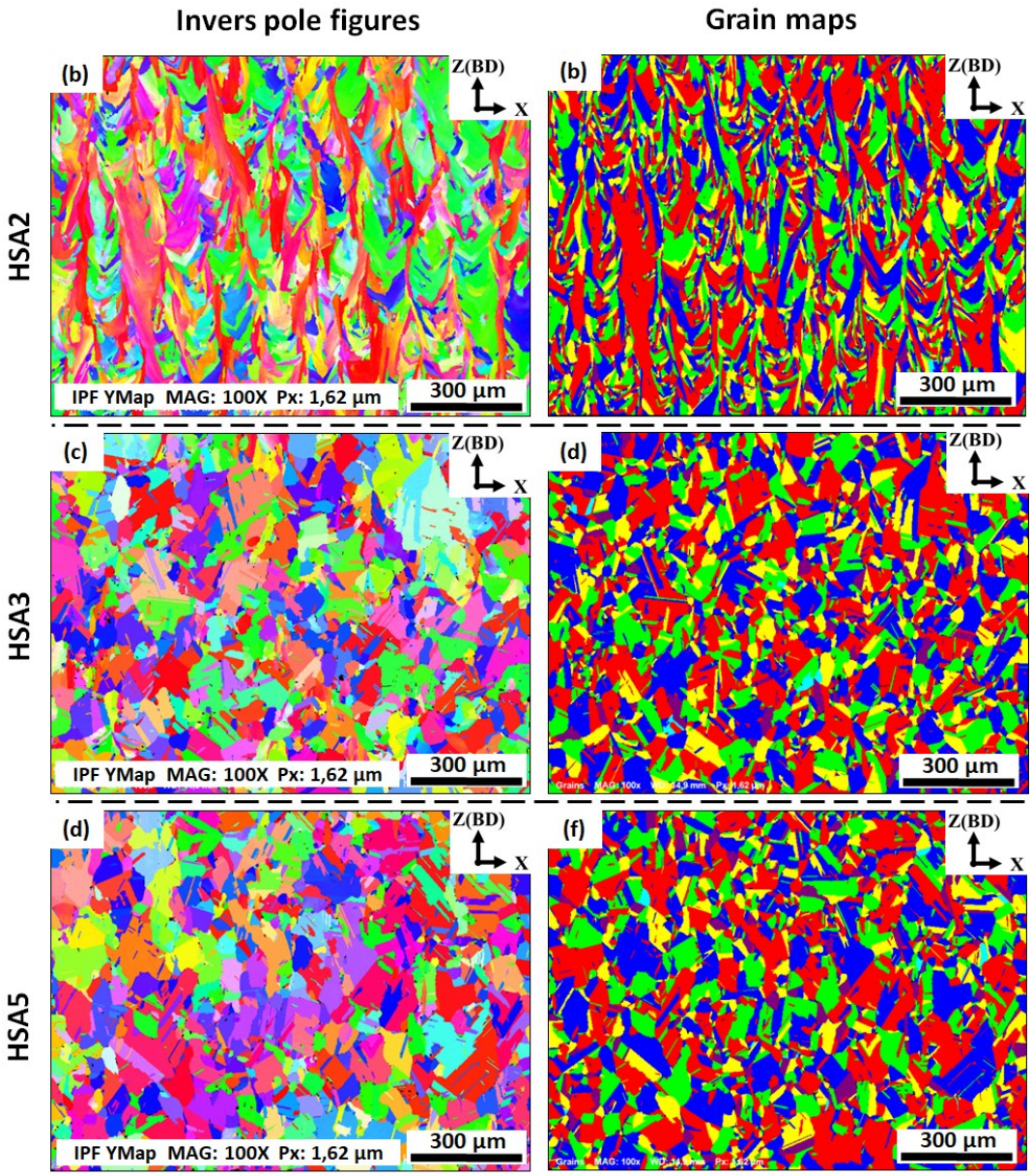

Figure 3-14: The EBSD inverse pole figures (a,c,e) and grain maps (b,d,f) in the xz-plane of laser powder bed fused IN718 specimens in conditions: (a,b) HSA2; (c,d) HSA3 and (e,f) HSA5. For the IPF color legend, please refer to that presented in Figure 3-8. All the EBSD crystallographic orientation maps were plotted using the y-based projected IPF.

On the other hand, after HSA3 and HSA5, a significant change in the crystallographic orientations and grain morphologies are observed as shown in Figure 3-14b and c. Non-distinct texture for laser powder bed fused IN718 components can be obtained using these conditions. The microstructure of the HSA3 and HSA5 conditions are characterized by the presence of mainly equiaxed randomly oriented grains with annealing twins, indicating that recrystallization has occurred as shown in Figure 3-14d and f, respectively. Such a change in grain morphologies and crystallographic orientations would have a beneficial effect on producing components with isotropic mechanical properties.

3.3.4 Room temperature Vickers hardness in both the as-printed and heat-treated conditions

Vickers microhardness testing was performed for both the as-printed and heat-treated conditions (before and after aging treatment) to investigate the effect of variations in the homogenization and solution treatment holding times on the strengthening of the laser powder bed fused IN718. Also, the evolution of the grain aspect ratio in the five heat treatment conditions was added to correlate the mechanical properties with the microstructure. As can be seen in Figure 3-15, changes in the heat treatment holding times have a significant impact on the hardness measurements. Before aging treatment, it can be seen that the as-printed condition exhibited higher hardness than any of the heat-treated conditions. This is attributed to the substructure/strain strengthening mechanism. It is well recognized that the microstructure of as-printed conditions contains a high density of dislocation tangles due to the fast melting and solidification during the printing process as reported by Cao *et al.* [78] and Tucho *et al.* [12] and shown in Figure 3-16 [12]. The presence of such a dislocation network strengthens the IN718 material through the strain strengthening mechanism.

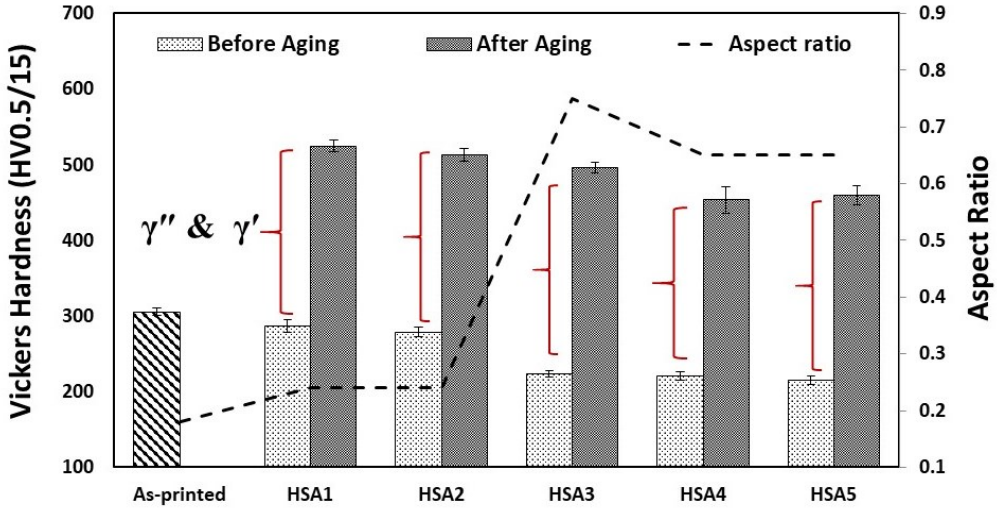

Figure 3-15: Vickers hardness and aspect ratio evolutions in the as-printed and post-processed samples before and after aging.

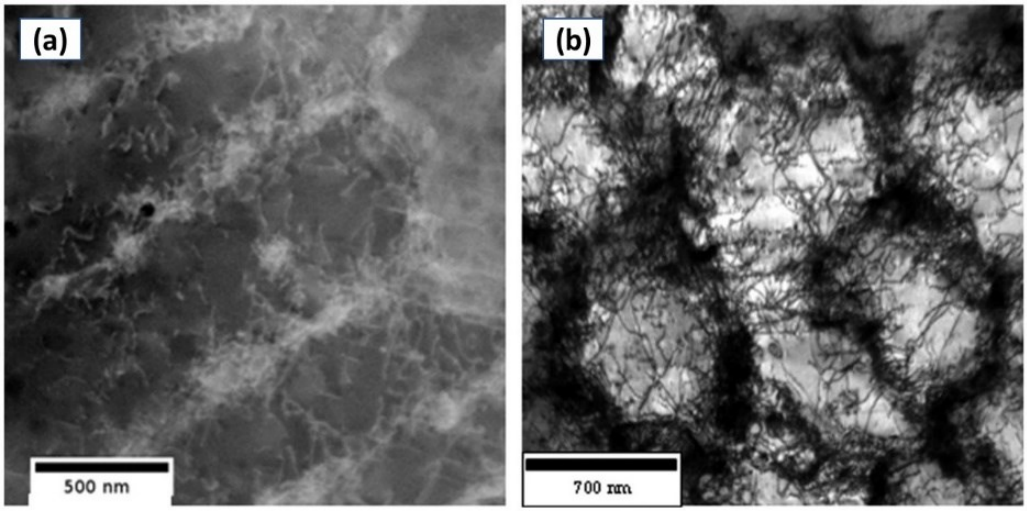

Figure 3-16: TEM image illustrating the dislocation network of the as-printed IN718 in: (a) columnar microstructure; (b) cellular microstructure [12]. Copyright 2017, Elsevier E. V.

After applying the heat treatments without aging, hardness measurements decreased by 6%–29% of the as-printed condition depending on the variation in the treatment times, as shown in Figure 3-15. This reduction in the hardness can be explained by the annihilation of some dislocations and other lattice defects with increasing the holding time. However, among the heat-treated conditions, the 1h homogenized condition, HS1 and HS2, exhibited a slight reduction in the hardness, 6% and 8.6%, respectively, of the as-printed conditions suggesting that the 1h

treatment was not enough to eliminate the substructure and dislocation network. On the other hand, after prolonged homogenization treatment, a significant reduction in the hardness in relation to the as-printed, HS1 and HS2 conditions is observed. This can be explained by the longer holding time of the homogenization treatment (4h) in HS3 results in promoting the recrystallization followed by grain growth after the longer homogenization time (7h) in the HS4 and HS5 conditions. These findings are consistent with the microstructure results and the aspect ratio development as shown in Figure 3-15.

Generally, under the same aging conditions, the hardness of the as-printed samples significantly increased by 51%–72% depending on the variation in the treatment time. This is because of the precipitation of the strengthening phases, γ′ and γ′′, after the aging treatment. As can be seen in Figure 3-15, the HSA1 and HSA2 conditions exhibited the highest hardness among the five treatment conditions, which is due to the combined effects of precipitate strengthening (γ′ and γ′′) and substructure strengthening (dislocation network) mechanisms. Moreover, by recalling the lattice parameter calculations of the γ-matrix after HSA1 and HSA2 treatments, significant back diffusion of the strengthening elements is observed in relation to the other treatment conditions. Thus, more precipitation of γ′ and γ′′ are expected after the HSA1 and HSA2, which consequently strengthens the material. After the HSA3, HSA4 and HSA5 conditions, however, lower hardness is observed in relation to the other heat treatment conditions due to the combination of grain growth accompanied by stress relief and precipitation of carbides. As confirmed by the microstructure results, the latter process consumed Nb and Ti at the expense of the γ′′ and γ′ precipitates. Based on the above analysis, it can be concluded that the precipitation hardening is the dominant strengthening mechanism of the laser powder bed fused IN718 superalloy after the application of the HSA3, HSA4 and HSA5 conditions.

3.4 Conclusions

In the present study, the influence of homogenization and solution treatment times on the microstructure, phases precipitation and/or dissolution, texture evolution and Vickers microhardness of IN718 alloy processed by laser powder bed fusion process has been investigated. The main observations can be summarized as follows:

- The as-printed microstructure of IN718 consists of elongated grain morphologies oriented parallel to the building direction and a very fine dendritic substructure that epitaxially grows across several solidified layers. Such a microstructure is completely different from that encountered in the cast and wrought materials. Thus, the kinetics during the heat treatment of the laser powder bed fused IN718 parts are different from its cast or wrought forms.
- Homogenization holding time has a significant impact on the microstructure, precipitates, crystallographic orientation and mechanical properties of the laser powder bed fused IN718. However, the 1h homogenization treatment at 1080°C is not enough to change the as-printed texture and grain structure. Also, Laves phase and inter-dendritic segregates are only partially dissolved after this treatment.
- Complete recrystallization and more dissolution of the (Nb, Ti)-rich segregates along with Laves phase are achieved after 4h homogenization treatment at 1080°C. Nevertheless, more carbide particles are formed with 4h homogenization treatment. Further increase in the homogenization time (7h) results in grain growth and carbides coarsening.
- The increase in the solution time at 980°C does not significantly affect the grain structure and material texture. However, the amount of δ-phase is directly proportional to the duration of the solution heat treatment.

- After post-treatments, the hardness significantly increases by 51%–72% depending on the treatment time because of the precipitation of γ′ and γ″. Among the heat-treated conditions, the 1h homogenization treatment conditions exhibit the highest hardness which decreases by increasing soaking time.
- Both substructure/strain (dislocation network) strengthening and precipitation hardening (γ′ and γ″) are the strengthening mechanisms in the 1h homogenized treatment condition, while in the 4h and 7h homogenized conditions, mainly precipitation hardening strengthening mechanism is attained.

A systematic investigation will continue focusing on the elevated-temperature mechanical behavior of the laser powder bed fused IN718 following the same post-treatment window scheme. Furthermore, analyzing the fracture surface and correlating the high-temperature mechanical properties with the initial microstructure evolution is in progress.

Chapter 4 : Effect of Homogenization and Solution Treatments Time on the Elevated-Temperature Mechanical Behavior of Inconel 718 Fabricated by Laser Powder Bed Fusion

Eslam M. Fayed[1], Mohammad Saadati[2], Davood Shahriari[2], Vladimir Brailovski[2], Mohammad Jahazi[2], and Mamoun Medraj[1,*]

[1]Department of Mechanical, Industrial and Aerospace Engineering, Concordia University, 1515 Sainte-Catherine Street West, Montreal, QC H3G 2W1, Canada
[2]Department of Mechanical Engineering, École de technologie supérieure, 1100 Notre-Dame Street West, Montreal, QC H3C 1K3, Canada
*corresponding: mmedraj@encs.concordia.ca; Tel.: +1-514-848-2424

This paper has been accepted for publication in Scientific Reports, Nature (January 2021)

Abstract

In the present study, the effect of homogenization and solution treatment times on the elevated-temperature (650°C) mechanical properties and the fracture mechanisms of Inconel 718 (IN718) superalloy fabricated by laser powder bed fusion (LPBF) was investigated. Homogenization times between 1 to 7h at 1080°C were used, while solution treatments at 980°C were performed in the range from 15 to 60 min. The as-printed condition showed the lowest strength but the highest elongation to failure at 650°C, compared to the heat-treated conditions. After heat treatments, the strength of the IN718 alloy increased by 20.3 to 31% in relation to the as-printed condition, depending on the treatment time, whereas the ductility decreased significantly, by 67.4 to 80%. Among the heat treatment conditions, the 1h homogenized conditions at 1080°C (HSA1 and HSA2) exhibited the highest strength and ductility due to the combined effects of the precipitation hardening and sub-structural changes. Further increases in the homogenization time to 4 and 7h led to a decrease in the strength and significant ductility loss of the LPBF IN718 due to the considerable annihilation of the dislocation tangles and a greater precipitation of coarse MC carbide particles. Furthermore, it was found that the solution treatment duration had a crucial

influence on the mechanical properties at 650°C due to the increase in the grain boundary strength through the pinning effect of the inter-granular δ-phase. In addition, the fracture mechanism of the LPBF IN718 was found to be dependent on the heat treatment time. Finally, this investigation provides a map that summarizes the effect of homogenization and solution treatment times on the high-temperature mechanical behavior of LPBF IN718 by relating it to the corresponding microstructural evolution. This effort strives to assist in tailoring the mechanical properties of LPBF IN718 based on the design requirements for some specific applications.

Keywords: High-temperature mechanical properties; additive manufacturing; laser powder bed fusion; nickel-based superalloy; IN718; fracture analysis; microstructure

4.1 Introduction

In the past decades, elevated-temperature applications have become more extensive, and have come to include different fields, such as aerospace, petrochemical, power plant, energy, and nuclear reactor industries [5,50]. Demand for materials withstanding harsh in-service conditions has consequently received considerable attention in these applications. For instance, the gas temperature in some hot zones of high-performance aircraft engines may reach 1090°C [5]. Different cooling techniques have accordingly been developed to reduce the actual metallic component's temperature to a level at which superalloys can still be used. Inconel 718 (IN718) is one of the superalloys that are widely used in different elevated-temperature applications because of its ability to retain high mechanical strength at high temperatures up to 650°C, and high resistance to surface deterioration, even in corrosive environments [47,57]. Nowadays, over 50% of the total weight of advanced aircraft engines components are fabricated from the IN718 superalloy [5].

The mechanical properties of IN718 superalloy are highly related to its microstructure, which itself consists of multiple phases, such as γ-matrix, which is the primary phase, along with γ′

($Ni_3(Al,Ti)$), γ″ (Ni_3Nb), Laves phase $(Ni,Fe,Cr)_2(Nb,Mo,Ti)$, δ-phase (Ni_3Nb) and carbides (MC, $M_{23}C_6$ and M_6C) [12]. Adjustment of the sizes, contents and distributions of these phases is key to obtaining enhanced mechanical properties. In order to attain high mechanical properties that meet in-service requirements, IN718 is post-processed through the full heat treatment regime of: (1) homogenization, (2) solid solution and (3) precipitation hardening [75]. The homogenization and solid solution treatments are carried out at temperatures between 980°C and 1200°C to dissolve detrimental phases, such as Laves phases, and release age-hardening elements into the γ-matrix, in addition to precipitation of the inter-granular δ-phase. The precipitation hardening treatment is performed in two consecutive steps to precipitate the strengthening phases (γ′ and γ″). The first step is realized at a temperature between 704°C and 899°C, and the second is carried out at a temperature between 593°C and 704°C [75].

To date, IN718 components have either been cast, wrought or made by powder metallurgy [28]. Nevertheless, with fast improvements of the performance of turbine engines in the aerospace and energy industries, complicated cooling features are continually added to IN718 components to improve their capability to withstand significant temperature increases inside the advanced turbine engines. For instance, more internal cooling channels have been included in turbine blades. Such design and cooling features increase the fabrication cost and the geometrical complexity of components, and in some cases, are even impossible to incorporate in the manufacturing process using existing traditional methods. Furthermore, the high hardness and poor machinability of the IN718 superalloy introduce several challenges during the conventional manufacturing of IN718 components [50]. Thus, more and more attention is being paid to additive manufacturing (AM) techniques as alternative fabrication methods for IN718 parts, especially in the aerospace and energy industries.

IN718 superalloy is characterized by its high weldability [75], and is highly promising as a candidate processed using AM. Among all AM techniques, the laser powder bed fusion (LPBF) process has gained considerable attention in various industrial sectors due to its outstanding potential versus conventional manufacturing routes. Compared to conventional methods, the LPBF process presents significant advantages, such as (i) the ability to fabricate complex-shaped components without geometrical limitations, (ii) a low buy-to-fly ratio (as little as 2) versus conventional manufacturing methods, where this metric can reach 50, (iii) production time and cost savings, and (iv) the production of fine microstructures and improved mechanical properties as compared to traditional fabrication methods, such as casting and powder metallurgy [24,33–35]. Furthermore, the LPBF process is capable of processing various engineering metallic materials, including IN718, with promising mechanical properties. However, LPBF-fabricated IN718 components usually require thermal post-treatment to reduce their level of residual stresses, homogenize their microstructure and precipitate the desired phases to enhance their mechanical properties, especially at elevated temperatures. On the other hand, it has been found that applying improper heat treatment conditions can lead to the retention of some of detrimental phases, such as Laves phase, which could have a negative impact on the mechanical behavior of LPBF IN718 [24]. Thus, suitable post-treatments are required to obtain a homogenized microstructure as well as high mechanical properties at elevated temperatures.

Although IN718 superalloy is mainly designed for elevated-temperature applications, the mechanical behavior of the LPBF IN718 reported in the literature is characterized mainly at room temperature [52,79–86], and only a few works have been reported on its behavior at elevated temperatures [34,35,87]. For instance, Trosch *et al*. [35] investigated the mechanical behavior of forged and LPBF-fabricated IN718 at room temperature (RT) and at 650°C. Both were heat-treated

using the standard heat treatment (SHT) conditions of wrought IN718 (solution annealing at 980°C for 1h + double aging at 720°C for 8h and at 620°C for 8h; designated as SA). Their results [35] illustrate that at RT, the LPBF IN718 samples exhibited a higher tensile strength (TS), equivalent yield strength (YS), and lower ductility than did the wrought IN718. However, at 650°C, the LPBF IN718 showed a significant drop in both strength and ductility as compared to the wrought alloy. The authors of this study [35] attributed this behavior to the precipitation of intra-granular δ-phase after the SHT of LPBF IN718. Thus, they suggested that homogenization treatment above 1030°C (the solvus temperature of δ-phase), before the solution annealing, would diminish the amount of intra-granular δ-phase, and consequently improve the mechanical properties at high temperatures [35]. Furthermore, Strößner *et al*. [34] studied the effect of different heat treatments on the mechanical properties at 650°C of IN718 alloy fabricated by LPBF. Before tensile testing, two AMS standard heat treatment conditions were applied to the as-printed IN718: (i) AMS 5662 (solution treatment at 980°C for 1h, followed by air cooling, and then aging at 760°C for 10h, furnace cooling to 650°C with a 50°C/h heating rate, and holding at 650°C for 8h with subsequent air cooling to RT); (ii) AMS 5664 (homogenization treatment at 1065°C for 1h, followed by the same cycle of the solution and aging treatments as described in AMS 5662). Their results revealed that at 650°C, the heat-treated LPBF IN718 exhibited a tensile strength (1115 MPa) comparable to that of its wrought equivalent, but a significantly lower elongation to failure (8%) [34]. Such elevated-temperature ductility loss (embrittlement) of the nickel-based superalloy fabricated by LPBF has been extensively reported in the literature [34,35,63,88]. In this context, Zhao *et al*. [63] investigated the evolution of the tensile properties of the conventionally heat-treated (SA) LPBF IN718 at different temperatures (500, 550, 600 and 650°C) to demonstrate the cause of the elevated-temperature ductility loss. Their [63] results show that 650°C is the critical temperature

of the embrittlement phenomenon of the LPFB fabricated IN718 due to the excessive grain boundary oxidation and the overaging behavior at this temperature.

The application of the industrial standard treatments developed for either cast or wrought IN718 to their LPBF equivalent appears to be inadequate to improve the high-temperature mechanical properties of the latter. This is attributed to dramatic differences in the initial microstructure obtained after the LPBF, casting and forging manufacturing methods. In our previous study [89], a post-heat treatment time window covering a wide range of soaking times for the homogenization (from 1 to 7h at 1080°C) and solution (from 15 to 60 min at 980°C) treatments was established, and the effects of these post-treatment conditions on the microstructure, material texture, precipitates and hardness were studied. The objective of that study [89] was to tune the homogenization and solution treatment times to improve the microstructure of LPBF IN718 components, with the ultimate goal of optimizing their mechanical properties. It was found that after the homogenization treatment for 1h at 1080°C, Laves phases and elemental segregation formed during the printing process were not completely dissolved, and the as-printed texture and grain structure were not significantly affected [89]. However, an increase in the homogenization treatment time at 1080°C significantly influenced the microstructure in terms of precipitates and texture [89], and the longer the duration of this treatment, the more intensive the dissolution of Laves phase, the diffusion of segregates and texture weakening [89]. A completely recrystallized material and stress-relived equiaxed grains were obtained after 4h of homogenization treatment at 1080°C [89]. From a negative perspective, more and coarser carbides were observed after the 4 and 7h homogenization times at 1080°C [89]. Furthermore, with a 1h homogenization treatment at 1080°C, it was found that the solution treatment time significantly affected the fraction of δ-phase precipitation along the grain boundaries, whereas at the prolonged

homogenization time (7h), the significance of the solution time decreased [89]. However, the effect of the solution treatment time on the material hardness at RT was not altogether significant in both cases [89].

As discussed above, changes in the homogenization and solution treatment times had a significant impact on the microstructural characteristics of the LPBF IN718, which consequently affected the mechanical properties. However, RT hardness testing did not provide comprehensive information about the effect of the evolution of the phases under different homogenization and solution times on the mechanical behavior of the LPBF IN718 [89]. For instance, the effect of δ-phase and the precipitation of carbides on the material strength and ductility, especially at high temperature, was not captured in our previous study [89]. Moreover, only limited studies have been published on the elevated-temperature mechanical behavior of the additively manufactured IN718 superalloy, hence the need for further studies to optimize the homogenization and solution treatment times.

The present study is a logical continuation of our previous work as we assess the elevated-temperature mechanical properties and the fracture mechanism of the LPBF IN718 as a function of the homogenization and solution treatment times. This will allow a correlation with, and further understanding of the effect of the microstructure and phase evolution obtained in the former study on the in-service mechanical behavior.

4.2 Material and methods

IN718 tensile samples were additively manufactured form a gas-atomized IN718 powder with a particle size distribution of D10 (18.2 μm), D50 (32.4 μm) and D90 (54.2 μm) using an EOS M280 (EOS, Krailling, Germany) LPBF system equipped with a Yb:YAG 400W fiber laser. A nominal chemical composition of the as-received IN718 powder is as follows (wt. %): Ni (49.19),

Cr (19.04), Nb (4.92), Mo (2.70), Al (0.33), Ti (1.08) and Fe (balance). The EOS Original Parameter Set IN718_Surface 1.0 (285 W laser with 100 µm beam diameter, 1000 mm/s scanning speed, 110 µm hatching space, and 40 µm layer thickness, and argon atmosphere) was used to manufacture two sets of coupons: 83 × 19 × 4 mm^3 for tensile testing and 22 × 17 × 10 mm^3 for microstructure analysis, as shown in Figure 4-1. As can be seen in Figure 4-1a, the coupons' longitudinal axes were oriented parallel to the building direction. Wire electro-discharge machining (WEDM) was used to remove the coupons from the printing platform, and no stress relief heat treatment was applied to preserve the as-printed microstructure.

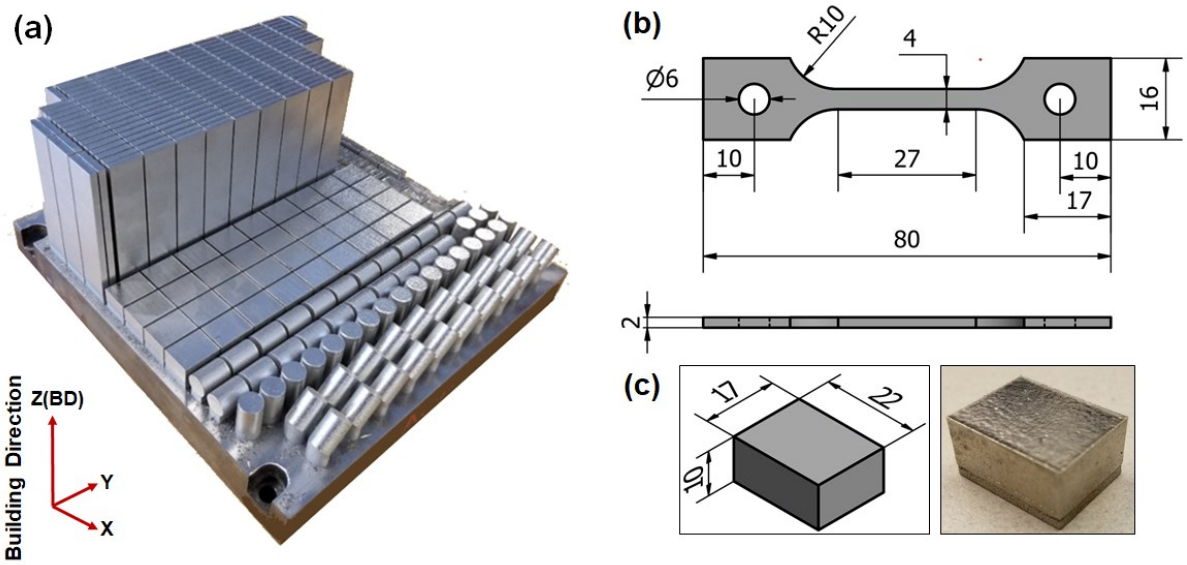

Figure 4-1: Building platform illustrating the building orientation of the prismatic coupons; (b) geometry of the tensile samples; (c) geometry of the cuboid samples (dimensions in mm).

To investigate the effect of both homogenization and solution treatment times on the high-temperature tensile properties of LPBF IN718, a treatment time window, consisting of five conditions, was established, as shown in Figure 4-2. This window combines a homogenization treatment time range at 1080°C from 1 to 7h, whereas for the solution treatment at 980°C, it goes from 15 to 60 min. Therefore, as can be seen in Figure 4-2, two samples were homogenization heat-treated at 1080°C for 1h: one of them was followed by solution treatment at 980°C for 15 min

(HSA1), and the other, for 60 min (HSA2), at the same temperature (980°C). Similarly, the other two samples were homogenization heat-treated at 1080°C for 7h: one of them was followed by solution treatment at 980°C for 15 min (HSA4) and the other, at 60 min (HSA5). Furthermore, a heat treatment condition with an intermediate time for homogenization and solution treatments was performed at 4h for homogenization and 37.5 min for solution treatment (HSA3) to follow the evolution of the mechanical properties within the time window. Then, the corresponding samples were aged at 720°C for 8h, followed by furnace cooling at 55°C/h to 620°C, and then held at 620°C for 8h, followed by air cooling to room temperature. The designations and details of the five heat treatment conditions are listed in Table 4-1. Further justifications for these heat treatment conditions are given in our previous study [89]. The IN718 coupons were heat-treated with an electric-resistance furnace under normal atmosphere using a set of K-type thermocouples to monitor the coupons' temperature during the treatment, with the temperature difference controlled within ± 5°C. The coupons were finally WEDM-machined to the final dimensions shown in Figure 4-1b. It is worth mentioning that the machining was realized after the heat treatments to avoid sample distortion due to the presence of residual stresses inherited from the printing process.

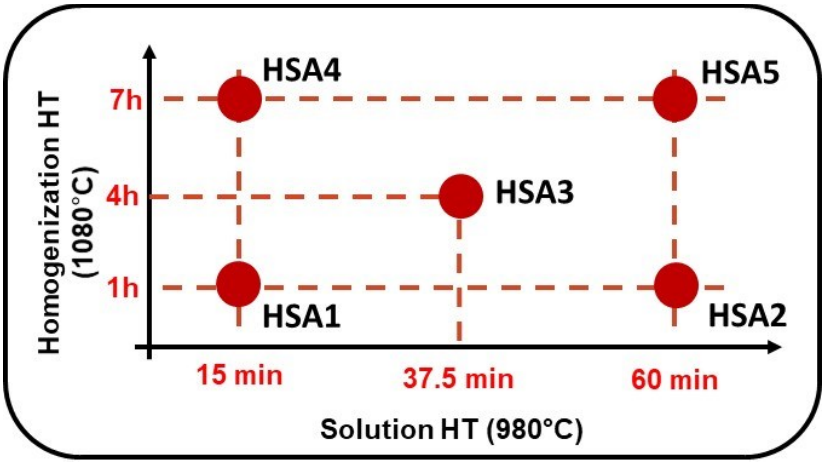

Figure 4-2: Schematic drawing shows the time window of post-heat treatment conducted in the present study

Table 4-1: Designations of the specimens and the details of the corresponding post-treatment conditions.

Designation	Homogenization Heat treatment (H)	Solution Heat treatment (S)	Aging Heat treatment (A)
As-printed	None	None	None
HSA1	1080°C for 1h/AC*	980°C for 15 min/AC	720°C/8h/FC** at 55°C/h to 620°C +620°C/8h/AC
HSA2	1080°C for 1h/AC	980°C for 1h/AC	
HSA3	1080°C for 4h/AC	980°C for 37.5 min/AC	
HSA4	1080°C for 7h/AC	980°C for 15 min/AC	
HSA5	1080°C for 7h/AC	980°C for 1h/AC	

*AC: air cooling, **FC: furnace cooling

Since the IN718 superalloy is mainly designed to fabricate components used in high-temperature applications, tensile testing at 650°C was conducted to allow greater representation of the mechanical behavior of LPBF IN718 alloy in the in-service environment. To this end, an MTS 810 tensile testing system equipped with an infrared radiant heating furnace was used, as shown in Figure 4-3. The tensile tests were conducted under a constant strain rate of 10^{-3} s^{-1}. The IN718 tensile specimens were heated to 650°C with a 1°C/s heating rate, and then held for 10 min before testing to guarantee thermal uniformity along the total length of the specimen. All tested samples were pre-loaded with a constant force of 50 N before testing to prevent the samples from buckling as a result of the thermal expansion of the IN718 during heating to 650°C. Three K-type thermocouples were used to monitor the thermal distribution along the gauge length. As can be seen in Figure 4-3b, one of these thermocouples was placed in contact with the center of the gauge length, while the others were placed close to its upper and lower ends. The central thermocouple was used for temperature control during the tensile testing. For greater accuracy, two or three specimens were tested per condition. An argon atmosphere was applied with a flow rate of 4.7 L/min to minimize oxidation. After failure, a forced argon flow was provided immediately to cool the IN718 test samples to RT.

The tensile fracture and gauge length surfaces (surfaces perpendicular and parallel to the tensile loading direction, respectively) were analyzed using a scanning electron microscope (SEM), (HITACHI S-3400N) equipped with an energy dispersive X-ray spectroscopy (OXFORD, EDS) detector for the chemical composition analysis of primary and secondary phases. For the metallographic analysis of the gauge length surface, the tested samples, sectioned by a Buehler slow cutter, were mounted using a conductive hot epoxy resin. Then, the mounted samples were manually ground using SiC abrasive paper from 320 up to 1200 grit, followed by polishing down to 0.5 μm, using an alcohol-based diamond suspension. After polishing, a solution of 10 ml hydrochloric acid + 1.5 ml 30% hydrogen peroxide was used to etch the polished samples [53]. The evolution of the grain structure and misorientation angles with different heat treatments was examined by a SEM (SU-8230 HITACHI) equipped with a Bruker e-Flash HR+ electron backscatter diffraction (EBSD) detector using 20 kV and a pixel size of 1.62 μm. The total map size for each condition was $1298 \times 973.4\ \mu m^2$ surface area, to cover the maximum number of grains. The EBSD data were post-processed using QUANTAX ESPRIT software. For the EBSD analysis, the specimens were mechanically polished down to 0.5 μm, followed by a vibromet polishing for 24h using a 0.05 grit size colloidal silica. Then, the residual fine scratches and deformed surfaces were eliminated using an IM4000Plus ion milling system under 6 kV accelerating voltage and 25 rpm rotation speed for 40 min. It is worth mentioning that only HSA2, HSA3 and HSA5 treatment conditions have been selected to illustrate the evolution of the grain boundaries through EBSD. This was based on the XRD and SEM analyses in our previous study [89] where the homogenization treatment time was found to have more significant impact on the grain structure and boundaries than the solution treatment time. Hence, to understand the effect of

homogenization time on the grain structure, HSA2, HSA3 and HSA5 treatments were selected representing 1, 4, 7h homogenization time, respectively.

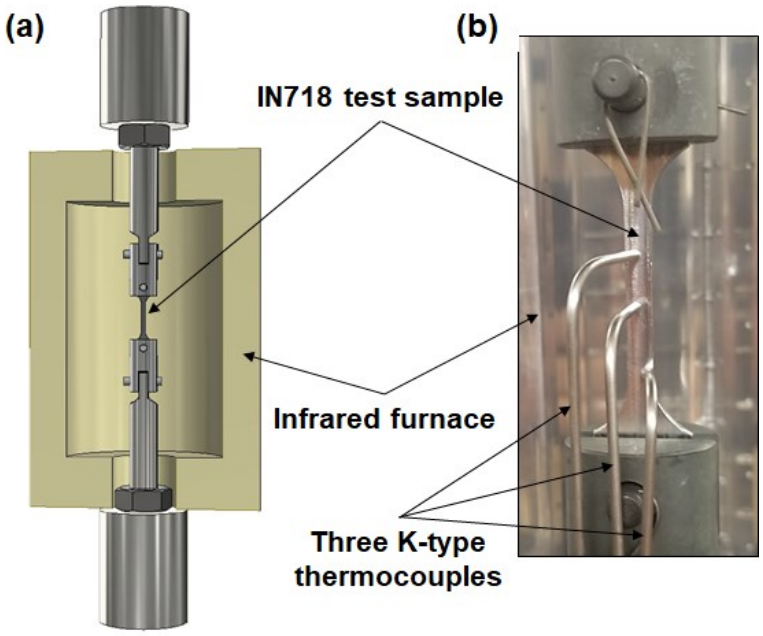

Figure 4-3: (a) Schematic illustration of the high-temperature (650°C) tensile testing setup; (b) actual IN718 test sample with thermocouple arrangement.

4.3 Results and discussions

4.3.1 The influence of the homogenization and solution times on the mechanical properties at 650°C

Figure 4-4a to g shows the high-temperature tensile (650°C) properties of the LPBF IN718 in the as-printed and heat-treated conditions. The detailed average values of the mechanical properties are listed in Table 4-2. For comparison, the mechanical properties of the conventionally heat-treated (AMS) wrought, cast and LPBF-fabricated IN718 superalloy obtained at 650°C by Gao *et al*. [62], Trosch *et al*.[35] and Zhao *et al*. [63], respectively, are included in Table 4-2. As can be seen in Figure 4-4a to f, the homogenization and solution treatment times affect the flow stress of the LPBF IN718 alloy significantly. A detailed explanation of the evolution of the flow stress is discussed in the next section.

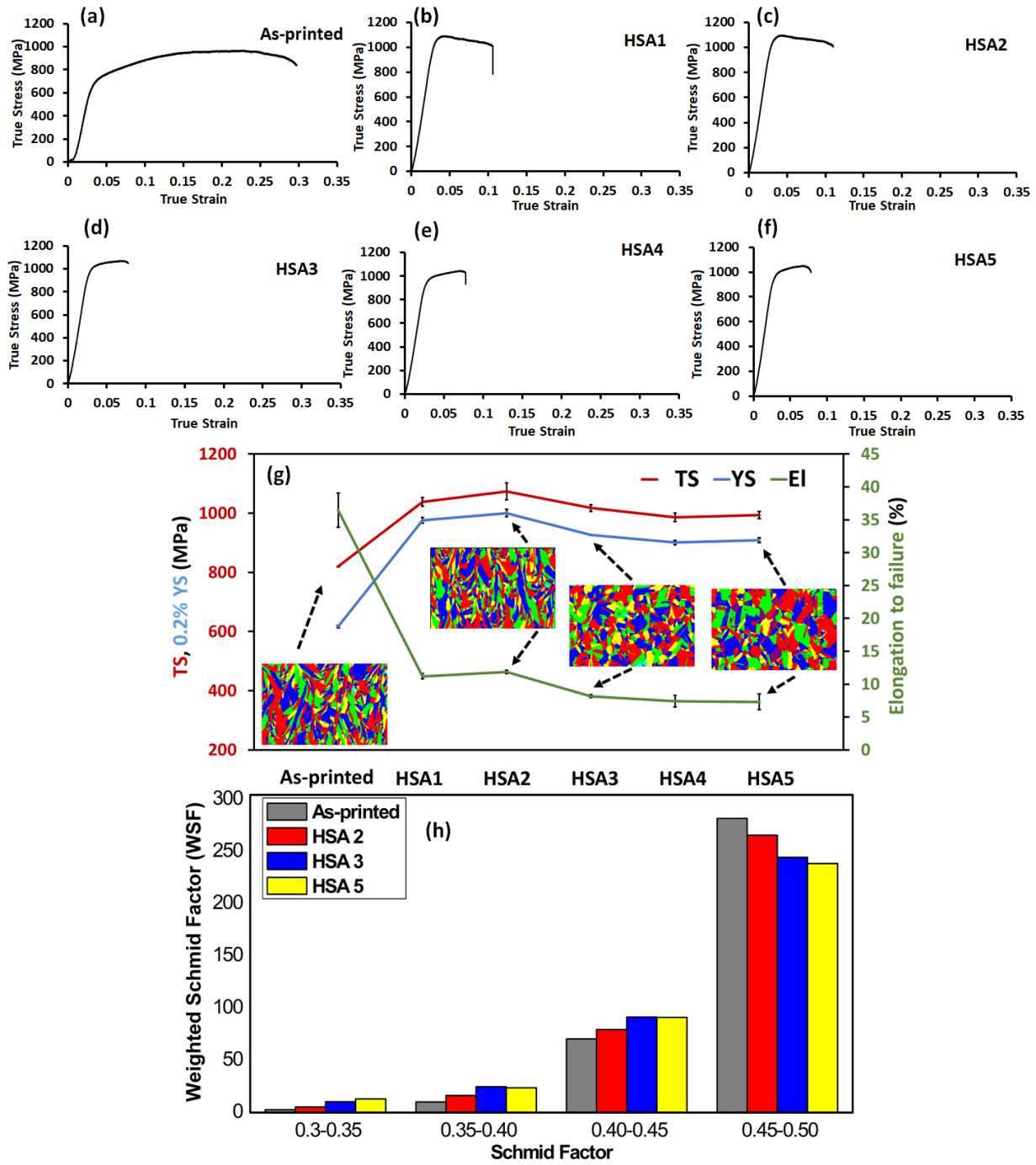

Figure 4-4: (a-f) True stress-true strain curves at 650°C of the LPBF IN718 in the following conditions: (a) as-printed, (b) HSA1, (c) HSA2, (d) HSA3, (e) HSA4 and (f) HSA5; (g) evolution of the high temperature of tensile properties and the grain structure map as a function of the heat treatment conditions; (h) distribution of the Weighted Schmid Factor (WSF) under the as-printed and heat treatment conditions.

Table 4-2: Elevated-temperature (650°C) tensile strength (TS), yield strength (YS) and elongation to failure (El) values of the as-printed and heat-treated conditions. The elevated-temperature (650°C) tensile properties of the connectionally heat-treated (AMS) IN718 fabricated by LPBF, wrought and cast routes, reported in the literature [35,62,63] are included for comparison.

Condition	TS (MPa)	YS (MPa)	El (%)	Reference
As-printed	820±2	617±3	36±3	↑
HSA1	1038±14	976±9	11.2 ±0.2	|
HSA2	1074±28	1001±12	11.8±0.3	This work
HSA3	1017±11	927±2	8.2±0.2	|
HSA4	986±14	901±7	7.4±0.9	↓
HSA5	994±11	909±8	7.3±1	
Heat-treated Wrought (AMS 5662)	1000	862	12	[62]
Heat-treated Cast	576	517	13.7	[35]
LPBF IN718 AMS5662	1025	915	5.5	[63]
LPBF IN718 ASM5383	1020	950	3.5	[63]

Figure 4-4g illustrates the changes in the high-temperature mechanical properties and grain morphology of the LPBF IN718 as a function of the heat treatment conditions. It is worth mentioning that the grain maps included in this figure were acquired form the vertical plane (xz) with respect to the building direction (the plane parallel to the tensile loading direction). As can be seen in Figure 4-4g, the as-printed condition exhibits the lowest tensile and yield strengths, as compared to those of the heat-treated LPBF IN718 in the present study and wrought (AMS 5662) IN718 in [62], while its elongation to failure is the highest. This can be attributed to a combined effect of a lack of strengthening phases (γ' and γ'') and the presence of Laves phase in the inter-dendritic regions, as well as at the grain boundaries, as reported in our previous study [89]. It is well-recognized that the precipitation of Laves phase in the microstructure degrades the high-temperature tensile properties. However, the tensile (820 MPa) and yield (617 MPa) strengths and the elongation to failure (36.4%) of the as-printed IN718; observed in the current work, are significantly higher than the tensile properties of the heat-treated cast IN718 at 650°C (576 and 517 MPa and 13.7%), as reported by Trosch *et al*. [35]. This can be explained by the fine

microstructure and microsegregation that result from the LPBF process of IN718 superalloy due to rapid solidification, as compared to the coarse microstructure and macrosegregation of the cast IN718, as reported by Zhang *et al*. [24]. The latter confirmed that the presence of such macrosegregation in cast IN718 is difficult to completely eliminate even after heat treatment, which consequently leads to the formation of larger irregular Laves phase in the inter-dendritic zones when compared to LPBF IN718 [24]. Moreover, the precipitation of coarse δ-phase was observed after post-treatment of cast alloy, which also had an adverse impact on the mechanical properties [24].

The high ductility of the as-printed condition, as compared to the heat-treated LPBF, wrought and cast IN718 equivalents, can also be attributed to the orientation of the elongated grains in the direction of tensile loading, as shown on the grains map in Figure 4-4g (as earlier mentioned, the tensile samples were printed parallel to the building direction (Figure 4-1a). Thus, there is less disruption of the motion of dislocations through the low angle grain boundaries during deformation, which consequently, results in higher elongation. In order to enlighten the influence of the favorable microstructure texture and the crystal orientation on the plastic flow and material elongation, the weighted Schmid factor (WSF), defined as the area under the Schmid factor curve in a given interval, was used. WSF represents the number of indexed pixels in an orientation imaging microscopy (OIM) analysis within a targeted Schmid factor range. It is worth noting that the zero-solution indexation for all studied EBSD maps were less than 0.3%, and therefore has a negligible impact on the WSF comparisons. As can be seen in Figure 4-4h, the Schmid factor (SF) of the {111} <110> slip system has been considered in four intervals from 0.3 to 0.5. It can be observed that, at the highest SF interval (0.45 to 0.5), the as-printed condition exhibits a higher WSF as compared to the heat-treated conditions, indicating a lower resistance to deformation

under loading along the z-direction (longitudinal axis of the tensile test coupons). This is attributable to the directional solidified microstructure and the strong texture along the building and the tensile loading directions (z-direction). Similar high as-printed elongations of the vertically-oriented LPBF IN718 are observed in [52,90,91]. It is worth mentioning that the calculated SF for the vertical as-printed samples reported in [52] is approximately 0.47, which is consistent with that obtained in the present study.

Generally, any of the five heat treatments applied significantly increased the tensile and yield strengths, while ultimately decreasing the elongation to failure at 650°C, as shown in Figure 4-4g. For comparison, the 1h homogenized treatments at 1080°C in HSA1 and HSA2 increased the tensile strength by 26.5 and 31%, as compared to the as-printed conditions, whereas the elongation to failure decreased by 69 and 67%, respectively. It is important to note that, among all the heat treatment conditions, the HSA1 and HSA2 exhibited the highest tensile strength and elongation to failure. Also, as compared to the wrought IN718 (AMS 5662), these conditions resulted in higher tensile and yield strengths and comparable elongations to failure. This is attributed to the greater precipitation with γ' and γ'' occurring after these conditions were applied than in the other heat treatments, as reported in our previous study [89]. However, precipitation hardening is not the only strengthening mechanism in the 1h homogenized conditions. The presence of a high density dislocation and misorientation substructure also contributed to relatively higher mechanical properties when compared to other heat treatments.

Figure 4-5 shows the kernel average misorientation (KAM) maps of the LPBF IN718 in the as-printed and heat-treated conditions. KAM helps to estimate the plastic strain in individual grains and to reveal local variations in lattice orientations, and is a good indicator of the dislocation density in the material [78]. In the KAM maps in Figure 4-5, the blue and red color codes represent

the lowest and the highest misorientation angles/dislocation density, respectively. For quantification, the evolution of the number fraction (NF) of the KAM in the as-printed and the selected heat treatments is shown in Figure 4-5e.

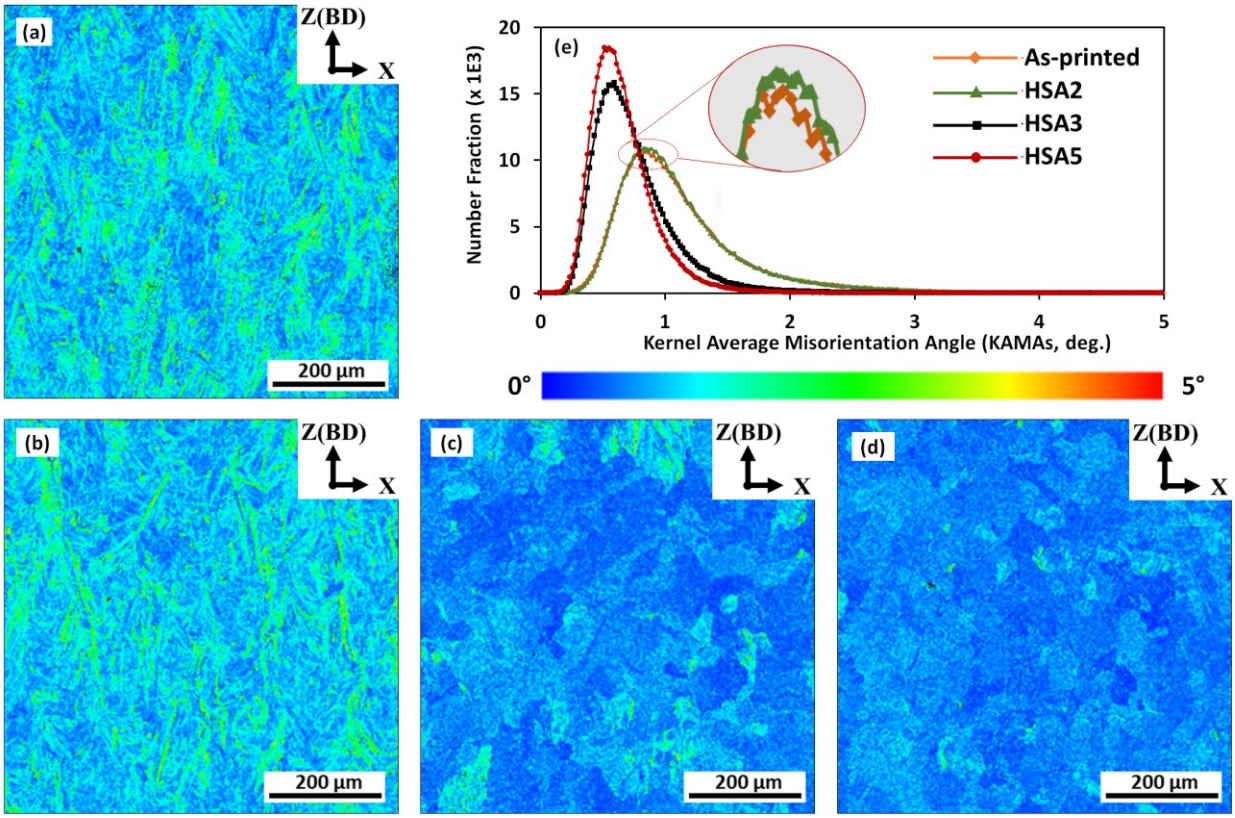

Figure 4-5: Kernel average misorientation (KAM) maps of the LPBF IN718 in the following conditions: (a) as-printed, (b) HSA2, (c) HSA3, (d) HSA5 and number fraction of KAM under as-printed and aforementioned heat treatment conditions

As can be seen in the KAM map in Figure 4-5a, a high plastic strain intensity is induced in the initial microstructure of the as-printed condition, suggesting a high dislocation density resulting from the complex thermal cycling and rapid heating, followed by rapid cooling, during the printing process. Even after the 1h homogenization condition, HSA2, is applied, a high intensity of the induced plastic strain is retained, as shown in Figure 4-5b. Further, it can be observed from Figure 4-5e that the as-printed and HSA2 exhibited nearly the same KAM values (≈ 0.83), higher than the heat-treated conditions (≈ 0.5). This clearly indicates that the 1h homogenization treatment at

1080°C is not sufficient to significantly annihilate the primary dislocation tangles inherited from the LPBF printing process, which consequently contributed to the high mechanical properties. After the HSA3 and HSA5 conditions, a significant reduction in the induced plastic strain is observed (Figure 4-5c and d), indicating that the internal plastic strain is mostly relieved.

Figure 4-6 also shows the evolution of the low and high angle grain boundaries, LAGBs and HAGBs, in the as-printed and heat treatment conditions, represented by red and black full lines, respectively. The misorientation angles (MAs) between 2° and 15° were defined as LAGBs, while the MAs greater than 15° were defined as HAGBs. As can be seen in Figure 4-6a, the microstructure of the as-printed condition is composed of columnar grains with a relatively high density of LAGBs, when compared to the heat treatment conditions. This finding is consistent with the microstructure analysis by Fayed *et al*. [89] of the as-printed condition, where it was found that elongated grains, composed of cellular and columnar dendrites, formed during the solidification process of LPBF, were divided by the LAGBs [89]. After the 1h homogenization treatment (HSA2), the columnar grains retained approximately the same LAGBs density as observed in Figure 4-6b. Figure 4-6e shows the number fraction (NF) evolution of the HAGBs, LAGBs and the coincidence site lattice (CSL Σ3) grain boundaries in the as-printed and heat-treated conditions. It has been reported that the CSL Σ3 are special grain boundaries that are used to identify the twin boundaries and to study the grain boundary character distribution in EBSD analysis [92]. As can be seen in Figure 4-6e, the as-printed and HSA2 conditions contain almost the same LAGBs density, with an NF of ≈ 40.4%. Furthermore, after the HSA2 treatment, a slight change in the CSL Σ3 grain boundaries is observed, indicating that the static recrystallization process only initiated but did not complete, which is consistent with the microstructure analysis reported in [89].

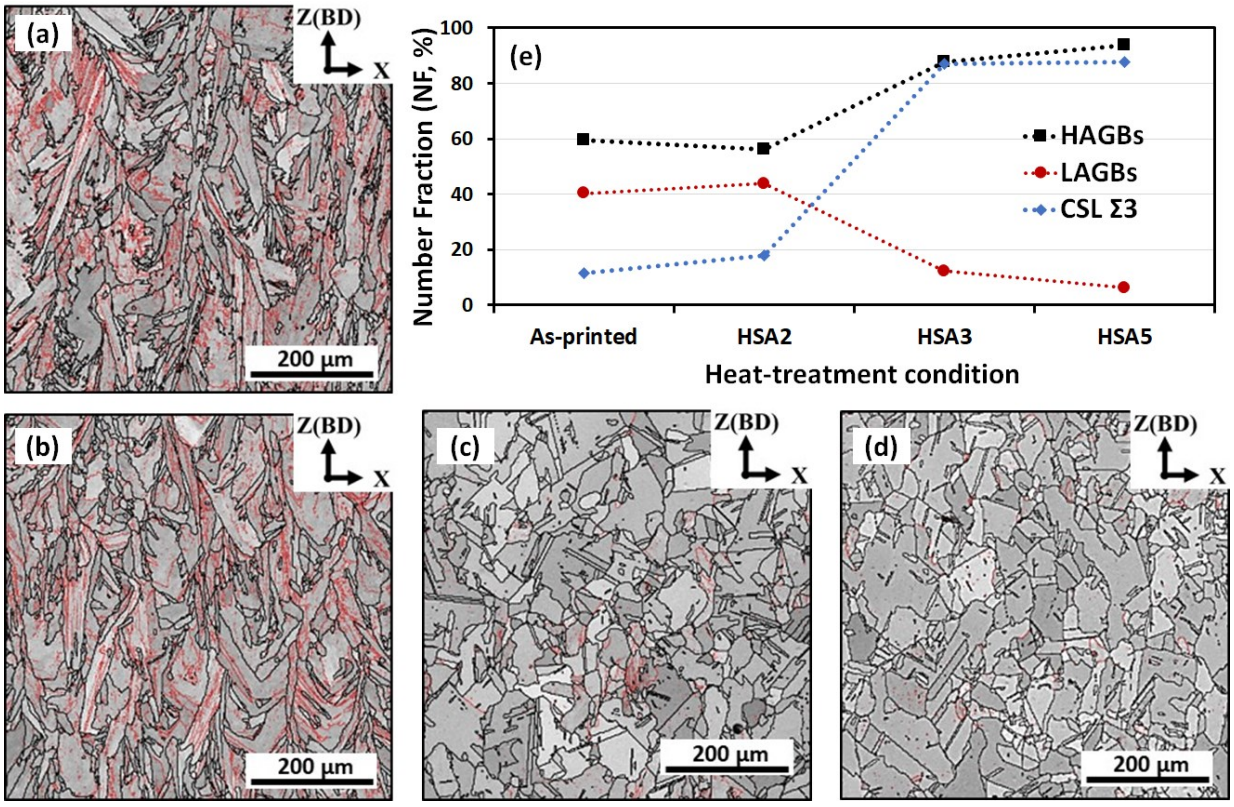

Figure 4-6: Distribution of LAGBs and HAGBs under different conditions: (a) as-printed, (b) HSA2, (c) HSA3, (d) HSA5, and (e) evolution of number fraction of LAGBs, HAGBs and CSL Σ3 grain boundaries under the aforementioned conditions. The LAGBs and HAGBs are indicated by red and black full lines, respectively.

When the homogenization treatment time at 1080°C increases to 4 and 7h, a significant decrease in LAGB density (Figure 4-6c and d) is observed with NFs of 12.4% and 6.3%, respectively (Figure 4-6e). Furthermore, a significant increase in the NFs of the CSL Σ3 and HAGBs is observed. It is interesting to note that the NFs of both the CSL Σ3 and HAGBs exhibited the same trends. However, a stable NF of the CSL Σ3 grain boundaries at ≈ 87.5% after the 4h homogenization treatment is observed, indicating that complete recrystallization took place after the HSA3 condition. It can be concluded that the 4h homogenization treatment at 1080°C is the heat treatment condition necessary to trigger the complete recrystallization process and reduce or remove the existing internal stresses.

It is important to mention in this context that the high mechanical strengths of the HSA1 and HSA2 at 650°C as compared to the other heat treatment conditions are consistent with the RT hardness results reported in [89]. Moreover, the relatively high elongations of the HSA1 and HSA2 conditions are attributable to the existence of elongated grains oriented parallel to the loading direction and the high SF as observed from the grains map and WSF distribution (Figure 4-4g and h). The 1h homogenization treatment at 1080°C did not significantly change the as-printed texture and columnar grain structure, which contributed to the relatively high elongations measured for these conditions.

On the other hand, after the 1h homogenization treatments, it was found that the selected solution treatment times at 980°C significantly affected the mechanical properties at 650°C. For example, the HSA2 condition, which included a longer solution time (60 min), exhibited higher tensile and yield strengths than those of the HSA1 condition (15 min solution time). This behavior can be explained by higher δ-phase precipitation along the grain boundaries after HSA2, with an approximate area fraction of ≈ 0.66%, than after HSA1 (≈ 0.16%), as shown in Figure 4-7. It is worth mentioning that the area fraction of δ-phase in those heat treatment conditions was quantified on the basis of digitized SEM micrographs and image threshold analysis using ImageJ software. Such a higher δ-phase fraction results in an increase in the grain boundaries' strength through their pinning. During high-temperature deformation, δ-phase acts as a barrier to the dislocation motion, which consequently increases the tensile strength. Gao *et al*. [62] also reported that a lack of δ-phase at the grain boundaries results in the high notch sensitivity seen at elevated temperatures. Nevertheless, having excess δ-phase is not favorable either, since it has a detrimental effect on the strength and ductility of the material, as reported in [93]. Thus, a moderate amount

of δ-phase (≈ 4%) [11] is required to ensure high mechanical strength characteristics at elevated temperatures.

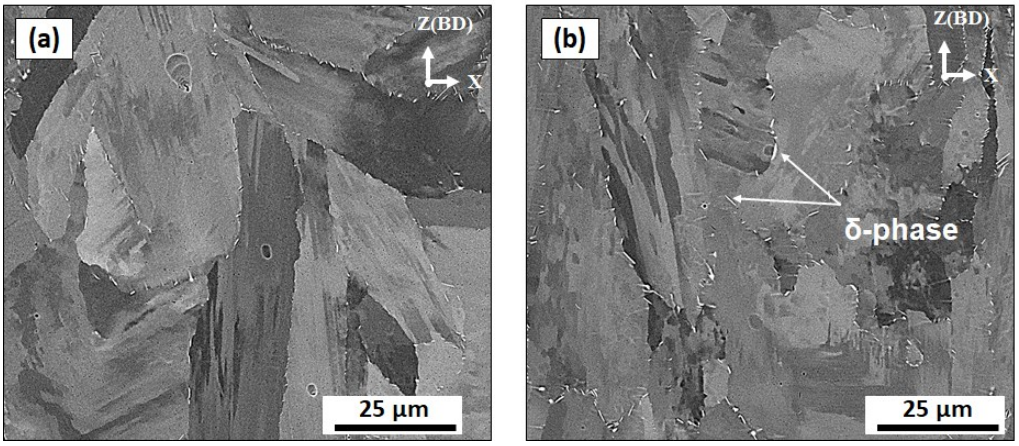

Figure 4-7: SEM micrograph of a non-etched LPBF IN718 illustrating the presence of δ-phase precipitated for heat treatment conditions: (a) HSA1; (b) HSA2

When the homogenization treatment time increased to 4h (HSA3), the strength of IN718 increased by 24% and became comparable with that of the wrought IN718 (AMS 5662), whereas the ductility was significantly reduced, by 77.6%. However, the HSA3 treatment resulted in lower strength and ductility than those of both HSA1 and HSA2, as shown in Figure 4-4g. This could be attributed to the combined effects of dislocation annihilation and the precipitation of coarse carbide particles, as shown in Figure 4-8a. The KAM and misorientation maps in Figure 4-5 and 6 clearly show the homogenization time increase to 4h significantly decreased the induced plastic strain and grain substructure by triggering a complete recrystallization process after HSA3. Although a significant amount of γ′ and γ″ forming elements were released through a further dissolution of Laves phase and the back diffusion of segregated elements after HSA3, a considerable amount of Nb and Ti was consumed in the precipitation of the carbide particles, resulting in the depletion of the γ-matrix, as shown in Figure 4-8d. Therefore, a smaller amount of γ″ and γ′ is expected to precipitate during the aging treatment in the HSA3 condition, as compared to the HSA1 and HSA2 conditions.

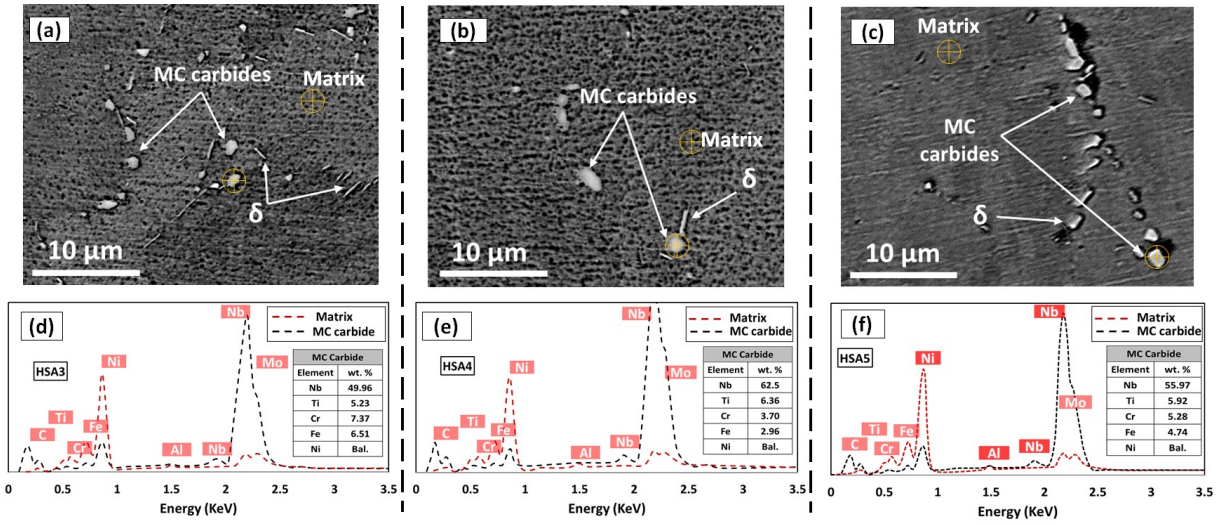

Figure 4-8: (a-c) SEM micrograph of LPBF IN718 in heat treatment conditions of: HSA3, HSA4 and HSA5, respectively, and (d-f) the corresponding EDS spectrum analysis diagram of the spots indicated in SEM micrographs, illustrating the concentration difference of the Nb between the γ-matrix and MC carbide.

A further increase in the homogenization time to 7h at 1080°C in HSA4 and HAS5 conditions led to a significant drop in tensile and yield strengths and ductility, when compared to the other heat treatments and to the wrought IN718 (AMS 5662). This is due to the combined effects of grain growth of the γ-matrix, the annihilation of dislocation density (Figure 4-5d and 6d) and the coarsening of the carbide particles, as shown in Figure 4-8b and c. Figure 4-8d to f shows the EDS analysis of the precipitated carbide particles after HSA3, HSA4 and HSA5 conditions. As seen in this figure, up to ≈ 60 wt. % of Nb and 6 wt. % of Ti are consumed in these carbide particles. Thus, the particles can be indexed as MC-type carbides according to the study by Mostafa *et al*. [45] and Kreitcberg *et al*. [88]. It is worth mentioning that, among all carbide types in IN718 alloy, MC carbides form at high temperature, and are distinguished by their high Nb and Ti contents, unlike M_6C and $M_{23}C_6$ carbides. Thus, the precipitation of MC carbides consumes a significant amount of Nb and Ti at the expense of the precipitation of γ′ and γ″. More detailed discussions on the consistency of the lattice parameter variations of the matrix with the depletion of Nb and Ti in the

γ-matrix of the HSA3, HSA4 and HAS5 heat treatments (EDS analysis) have been presented in [89].

As can be seen, after the application of the HSA3, HSA4 and HSA5 conditions, the LPBF IN718 exhibited a significant ductility loss at 650°C. This can be explained by the weakening of the grain boundaries' strength, as many nickel-based superalloys often experience such embrittlement behavior at elevated temperature [88]. Several reasons have been advanced in the literature to explain the driving force for this phenomenon. These include precipitation of secondary carbides during hot deformation, micro-twinning during deformation, and interactions of dislocation and intermetallic particles [88]. Accordingly, all the aforementioned mechanisms are likely to be responsible for the embrittlement observed in the present study. However, further investigations are required to determine the dominant mechanism at play here.

4.3.2 The effect of homogenization and solution treatment times on the flow stress at 650°C

Figure 4-4a to f shows typical true stress-strain curves obtained at 650°C for the as-printed and heat-treated conditions. The influence of the heat treatment holding time on the stress-strain curves can be clearly revealed. In Figure 4-4a, the stress-strain curve of the as-printed condition exhibits three distinct stages, starting from the work hardening stage, in which a rapid increase in the stress with strain is observed, followed by a steady stress stage, in which the stress remains approximately constant, and finally, the softening stage which proceeds till failure.

Conversely, the flow stress of the 1h homogenized conditions at 1080°C (HSA1 and HSA2) shows a yield strength peak followed by work softening until failure, and the steady stress stage disappears completely, as shown in Figure 4-4b and c. Such a rapid decrease in the mechanical strength can be explained by the occurrence of dynamic structural changes during the high-temperature deformation, and could be associated with dynamic recrystallization (DRX). For the

IN718 superalloy, with its low to intermediate stacking fault energy [78,94,95], the softening mechanism is mainly driven by the recrystallization process (i.e., with minor contribution from dynamic recovery). This is because, in metals with low stacking fault energy, the total dislocation network in the material decomposes into extended dislocations with large stacking fault widths, making their bundling very difficult during the recovery process [78]. Thus, dynamic recrystallization only becomes the dominant softening mechanism in IN718 once the critical dislocation density for recrystallization is attained. According to Figure 4-5a and b, both the as-printed and 1h homogenized conditions preserve a high density of the primary dislocation network inherited from the LPBF printing process. However, the as-printed conditions did not exhibit such DRX behavior, as seen in Figure 4-4a. This finding indicates that the sum of the primary dislocation density and the accumulated dislocations generated during the hot deformation process were not enough to promote the DRX process, and that other mechanisms probably played a role in the occurrence of DRX. In the other words, the occurrence of the dynamic recrystallization process during the hot deformation of the HSA1 and HSA2 treated conditions could be attributed to another factor, combined with the primary and generated dislocation network.

Kreitcberg *et al*. [88] reported that the presence of a needle-like δ-phase along the grain boundaries during the hot deformation of nickel-based superalloys can accelerate dynamic recrystallization. Similarly, it has been reported by Wang *et al*. [96] that the presence of the needle-like δ-phase in IN718 during plastic deformation increases the dislocation generation rate, which consequently promotes the dynamic recrystallization process. This is because of the pinning effect of the δ-phase at the grain boundaries, and the impediment of the dislocation movements during the plastic deformation, which induces strain gradients, and consequently initiates local recrystallization. The initial microstructure of both HSA1 and HSA2 conditions contains columnar

grains with needle-like δ-phase along the grain boundaries [89]. The finely recrystallized equiaxed grains observed in the areas surrounded by δ-phase, as reported in Figure 4-9, could therefore be explained by the above analysis.

Figure 4-9 shows the longitudinal cross-sectional plane of the fracture surface of HSA2 after tensile testing at 650°C. As can be seen in Figure 4-9a, the microstructure mainly consists of columnar grains oriented parallel to the loading direction, accompanied by needle-like δ-phase along the grain boundaries. Moreover, equiaxed grains with shorter δ-phase needles at the grain boundaries are similarly observed (Figure 4-9b). This suggests that during the plastic deformation at 650°C, the δ-phase needles impeded the dislocation movements and induced a gradient of plastic strain until reaching a critical point, after which new recrystallized equiaxed grains nucleated and formed as a result of the DRX process. The presence of such a short δ-phase (fractured δ-phase) along the new equiaxed grains could be attributed to the accumulation of the dislocations impeded by this phase and a high-level of stress concentration, which finally ended up forming cracks, leading to fracture. The above findings are in agreement with those of Hong *et al*. [97], who also observed the presence of the fractured δ-phase along the boundaries of the new recrystallized grains.

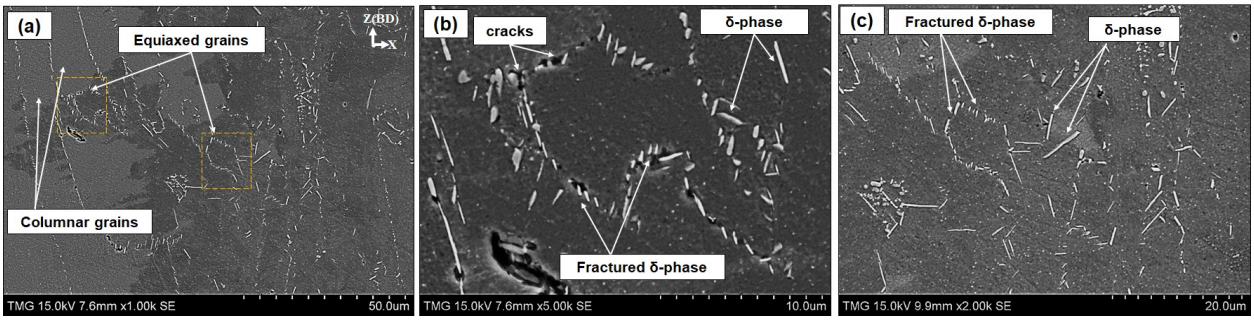

Figure 4-9: SEM micrograph displaying the longitudinal plane of the fracture surface of the HSA2 sample: (a) overall view of the fracture surface; (b and c) magnified view of the fracture surface as indicated in the overall view (a).

Despite the needle-like δ-phase precipitated along the grain boundaries after the application of the HSA3, HSA4 and HSA5 treatments, the flow behavior (Figure 4-4d to f) after these post-treatments was completely different from that obtained after the HSA1 and HSA2 conditions, and manifested work hardening until failure. This behavior could be attributed to the combined effects of the presence of coarse carbide particles (brittle phase), which adversely affect the ductility, and the lower dislocation density in the initial microstructure of these treatment conditions prior to deformation (Figure 4-5c and d). Thus, it can be concluded that the occurrence of the DRX process during the hot deformation of LPBF IN718 of the HSA1 and HSA2 conditions is attributable to the combined effects of the δ-phase along the grain boundaries and the presence of dislocation tangles inherited from the LPBF printing process.

To further understand this interaction, the evolution of the peak strain and the grain morphology represented by the grain aspect ratio as a function of the homogenization and solution treatment times was investigated, and is presented in Figure 4-10. The aspect ratio reported in this figure corresponds to the grain width-to-length ratio, meaning that the closer this ratio to 1, the more equiaxed the grains are. The inclusion of the aspect ratio evolution in this figure is due to its importance to indicate the occurrence of the static recrystallization process during the heat treatments (prior to the hot deformation) that in turn reduce the primary dislocation density and refine the as-printed grain structure which are ones of the main driving forces of the DRX. As discussed above, the occurrence of the DRX can be indicated by the presence of a well-defined peak stress on the experimental true stress-true strain curve, as observed in Figure 4-4b and c. However, the onset of the DRX process occurs at a specific strain value (critical strain, ε_c) lower than that corresponding to the peak stress (peak strain, ε_p). The value of the ε_c is not easily extracted from the true stress-true strain curve, and some authors have used the relation of $\varepsilon_c =$

$a\,\varepsilon_p$ to identify the onset of the DRX, where a is a proportionality coefficient which ranges between 0.5 and 0.9 [98]. Therefore, according to [98], it is reasonable to assume that the peak strain is closely related to the critical strain for DRX since evaluating the ε_c is out of focus of the present study.

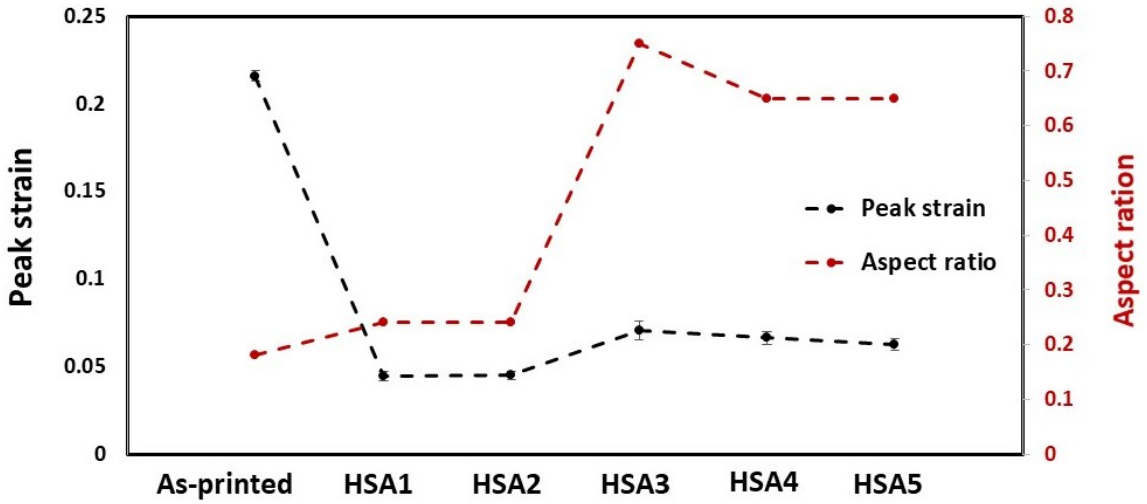

Figure 4-10: Evolution of the peak strain at 650°C and aspect ratio with the heat treatment conditions.

Generally, after heat treatments, the peak strain significantly decreased, in contrast with the as-printed condition, as shown in Figure 4-10. Several factors have been advanced in the literature to explain such a decrease in the critical/peak strain, including precipitations of secondary phases, decreases in the strain rate, decreases in the grain size prior to deformation, increases in the primary dislocation density and/or increases in the deformation temperature [98]. In the present study, the precipitation of secondary phases in the initial microstructure, such as δ, γ′ and γ″, the retention of primary dislocation density and the refinement of as-printed grain structure in the initial microstructure, after some heat treatments, are more likely to be the driving force for the decrease in the peak strain after heat treatments since the hot deformation conditions (temperature and strain rate) did not change. Concerning the secondary phases, Yuan *et al*. [93] found that the effect of the δ-phase on decreasing the peak strain is more significant than that of the γ′ and γ″ phases.

Among the post-treated conditions, both conditions of 1h homogenization treatments (i.e., HSA1 and HSA2) exhibited the lowest peak strain, in contrast with the other treatments and the as-printed condition. Combined with the effect of the δ, γ′ and γ″ phases, it can be confirmed that the dislocations network in the initial microstructure of the HSA1 and HSA2 conditions prior to deformation also contributed to the reduction in the peak strain.

Although the increase in the homogenization treatment time to 4 and 7h in HSA3, HSA4 and HSA5 conditions resulted in a refinement of the as-printed microstructure by promoting complete recrystallization (static recrystallization), as indicated by the aspect ratio evolution, a relatively slight increase in the peak strain is observed, as compared to the HSA1 and HSA2 conditions. This can be explained by the annihilation of the initial dislocation network after these conditions, and confirms the significance of both the δ-phase and primary dislocation density in promoting the DRX during the hot deformation of IN718, and the lesser role of other driving forces such as grain refinement.

4.3.3 Fracture surface analysis

The fracture surfaces of both the as-printed and heat-treated LPBF IN718 samples after tensile testing at 650°C were investigated using an SEM to correlate the tensile characteristics with microstructures and determine the fracture mechanisms. Figure 4-11 illustrates the transverse cross-section (perpendicular to the tensile loading direction) of the tensile fracture surface of the as-printed and post-treated samples. In the as-printed condition, the cracks propagated in a mixed fracture mode: inter-dendritic (ductile), inter-granular and inter-melt pool fractures. As can be seen in Figure 4-11a, a pattern of parallel valleys-like shapes is observed, similar to the laser track pattern observed in the microstructure analysis of a transverse plane of the as-printed condition. The presence of this pattern indicates that large cracks propagated mainly along the melt pool

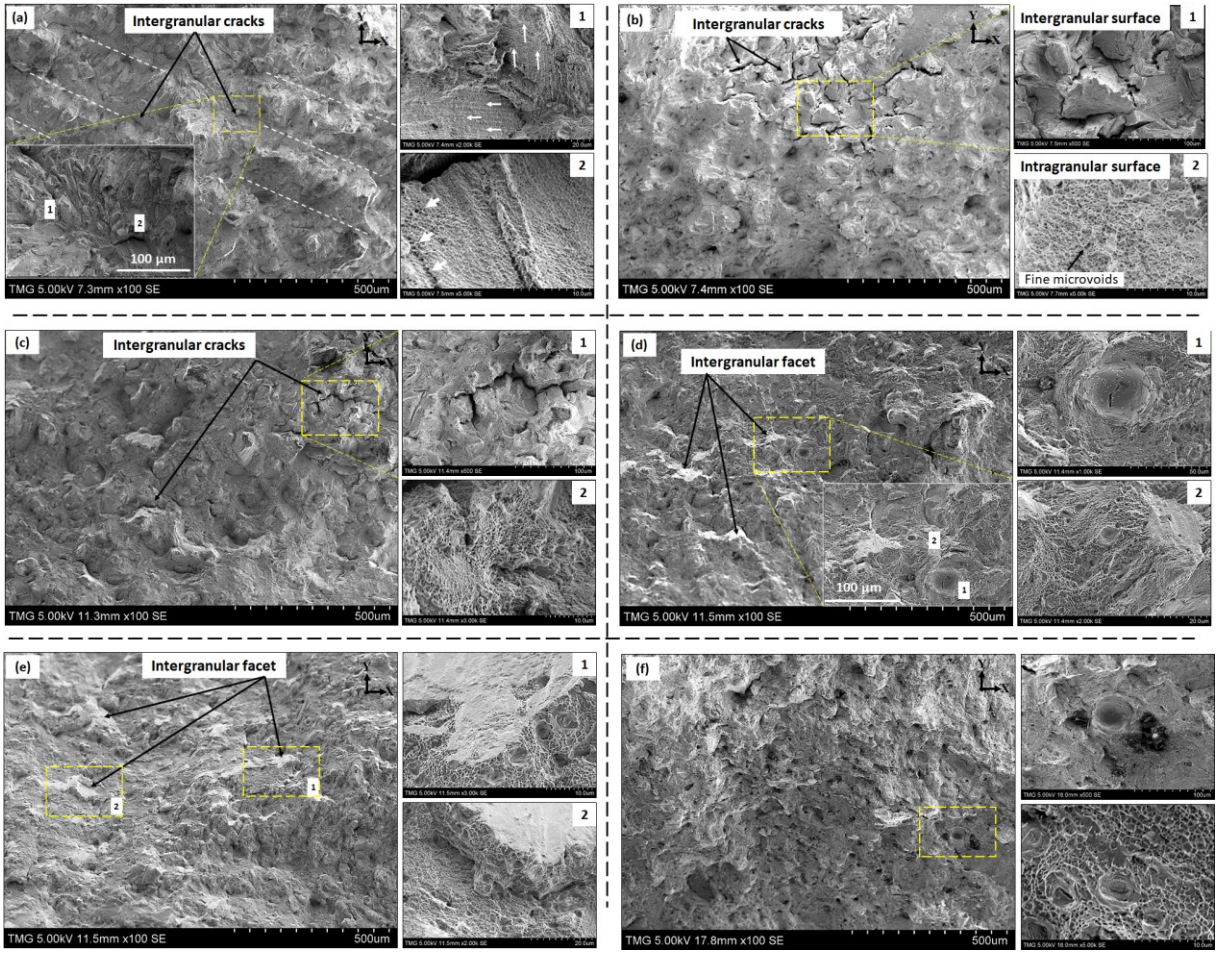

Figure 4-11: Fracture surface on the transverse plane of LPBF IN718: (a) as-printed; (b) HSA1; (c) HSA2; (d) HSA3; (e) HSA4; (F) HSA5. Fractures on melt-pool boundaries are highlighted by dotted lines in (a). Arrows in (a (1 and 2)) indicate the aligned intra-granular dimples along the dendrites pattern in two different grains, and the coalescence of some microvoids along these dendrites, respectively.

boundaries. Such a fracture surface is consistent with that observed by Hilaire *et al*. [90]. Further clarification for these transverse cracks along the melt pool boundaries is shown in the facture surface of the longitudinal plane of the as-printed condition in the next section. In addition, large cracks are also observed along the grain boundaries, as shown in the inset image in Figure 4-11a. The occurrence of the aforementioned inter-granular and inter-melt pool fracture modes could be explained by the presence of relatively large brittle Laves precipitates along the melt pool boundaries, as well as the grain boundaries, which is consistent with the microstructural results

[89]. It was confirmed in our previous work [89] that the top border of the melt pool boundaries is occupied by relatively larger size Laves particles than those in the lower border because of the lower cooling rate in the top border. Crack nucleation and propagation thus occurs mainly along these borders. Furthermore, intra-granular dimples aligned preferentially in a dendrite-like pattern and oriented differently from one grain to another were observed, as indicated by white arrows in Figure 4-11a(1). Furthermore, some coalesced microvoids along the dendrite substructure were observed, and are indicated by white arrows in Figure 4-11a(2). The presence of these microvoids is also attributable to the presence of Laves phase in the inter-dendritic regions.

On both HSA1 and HSA2 fracture surfaces, the inter-melt pool fracture mode (pattern of parallel valleys) and the preferred alignment of intra-granular dimples disappeared completely. Such fracture surfaces are consistent with the microstructure analysis of the HSA1 and HSA2 conditions, where the as-printed features, such as melt pool boundaries, are eliminated. However, a mixture of inter-granular and intra-granular fracture modes was observed, as indicated by the presence of grain boundary cracks (see Figure 4-11 b(1) and c(1)) and typical dimple feature (Figure 4-11 b(2) and c(2)). Considering the microstructure analysis of both the HSA1 and HSA2 conditions, we see that the 1h homogenization treatment at 1080°C is not enough to completely dissolve Laves phase and cellular segregates, in addition to the precipitation of needle-like δ-phase along the grain boundaries [89]. Thus, large inter-granular cracks and fine microvoids are observed in the areas occupied by the Laves and δ-phases, such as grain boundaries and inter-dendritic regions. In the HSA3, HSA4 and HSA5 conditions, the fracture surfaces show a mainly brittle mode, as indicated by the presence of mostly inter-granular facets, as shown in Figure 4-11 d to f. The brittle fracture surface results from the embrittlement phenomenon discussed above and the

presence of the coarse brittle MC carbides after HSA3, HSA4 and HSA5 treatments, which is confirmed by the microstructure and EDS analysis, shown in Figure 4-8.

4.3.4 Effect of Laves, carbides and δ-phase on the fracture behavior

As discussed earlier, the heat treatment time window is established in a bid to optimize the heat treatment conditions for the LPBF IN718 by homogenizing the as-printed microstructure, dissolve the undesired phases, such as Laves phase, and control the precipitation of δ-phase to improve the mechanical behavior, especially at elevated temperatures. Thus, the effect of Laves, carbides and δ-phase on the fracture properties at 650°C need to be examined. Figure 4-12 shows the longitudinal cross-section (parallel to the tensile loading direction) of the tensile fracture surface of the LPBF IN718 tensile samples in both the as-printed and post-treated conditions. As can be seen in Figure 4-12a and b, in the as-printed condition, large transverse cracks (perpendicular to the building direction and tensile loading direction) are formed close to the melt pool boundaries. The presence of these transverse cracks could be explained by a high-stress level applied on the layer-layer melt pool boundaries, where a relatively large amount and size of brittle Laves phase formed. Furthermore, microvoids are observed along the grain boundaries and inter-dendritic zones, as indicated by white arrows in Figure 4-12b. It is evident that Laves phases act as favorable sites for the formation of microvoids and crack propagation along the grain boundaries and melt pool boundaries.

In the HSA1 and HSA2 conditions, large inter-granular cracks initiated and propagated along the grain boundaries where the Laves and δ-phases precipitated, as shown in Figure 4-12c to f. It is worth noting that the δ-phase precipitating after HSA2 has a large size, and can easily crack and form voids, as shown in Figure 4-12f. The dislocation accumulation near the δ-phase during the plastic deformation led to local stress concentration, causing microvoids and crack initiation near

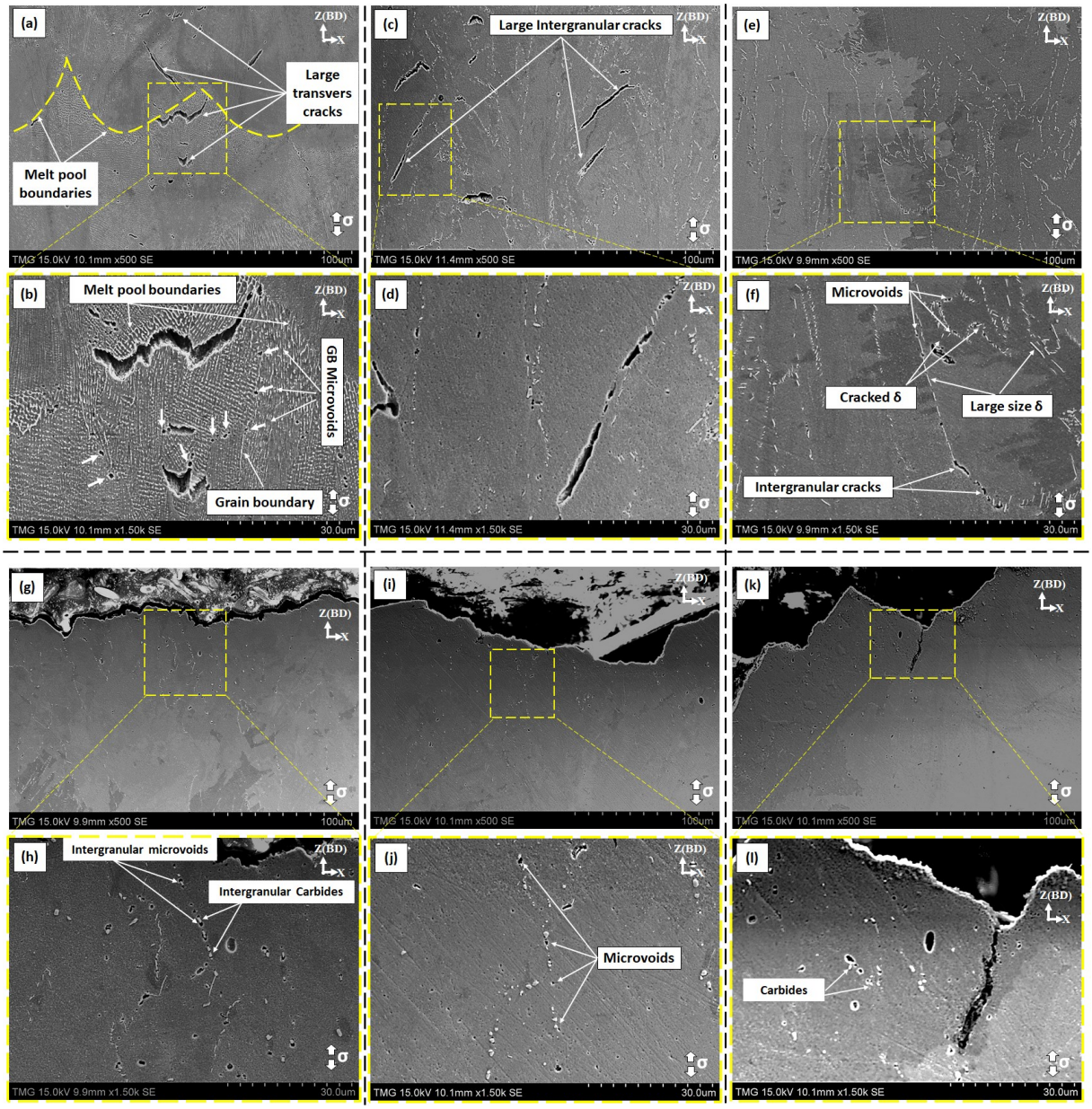

Figure 4-12: Fracture surface on the longitudinal plane of tensile testing of the LPBF IN718 at 650°C: (a-b) as-printed; (c-d) HSA1; (e-f) HSA2; (g-h) HSA3; (i-j) HSA4; (k-l) HSA5. Arrows in (b) indicates the formation of microvoids along the grain boundaries and across the grains' interior.

the δ-phase sites. By comparison, after the HSA3 treatment, the Laves phase almost completely dissolved, and a moderate amount of δ-phase precipitated, but coarser MC carbides precipitated along the grain boundaries. Therefore, large voids are observed close to the coarse carbide particles, as shown in Figure 4-12g and h. Similarly, after HSA4 and HSA5 treatments, large size

voids formation is observed around the MC carbides. This is consistent with the significant ductility reduction in the IN718 after the application of HSA3, HSA4 and HSA5 treatments. Based on the known effect of Laves, δ and carbides on the fracture behavior, it is important to select the treatment having an intermediate homogenization time between HSA2 and HSA3 to completely dissolve the Laves phase, along with precipitation of smaller amounts and finer carbides in order to obtain a good combination of strength and ductility in the LPBF IN718 alloy. This condition could represent the starting point for further analysis in order to optimize the heat treatment conditions for LPBF IN718.

4.3.5 Post-heat treatment map for LPBF IN718

Figure 4-13 shows the thermal post-heat treatment map of the LPBF IN718. The map was established using the information obtained in this and our previous study [89] on the microstructure, precipitates, crystallographic texture, RT hardness and high temperature (650°C) tensile properties of the LPBF IN718 alloy. It is established mainly to summarize and comprehensively understand the effect of the heat treatment time on the microstructural characteristics (phase transformation, homogeneity, grain structure and material texture) and mechanical properties of LPBF IN718 alloy at RT and 650°C, and can be used as a decision making tool, when selecting the best-suited post-treatment conditions for LPBF IN718 alloy. It is worth mentioning that the texture degree, presented in Figure 4-13b, is defined by the intensity ratio $I_{(111)}$ / $I_{(200)}$, where the $I_{(111)}$ and $I_{(200)}$ designate the diffraction peak intensity of the planes of (111) and (200), respectively, which were obtained from the XRD analysis in the previous study [89]. Thus, the lowest values (fractions) represent a strong textured material, whereas values over unity refer to weak texture.

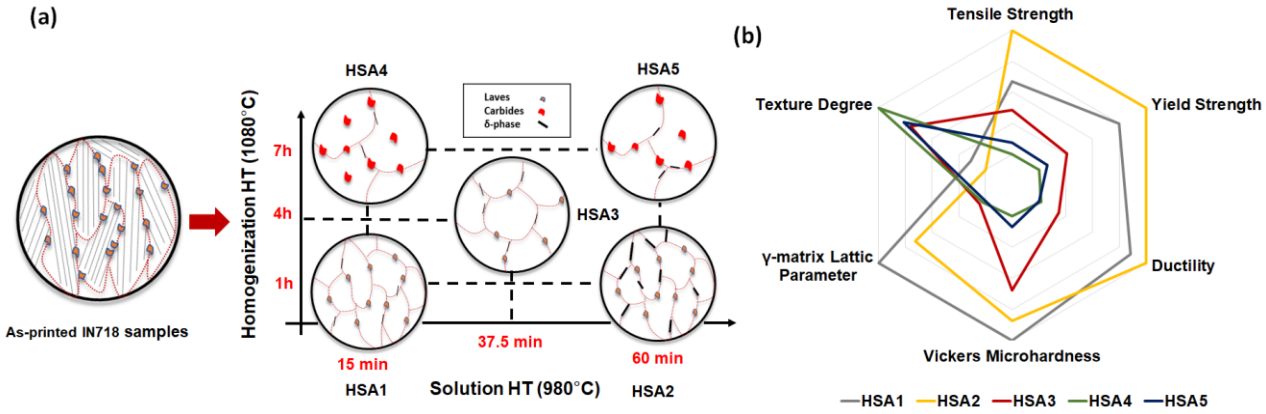

Figure 4-13: (a) Thermal post-processing map of LPBF IN718 alloy displaying the microstructure, phases and grain morphologies as functions of the heat treatment times; (b) radar chart summarizing the effect of the heat treatment time window on the texture, γ-matrix lattice parameter and mechanical properties.

As can be seen in Figure 4-13a, this map shows the development of the as-printed microstructure, which is characterized by directional solidification along the building direction, with fine particles precipitating along the grain boundaries and inter-dendritic regions. After thermal post-processing, a significant change in the as-printed microstructure, in terms of precipitates and grain structure, occurred, as illustrated in Figure 4-13a. For the post-treated conditions, the map consists of two perpendicular axes: the vertical axis, illustrating the change in the microstructure, along with the homogenization treatment time at 1080°C, and the horizontal axis, showing the microstructure change with the solution treatment time at 980°C. Along the vertical axis, a significant change in the grain structure and texture is observed by increasing the duration of the homogenization treatment at 1080°C: starting from a mixture of columnar and equiaxed grains at the relatively short treatment time (1h), then on to more equiaxed recrystallized grains at the intermediate soaking time (4h), and finally, coarse equiaxed grains after the prolonged treatment condition (7h). Furthermore, more Lave phase dissolution is observed by increasing the homogenization treatment duration. However, the intermediate (4h) and the prolonged (7h) homogenization treatment times resulted in greater precipitations of coarse MC carbides.

Moreover, it was found that the homogenization treatment time has a significant impact on the mechanical properties at RT and 650°C. The 1h homogenized conditions exhibited the highest RT hardness and tensile properties at 650°C due to the effect of dislocation tangles and the relatively higher contents of the Nb and Ti released into the γ-matrix, as indicated by the calculated lattice parameter in the radar chart in Figure 4-13b, which are necessary for precipitation of γ′ and γ″ as compared to the longer homogenization time.

Along the horizontal axis, the solution heat treatment time at 980°C does not impose a noticeable change in the grain structure. However, the amount of precipitated δ-phase was significantly affected by the solution treatment time. Increasing the duration of the solution treatment resulted in an increase in δ-phase amount. Also, the precipitation of δ-phase along the grain boundaries plays an important role in improving the tensile strength of LPBF IN718 alloys at 650°C. Thus, the HSA2 condition exhibited a relatively higher strength than that of the HSA1 condition, as shown in Figure 4-13b, due to the increased precipitation of δ-phase at the grain boundaries in the former condition. The same behavior is observed between the HAS4 and HSA5 conditions. Based on the observations and analysis of the results obtained so far, there is a conflict between the mechanical properties and the material texture since the highest mechanical properties are obtained after applying the conditions (HAS1 and HSA2) under which the as-printed strong texture does not change significantly. Thus, an intermediate homogenization holding time of between two and four hours at 1080°C could help produce IN718 parts with high and isotropic mechanical properties.

4.4 Conclusion

In the present study, the influence of the homogenization and solution treatment times on the elevated-temperature (650°C) mechanical properties of LPBF-fabricated IN718 has been investigated. The main findings can be summarized as follows:

- The as-printed IN718 shows the lowest strength, but the highest ductility, as compared to the post-heat-treated conditions, due to a combined effect of the absence of γ′ and γ″ phases and the precipitation of Laves phase. Moreover, high elongations in the as-printed conditions are attributable to the as-printed grain structure, with grains elongated along the tensile loading direction. The Laves phase in the as-printed IN718 provides a favorable site for microvoids nucleation and crack propagation.
- After heat treatments, the tensile and yield strength significantly increased by 20.3-31% and 46.1–62.3%, respectively, as compared to the as-printed condition, depending on the solution and homogenization treatment time, while the ductility correspondingly decreased by 67.4-80%.
- Among the heat-treated conditions, the highest strength and ductility were obtained after the 1h homogenization treatment conditions, HSA1 and HSA2, due to the relatively high content of γ′ and γ″ phases and dislocation density, as compared to other heat treatments.
- Further increases in the homogenization treatment time in the HSA3, HSA4 and HSA5 conditions resulted in a significant loss of ductility of LPBF IN718 at 650°C. This is attributable to the increase in the precipitation of coarse MC carbide particles along the grain boundaries after these conditions.
- The presence of δ-phase at the grain boundaries improved the elevated-temperature mechanical properties of IN718 alloy. Thus, the HSA2 condition resulted in higher strength

than did the HSA1 condition, which was related to an increased precipitation of δ-phase after HSA2.

- The inter-granular δ-phase accelerates the dynamic recrystallization process during the hot deformation of IN718 alloy. Furthermore, dynamic recrystallization process is promoted only after the application of HSA1 and HSA2 due to a combined effect of the initial dislocation network, as well as the presence of δ-phase along the grain boundaries.

Chapter 5 : Optimization of the Post-Process Heat Treatment of Inconel 718 Superalloy Fabricated by Laser Powder Bed Fusion Process

Eslam M. Fayed[1], Mohammad Saadati[2], Davood Shahriari[2], Vladimir Brailovski[2], Mohammad Jahazi[2], and Mamoun Medraj[1,*]

[1]Department of Mechanical, Industrial and Aerospace Engineering, Concordia University, 1515 Sainte-Catherine Street West, Montreal, QC H3G 2W1, Canada
[2]Department of Mechanical Engineering, École de technologie supérieure, 1100 Notre-Dame Street West, Montreal, QC H3C 1K3, Canada
*corresponding: mmedraj@encs.concordia.ca; Tel.: +1-514-848-2424

This paper has been accepted for publication in Metals (January 2021)

Abstract

In the present study, multi-objective optimization is employed to develop the optimum heat treatments that can achieve both high-mechanical performance and non-distinctive crystallographic texture of 3D printed Inconel 718 (IN718) fabricated by laser powder bed fusion (LPBF). Heat treatments including homogenization at different soaking times (2 to, 2.5, 3, 3.5 and 4h) at 1080°C, followed by a 1h solution treatment at 980°C and the standard aging have been employed. 2.5h is found to be the homogenization treatment threshold after which there is a depletion of hardening precipitate constituents (Nb and Ti) from the γ-matrix. However, a significant number of columnar grains with a high fraction (37.8%) of low-angle grain boundaries (LAGBs) have still been retained after the 2.5h homogenization treatment. After a 4h homogenization treatment, a fully recrystallized IN718 with a high fraction of annealing twins (87.1%) is obtained. The conditions of the 2.5 and 4h homogenization treatments result in tensile properties at RT and 650°C superior to those of the wrought IN718. However, considering the texture requirements, it is found that the 4h homogenization treatment represents the optimum post-treatment, which can be used to produce IN718

components offering a balanced combination of high mechanical properties and adequate microstructural isotropy.

Keywords: Heat treatment optimization; additive manufacturing; laser powder bed fusion; nickel-based superalloy; IN718; high-temperature mechanical properties; microstructure.

5.1 Introduction

Among nickel-based superalloys, Inconel 718 (IN718) is the most widely alloy used in different industrial spheres such as the petrochemical, aeronautics, energy, and aerospace sectors [45,69]. Thanks to its outstanding combination of superior strength, high creep performance, and high resistance to wear, corrosion and oxidation, even at cryogenic and elevated temperatures (up to 650°C), IN718 is a suitable candidate for numerous applications. It is typically used in critical components subjected to aggressive environments in jet and gas turbine engines, nuclear plants and cryogenic tanks, which are produced using conventional manufacturing processes such as forging and casting [69]. However, as components are becoming ever more complex and advancements in engine performance accelerate, attention is shifting from the traditional material processing technologies to additive manufacturing (AM) processes [1,95]. For instance approximately 100,000 parts were anticipated to be produced using the AM technology by General Electric aviation by 2020 [99]. Among AM techniques, the laser powder bed fusion (LPBF) process has gained the most attention due to its ability to customize IN718 components with high density and mechanical properties comparable to those of wrought alloy after appropriate heat treatments. Nevertheless, the widespread use and implementation of this technique in some specific applications, that demand isotropic mechanical properties, are only just beginning due to the vertically <100> aligned columnar

microstructure of the as-printed LPBF IN718 alloy, in addition to other manufacturing drawbacks [28,100].

Directional solidification, as a well-known phenomenon in as-printed IN718 and in other engineering materials fabricated using the LPBF process, occurs as a result of directional heat transfer along the building direction during the printing process: the heat transfers from the upper surface of the powder bed, where the laser beam is focused, toward the building platform [91]. Such a significant uniaxial thermal gradient culminates in the production of materials characterized by a strong texture, and consequently, anisotropic properties. In addition, other difficulties prevented obtaining consistent mechanical properties from different LPBF machines due to the high dependence of the properties on the part orientation during printing, as well as on the laser scanning strategy adopted [101]. It is realized that the columnar grain morphology with strong fiber texture leads to improving the creep resistance for some specific applications such as turbine blades and turbine disks [102]. However, numerous other applications are demanding microstructure with fine equiaxed grains to improve the material strength, fatigue properties and inter-granular crack propagation resistance as well as producing components with isotropic properties [103,104]. Therefore, several in-situ solutions have been introduced to control and mitigate the thermal gradient, such as pre-heating of the building chamber. Furthermore, customization of the laser process parameters, such as laser beam intensity profile (beam shape) and scanning strategy, is performed to control solidification, and thus grain structure and texture, depending on the fact that the grain structure is strongly governed by the variation of the ratio of thermal gradient (G) along the building direction and the solidification growth rate (R) [103,105].

For instance, Shi *et al*. [103] and Rongpei *et al*. [105], investigated the impact of different laser beam profiles, circular Gaussian (CG), longitudinal elliptical (LE) and transverse elliptical (TE), on the microstructure of a single track of LPBF-fabricated 316 L stainless steel. Their [103,105] results show that the elliptical laser profile, in general, had a significant impact on the solidification microstructure that allowed the freedom to tailor the grain morphology and material texture. For comparison, the use of the TE laser profile resulted in wider, shorter and shallower melt pool dimensions along the transverse, scanning and building direction, respectively, when compared to CG and TE ones. Thus, a lower thermal gradient across the melting pool after TE laser scanning was obtained when compared to the CG and LE laser profiles which significantly reduced the G/R ratio and resulted in equiaxed grain morphology. However, the columnar grain structure was not completely prevented especially at the start of the scanned track [103].

As discussed, microstructure with complete equiaxed grain morphology and random texture via the manipulating of the printing process parameters has not been achieved yet. Most importantly, violating the optimized process parameters of IN718, via changing the scanning strategy and laser beam intensity, might end up with other manufacturing defects such as pores, lack of fusion, poor substrate wetting as reported by [105]. Besides, the intrinsic <100> preferred crystallographic orientation of the face-centered cubic (FCC) IN718 superalloy [53,91] is not likely to be overcome through changing the printing process parameters. Therefore, to secure consistent properties in components produced using different AM machines with different scanning strategies and to obtain isotropic mechanical properties comparable to those of wrought IN718, recrystallization is required to refine the components' as-printed microstructure and eliminate their columnar morphology [101]. Ultimately, the use

of post-LPBF heat treatments would be required to eliminate the as-printed texture of LPBF IN718 parts and improve their mechanical properties.

Most of the literature on thermal post-processing of LPBF IN718 examines different treatment regimes aiming to optimize the microstructure and mechanical properties of the alloy. However, most of the concerns they address are directed towards the evolution of precipitates and how to dissolve the detrimental phases resulting from the LPBF process. Only limited attention has been paid to the evolution of the grain structure and of the material texture during heat treatments, which are also crucial to improving the mechanical properties of LPBF IN718. Chlebus *et al.* [46], for instance, investigated the influence of different heat treatments, including homogenization at 1100°C for 1h, followed by aging treatment, on the microstructure and mechanical properties of LPBF IN718 samples printed at different orientations (0°, 45° and 90°) with respect to the building direction [46]. From their results [46], the heat-treated samples exhibited higher mechanical strengths (1320±6, 1371±5 and 1377±66 MPa, respectively) in all directions, as compared to that of the wrought IN718 alloy (1317 MPa). However, the treatment conditions applied did not significantly change the shape of as-printed elongated grains and their crystallographic orientations, which consequently resulted in such variations in the mechanical properties between the 0°, 45° and 90° printed samples [46]. Similarly, Vilaro *et al.* [106] reported that significantly anisotropic mechanical properties were obtained even after the application of standard treatment conditions for nickel-based superalloys. It has been extensively reported that the standard heat treatments developed for cast (AMS5383) and wrought (AMS5662) IN718 do not eliminate the textured and columnar microstructure of the LPBF IN718 alloy [13,46,101,106,107]. Therefore, modified homogenization and solution heat

treatments are required to obtain AM components with the same isotropic mechanical and homogeneous microstructures as those made from the wrought alloy.

Aside from the standard heat treatment, Diepold *et al*. [108] investigated the effect of different modified heat treatments, SHT930, SHT954 and SHT1000, on the microstructure and mechanical properties aiming to optimize the post-heat treatments of the LPBF-fabricated IN718. They [108] reported that the SHT1000 achieved the optimum strength due to the higher volume fraction of γ′ and γ″ phases with no precipitation of δ-phase, as compared with those of SHT930 and SHT954 treatments. However, the as-printed texture and grain morphology did not change even after SHT930, SHT954 and SHT1000 treatments due to the lower heat treatments temperature than the recrystallization temperature [108]. Similarly, Huang, *et al*. [102] studied the influence of different solution treatment temperatures (from 980 to 1280°C) on the microstructure and mechanical properties of LPBF-fabricated IN718 intending to obtain the optimum solution treatment parameters. Their [102] microstructure results show that the increase of the solution temperature from 980 to 1230°C for 1h resulted in more dissolution of Laves phase to reach the appropriate homogenized microstructure at 1080°C for 1h. Furthermore, complete recrystallization was obtained just after the solution temperature of 1130°C for 1h [102]. However, a solution temperature above 1080°C for 1h resulted in a deterioration in the mechanical properties indicating the presence of conflict between obtaining high mechanical properties and fully recrystallized material [102].

In fact, obtaining isotropic mechanical properties through the transformation of the as-printed columnar grain structure into an equiaxed structure is not the only benefit provided by the material recrystallization. The development of grain boundaries during high-temperature heat treatments also has a beneficial effect on mechanical properties. Pande *et al.* [109] reported

that the presence of annealing twin boundaries improves the RT mechanical strength of IN718 alloy. In addition, Yuan *et al.* [110] reported that the annealed twin boundaries act as barriers to the dislocation glide, which consequently enhances the high-temperature creep properties. It is generally acknowledged that the transformation of columnar grains into equiaxed grains occurs as a result of the recrystallization process triggered by selecting the proper post-LPBF heat treatment. To this end, Fayed *et al.* [89,111], established a post-LPBF heat treatment window covering a wide range of homogenization (1080°C; 1 to 7h) and solution (980°C; 15 to 60 min) treatment soaking times, and studied the effects of these treatments on the microstructure and elevated-temperature (650°C) mechanical properties of LPBF IN718 alloy. They [89,111] concluded that the homogenization soaking time significantly affects the microstructure, precipitates, crystallographic texture and mechanical properties of this alloy. Samples subjected to a 1h homogenization treatment exhibit higher mechanical properties than those subjected to prolonged treatment times (4h and 7h) [89]. However, near-complete recrystallization and equiaxed grain morphologies were obtained only after the 4h homogenization treatment [89]. It can be observed that a trade-off between an LPBF IN718 alloy with high mechanical properties and one having a fine equiaxed microstructure with non-distinct texture appears to persist for this material [89]. Therefore, in the present study, it is a logical step to obtain the heat treatment conditions that can achieve a balance between these properties.

The objective of this study is to achieve the highest possible mechanical properties, while approaching a random crystallographic texture of LPBF IN718 components, using post-LPBF heat treatments. To provide an initial understanding of the combined effect of the homogenization and solution treatment times on the grain structure, the crystallographic texture

and the mechanical properties, the design of experiments (DOE) approach was first employed. Next, a multi-objective optimization procedure was applied to identify the most desirable heat treatment conditions. Finally, the effects of the proposed treatment conditions on the microstructure and mechanical behavior at RT and at 650°C of the post-treated LPBF alloy were studied.

5.2 Material and methods

A gas atomized IN718 powder with a particle size distribution of D10 (18.2 μm), D50 (32.4 μm) and D90 (54.2 μm) was used to manufacture IN718 coupons of this study. The nominal composition of the IN718 powder is listed in Table 5-1. An EOS M280 (EOS, Krailling, Germany) LPBF system, equipped with a fiber laser with a maximum power of 400 watts, was employed to additively manufacture the IN718 coupons using the EOS Original IN718_Surface 1.0 Parameter Set. The process parameters are listed in Table 5-2. In the present study, 22 × 17 × 10 mm^3 cuboid coupons were fabricated for the microstructural analysis, whereas 19 × 4 × 83 mm^3 rectangular prismatic coupons were manufactured for the tensile testing. Details of the scanning strategy and the printing direction of these coupons, with respect to the building direction (BD), are illustrated in Figure 5-1. To retain the as-printed microstructure, the IN718 coupons were removed from the building platform using wire electric discharge machining (WEDM) just after the LPBF printing process.

Table 5-1: Nominal chemical composition of the as-received gas atomized IN718 powder

Element	**Ni**	**Cr**	**Nb**	**Mo**	**Ti**	**Al**	**Fe + Traces**
wt.%	49.19	19.04	4.92	2.70	1.08	0.33	Bal.

Table 5-2: LPBF process parameters used in the present study

Process Parameter	Value
Laser power (Watt)	285
Laser scanning velocity (mm/s)	1000
Laser beam diameter (µm)	100
Layer thickness (µm)	40
Hatching space (µm)	110
Hatch angle (degree)	67
Building plate pre-heating temperature (°C)	80

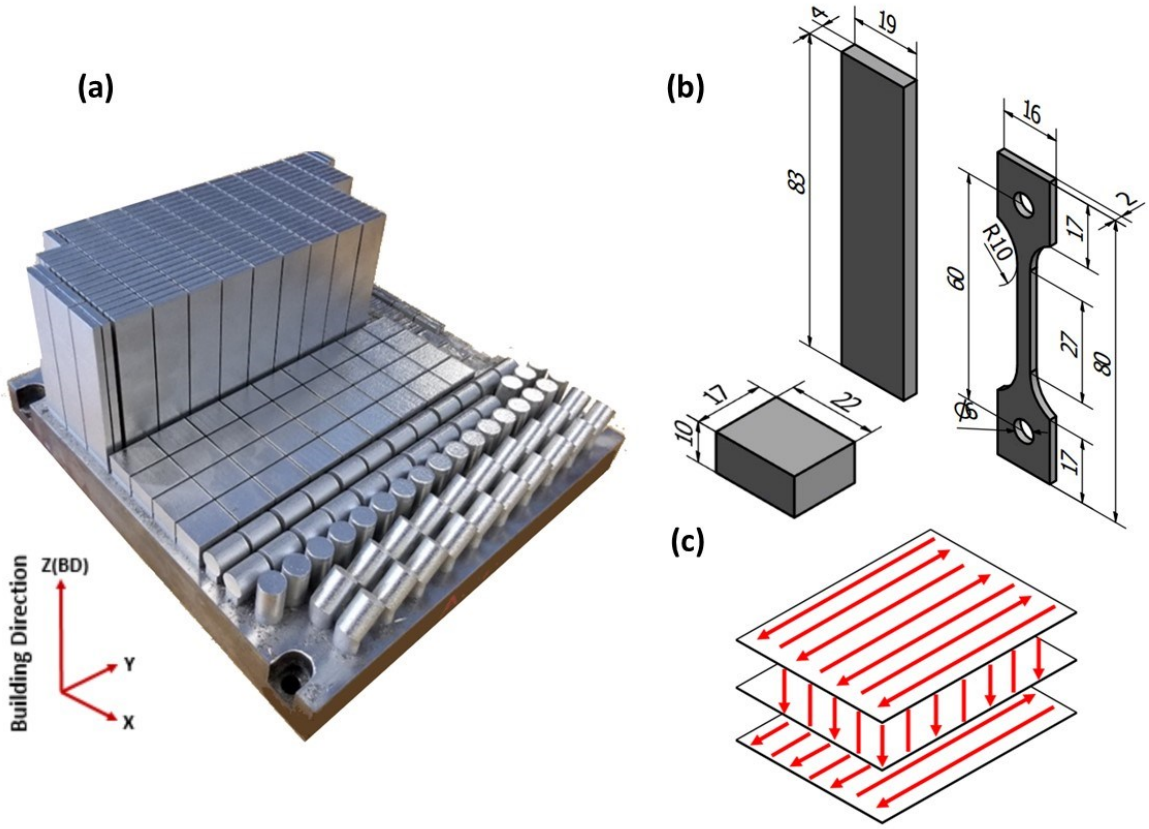

Figure 5-1: (a) LPBF building platform illustrating the orientation of the as-printed coupons with respect to the building direction (BD); (b) geometry and dimensions of the microstructure and tensile samples; (c) schematic drawing showing the scanning strategy utilized in the present study. (a) and (b) were also used in [89]. All dimensions in (b) are in mm.

To identify the optimum heat treatment conditions to be applied in the present study and to understand the effect of interaction of the homogenization and solution treatment times on the

microstructure and mechanical properties, the DOE approach was employed, using the previously obtained results [89,111] and Design-Expert 12 software [112]. Details of the optimization criterion and the proposed treatment conditions are discussed in section 3.1. The heat treatments were performed using an electric resistance furnace with a set of K-type thermocouples to monitor the samples' temperature during the heat treatments, where the temperature difference was controlled within ± 5 °C.

The microstructure of the as-printed and heat-treated IN718 samples was examined using a scanning electron microscope (SEM TM3000 HITACHI). For the microstructural analysis, the as-printed and heat-treated IN718 samples were sectioned using a slow cutter with a mineral oil bath to prevent heat generation. The sectioned samples were hot-mounted using a conductive epoxy, and mechanically ground from 240 up to 1200 grit size using silicon carbide emery papers; they were then polished down to 1 μm using alcohol-based diamond suspension. Furthermore, the microstructure orientation and grain structure were investigated using a SEM (SU-8230 HITACHI) equipped with a Bruker e^-Flash HR^+ electron backscatter diffraction (EBSD) detector with 20 kV and a pixel size of 1.62 μm. An EBSD analysis was carried out on the vertical cross-sections (parallel to the building direction) only, since the grain structure and crystallographic orientation in this plane are of main interest. To cover the maximum number of grains, the total surface area analyzed by EBSD for each condition was $1298 \times 973.4\ \mu m^2$. The extracted EBSD data were post-processed using ATEX [113] and QUANTAX ESPRIT software [114]. For the EBSD samples, similar aforementioned surface preparation procedures were performed, after which further polishing was performed using the VibroMet™ for 24 hours, with a 0.05 size colloidal silica. Finally, an IM4000Plus HITACHI ion milling system was used to eliminate residual scratches and deformed traces with an

accelerating voltage of 6 kV and a rotation speed of 25 rpm, for 40 minutes. For texture and phase analyses, X-ray diffraction (XRD) with a CuKα radiation at 45 kV and 35 mA was employed. A 2θ scanning range was selected from 30° to 100° to cover the maximum possible number of diffraction peaks. For the heat-treated samples, XRD analysis was conducted prior to the aging step to monitor the effect of the soaking times of the preceding homogenization treatment on the as-printed microstructure. For consistency, all XRD patterns were acquired from the xy-plane (perpendicular to the building direction) of the as-printed and heat-treated samples.

The standard tensile properties of the as-printed and heat-treated conditions at RT and at elevated-temperature (650°C) were determined with a strain rate of 10^{-3} s^{-1}. The tensile specimens, according to the ASTM E8M standards, were machined from the as-printed rectangular coupons with the dimensions shown in Figure 5-1b. All the heat treatments were performed before the WEDM, to avoid the sample distortion caused by LPBF-induced residual stresses during the machining process. The tests were performed using an MTS 810 machine, and two to three tensile samples were tested for each condition, and their average values reported. For the elevated-temperature tensile testing, the machine was equipped with an infrared radiant heating furnace. The tensile samples were heated up to 650°C with a heating rate of 1°C/sec, and then held for 10 minutes to obtain a uniform temperature distribution along the sample. To this end, three K-type thermocouples were equally spaced along the gauge length. The central thermocouple was used to control the temperature of tensile samples during testing. To avoid the thermal expansion effect during heating, all tensile samples were preloaded with a constant force of 50 N. Furthermore, an argon shielding gas flow (4.7 L/min) was used to minimize oxidation during the elevated-temperature testing.

5.3 Results and discussion

5.3.1 Effect of the interaction between homogenization and solution treatment times on the mechanical properties and crystallographic texture

Based on the previously obtained experimental results [89], three-dimensional (3D) response surface graphs of the evolution of a) the tensile properties of LPBF IN718 alloy at 650°C (tensile strength (TS), yield strength (YS), elongation to failure (EL)), b) the room temperature Vickers microhardness (HV0.5/15), and c) the texture degree (f) were plotted in Figure 5-2 as functions of the homogenization and solution treatment times, using Design-Expert 12 software [112]. The soaking times for both the homogenization and solution treatments were defined as factors, whereas the TS, YS, El, HV and f values of the heat-treated LPBF IN718 were defined as responses. The homogenization treatment time ranged from 1 to 7h, while for the solution treatment, it went from 15 to 60 min. Details of the heat treatment conditions and their corresponding responses, which were used to plot the response surface graphs, are listed in Table 5-3. The degree of the material texture in the heat-treated conditions is defined by the intensity ratio *f* as reported in [52,115], which can be defined as:

$$f = \frac{I_{(111)}}{I_{(200)}} \qquad (5\text{-}1)$$

where $I_{(111)}$ and $I_{(200)}$ designate the diffraction peak intensity of the {111} and {200} planes, respectively, which were obtained from the XRD analysis [89]. Thus, the lower the value of ratio *f*, the stronger the {200} texture, whereas the larger this value, the closer it is to a non-distinct {111} texture.

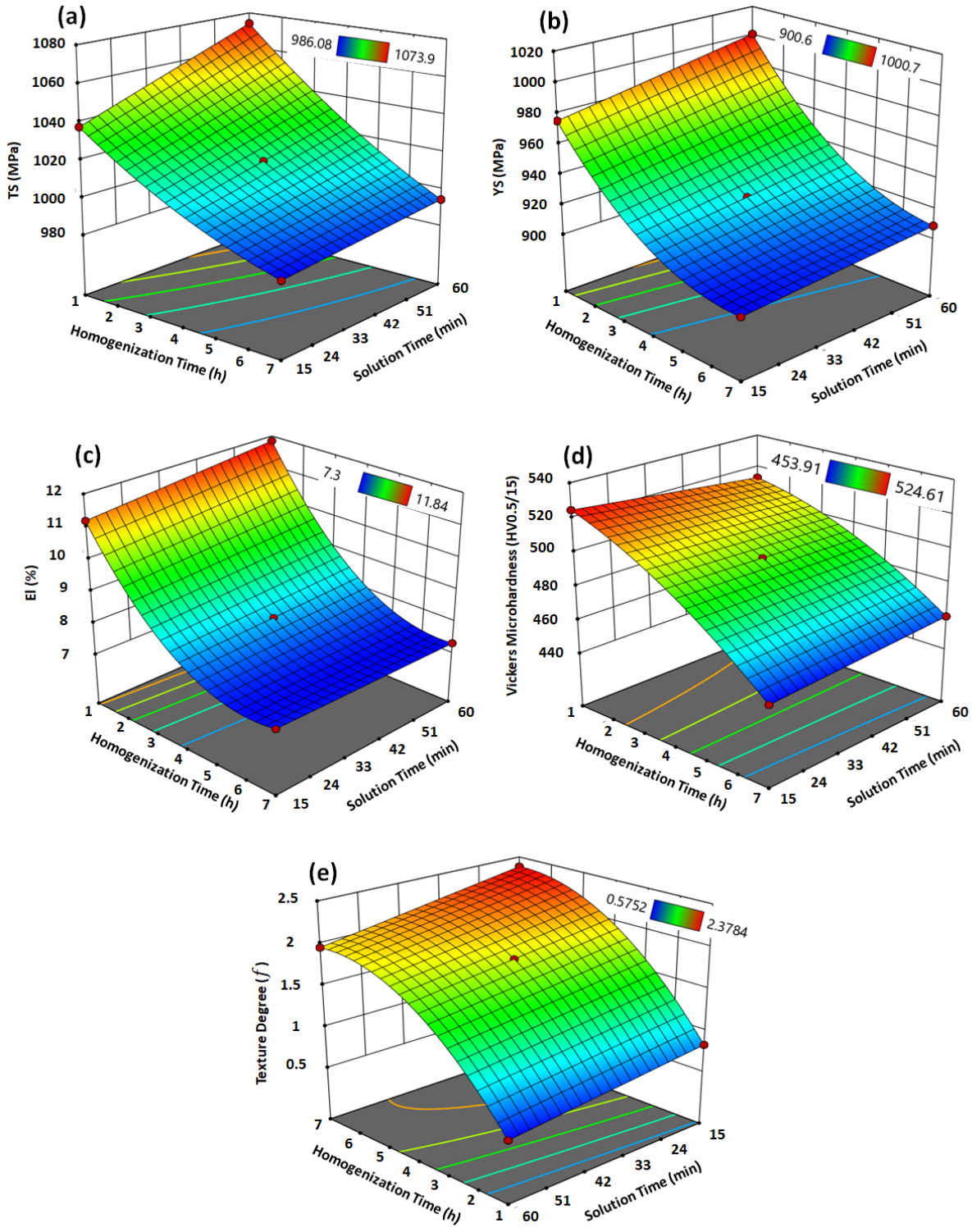

Figure 5-2: Three-dimensional (3D) response surfaces of the effect of the interaction between the homogenization and solution treatment times on: (a) TS, (b) YS and (c) El (all at 650°C), (d) Vickers microhardness (room temperature), and (e) texture degree

Table 5-3: Details of heat treatment conditions and the corresponding tensile properties at 650°C (TS, YS and El), hardness measurements and texture degree [89,111]

Heat treatment conditions			Tensile properties at 650°C			HV	Texture degree
Homogenization (at 1080°C)	Solution (at 980°C)	Aging	TS (MPa)	YS (MPa)	El (%)		
1h/AC*	15min/AC		1038± 14	976± 9	11.2± 2	525± 8	0.83
1h/AC	1h/AC	720°C/8h/ FC** at	1074± 28	1001± 12	11.8± 0.3	513± 9	0.57
4h/AC	37.5min/AC	55°C/h to 620°C+	1017± 11	927± 2	8.2± 0.2	496± 7	1.84
7h/AC	15min/AC	620°C/8h/ AC	986± 14	901± 7	7.4± 0.9	454± 17	2.38
7h/AC	1h/AC		994± 11	909± 8	7.3± 1	460± 13	1.96

*AC: air cooling, ** FC: furnace cooling

Generally, as can be seen in Figure 5-2a to e, changes in the homogenization time at 1080°C have a significant influence on all the responses (TS, YS, El, HV and *f*), regardless of the solution treatment time. The 1h homogenization treatment resulted in the highest tensile and yield strengths, ductility and RT hardness, whereas increasing the treatment time to 4 and 7h led to a significant reduction in the intensity of the changes, as can be seen in Figure 5-2a to d. Such high mechanical properties appearing after the 1h homogenized conditions are attributable to the retention of the as-printed dislocation networks inherited from the printing process, due to the rapid and repetitive heat and cooling, as observed from the kernel average misorientation angle (KAM) analysis in [111]. Furthermore, a high release of the strengthening phase constituents (Nb and Ti) into γ-matrix after the 1h homogenization treatments, as indicated by the remarkable expansion of lattice parameters of γ-matrix in [89], is expected to lead to more precipitation of γ′ and γ″ phases during aging treatment as compared to the prolonged homogenization conditions, which consequently improved the mechanical properties at both RT and 650°C. A high elongation to failure after the 1h homogenization treatment (Figure 5-2e)

can be attributed to the orientation of the elongated grain longitudinal axes along the tensile loading direction, since these heat treatment conditions did not significantly modify the as-printed grain structure and strong crystallographic orientation, as was previously observed in Figure 14b in [89].

For the prolonged homogenization heat treatments (4 and 7h), reductions in the tensile strength, ductility and hardness are attributable to the significant impact of this process on the annihilation of the dislocation tangles and on the intensification of the precipitation of MC-type carbides. The latter consumes significant amounts of Nb and Ti, which are the main contributors to γ′ and γ″ phase precipitations during aging treatment, as confirmed by the lattice parameter calculations and peak shift analysis in [89].

For the solution treatment at 980°C, it is important to note that after the 1h homogenization treatment, the solution time had a considerable impact on the tensile and yield strengths of the LPBF IN718 alloy, as shown in Figure 5-2a and b. This can be attributed to a more intense needle-like δ-phase precipitation along the grain boundaries (≈ 0.7% area fraction) with longer solution treatments (60 min) as quantified in our previous study [111], which contributes to an improvement of the grain boundary strength. During plastic deformation at high temperatures, the pinning effect of the δ-phase on the sliding of the grain boundary and impediment of the dislocation movements improves the mechanical strength of the IN718 superalloy [24]. However, after the longest homogenization treatment (7h), the solution time had a very limited impact on the TS and YS values, as illustrated in Figure 5-2a and b. This is attributable to a significant impact of the 7h homogenization treatment to eliminate the Nb-enriched regions along the grain boundaries inherited from the LPBF printing process, and distribute it more uniformly in γ-matrix [89]. Thus, the Nb concentration along the grain boundaries becomes

insufficient to drive the precipitation of δ-phase, which preferentially precipitates in Nb-enriched areas (at least 6 – 8 wt.%) [12]. Such a decrease in the amount of δ-phase precipitates results in a smaller impact of the solution time on the mechanical properties after the 7h homogenization treatment.

Regarding the RT microhardness after the 1h homogenization treatment, the effect of the presence of δ-phase is the opposite of the effect of the treatment on the tensile and yield strengths, since the greater the concentration of needle-like δ-phase precipitates (≈ 0.7% area fraction) after solution treatment for 60 min [111], the lower the material hardness (see Figure 5-2d). This suggests that a greater precipitation of δ-phase (Ni_3Nb) consumes more Nb at the expense of the formation of the primary strengthening phase (γ″), which consequently resulted in a decrease of the hardness values. In contrast, after the 7h homogenization treatment, both solution treatment conditions (15 and 60 min) resulted in comparable RT hardness values, which again can be explained by the precipitation of comparable amounts of δ-phase after these treatments led to formation of approximately comparable amounts of γ″ phase during the subsequent aging treatment.

Although the 1h homogenization treatment conditions had a significant impact in terms of improving the mechanical behavior of the LPBF IN718 alloy at RT and at 650°C, its contribution to the crystallographic texture and grain structure was very limited. It is well-known that the as-printed LPBF IN718 has a strong fiber texture along the building direction, which is the main reason why components with highly anisotropic mechanical properties are produced. However, significant changes in the as-printed texture and a transformation of the grain morphology from columnar into an equiaxed structure are observed after the prolonged homogenization treatments (4 and 7 h), as shown in Figure 5-2e.

Based on the aforementioned results, a multi-objective optimization was conducted to find the most suitable soaking times for both the homogenization and solution treatments that can achieve a specified target for all of the responses. The optimization criteria and the target used in the present study are detailed in Table 5-4. A multi-objective optimization routine was carried out using an objective function named "desirability", which ranges from 0, for the least desirable setting, to 1, for the best target achieved. It is worth mentioning that for all the responses, the same importance level, 5 (maximum importance level), was selected, as shown in Table 5-4. Regarding the responses criteria, as can be seen in Table 5-4, the optimization target for TS, YS, El and HV0.5/15 responses was selected as "maximize", whereas for the texture degree, the target selected was "in range", and its lowest bound was defined to be greater than 1. The latter conditions only retain solutions corresponding to the highest $I_{(111)}$ to $I_{(200)}$ intensity ratios.

Table 5-4: Details of multi-objective optimization target and criteria

Variables/ Reponses	Input/output	Criterion	Limit		Impo-rtance
			Lower	Upper	
Variables	Homogenization soaking time (h)	In range	1	7	-
	Solution soaking time (min)	In range	15	60	-
Responses	Tensile strength, TS (MPa)	Maximize	986	1074	5
	Yield strength, YS (MPa)	Maximize	901	1001	5
	Elongation, El (%)	Maximize	7	12	5
	Vickers Microhardness (HV)	Maximize	454	525	5
	Texture degree, *f* (ratio)	In range	>1	2.4	5

Given the aforementioned inputs, 35 solutions were introduced, with different combinations of homogenization and solution treatment times. However, only one condition was proposed and expected to correspond to the optimized heat treatment conditions: a homogenization treatment at 1080°C for 2.15h, followed by a solution treatment at 980°C for 60 min. It is worth

mentioning that this combined treatment includes the longest solution time, 60 minutes, as the presence of inter-granular δ-phase has a crucial impact on the improvement of the mechanical properties, especially at elevated temperatures [24,111]. Figure 5-3 shows the contour line graphs of the desirability function and the five responses as functions of the soaking times of both the homogenization and solution treatments. It is important to note that, depending on the desirability value, the application of the aforementioned treatment (1080°C/2.15h/AC + 980°C/1h/AC) is expected to achieve the objective by 71%, which is the maximum desirability value achieved in this study, as compared to the other 35 proposed conditions. Figure 5-3b to f shows and allocates the predicted responses after the application of these combined treatment conditions. It is interesting that the predicted texture degree ratio after the proposed treatment is 1.1, which indicates the treatment after which the peak intensity of $I_{(111)}$ starts to dominate that of $I_{(200)}$. The heat treatment conditions listed in Table 5-5 are applied in the sequel of this study based on this multi-objective optimization output and our previous findings.

As mentioned earlier, the approach adopted in the present study aimed to obtain the heat treatment conditions which can lead to the maximum desirability. Accordingly, the 2H/1S conditions, which correspond to a homogenization treatment at 1080°C for 2.15h, followed by a solution treatment at 980°C for 60 min, were introduced (H and S refer to the homogenization and solution treatments, respectively, and the numbers refer to the approximate times in hours). In addition, heat treatments with a homogenization time gradually increasing by a step of 0.5h, 2.5H/1S, 3H/1S, 3.5H/1S and 4H/1S were also included in this study, as shown in Table 5-5. These conditions were added in case the 2H/1S conditions did not allow obtaining the desired mechanical properties and material texture. The decision to modify the homogenization treatment time without varying that of the solution treatment was based on the significant effect

of the homogenization process on the crystallographic texture and grain structure, as shown by the previously obtained results. Figure 5-4 shows the full window of all the heat treatment regimes and their allocations.

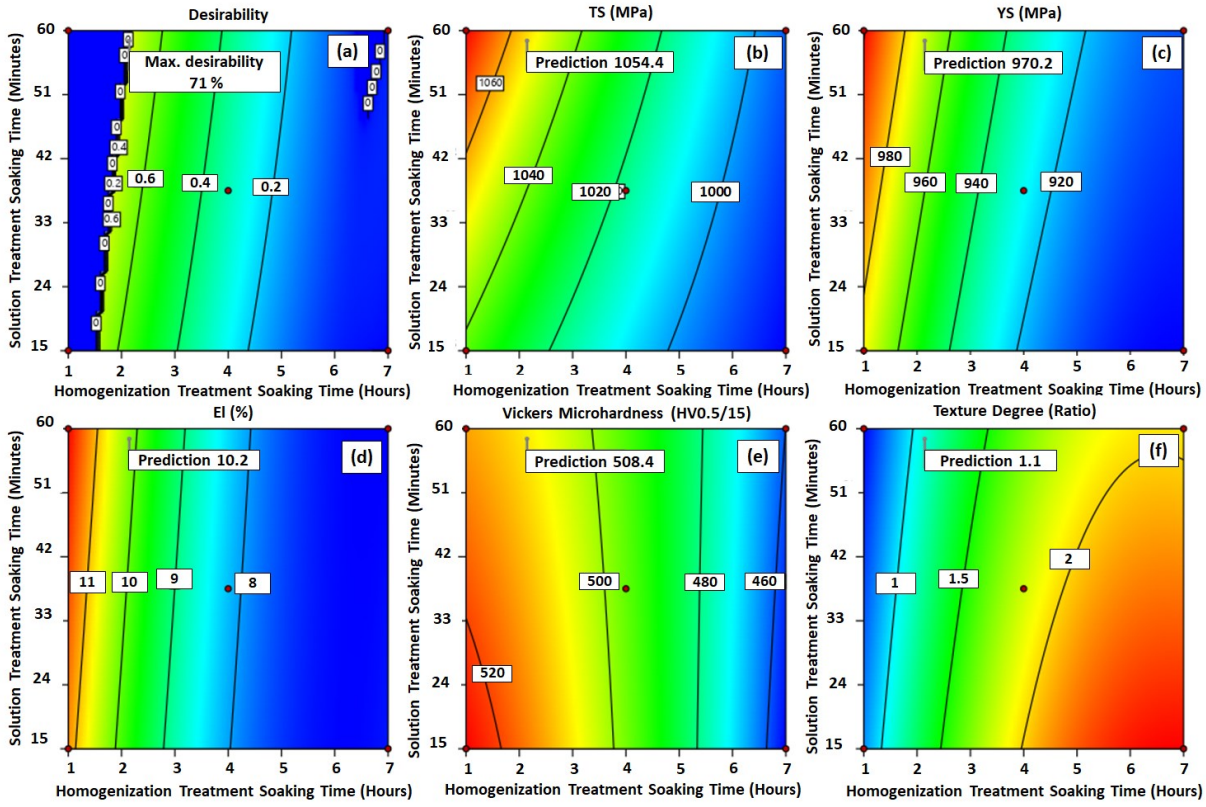

Figure 5-3: Contour lines curves: (a) maximum desirability function and predicted values of (b) TS, (c) YS, (d) El, (e) Vickers microhardness, and (f) texture degree

Table 5-5: Details of proposed heat treatments conditions in the present study

Designation	Homogenization Heat Treatment (H)	Solution Heat Treatment (S)	Aging Heat Treatment
As-printed	None	None	None
2H/1S	1080°C for 2h/AC	980°C for 1h/AC	720°C/8h/FC at 55°C/h to 620°C+620°C /8h/AC
2.5H/1S	1080°C for 2.5h/AC		
3H/1S	1080°C for 3h/AC		
3.5H/1S	1080°C for 3.5h/AC		
4H/1S	1080°C for 4h/AC		

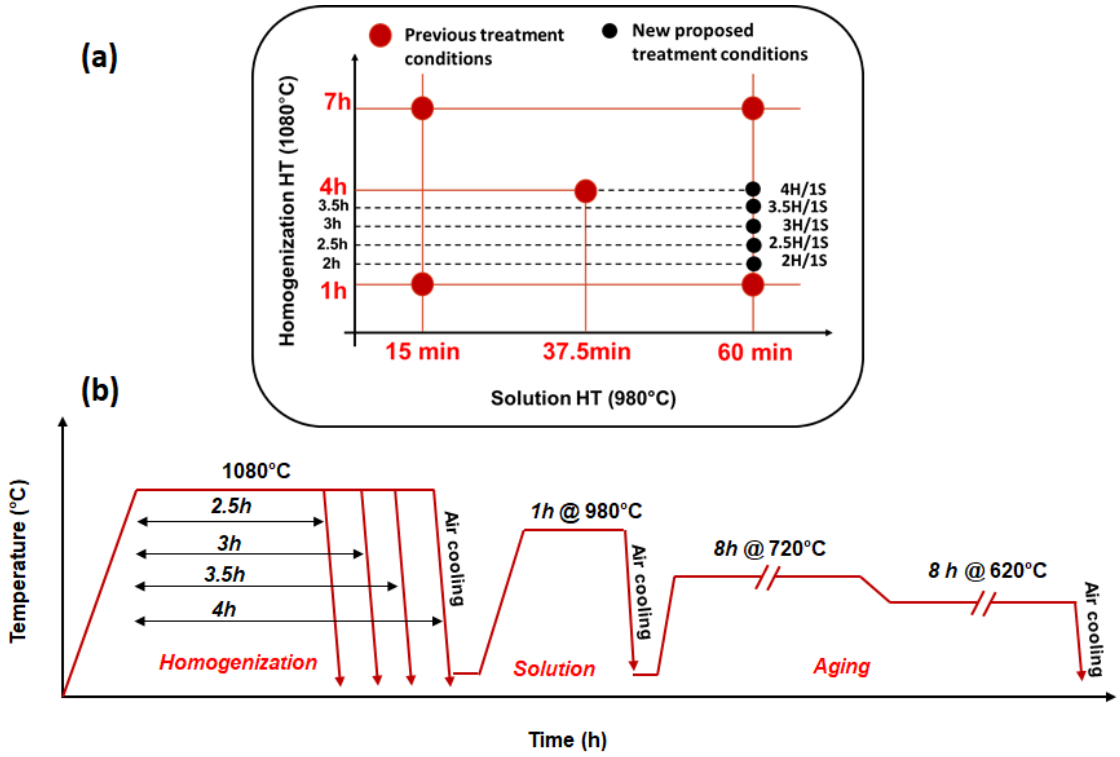

Figure 5-4: (a) Schematic drawing illustrating the position of the new proposed treatment conditions within the treatment time window with respect to the previous treatments; (b) the full regime of the heat treatment cycle applied in the current study

5.3.2 Texture and phase evolution using XRD analysis

XRD analysis was employed as an initial characterization and screening method because it provides quick and informative feedback about the microstructural evolution in terms of texture changes and phase precipitation and/or dissolution, which are the main concerns in the optimization process. Figure 5-5 shows the XRD patterns of the as-printed and heat-treated samples. As can be seen in this figure, the as-printed and 2H/1S conditions exhibited higher peak intensities of γ (200) than those of γ (111), indicating that the 2H/1S treatment did not significantly change the as-printed texture due to a potentially insufficient activation energy. Thus, this condition was excluded from further analysis since it did not allow to achieve the desired texture. However, an increase in the homogenization time to 2.5, 3, 3.5 and 4h resulted in noticeable changes in the as-printed texture and revealed higher peak intensities of γ (111)

as compared to those of γ (200) with intensity ratios (*f*) of 1.38, 1.51, 2.05 and 1.83, respectively. This means that after a homogenization treatment at 1080°C for 2.5h, the as-printed texture was already significantly affected by the homogenization time.

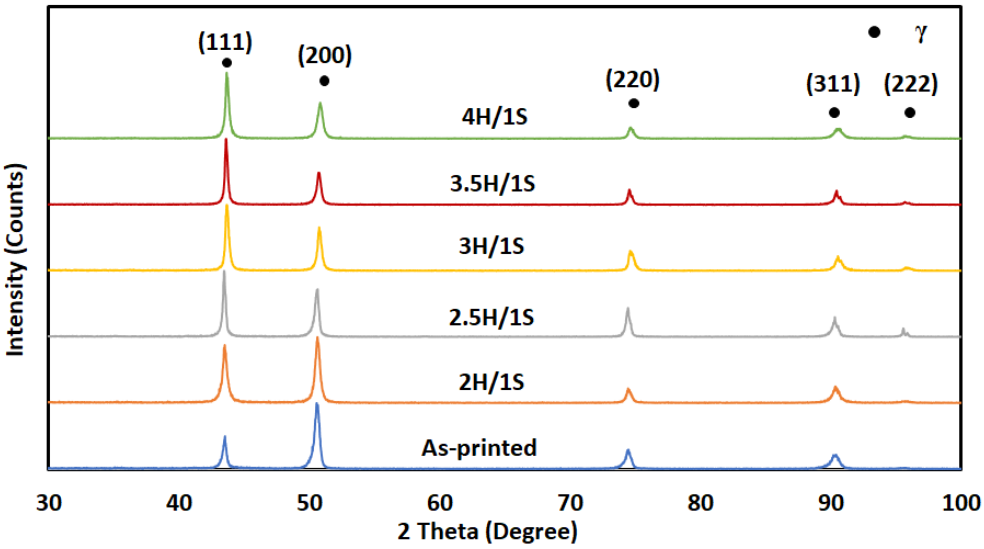

Figure 5-5: X-ray diffraction of the LPBF IN718 in the as-printed and heat-treated conditions

Furthermore, to follow the precipitation/dissolution of phases containing Nb, Ti and Mo, the lattice parameter of γ-matrix in the heat-treated IN718 (2H/1S, 2.5H/1S, 3H/1S, 3.5H/1S and 4H/1S) conditions was calculated, as shown in Figure 5-6. For comparison, the lattice parameter of γ-matrix in the as-printed condition, as a reference (illustrated by a dashed line), and in the 1H/1S-treated conditions reported in the previous work [89], are included in this figure. As can be seen, the lattice parameter of γ-matrix increased from 3.5999 ± 0.0034 Å, in the as-printed condition, to 3.6039 ± 0.0016 Å, 3.6031± 0.0008 Å and 3.6035 ± 0.0007 Å, after the 1H/1S, 2H/1S and 2.5H/1S conditions, respectively. This can be attributed to the dissolution of the segregated Nb, Ti and Mo (present in the inter-dendritic regions and grain boundaries) back into the γ-matrix, causing an expansion in the lattice parameter, since the atomic size of these elements is 33, 18 and 27.5%, respectively, larger than that of Ni [89]. Such a back

diffusion phenomenon has a beneficial effect on the mechanical properties of the LPBF IN718 alloy as it releases more age-hardening constituents such as Nb and Ti, which are required for the precipitation of γ″ and γ′ phases.

However, the application of the 3H/1S, 3.5H/1S and 4H/1S treatments resulted in a significant reduction in the γ-matrix lattice parameter (Figure 5-6) relatively to the as-printed condition, being 3.5965 ± 0.0015 Å, 3.5964 ± 0.0029 Å and 3.5931 ± 0.0036 Å, respectively. It is interesting to note that the lattice parameter gradually decreases with an increase in the homogenization time to 3, 3.5 and 4h. This can be explained by the depletion of some alloying elements (Nb and Ti) from γ-matrix during the heat treatments. Therefore, a drop in the mechanical properties after the 3H/1S, 3.5H/1S and 4H/1S heat treatments is expected given the smaller precipitation of γ′ and γ″ phases. Such a γ-matrix lattice parameter reduction with longer annealing treatments was also reported by Jiang *et al*. [76]. Accordingly, it can be concluded that the homogenization treatment at 1080°C for 2.5h is a threshold after which there is a degradation in the hardening due to a depletion of precipitate-forming elements.

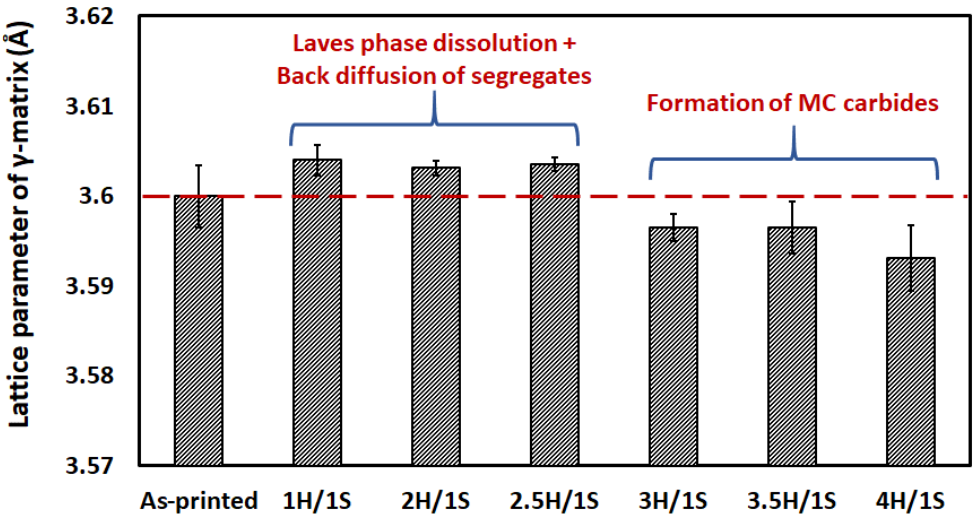

Figure 5-6: Lattice parameter evolution of the as-printed γ-matrix as a function of the heat treatment conditions

5.3.3 Microstructure and elemental analysis

5.3.3.1 Precipitates and grain morphology evolution

Figure 5-7 shows the precipitate distribution in the as-printed and heat-treated conditions. As can be seen in the as-printed micrograph (Figure 5-7a and b), continuous chains of small regions enriched in segregated elements and Laves phase are distributed along the inter-dendritic and grain boundary zones. The homogenization treatment (1080°C) is intended to dissolve these segregated elements and detrimental phases, such as Laves phase, whereas the subsequent solution treatment (980°C) is intended to precipitate δ-phase since the δ-phase precipitation temperature range in IN718 superalloy lies between 750 and 950°C [78].

After the heat treatments with different homogenization times (2.5, 3, 3.5 and 4h), these inter-dendritic and grain boundary Laves phase chains are dissolved, allowing a greater release of the segregated elements into γ-matrix, as can be seen in Figure 5-7c to j. Furthermore, only inter-granular δ-phase precipitated after these heat treatments, which indicates a nearly complete dissolution of the Nb-enriched regions inside the grains (inter-dendritic zones). At the end of the solidification stage, the grain boundaries accumulated more segregated elements as compared to the inter-dendritic zones with a higher concentration of Nb, as was previously observed in Figure 7 in [89]. This is because the segregation energy of Nb at the grain boundaries is twice that in the matrix [116]. During the homogenization treatment, the inter-dendritic segregates easily vanished, while retaining a sufficient Nb concentration along the grain boundaries for the precipitation of inter-granular δ-phase during the consecutive solution treatment. Although the heat treatments involved the same solution time (1h), the amount of the precipitated δ-phase along the grain boundaries decreased as homogenization treatment time increased, as shown in Figure 5-7d, f, h and j. This is mainly because of the decrease in the Nb

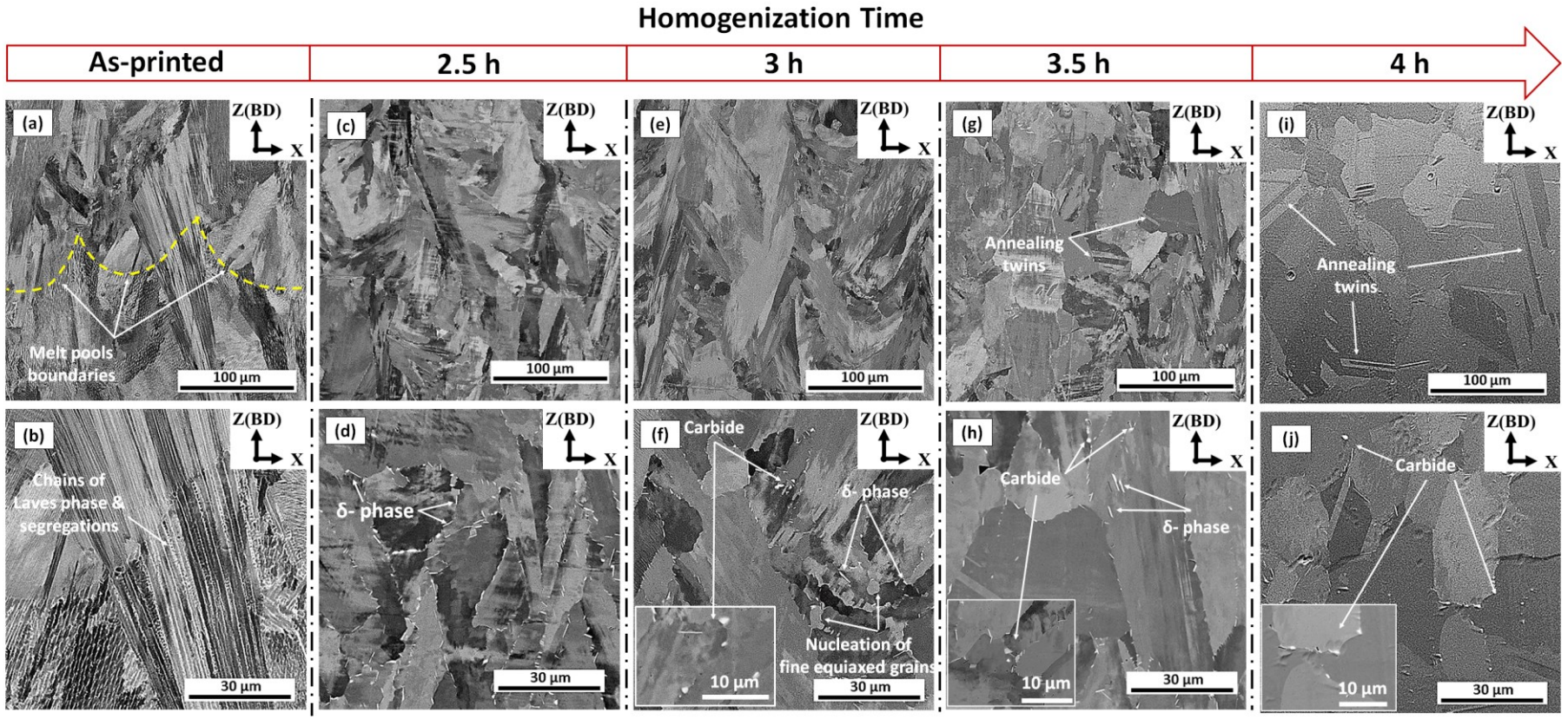

Figure 5-7: SEM micrographs of the vertical (xz) plane of LPBF IN718 under: (a-b) as-printed, (c-d) 2.5H/1S, (e-f) 3H/1S, (g-h) 3.5 H/1S and (i-j) 4H/1S condition

concentration along the grain boundaries with such homogenization time increase. However, after these conditions, the image threshold for digitized SEM micrographs must be analyzed using ImageJ software in order to quantify the amount of δ-phase precipitation.

After the 3H/1S, 3.5H/1S and 4H/1S treatments, more irregular-shaped particles were formed along the grain boundaries, as shown in the inset image in Figure 5-7f, h and j. According to the EDS analysis shown in Figure 5-8, these particles are highly enriched with Nb (≈ 51 wt. %) and Ti (≈ 6.5 wt. %) and, therefore, they have been indexed as MC carbides. These findings are consistent with the results of the γ-matrix lattice parameter analysis, in which a decrease in the lattice parameter of γ-matrix was observed, due to the depletion of Nb and Ti from the matrix to form MC carbides.

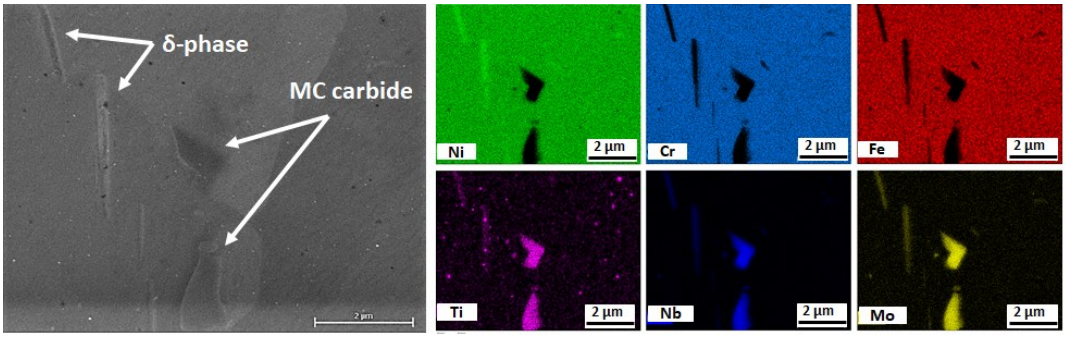

Figure 5-8: EDS elemental distribution in MC carbides and δ-phase

Although the purpose of the homogenization treatment is to dissolve the segregates and to homogenize the elemental distribution in γ-matrix, it can also trigger static recrystallization, which is necessary to refine the as-printed microstructure and consequently improve the mechanical properties of LPBF IN718. As mentioned earlier, in most pertinent literature consulted examines how to homogenize the as-printed microstructure and improve the mechanical properties through the dissolution of the detrimental phases and the precipitation of the strengthening phases (γ′ and γ″). However, less attention is paid to the grain structure, which

must also be known in order to obtain isotropic mechanical properties, especially in the case of a typical elongated grain morphology of the as-printed LPBF IN718.

The high level of residual stresses which are generated due to the rapid and repetitive heating and cooling inherent to the LPBF process is the driving force triggering the static recrystallization process during homogenization treatment [78]. As can be seen in Figure 5-7 c to f, the microstructure after the 2.5h and 3h homogenization conditions is mainly composed of a significant number of elongated grains with longitudinal axes parallel to the building direction, surrounded by a small number of equiaxed grains which were concentrated along the grain boundaries of the elongated grains (see Figure 5-7f). Thus, the mechanical properties of LPBF IN718 are expected to be anisotropic even after the 2.5H/1S and 3H/1S conditions. It is worth mentioning that the microstructure and grain morphology features obtained in this study after the 2.5H/1S and 3H/1S conditions do not match those obtained by some other researchers [34,63], who reported that a complete equiaxed grain IN718 matrix was obtained after a homogenization treatment at 1080°C for 1.5h, followed by a solution treatment at 980°C for 1h. The discrepancy can be explained by the fact that the variations in the printing process parameters as well as the performed scanning strategies would result in changes in the stored energy from one as-printed material to another, which consequently leads to changes in temperature and incubation time of the static recrystallization process [117].

In contrast with the 2.5h and 3h conditions, after the homogenization treatment for 3.5H/1S, more equiaxed grains with some annealing twins in the grain interiors are observed, as shown in Figure 5-7g and h. However, elongated grains were still present under this condition, indicating that a longer homogenization time is required to obtain a completely recrystallized material. After the 4H/1S treatment, distinct microstructural changes and dominant equiaxed

grains with interior annealing twins are observed, suggesting that the recrystallization process is almost complete, since annealing twins exist only in unstrained recrystallized grains [78]. Furthermore, in the current study, the average measured grain size in the completely recrystallized IN718 is 62.5 μm, which is consistent with that obtained in [92] (65 μm) after homogenization treatment at 1150°C for 2h, followed by aging treatment (700°C for 12h, followed by water cooling) for LPBF IN718.

5.3.3.2 Texture and grain structure evolution

Figure 5-9 shows the grain morphology, inverse pole figures (IPF) and pole figures (PF) of the as-printed and heat-treated conditions used to investigate the evolution in the crystallographic orientation alignment and grain structure. Based on the XRD and microstructure analyses, the 2.5H/1S and 4H/1S treatment conditions were selected to be analyzed using the EBSD, since the 2.5H/1S conditions are the threshold after which the depletion of age-hardening constituents (Nb and Ti) from γ-matrix occurs, while the 4H/1S conditions correspond to those after which a near-completely-recrystallized material is obtained.

As can be seen in Figure 5-9a and c, the alloy in the as-printed conditions exhibit an elongated grain microstructure with a strong fiber texture along the (100) plane, which is parallel to the building direction. Such a textured material and grain morphology are typical of IN718 alloy fabricated by LPBF. After the 2.5H/1S conditions, noticeable changes in the crystallographic orientation are observed, and are shown by a decrease in the red areas in Figure 5-9e and a lower texture intensity value of the maximum uniform density along the (100) orientation in the pole figure (MUD = 2.04) (Figure 5-9f). This points to the weakening of the (100) texture, as compared to the as-printed conditions (MUD = 3.13). These results are

consistent with those of the XRD analysis (Figure 5-5). However, the alloy microstructure in the xz-plane (parallel to the building direction) is still composed of columnar grains (Figure 5-9d), thus indicating no significant changes as compared to the as-printed grain morphology.

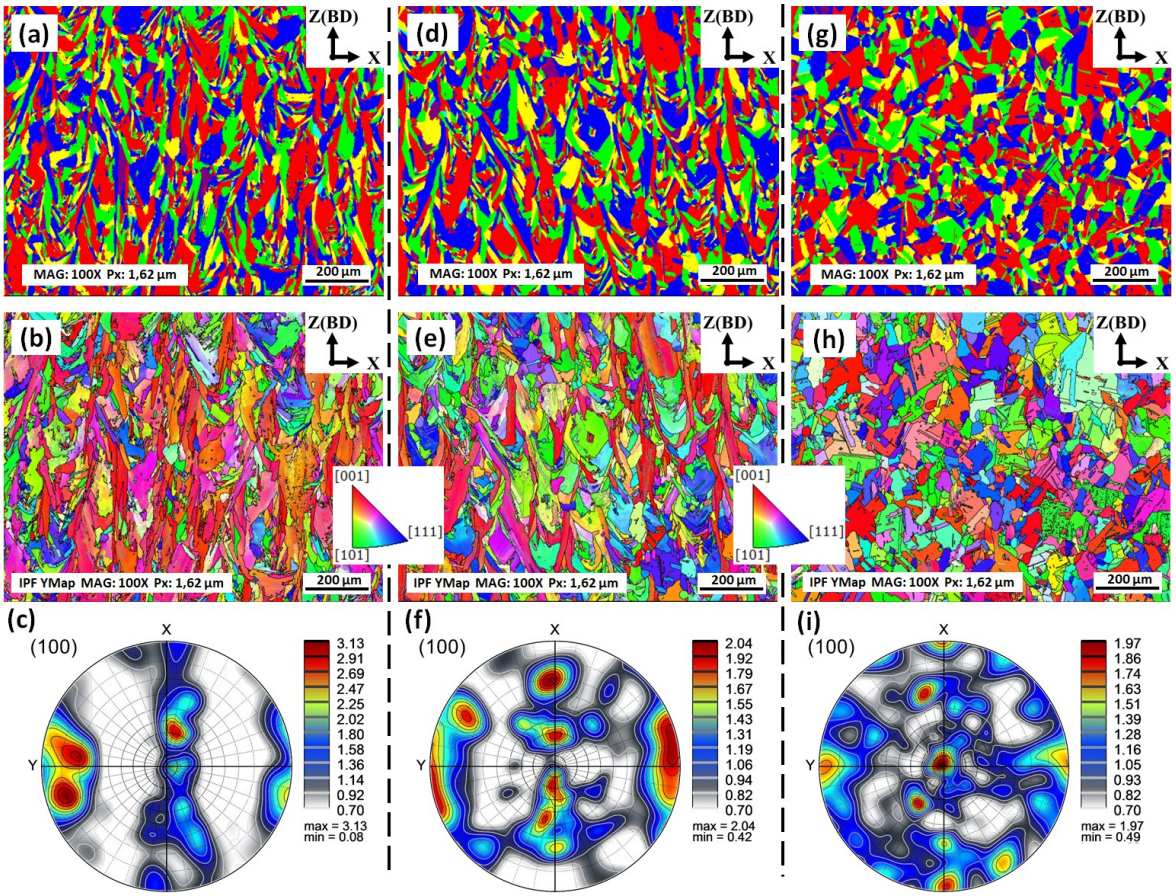

Figure 5-9: EBSD grain map, inverse pole figure (IPF) and pole figure (PF) of LPBF IN718 under: (a-c) as-printed, (d-f) 2.5H/1S treatment, and (g-i) 4H/1S treatment conditions. The EBSD mappings of the as-printed and heat-treated samples were plotted using the y-based projected IPF. (a) and (b) were used also in [89].

Figure 5-10a and b show the grain aspect ratio histograms of the as-printed 2.5H/1S and 4H/1S conditions extracted from the EBSD data. The aspect ratio reported in this figure corresponds to the grain width-to-length ratio, meaning that the closer this ratio is to 1, the more equiaxed the grains are. As can be seen in this figure, the histogram peaks of the as-printed and 2.5H/1S conditions are observed to be closer to the lower aspect ratio values, indicating the

presence of a significant number of columnar grains even after the 2.5H/1S heat treatment. This result suggests that the 2.5H/1S treatment is still insufficient to significantly change the as-printed grain structure, which, once again, is consistent with the microstructure analysis (see Figure 5-7c and d).

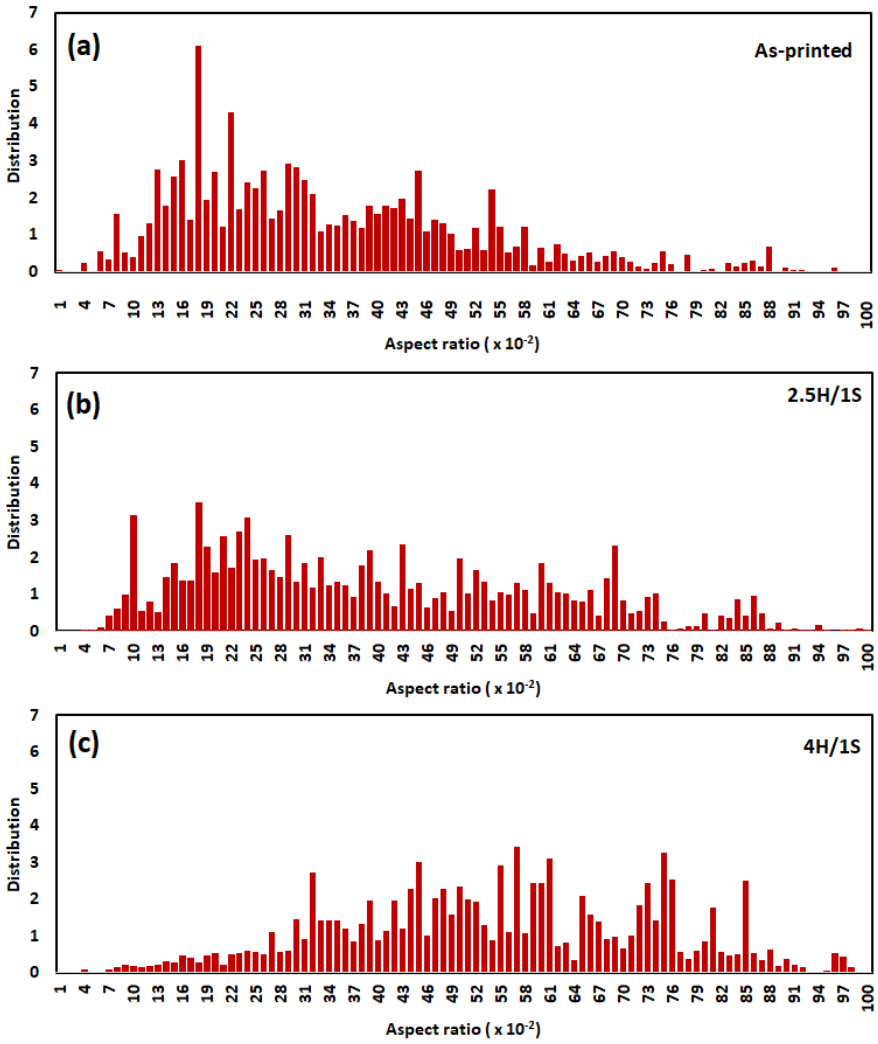

Figure 5-10: Evolution of the grains' aspect ratio with the heat treatment conditions: (a) as-printed; (b) 2.5H/1S; (c) 4H/1S

After the 4H/1S treatment, fully recrystallized equiaxed grains with annealing twins are observed, and become the dominant grain morphology as shown in Figure 5-9g. This state of complete recrystallization is characterized by a relatively weak texture, with an MUD of 1.97

along the (100) plane (Figure 5-9i) and an orientation of the measured grain map that is less aligned with (100) plane, as compared to the 2.5H/1S and as-printed conditions. In addition, a significant increase in the aspect ratio of the grain structure corresponding to the 4H/1S conditions (Figure 5-10c) is observed, as indicated by the peak shift towards the higher aspect ratio values, thus suggesting the nucleation of new equiaxed grains via the complete recrystallization process, which is also consistent with the microstructure results (Figure 5-7i and j).

5.3.3.3 Misorientation angle evolution

The formation of a sub-grain misorientation network during the LPBF solidification process and its evolution under different post-heat treatments strongly affect the mechanical properties of IN718. In this context, Figure 5-11 shows the evolution of the high- and low-angle grain boundaries (HAGBs and LAGBs) of LPBF IN718 alloy under the as-printed and heat-treated conditions, respectively indicated by the black and red full lines. According to the study by Li *et al.* [92], the misorientation angles (MAs) between 2° and 15° are identified as LAGBs, whereas angles greater than 15° are defined as HAGBs.

As can be seen in Figure 5-11a, the microstructure of the as-printed condition contains columnar grains with a relatively high density of LAGBs having a number fraction (NF) of 40.4%. Such a high NF of LAGBs is consistent with the microstructure of the as-printed conditions, in which the sub-grains are composed of columnar dendrites (Figure 5-7a and b), which formed during the solidification process, and are divided by the LAGBs. After the 2.5H/1S condition, the density of the LAGBs decreases slightly to 37.8%, which is also consistent with the microstructure results, since most of the substructure features (columnar dendrites) disappear in the micrographs shown in Figure 5-7c and d. Furthermore, the

transformation of some columnar grains to equiaxed grains (incomplete recrystallization process) also contributes to such a slight increase in HAGBs, from 59.6 to 62.1%, at the expense of LAGBs, as can be seen in Figure 5-11d.

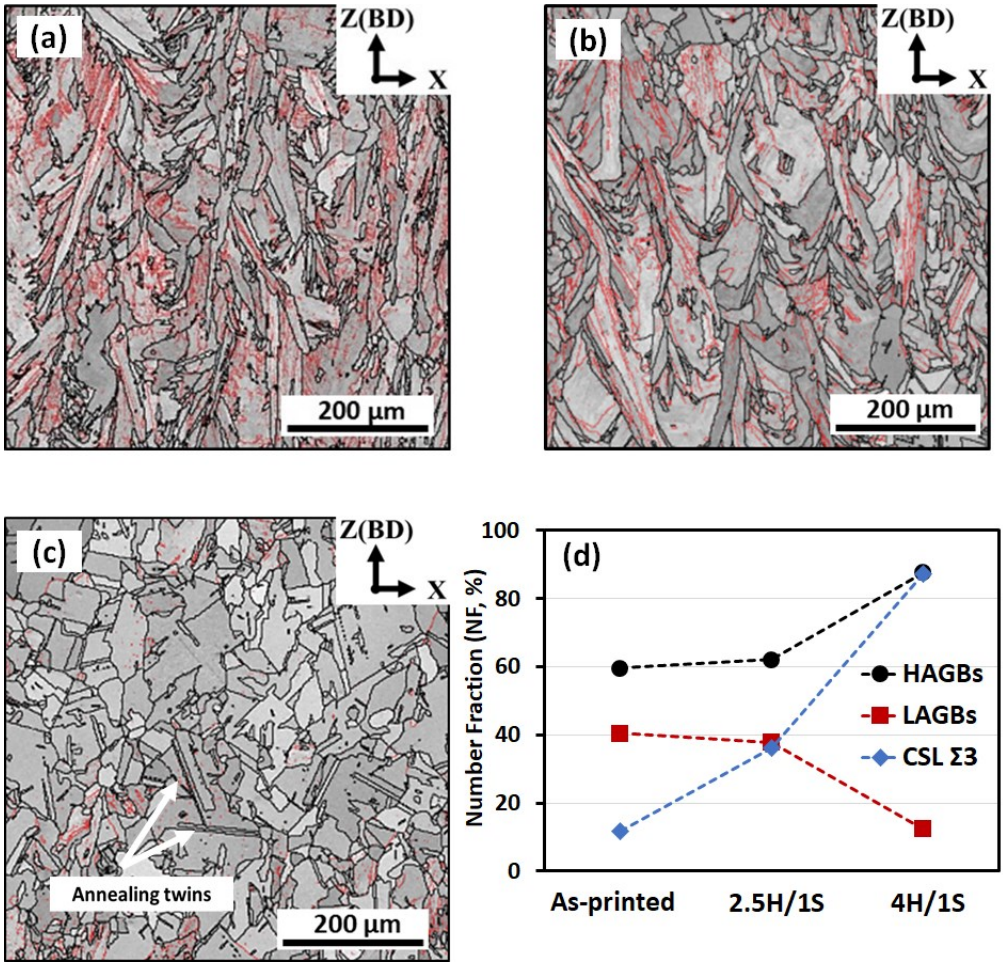

Figure 5-11: Evolution of the misorientation distribution of LAGBs (2°<θ<15°) and HAGBs (θ>15°) under different conditions: (a) as-printed, (b) 2.5H/1S, (c) 4H/1S, and (d) the evolution of the number fraction of LAGBs, HAGBs and coincidence site lattice (CSL Σ3) grain boundaries under the aforementioned conditions. The LAGBs and HAGBs are indicated by the red and black full lines, respectively, in (a to c).

After the 4H/1S treatment, a significant decrease in LAGBs, from 37.8 to 12.4%, is observed, to the benefit of HAGBs, which increase from 62.1 to 87.7%, as shown in Figure 5-11c and d. This is attributable to a complete elimination of sub-grain features: full

recrystallization is achieved after the 4H/1S treatment, since there is a high fraction of annealing twins (MAs ≈ 60°).

Coincidence site lattice (CSL) boundaries are characterized by the specific misorientation values and the reciprocal density of coinciding sites defined as Σ. CSL is widely used to identify twin boundaries and to analyze the grain boundary character distribution. Primary twins, Σ3, are characterized by 60° misorientation around the (111) plane, and twins can be formed during either heat treatments or recrystallization. For further tracking of the annealing twins after heat treatments, the NF evolution of the coincidence site lattice (CSL Σ3) grain boundaries in the as-printed and heat-treated conditions was investigated, as shown in Figure 5-11d. It should be noted in this figure that, as compared to the as-printed and 2.5H/1S conditions, the 4H/1S treatment shows a relatively higher fraction (87.1%) of the CSL Σ3 grain boundaries, thanks to the presence of a large number of annealing twins. These new annealing twin boundaries may form due to the interaction of pre-existing Σ3 boundaries during the grain boundary migration or growth accidents at the migration grain boundaries [118].

It is also important to note that the NF of the annealing twins, indicated by CSL Σ3, exhibits the same trend as HAGBs in Figure 5-11d. Such a high fraction of HAGBs and annealing twin boundaries (Σ3) in the interior of the grains indicate that the 4H/1S treatment clearly provides a sufficient activation energy for the grain boundary migration, which results in the material grain boundaries being engineered via the promotion of a near-complete recrystallization process and introduction of annealing twins. The twinned structure in the materials is regarded as one of the grain boundary engineering (GBE) techniques that can significantly improve the mechanical properties of metallic alloys [78,92]. Therefore, improved mechanical properties are expected to be obtained after the application of this heat treatment.

Generally, the Kernel Average Misorientation (KAM) value calculated from the EBSD data can qualitatively reflect the degree of microscopic plastic strain in samples, as indicated by changes in colors, which is nearly associated with the dislocation density, and is strongly linked to the material mechanical properties [78]. Figure 5-12 shows the evolution of the average KAM value in the as-printed 2.5H/1S and 4H/1S heat-treated conditions with misorientation angle values ranging from 0 to 5°. The blue to red colors in the KAM maps represent the lowest to highest kernel misorientation angles, respectively, as indicated by the color bar below Figure 5-12d. As seen in Figure 5-12a, a large local misorientation (0.85°) in the as-printed conditions is observed, indicating the presence of large local plastic strains and high dislocation densities. Such large local plastic stains in the as-printed condition are related to the presence of high residual stresses resulting from high thermal stresses generated during the LPBF printing process. These residual stresses provide the driving force for the static recrystallization process when adequate post-process heat treatments are applied.

After the 2.5H/1S treatment conditions, a slight decrease in the KAM values is observed (0.75°) (see Figure 5-12b), indicating that the homogenization treatment for 2.5h is insufficient to completely release the stored distortion energy, and that high plastic strains are still present. When the homogenization time increases to 4h (4H/1S condition), a significant decrease in the KAM values is observed (0.5°) (see Figure 5-12c), indicating that more of the stored energy has been released via the annihilation of dislocation tangles. Considering the equiaxed grain morphology (see Figure 5-9g), along with the low KAM values of the 4H/1S conditions, it can be concluded that the 4H/1S treatment is an adequate post-process heat treatment for LPBF IN718 alloy, since it triggers a complete recrystallization process, accompanied by a significant relief of processing-induced residual stresses.

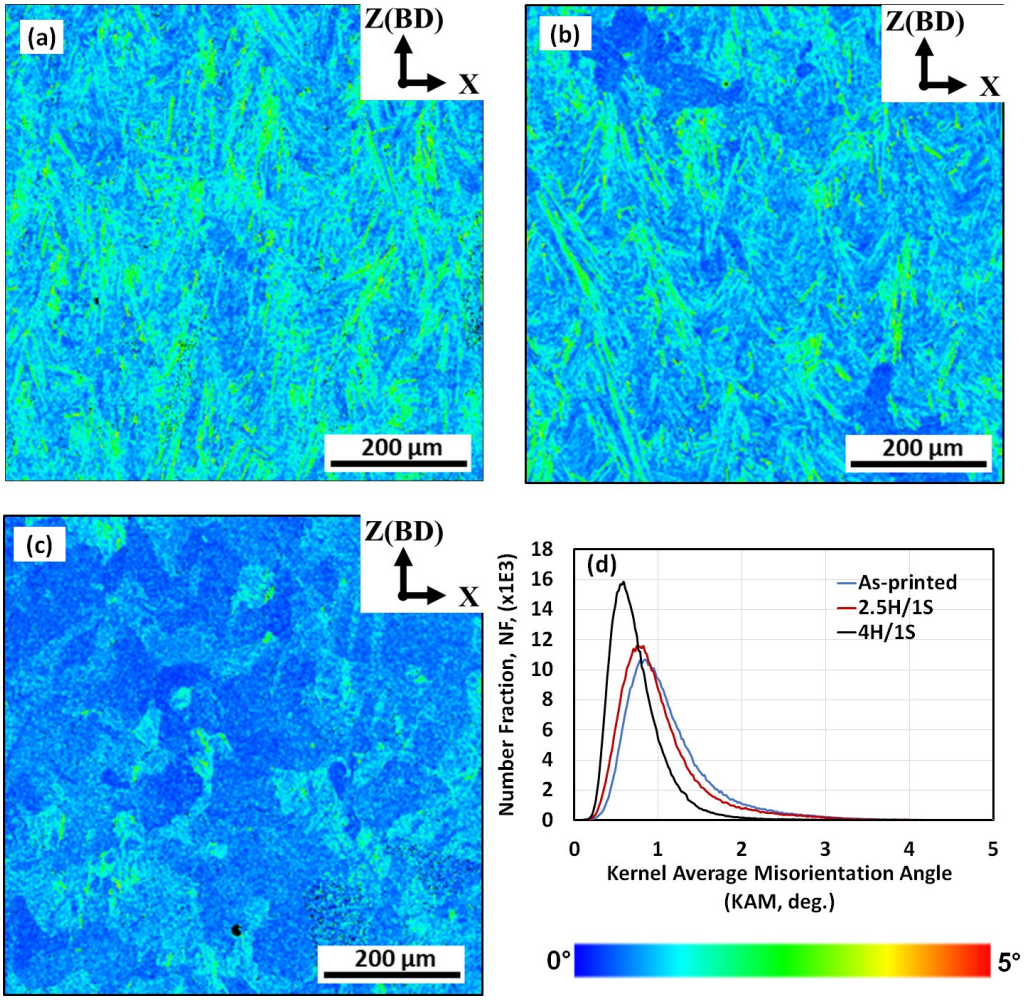

Figure 5-12: Evolution of the kernel average misorientation angles (KAM) of the LPBF IN718 under (a) as-printed, (b) 2.5H/1S, and (c) 4H/1S conditions and (d) the number fraction of KAM under as-printed and aforementioned heat treatment conditions

5.3.4 Mechanical properties

5.3.4.1 Room temperature tensile properties

Figure 5-13 shows the RT tensile properties of LPBF IN718 alloy in the as-printed and heat-treated conditions. Furthermore, the RT tensile properties of the heat-treated (AMS5662) wrought IN718 reported in [62] are included in this figure for comparison. Detailed average RT mechanical properties values are listed in Table 5-6. It can be seen that the as-printed samples exhibit the lowest tensile strength (978 MPa), but the highest elongation to failure

(29%), as compared to the heat-treated conditions. This is attributable to the ease of dislocation glide and multiplication during the tensile deformation in the absence of the strengthening phases (γ′ and γ″), resulting in an inferior strength and enhanced ductility. After the 2.5H/1S heat treatment, the TS significantly increases to 1366 MPa, whereas the ductility significantly decreases to 16%. This is due to the precipitation of γ′ and γ″ phases, which play a crucial role in strengthening the IN718 alloy by interacting with the dislocation movement during deformation. After 4H/1S heat treatment of the LPBF IN718 alloy, the TS is comparable to that of the 2.5H/1S condition (1367 MPa), while the elongation to failure increases (20.3%), as shown in Figure 5-13. As well, the tensile properties (TS, YS and El) after the both heat-treated conditions exceed those of the wrought alloy [62]. Furthermore, the 4H/1S treatment leads to a significant improvement in plasticity, and provides tensile and yield strengths comparable to those of the conventionally heat-treated LPBF IN718, as shown in Table 5-6 (heat treatment conditions correspond to the AMS standards [26,62]).

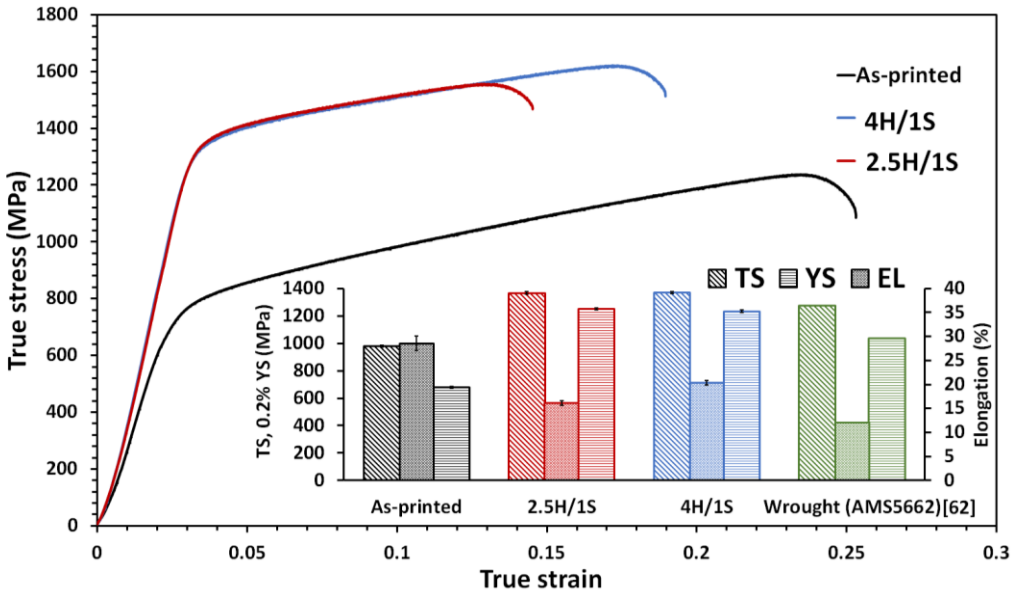

Figure 5-13: Room temperature tensile properties of the LPBF IN718 in as-printed and heat-treated conditions. For comparison, the RT tensile properties of wrought IN718 (AMS 5662) [62] are included

Table 5-6: RT tensile strength (TS), yield strength (YS) and elongation to failure (El) values in the as-printed and heat-treated conditions. The RT tensile properties reported in [26,62,63] are included for comparison.

Material condition	TS (MPa)	YS (MPa)	El (%)	Reference
As-printed	978 ± 6	678 ± 7	29 ± 1.5	↑
2.5H/1S	1366 ± 8	1250 ± 8	16±0.5	This work
4H/1S	1367 ± 7	1234 ± 9	20 ± 0.5	↓
Wrought AMS 5662	1280	1030	12	[62]
Wrought AMS 5662	1276	1034	12.1	[26]
Cast AMS 5383	862	758	5	[26]
LPBF IN718 AMS 5662	1370	1084	10.1	[62]
LPBF IN718 AMS 5662	1380	1240	15.5	[63]
LPBF IN718 ASM 5383	1371	1046	12.3	[26,62]
LPBF IN718 ASM 5383	1350	1238	13	[63]

Although the 4H/1S treatment leads to smaller γ-matrix lattice parameters (Figure 5-6) and lower KAM values (Figure 5-12c and d) than those after the 2.5H/1S treatment, thus indicating the depletion of the constituents that promote precipitation hardening in the γ-matrix and a decrease in dislocation density, the mechanical strengths are nearly similar, while the plasticity is improved (after 4H/1S treatment). This suggests that the presence of another strengthening mechanism, rather than γ′ and γ″, contributes to improvements of both the strength and ductility at RT. It has been reported that the material strengthening following precipitation of γ″ results in a deterioration of the material ductility, also known as the strength-plasticity trade-off phenomenon [92]. To obtain such a good balance between the strength and ductility, a GBE method, such as one introducing annealing twins, can be used, as proposed by Watanabe *et al*. [119]. In this context, as mentioned earlier, in the 4H/1S treatment, the homogenization treatment at 1080°C for 4h significantly affects the grain structure and provides additional activation energy for the grain boundary migration. Thus, a high fraction of annealing twins within the recrystallized grains after the 4H/1S treatment is observed, as evidenced by a high

number fraction of CSL and HAGBs (Figure 5-11d). It has been reported that the presence of a high fraction of annealing twins can effectively block and hinder the dislocation movements during deformation, resulting in material strength improvements [78,92]. Furthermore, an improved material plasticity can be obtained following the sliding of HAGBs [92]. Thus, it is reasonable to expect both a high strength and ductility after the application of the 4H/1S treatment conditions. Furthermore, a relatively lower dislocation density in the recrystallized 4H/1S-treated conditions (Figure 5-12c) also contributes to a higher ductility, as compared to that of the 2.5H/1S-treated conditions. Therefore, it can be concluded that the 4H/1S heat-treated LPBF IN718 alloy manifests an optimized level of RT mechanical properties, i.e., the highest strength and elongation to failure.

5.3.4.2 High-temperature tensile testing (650°C)

Figure 5-14 shows the high-temperature (650°C) tensile properties of LPBF IN718 alloy in the as-printed and heat-treated conditions. For comparison, the tensile properties of the wrought IN718 (AMS5662) at 650°C obtained in [62] are included in this figure. As can be seen in Figure 5-14a, the tensile strength in the as-printed condition is lower than that in the heat-treated conditions, but its elongation to failure is the highest. This is consistent with the RT tensile properties, and is once again attributed to the absence of γ' and γ'' phases in the as-printed material. After both heat treatments (2.5H/1S and 4H/1S), the TS and YS increased significantly, exceeding those of the heat-treated (AMS5662) wrought IN718, whereas their elongations to failure decrease significantly, and become slightly lower than that of the wrought IN718, and are about ¼ the elongation of the as-printed samples. However, the comparison with the tensile properties of the standard heat-treated LPBF IN718 reported in [63] reveals that the 2.5H/1S and 4H/1S treatments lead to significant improvements in both the strength and

elongation to failure at 650°C, as shown in Table 5-7. Generally, this is attributed to the precipitation of dispersed strengthening phases (γ′ and γ″) and inter-granular δ-phase, which restrict the motion of dislocations and grain boundaries.

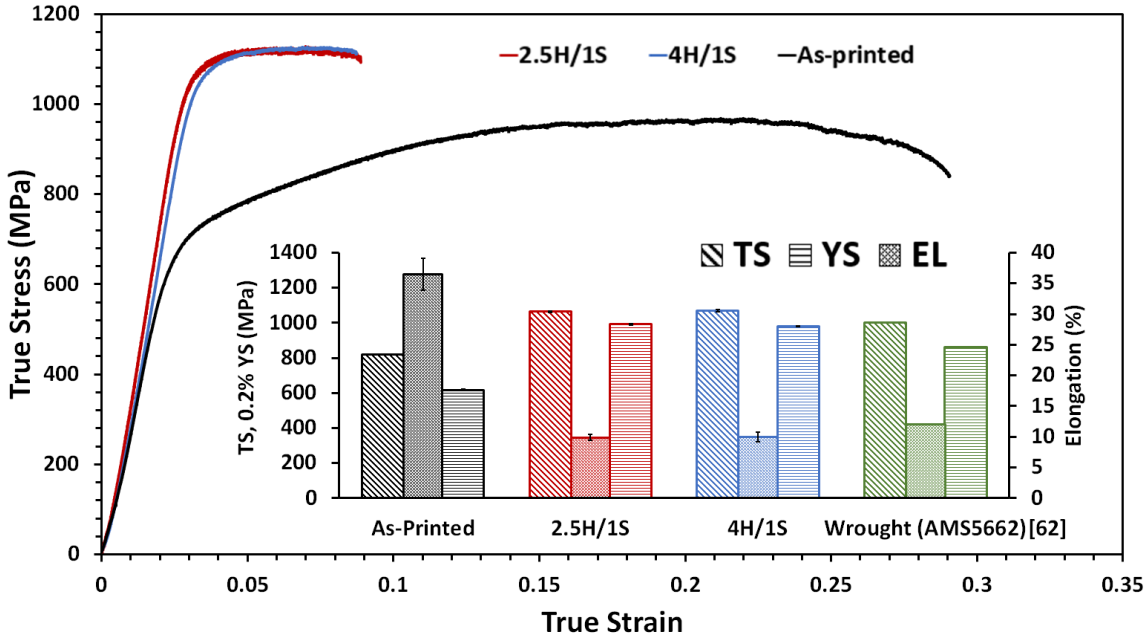

Figure 5-14: High-temperature (650°C) tensile properties of LPBF IN718 in as-printed and heat-treated conditions. For comparison, the high temperature (650°C) tensile properties of wrought IN718 (AMS 5662) [62] are included

Table 5-7. Elevated-temperature (650°C) tensile strength (TS), yield strength (YS) and elongation to failure (El) values of the as-printed and heat-treated conditions. The tensile properties at 650°C reported in [62,63] are included for comparison.

Material condition	TS (MPa)	YS (MPa)	El (%)	Reference
As-printed	820 ± 2	617 ± 4	36 ± 3	↑
2.5H/1S	1063 ± 6	991 ± 5	10 ± 0.4	This work
4H/1S	1069 ± 8	979 ± 3	10 ± 0.8	↓
Wrought AMS 5662	1000	862	12	[62]
LPBF IN718 AMS 5662	1025	915	5.5	[63]
LPBF IN718 ASM 5383	1020	950	3.5	[63]

Moreover, notwithstanding the different strengthening mechanisms during both the 2.5H/1S and 4H/1S treatments, they exhibited a similar strength and ductility at 650°C. Reiterating the KAM and sub-grain maps, the high strength of the 2.5H/1S-treated samples at high temperatures can be related to a combined effect of the incomplete annihilation of the as-printed lattice imperfections (Figure 5-12b), i.e., the sub-grain structure (Figure 5-11b and d), where a high number fraction of LAGBs is accompanied by the precipitation of γ′, γ″ and δ phases. Furthermore, the orientation of the elongated grains along the tensile loading direction also contributes to the ductility of the 2.5H/1S-treated samples. However, after the 4H/1S treatment, the material strengthening is due to a high percentage of annealing twins, as indicated by a relatively high number fraction of the CSL Σ3 boundaries and HAGBs (Figure 5-11d), along with the precipitation of γ′, γ″ and δ phases. Therefore, despite having quite different microstructures and underlying strengthening mechanisms, the 2.5H/1S- and 4H/1S-treated samples ended up having very similar high-temperature mechanical properties.

Compared with the RT tensile properties, the tensile strength of the as-printed samples at 650°C decreases moderately by 16%, while the elongation to failure increases significantly by 24% (see Figure 5-15), which can be explained by a decrease in the grain boundary strength due to a decrease in the grain boundary adhesion between the adjacent grains at elevated temperature [62]. Moreover, the improvement in the material plasticity at elevated temperatures can be explained by the thermal activation of the atoms and vacancies that further promote the plastic deformation via the dislocation slip [62]. Unlike the as-printed samples, the ductility of both the 2.5H/1S and 4H/1S-treated samples was reduced by 37.5 and 50%, respectively, when tested at 650°C, as opposed to RT (see Figure 5-15). This could be explained by the well-known high temperature ductility loss phenomenon in nickel-based superalloys [88]. It is worth noting

that at 650°C, the 4H/1S-treated samples exhibit a more significant drop in ductility than the 2.5H/1S-treated samples due to a relatively more intensive precipitation of coarse MC carbides.

Therefore, in situations where the product will be used in RT applications, 4H/1S treatment is recommended, while the 2.5H/1S treatment is recommended for high-temperature applications, but only if having isotropic properties is not mandatory. Having directional solidified material with anisotropic properties has some beneficial effects in some aerospace applications, including providing better creep and thermal fatigue resistance. If an IN718 component is subjected to high mechanical stresses both at room and elevated temperatures (650°C), 4H/1S treatment is obviously a better choice, especially if the application requires isotropic materials with homogenous mechanical properties. For some other applications in which IN718 is to be processed by LPBF followed by forging, we recommend the forging process after printing, followed by either the 2.5H/1S or 4H/1S heat treatment.

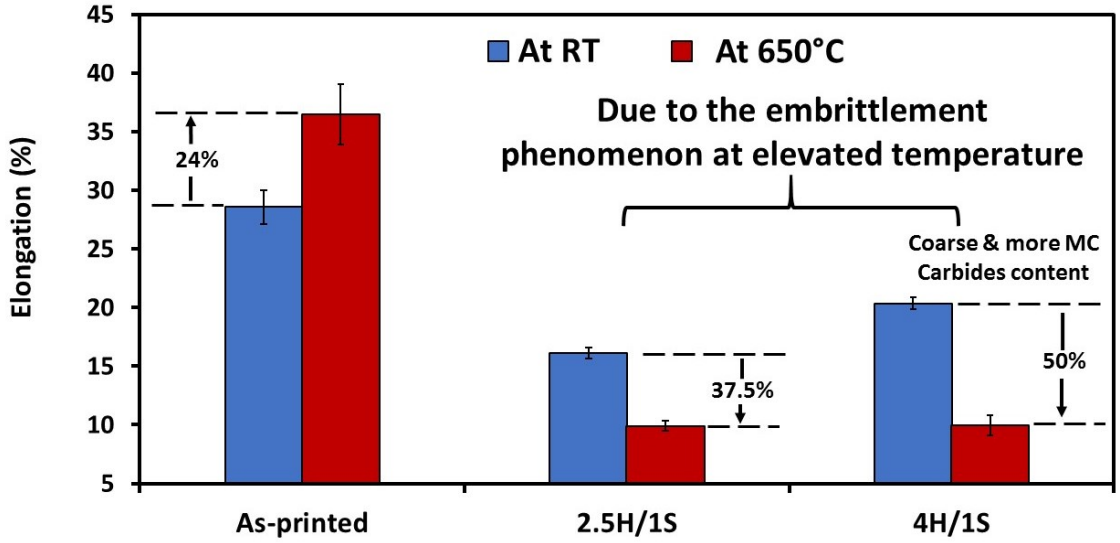

Figure 5-15: Comparison of the RT and 650°C elongations to failure of the as-printed and heat-treated LPBF IN718 samples illustrating the elevated-temperatures ductility loss

5.4 Conclusion

The need to compromise the high-mechanical performance of 3D printed Inconel 718 in order to obtain non-distinctive crystallographic texture is one of the main challenges facing the laser powder bed fusion process specially for applications requiring isotropic properties. DOE was employed in the present study to optimize the soaking times of homogenization and solution treatments that yield high and isotropic mechanical properties of LPBF IN718 components. The main findings of the current study can be summarized as follows:

- The as-printed microstructure shows an elongated grain morphology with a continuous chain of segregates and Laves phase in the inter-dendritic zones and along the grain boundaries. In addition, a strong texture along the (100) plane is observed.
- After heat treatments, there is a significant back diffusion of the segregated elements and a dissolution of Laves phase. However, a homogenization treatment for more than 2.5h results in the depletion of the elements (Ti and Nb) necessary for the precipitation of γ′ and γ″ phases from the γ-matrix, as a drop in the γ-matrix lattice parameter after 3, 3.5 and 4h-long treatment supports this hypothesis.
- Noticeable changes in the preferred crystallographic (100) texture are observed after a 2.5h homogenization treatment. However, a nearly complete recrystallization with a significantly weakened texture along the (100) direction is obtained after a 4h homogenization treatment.
- At room temperature, the 2.5H/1S and 4H/1S treatments lead to a significant improvement in the tensile properties (TS, YS and El) of LPBF IN718 alloy, as compared to those of the conventionally heat-treated LPBF IN718 (AMS

standards) and the wrought (AMS5662) alloy. Moreover, a superior balance between the material strength and ductility is obtained after the 4H/1S treatment due to the presence of a high fraction of annealing twins.

- Both the 2.5H/1S and 4H/1S-treated samples show comparable strengths at RT and at 650°C. However, the strengthening mechanisms after both treatments are different: a precipitation hardening combined with the contribution of a primary dislocation network are the strengthening mechanisms during the 2.5H/1S treatment, whereas during the 4H/1S treatment, precipitation hardening becomes the main strengthening mechanism.
- At 650°C, the 2.5H/1S- and 4H/1S-treated samples exhibit higher tensile and yield strengths than, and a comparable ductility to those of the (AMS5662) wrought IN718.
- It is concluded that the 4H/1S treatment offers optimized mechanical properties at RT and at 650°C and a desirable random crystallographic texture.

Chapter 6 : Effect of Long-Term In-Service Thermal Exposure on the Microstructure and Elevated-Temperature Mechanical Properties of Additively Manufactured Inconel 718 Superalloy

Eslam M. Fayed[1], Vladimir Brailovski[2], Mohammad Jahazi[2], and Mamoun Medraj[1,*]

[1]Department of Mechanical, Industrial and Aerospace Engineering, Concordia University, 1515 Sainte-Catherine Street West, Montreal, QC H3G 2W1, Canada
[2]Department of Mechanical Engineering, École de technologie supérieure, 1100 Notre-Dame Street West, Montreal, QC H3C 1K3, Canada
*corresponding: mmedraj@encs.concordia.ca; Tel.: +1-514-848-2424

This paper is to be submitted

Abstract

In the present study, the influence of long-term in-service thermal exposure on the microstructure and elevated-temperature (650°C) mechanical properties of the additively manufactured Inconel 718 (IN718) fabricated by the laser powder bed fusion (LPBF) process has been investigated. To this end, the as-printed and heat-treated samples were subjected to thermal cycling conditions similar to what is encountered in the aircraft turbine engines for different periods up to 3000h. Before thermal cycling, the IN718 parts were heat-treated using two conditions including different homogenization soaking times, 2.5h and 4h, at 1080°C followed by solution treatment at 980°C for 1h and standard aging treatment which were designated as 2.5H/1S and 4H/1S, respectively. The results show that, after thermal exposure, both 2.5H/1S and 4H/1S treated conditions exhibited initially a slight increase in their tensile strength (TS) from 1063 ± 6 and 1067 ± 8 to reaches their maximum values of 1096 ± 5 and 1089 ± 1 after 500 and 1000h, respectively. Further thermal exposure time resulted in a progressive deterioration in TS to reach their lowest values of 1006 ± 8 and 1034 ± 5, respectively, after 3000h. The microstructural analysis and X-ray diffraction (XRD) results of these conditions revealed that such initial strength improvement is mainly due to the greater

precipitation of γ″ and inter-granular δ-phases after thermal exposure, whereas the prolonged thermal exposure time resulted in undesired phase transformation of the metastable γ″ to intra-granular δ-phase which adversely affected the mechanical properties at 650°C. However, comparing the tensile results of both treated conditions revealed that the 4H/1S treatment effectively delayed the deteriorations of the material strength until after 2000h in relation to the 2.5H/1S condition for which the strength deterioration occurred after 1000h due to the slower phase transformation of γ″ into δ-phase in the former condition. Considering the thermal stability over the in-service exposure, it was found that the 4H/1S condition has higher strength stability than the 2.5H/1S condition as its TS and yield strength (YS) decreased after thermal exposure for 3000h by only 3.3 and 1.3% of the initial state, respectively, while in the 2.5H/1S condition, the TS and YS decreased by 5.3 and 3.8%.

Keywords: Long-term thermal cycling, high-temperature mechanical properties; additive manufacturing; laser powder bed fusion; nickel-based superalloy; IN718; microstructure

6.1 Introduction

Inconel 718 (IN718), a nickel-based superalloy, has been widely used for the manufacturing of turbine engine components such as rotation turbine disc, turbine blades and turbine seal rings because of its capability to retain superior mechanical properties even at elevated temperatures up to 650°C and harsh corrosive environment for prolonged periods [120]. Such high capabilities at elevated temperatures are attained from the size and distribution of its fine age-hardening precipitates such as γ′ and γ″ in the matrix. These strengthening phases have an ordered face-centered cubic $L1_2$ and an ordered body-centered tetragonal $D0_{22}$, respectively, and are coherent with the γ-matrix [121,122]. In addition, some other phases such as δ-phases may have beneficial or harmful impacts on the material properties depending on its size,

quantity and precipitation sites. Indeed, during the long exposure of IN718 components to such harsh in-service conditions, changes in size, morphology and structure of these phases are expected to occur that consequently leads to changing its mechanical behavior. For instance, a deterioration in the creep and tensile properties of nickel-based superalloy has been observed after long exposure to in-service conditions due to the precipitation of intermetallic phases and/or growth of the strengthening phases (γ′ and/or γ″) [120,123–126]. Furthermore, a progressive transformation of the metastable Ni_3Nb-γ″ phase into the thermodynamically stable Ni_3Nb-δ phase is also widely reported during the long-term in-service exposure [127]. Such microstructural instability is a crucial factor that impacts the reliability of using IN718 components at high temperatures for a long time.

Considering the microstructural evolution during the long-term thermal exposure, the standard heat treatments (SHT) were developed to improve the stability of the microstructure and mechanical properties of the conventionally manufactured (cast and wrought) IN718 components to withstand the harsh in-service conditions for long periods [11,26]. However, the performance development of the advanced turbine engine generations, where higher operating temperature is required, adversely affected the microstructural stability of cast and/or wrought IN718 components over the in-service thermal exposure which in turn leads to premature replacement of these components [124]. From an industrial perspective, improving the material capabilities of IN718 components are much less risky and costly than developing new superalloys to cope with the fast development of the turbine engines [124]. Therefore, changes in the design of the IN718 components were introduced to improve their capabilities. The turbine blades are an excellent example for such a proposed new design, as more complicated internal cooling channels were designed and included in turbine blades to maximize their ability

to withstand such changes in the operating temperatures. However, conventional manufacturing constraints do not provide freedom for such a broad design range. In addition, a high cost and long processing time are required to manufacture these complex geometrical components using traditional methods.

These challenges pushed the industry towards shifting the focus from the conventional manufacturing methods to additive manufacturing (AM) as an alternative method to manufacture IN718 parts, especially in the aerospace and energy industries. IN718 superalloy emerged as a suitable candidate to be manufactured using AM techniques and, in particular, the laser powder bed fusion (LPBF) process [128]. However, the absence of standard heat treatment conditions of LPBF IN718 and its microstructure evolution during the in-service conditions prevented this technique from being adopted in the industry. Several studies have been conducted to investigate the effect of the post-heat treatment on the microstructure and mechanical behavior of the LPBF IN718 aiming to develop the optimum heat treatment conditions which can satisfy the design requirements [13,26,45,46,54,58,76,78,89,92,129]. Nevertheless, investigating and assessing the thermal stability of these treatment conditions during the long-term in-service exposure have not been found in the literature which an important step to evaluate the reliability of IN718 components fabricated by LPBF.

In our previous work [130], a multi-objective optimization approach was employed to obtain the optimum heat treatment conditions for the LPBF IN718 components. As a consequence, two heat treatments were concluded to be the optimum thermal post-processing for the LPBF IN718 components due to their ability to homogenize the as-printed microstructure and improve the mechanical properties at both room and elevated temperature. However, the evaluation of the material properties and microstructural stability after exposure

to the in-service condition is still required to provide more confidence and reliability about the obtained optimum heat treatments. Therefore, in the present study, thermal cycling similar to what is encountered in the aircraft turbine engines is applied to the IN718 alloy in the as-printed and heat-treated conditions for long period (up to 3000h) to investigate the impact of in-service exposure on the microstructure and elevated-temperature mechanical properties.

6.2 Experimental procedure

6.2.1 Material and manufacturing procedure

A gas atomized IN718 powder with a particle size distribution of D10 (18.2 μm), D50 (32.4 μm) and D90 (54.2 μm) and chemical composition (in wt.%) of Ni (49.19), Cr (19.04), Nb (4.92), Mo (2.70), Al (0.33), Ti (1.08) and Fe (balance) was used to manufacture the IN718 samples using an EOS M280 laser powder bed fusion (LPBF) system. The EOS Original IN718_Surface 1.0 Parameter Set (285 W laser with 100 μm beam diameter, 1000 mm/s scanning speed, 110 μm hatching space, and 40 μm layer thickness, and an argon atmosphere) was used to manufacture the IN718 samples. The dimensions of the IN718 samples for the microstructural analysis were 22 × 17 × 10 mm^3, whereas for the tensile testing were 19 × 4 × 83 mm^3. After the printing process, the IN718 samples were removed from the building platform using a wire electric discharge machining (WEDM) without stress relief treatment to preserve the as-printed condition.

6.2.2 Heat treatment and thermal cycling conditions

To evaluate the behavior of the LPBF IN718 parts during the in-service working condition, IN718 samples were initially heat-treated using the treatment conditions listed in Table 6-1. The entire cycle of the applied heat treatments is shown in Figure 6-1a. These treatment conditions are selected to be examined under the in-service conditions based on the multi-

optimization approach conducted in our previous study [130], as these conditions significantly enhanced the microstructure and mechanical properties of the LPBF IN718. All heat treatments were performed inside an electric-resistive furnace. The samples' temperature during heat treatment was monitored using a K-type thermocouple placed immediately at its vicinity where the temperature variation was controlled within ±5°C. Then, the as-printed and heat-treated conditions were subjected to a thermal cycling condition similar to the thermal cycle of the aircraft engine [131] to simulate the in-service environment of the engine components. Figure 6-1b shows the actual thermal cycling condition used in the present study. As can be seen in this figure, the IN718 samples were rapidly heated to the operating temperature of 650°C with a heating rate of ≈ 105°C/min for temperatures below 550°C, and ≈ 23°C/min for temperatures between 550 and 650°C. Then, the samples were held at 650°C for a dwell time of 45 min followed by rapid cooling with a rate of ≈ 245°C/min down to 160°C and ≈ 20°C/min till room temperature. This cycle was frequently repeated 2641 times for a period of 3000h to cover most of the lifetime of turbine engine components. It is worth mentioning that there was no holding time at room temperature between cycles.

Table 6-1: The details of the conducted heat treatment conditions in the present study

Designation	**Homogenization Heat treatment**	**Solution Heat treatment**	**Aging Heat treatment**
As-printed	None	None	None
2.5H/1S	1080°C for 2.5h/AC	980°C for 1h/AC	720°C/8h/FC at 55°C/h to 620°C + 620°C/8h/AC
4H/1S	1080°C for 4h/AC		

To follow the evolution of the microstructure and elevated-temperature (650°C) mechanical properties during the in-service exposure, the LPBF IN718 samples were examined at different *Times Since New* (TSN), from TSN(0) up to TSN(3000) as listed in Table 6-2. The TSN represents the total time during which the turbine engine components are expected to be

subjected to the in-service conditions [132]. This approach was used by the Republic of Korea Air Force [132] in order to study the effect of the service exposure on the mechanical behavior of the cast IN718 superalloy at elevated temperature. The TSN(0) represents the new samples (without the thermal cycling), while the TSN(4) represents the IN718 samples after 3000h thermal cycling.

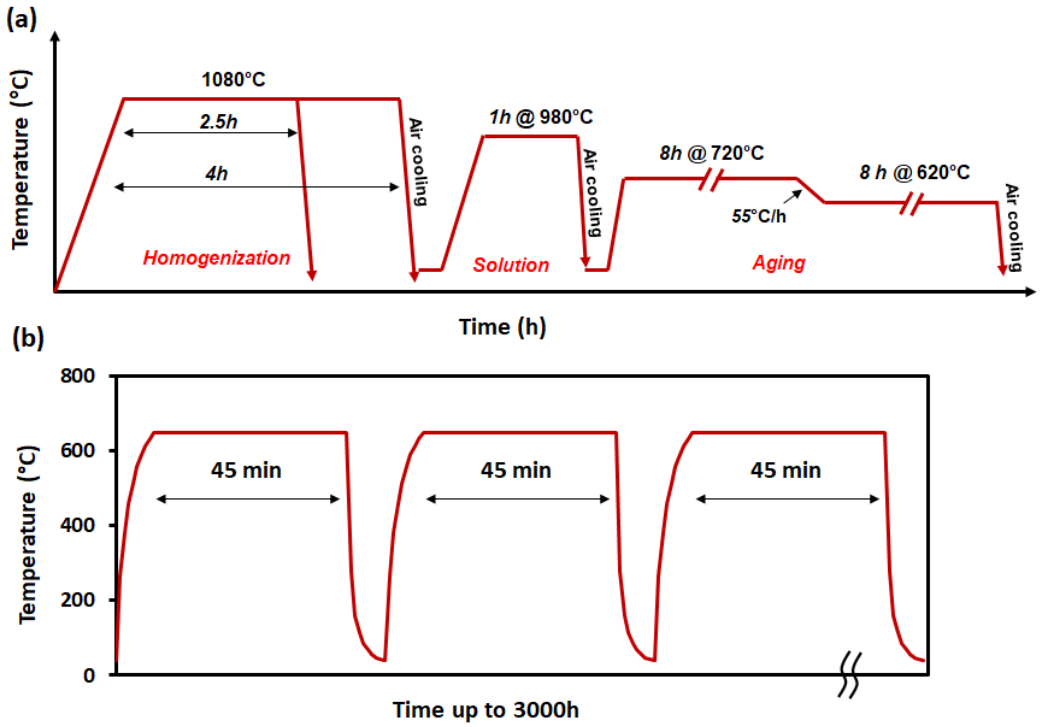

Figure 6-1: (a) Schematic representation of the full regime of the optimum heat treatments of LPBF IN718 applied in the current study; (b) schematic drawing of the thermal cycling process.

Table 6-2: Details of the thermal exposure periods corresponding to the TSN of the as-printed and heat-treated LPFB IN718

TSN	**Thermal exposure period**
TSN (0)	New Components (Before thermal cycling)
TSN (500)	After 500h
TSN (1000)	After 1000h
TSN (2000)	After 2000h
TSN (3000)	After 3000h

Such thermal cycling was performed using a Carbolite thermal cycling rig (TCR) shown in Figure 6-2. As can be seen in this figure, the TCR is equipped with a sample holder fixed on a moving lever arm that allows the processed samples to be rapidly heated to the operating temperature (650°C). To ensure such a high heating rate, the furnace was preheated to 650°C before raising the sample holder to be inside the furnace tube. Furthermore, TCR allows controlling the cooling rate using either natural cooling, by placing the sample holder downside from the furnace tube to be subjected to natural air or fan cooling using the equipped two fans (see Figure 6-2) for fast cooling. In the present study, fan cooling was used to rapidly cool the IN718 to room temperature.

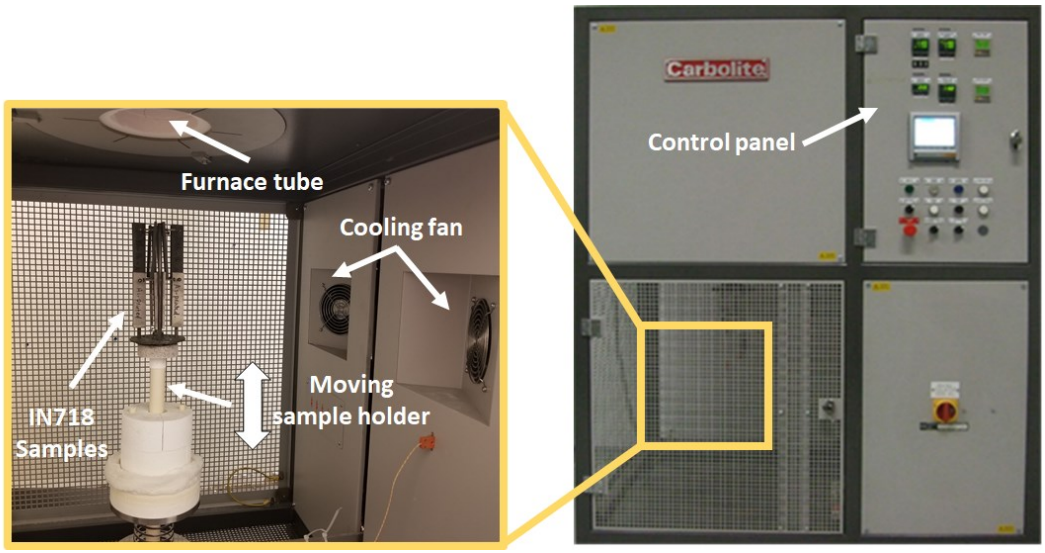

Figure 6-2. The thermal cycling rig used to simulate the operation condition of the aircraft engine.

6.2.3 Tensile testing at 650°C

After thermal cycling, the IN718 samples were machined for mechanical testing using WEDM. The dimensions of the tensile test samples are shown in Figure 6-3. The tensile testing was performed at 650°C and a strain rate of 10^{-3} s^{-1} using an MTS 810 tensile testing system

equipped with infrared radiant heating. Before the tensile loading, the IN718 samples were held at 650°C for 10 min to guarantee the uniform temperature distribution along the gauge length. Three K-type thermocouples were evenly distributed along the gauge length to monitor the temperature uniformity. An argon shielding gas was used during the elevated-temperature tensile testing to minimize the oxidation effect. As mentioned above, for each condition (as-printed, 2.5H/1S and 4H/1S), the tensile properties were evaluated after different thermal cycling periods: 500, 1000, 2000 and 3000h. At each period, two to three samples were tested and the average value was concluded.

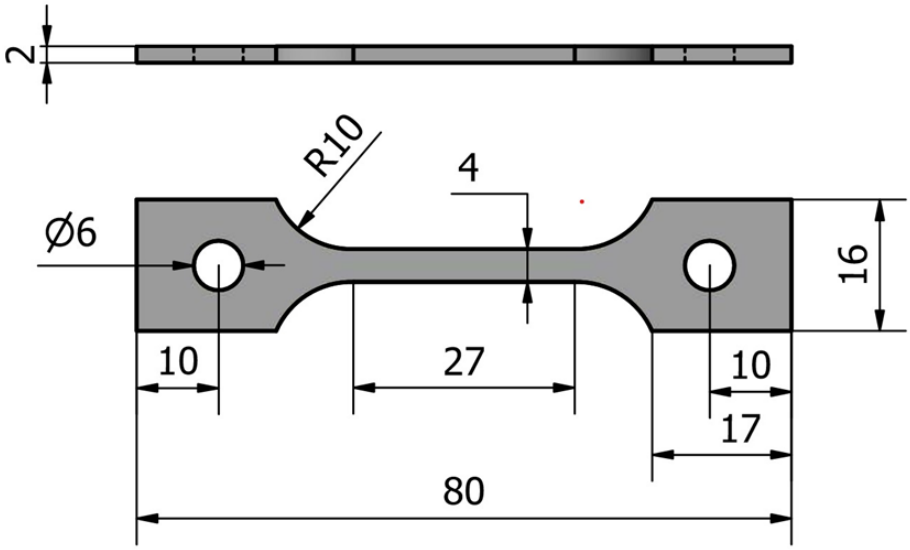

Figure 6-3: The dimensions of the tensile test samples (in mm).

6.2.4 Characterization methods

Characterizations of the microstructure evolution were performed using scanning electron microscopy (SEM) equipped with an energy dispersive spectroscopy (EDS) for elemental analysis. For the SEM analysis, the IN718 samples were ground from 240 up to 1200 grit size using silicon carbide emery paper, and then polished down to 1 μm using an alcohol-based diamond suspension. The polished samples were etched using a solution of Marble's Reagent

(10 grams $CuSo_4$ + 50 ml HCl + 50 ml H_2O). For phase evolution analysis, X-ray diffraction (XRD) was employed for the as-printed and heat-treated conditions after different exposure times 500, 1000, 2000 and 3000h. The scanning parameters were selected to be 0.01 degree 2-theta step size per 1 sec step time to gather high-resolution data and accurately define the diffracted peaks. It is worth mentioning that the scanning plan (xy) of the IN718 samples were fixed for consistent results.

6.3 Results

6.3.1 Effect of the in-service exposure on the elevated-temperature (650°C) mechanical properties

Figure 6-4 shows the impact of the in-service thermal exposure at 650°C for different periods of 500, 1000, 2000 and 3000h on the elevated-temperature (650°C) tensile properties of the as-printed, 4H/1S and 2.5H/1S conditions. The detailed average values of the elevated-temperature tensile properties of each condition at these thermal exposure times are listed in Table 6-3. For the as-printed condition, after the in-service exposure, both tensile (TS) and yield (YS) strengths significantly increased by 30.3 - 40.6 % and 55.1 - 68.1%, respectively, in relation to those of the initial state, depending on the exposure time, whereas the elongation to failure ultimately decreased by 53.6 - 66.1% as shown in Figure 6-4a. For comparison, after 500h, both TS and YS reached their maximum values, 1153 ± 16 and 1036 ± 6 MPa, respectively, and then they monotonically decreased with further increase in the thermal exposure time to reach 1068 ± 7 and 956 ± 11 MPa after 3000h exposure time as shown in Figure 6-4a. Conversely, the elongation to failure significantly decreased to reach its lowest value of 12.3 ± 0.7 % after 500h, and then it gradually increased with the increase of the thermal exposure time to reach 16.5 ± 0.1 % after 3000h.

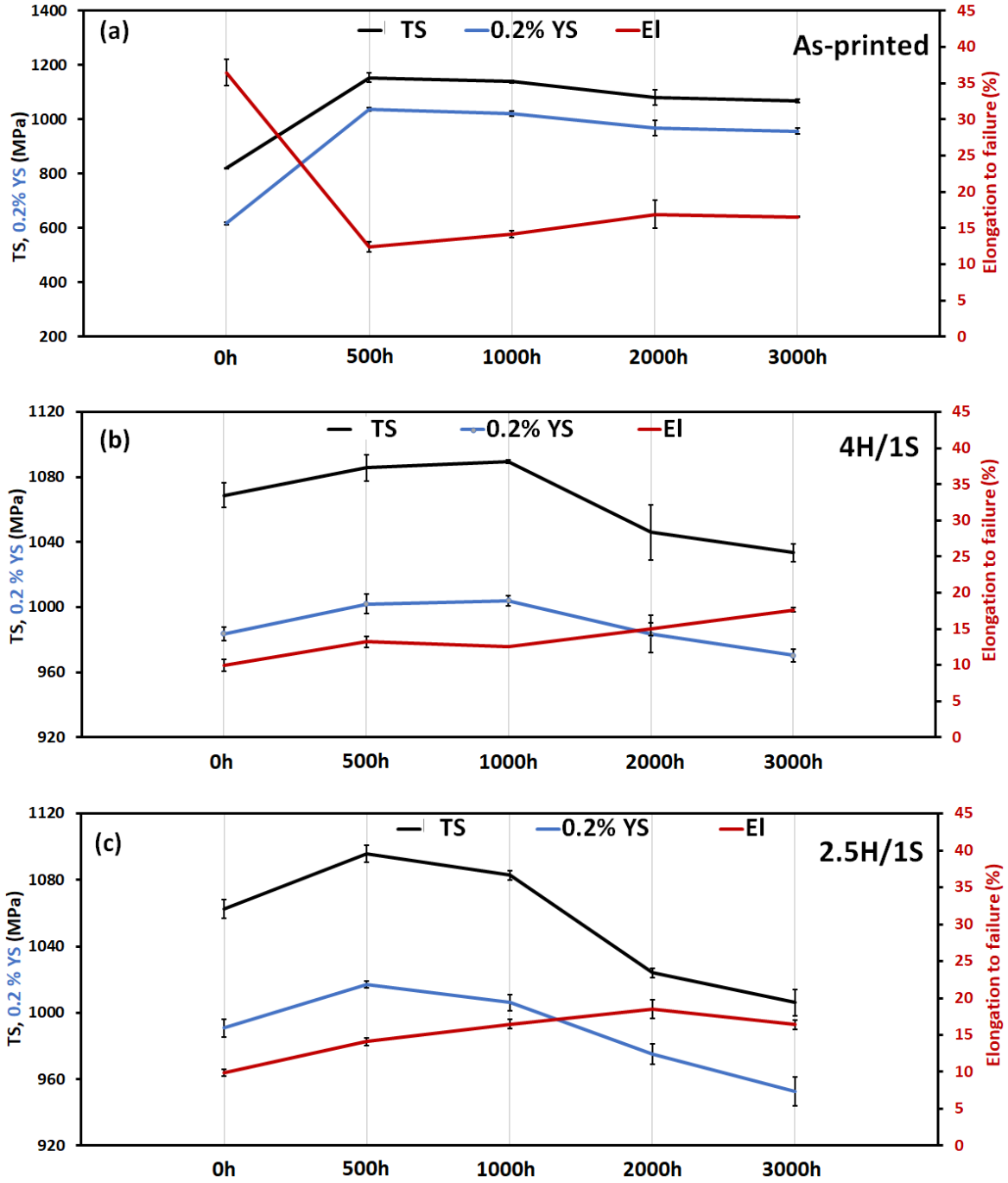

Figure 6-4: Elevated temperature (650°C) tensile properties after in-service exposure for a long period (0 to 3000h) of as-printed and heat-treated LPBF IN718: (a) as-printed, (b) 4H/1S and (c) 2.5H/1S conditions.

Table 6-3: The elevated-temperature (650°C) tensile strength (TS), yield strength (YS) and elongation to failure (El) values of the as-printed and heat-treated conditions after in-service thermal exposure for different periods (0 to 3000h).

Condition	In-service thermal exposure period	Tensile properties at 650°C		
		TS (MPa)	YS (MPa)	El (%)
As-printed	0h	820±1	617±4	36.4±2
	500h	1153±16	1036±6	12.3±0.7
	1000h	1139±4	1021±8	14±0.5
	2000h	1081±27	968±28	16.8±2
	3000h	1068±7	956±11	16.5±0.1
4H/1S	0h	1067±8	984±4	10±0.8
	500h	1086±8	1002±6	13.2±0.7
	1000h	1089±1	1004±3	12.6±0.1
	2000h	1046±17	983±11	15±0.9
	3000h	1034±5	970±4	17.6±0.3
2.5H/1S	0h	1063±6	991±5	10±0.4
	500h	1096±5	1017±2	14±0.5
	1000h	1083±3	1006±5	16.4±0.6
	2000h	1024±3	975±6	18.5±1
	3000h	1006±8	953±9	16.4±0.6

Concerning the heat-treated conditions, the mechanical behavior of both 4H/1S and 2.5H/1S exhibited a different trend compared with that of the as-printed condition. For the 4H/1S condition, after thermal exposure, both TS and YS slightly increased from 1069 ± 7 and 984 ± 4 MPa in the initial state to reach their maximum values of 1089 ± 2 and 1004 ± 3 MPa after an exposure time of 1000h, respectively, as shown in Figure 6-4b. Then, further thermal exposure resulted in a deterioration in both strengths to reach their lowest values of 1034 ± 5 and 970 ± 4 MPa after 3000h. This means that the 4H/1S condition experienced more strengthening during the thermal exposure until 1000h exposure, after which deteriorations in the mechanical propitiates occurred. However, continuous improvement in the material ductility is observed over the whole thermal exposure span up to 3000h to reach 17.6% from 10% in the initial state (see Figure 6-4b).

Similarly, in the 2.5H/1S treated condition, the TS and YS initially increased to their maximum values of 1096 ± 5 MPa and 1017 ± 2 MPa, respectively, after a thermal exposure period of 500h and then returned to monotonically decrease with further exposure time to reach 1006 ± 7 MPa and 953 ± 9 MPa after 3000h. Furthermore, the elongation of 2.5H/1S condition progressively increased with increasing the exposure period until its maximum value of 18.4 ± 1.2 % at 2000h, and then it returned to decrease with further exposure time to reach 16.4 ± 0.5% after 3000h.

6.3.2 Microstructure evolution during the in-service thermal exposure

As mentioned earlier, during the in-service thermal exposure for long periods, progressive changes in the microstructure of IN718 components are expected to occur, in terms of precipitation and/or dissolution of secondary phases and changes in the size and quantity of some existing phases, which are strongly linked to their mechanical properties. Thus, it is an important step to understand the impact of such operating conditions of turbine engines on the microstructural evolution which in turn helps to obtain more information about the durability of the IN718 components produced by LPBF. For this purpose, the microstructure characteristics in the as-printed and heat-treated conditions during the long-term in-service exposure at 650°C for periods up to 3000h were investigated using SEM and EDS analysis.

6.3.2.1 As-printed IN718 superalloy

Figure 6-5 shows the effect of the in-service exposure for periods up to 3000h on the microstructure of the as-printed condition. As can be seen in Figure 6-5a and b, the initial microstructure (0h) of the as-printed condition (acquired prior to the thermal exposure) mainly consists of γ-matrix with a very fine aligned columnar and cellular dendrite structure. In addition, a large amount of fine Lave phase and microsegregations were embedded in the inter-

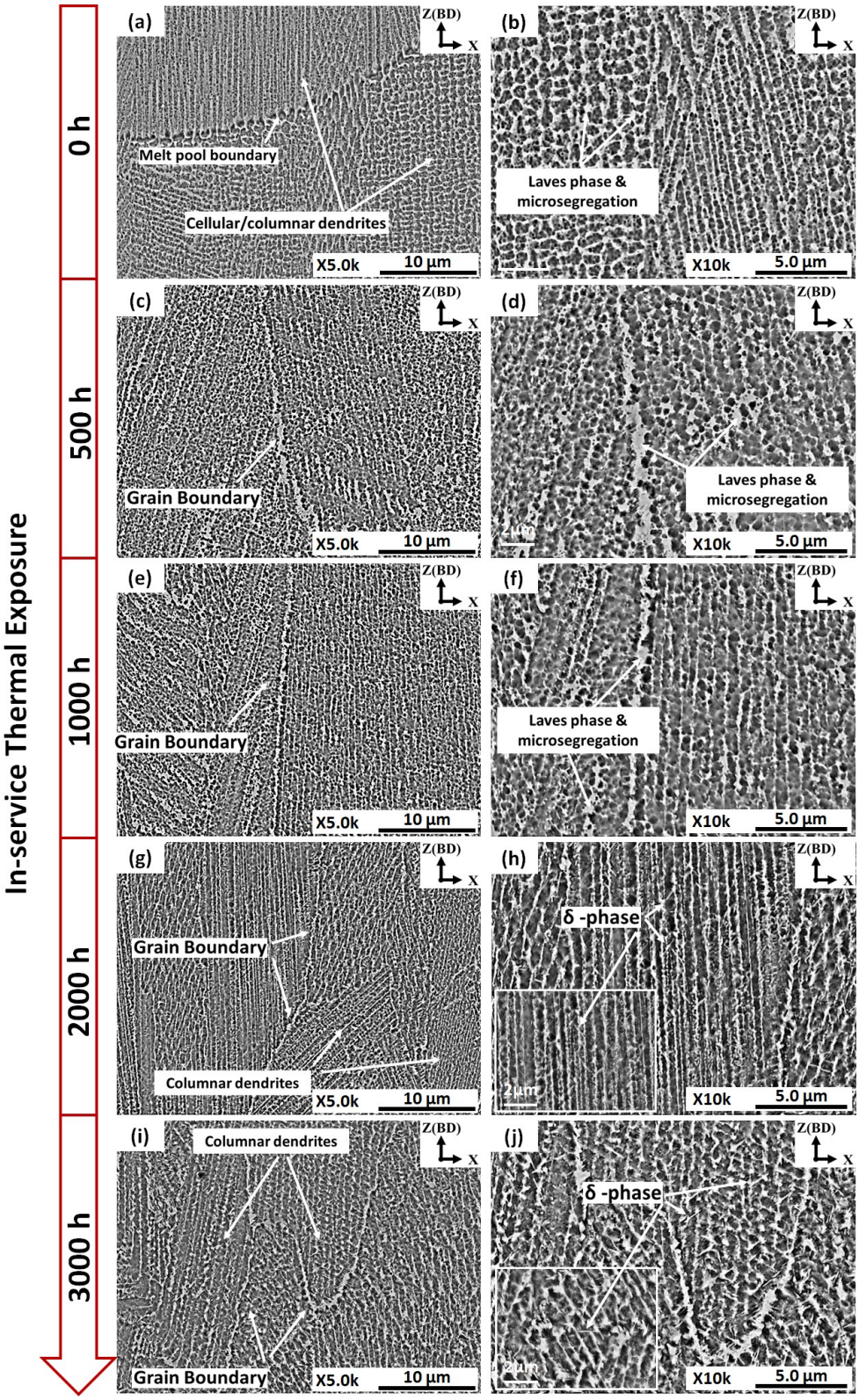

Figure 6-5: SEM micrographs of the as-printed condition after in-service thermal exposure for periods of: (a-b) 0h; (c-d) 500h; (e-f) 1000h; (g-h) 2000h and (i-j) 3000h.

dendritic and grain boundary regions which formed during solidification. The solidification path sequence of IN718 alloy is as follows: Liquid (L) → L + γ → L+ γ + NbC → L + γ + NbC + Laves → L + γ + NbC + Laves + δ which was predicted using Scheil-Gulliver solidification mode in Thermo-Calc software [129]. However, δ-phases have not been observed in the initial microstructure owing to the rapid solidification process as the cooling rate during the LPBF process can reach 10^5 ~10^7 K/s as reported by Choi *et al.* [41] and Li *et al*. [13].

Generally, after the thermal exposure at 650°C (regardless of the exposure period), the dendrite patterns are still present and identical as in the initial as-printed microstructure as shown in Figure 6-5c to j. Furthermore, the Laves phase and elemental microsegregation of Nb, Ti and Mo remain with the same size and morphology occupying the inter-dendritic and grain boundary regions. Figure 6-6 shows the EDS line scan profiles of the Nb, Ti and Mo-microsegregations crossing the inter-dendritic regions in the initial (0h) and final (3000h) states. It can be confirmed that there are no noticeable changes in the inter-dendrites microsegregations, and fluctuation in the Nb, Ti and Mo composition between the dendritic and inter-dendritic zones still exists even after 3000h exposure time. This is because the maximum temperature (650°C) during the thermal cycling is too low to homogenize the initial as-printed microstructure, dissolve the Laves phase and eliminate these microsegregations, as the dissolution temperature of Laves phase is ≈ 1165°C [133]. Also, the back diffusion of Nb, Ti and Mo into dendrites cores is very hard even after this long exposure time at 650°C due to its larger atomic radii compared with that of the solvent atoms (Ni) [13].

After the prolonged thermal exposure time (2000 and 3000h), δ-phase with a very fine needle-like shape formed within the inter-dendritic regions where Nb was enriched, and their precipitation amount increased with increasing the exposure period, thus the microstructure

acquired after 3000h (see Figure 6-5j) contains more δ-phase content as compared with the microstructure after 2000h (see Figure 6-5h). Also, the distribution of needle-like δ-phase was not uniform due to the non-homogeneous chemical composition of the as-printed microstructure even after the prolonged thermal exposure. As mentioned earlier, the microstructure of the thermal cycled as-printed conditions even after 3000h still retain a high concentration of Nb (see Figure 6-6b) which easily promotes the formation of δ-phase, as at least 6 to 8 at.% Nb is required to form δ-phase according to [134,135]. The presence of such a high fraction of δ-phase at the inter-dendritic regions as well as the microsegregations is expected to degrade the mechanical properties and consequently the product quality [107]. Therefore, applying post-heat treatment for the as-printed condition prior to the in-service thermal exposure is necessary to homogenize the microstructure and address the expected inferior mechanical properties.

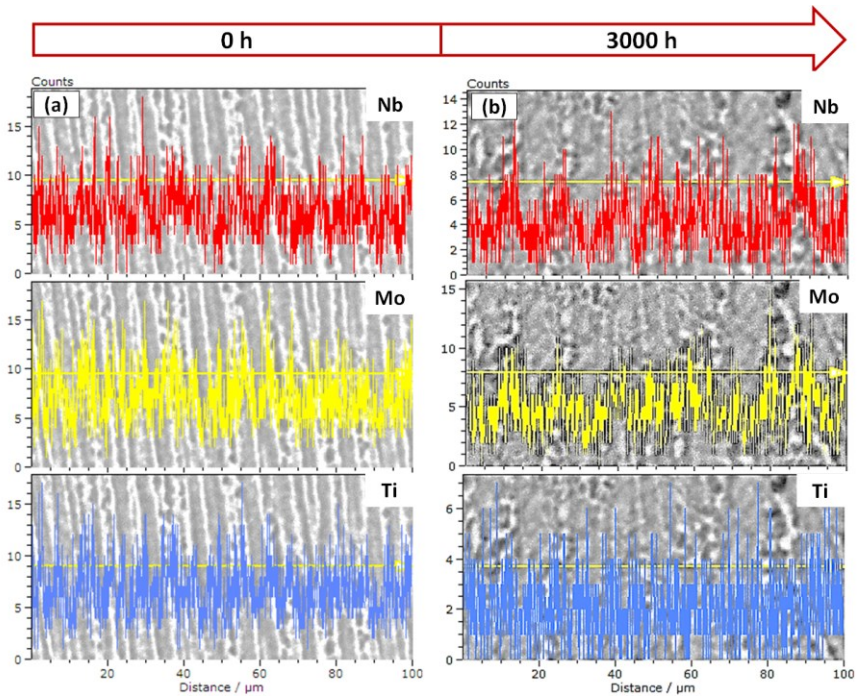

Figure 6-6: EDS line scan analysis of the as-printed conditions illustrating the evolution of the Nb, Ti and Mo-microsegregations as a function of thermal exposure time: (a) 0h, (b) 3000h.

6.3.2.2 Heat-treated IN718 superalloy

Figure 6-7 shows the microstructural evolution of the 4H/1S heat-treated condition as a function of the in-service exposure time. As can be seen in Figure 6-7a and b, the initial microstructure of the 4H/1S is completely free from the as-printed dendrite patterns and inter-dendritic microsegregations. This is attributable to the high temperature (1080°C) homogenization treatment for 4h included in the 4H/1S treatment, applied prior to the thermal exposure, after which most of the as-printed Laves phases and segregated elements were dissolved and diffused back to the γ-matrix. Also, the initial microstructure consists of inter-granular δ-phases and MC carbides precipitated along the grain boundaries (see Figure 6-7a and b). Table 6-4 summarizes the EDS analysis that confirms the presence of these phases.

After thermal exposure, although no new phases precipitated, changes in sizes and quantities of some existing phases are observed along with the transformation of some metastable phases. For instance, a significant increase in the amount and size of δ-phases are observed with increasing the exposure time which formed with a lamellar needle-like shape at the grain boundaries and oriented toward the center of the grains as shown in Figure 6-7d, e, g and h. Within the same micrograph, variations in the size of the needle δ-phases are observed which correspond to that formed in the initial microstructure (Figure 6-7a) mixed with that recently precipitated as shown in Figure 6-7c to l. Such precipitation of lamellar δ-phases seems to occur by a cellular precipitation mechanism starting from the grain boundaries. Similar observation was reported by Slama *et al*. [136] after isothermal exposure at 680°C for 100h. They reported that the precipitation of lamellar δ-phases along the grain boundaries occurs at low temperatures via the cellular precipitation mechanism which is consistent with the precipitation conditions in the present study [136].

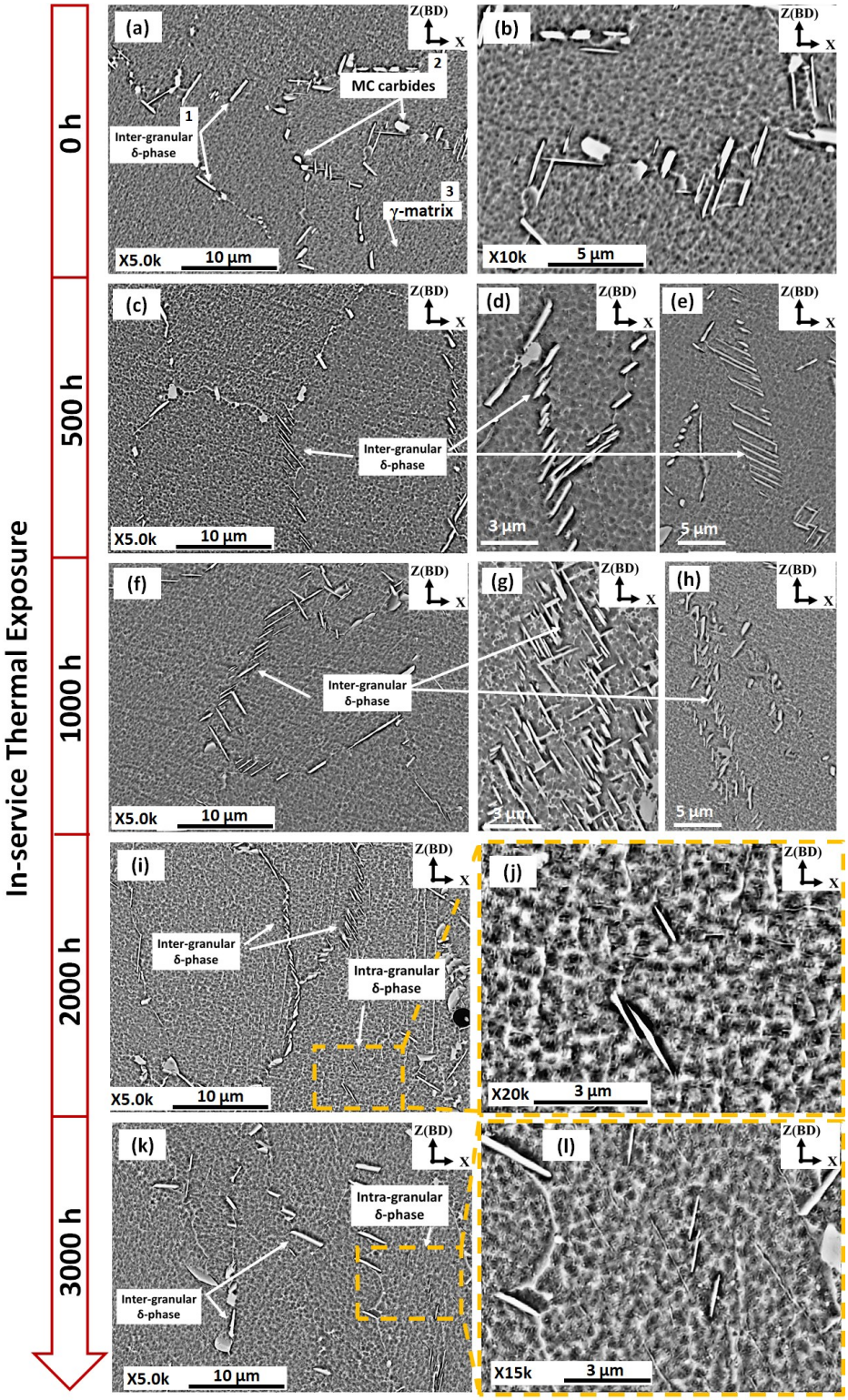

Figure 6-7: SEM micrographs of the 4H/1S heat-treated condition after the in-service thermal exposure for periods of: (a-b) 0h, (c-e) 500h, (f-h) 1000h, (i-j) 2000h and (k-l) 3000h. Arrows 1, 2 and 3 in (a) indicate the EDS spot analysis of inter-granular δ-phase, MC carbides and γ-matrix, respectively, as listed in Table 6-4.

Table 6-4. EDS spot analysis results of the initial microstructure of 4H/1S heat-treated conditions in Figure 6-7a (wt.%).

Spectrum	Phase	Fe	Ni	Cr	Nb	Ti	Mo	Al
1	δ- phase	Bal.	53.70	10.94	15.44	1.57	2.40	0.30
2	MC Carbides	Bal.	14.52	6.44	52.17	5.80	-	-
3	Matrix	Bal.	49.70	18.28	5.46	0.96	3.36	0.50

After the prolonged thermal exposure time (2000 and 3000h), very fine intra-granular δ-phases with a size of few microns crossing over the grain interiors are observed as shown in the magnified micrographs of Figure 6-7j and l. This finding can be explained by the transformation of some metastable γ″ phases dispersed in the γ-matrix into the δ-phases after an exposure time of 2000 and 3000h since the δ-phase is thermodynamically stable at this temperature (650°C). During this kind of phase transformation, the disc-shaped γ″ phase starts to coalescence together to form this shape of the stable δ-phases as reported by [137]. However, the transformation of γ″ phases to δ is still far from complete even after 3000h exposure time, as a very limited quantity of these intra-granular δ-phases are observed (see Figure 6-7j and l). This indicates that the phase transformation kinetics of γ″ into δ is very slow at 650°C. Yu *et al*. [138] also confirmed this finding by reporting that, after isothermal exposure at 700°C for 10000h, a non-complete phase transformation of γ″ into δ phase in IN718 alloy was observed. Such a phase transformation of γ″, the primary strengthening phase of IN718 alloy, is expected to adversely affect its mechanical properties.

For the 2.5H/1S treated condition, Figure 6-8 shows the impact of the in-service exposure time on the microstructure characteristics. As can be seen from the initial microstructure (0h) of the 2.5H/1S condition in Figure 6-8a and b, most of the Laves phase and dendrite patterns of the as-printed condition were eliminated. However, it can be noticed that there are slight traces of some sub-grain features as indicated by the presence of very fine black parallel lines

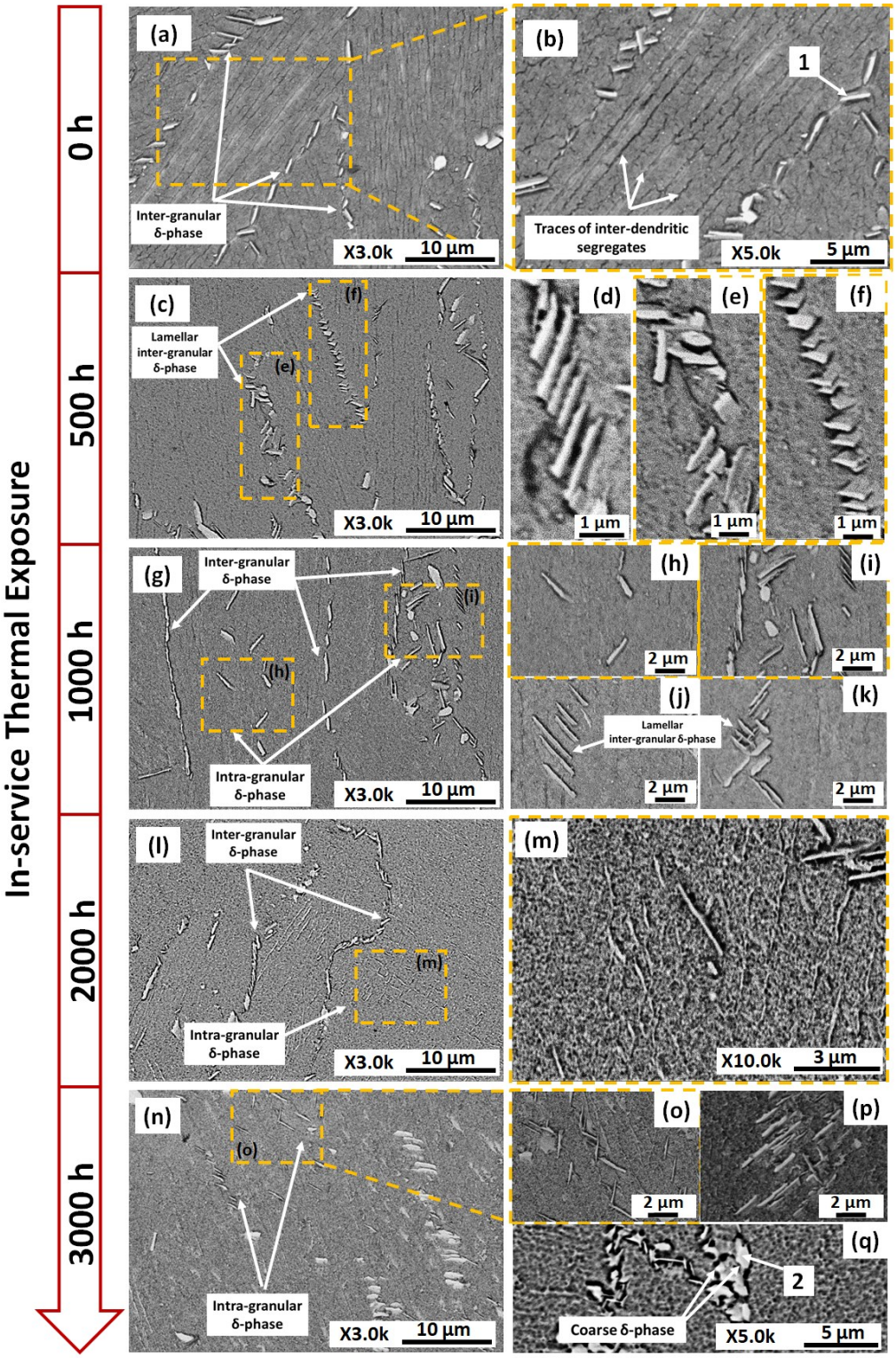

Figure 6-8: SEM micrographs of the 2.5H/1S heat-treated condition after the in-service thermal exposure for periods of: (a-b) 0h, (c-f) 500h, (g-k) 1000h, (l-m) 2000h and (n-q) 3000h. Arrows 1 and 2 in (b) and (q) indicate the EDS spot analysis of the δ-phase as listed in Table 6-5.

in Figure 6-8b. In this context, EDS lines scan analysis was employed to examine these traces as shown in Figure 6-9. It was found that some residuals of the as-printed segregated elements such as Nb still occupied the inter-dendritic regions as indicated by white arrows in Figure 6-9. It is important to notice that such residual segregates did not exist in the initial microstructure of the 4H/1S treated condition (Figure 6-7a and b) since the homogenization treatment in this treatment was much longer (4h) than that of the 2.5H/1S condition (2.5h), thus a more uniform distribution of alloying element was observed after the former treatment. Furthermore, the initial microstructure of the 2.5H/1S treated condition mainly consists of a needle-like δ-phase precipitated along the grain boundaries.

After thermal exposure, similar to the 4H/1S case, a significant increase in the precipitation amount and size of δ-phase is observed which again precipitated in a lamellar pattern at the grain boundaries and oriented to the center of the grain interior as seen in Figure 6-8(d-f), j, k and p. Furthermore, significant coarsening in the δ-phase size is observed after prolonged thermal exposure (3000h) as shown in Figure 6-8q. It is worth mentioning that these particles were indexed as δ-phases based on the EDS spot analysis as listed in Table 6-5. Unlike the 4H/1S condition, the microstructure of the 2.5H/1S treated condition acquired after thermal exposure for 1000h showed the first precipitation of intra-granular δ-phases as shown in Figure 6-8h and i, whereas in the 4H/1S condition, the first precipitation of the intra-granular δ-phases was observed after 2000h (Figure 6-7j) exposure time. Such earlier precipitation of intra-granular δ-phases in 2.5H/1S condition could be related to two distinct factors: (i) the presence of residual inter-dendritic Nb segregates (Figure 6-9) in the initial microstructure which in turn promoted to precipitate δ-phases after such long thermal exposure; (ii) the accelerated phase

transformation of γ″ into δ-phase due to the high dislocation density in the initial microstructure of the 2.5H/1S.

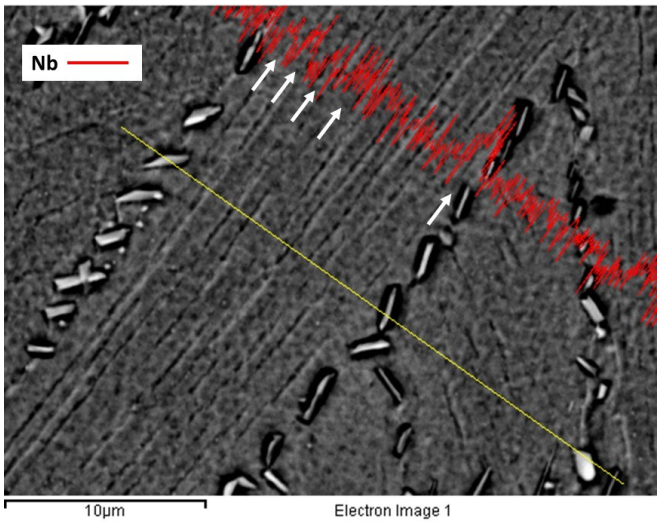

Figure 6-9: EDS line scan profile of Nb traces across the inter-dendritic regions in the initial microstructure of the 2.5H/1S condition.

Table 6-5: EDS spot analysis results of the 2.5H/1S heat-treated conditions in Figure 6-8b and q (wt.%).

Spectrum	Phase	Fe	Ni	Cr	Nb	Ti	Mo	Al
1	δ- phase	Bal.	55.01	8.13	20.29	1.62	2.39	0.21
2	δ- phase	Bal.	56.41	7.63	20.87	1.83	1.80	0.17

Regarding the second factor, we have previously reported that the 2.5H/1S treatment was not sufficient to completely annihilate the primary dislocation density in the as-printed condition inherited from the rapid and repetitive heating and cooling during the LPBF process [130]. It has been reported that the presence of these dislocation tangles plays a crucial role to enhance the elemental diffusion and exchange at high temperatures [120]. It is well-known that Nb is present in both γ″ and δ phases. Thus, the nucleation of δ phases in the grain's interior is possible if the metastable γ″ phases tend to evolve to a more stable structure. At high temperature, the material dislocations act as a diffusion pipeline through which the solute

elements, such as Nb, can easily exchange from γ″ (Ni_3Nb) to form δ-phase which in turn accelerated the phase transformation of γ″ into δ-phase in 2.5H/1S condition (after 1000h) as compared to the 4H/1S condition (after 2000h) [120]. Such findings are consistent with what Jouiad *et al*. [120] observed, as they investigated the effect of the isothermal and non-isothermal (thermal cycling) aging treatment at 750°C for 100h on the phase transformation of γ″ phases into stable δ-phase in wrought IN718 alloy. Their TEM analysis showed that, in the thermally cycled samples, both γ″ and δ phases were observed and located near the dislocations inherited from the thermal cycling condition, whereas in the isothermal condition, δ phase was not formed [120]. They explained this phenomenon by the role of the dislocation tangles, formed during the thermal cycling condition (non-isothermal exposure), to effectively accelerate the phase transformation of γ″ into δ-phase as these dislocations acted as an easy shortcut for elemental exchange at high temperature [120].

6.3.3 Precipitates evolution during the in-service exposure

XRD analysis of the as-printed and heat-treated conditions was employed to follow phases evolution during thermal exposure and obtain more details about some of the phases that were not detected using SEM analysis such as γ′ and γ″ due to their small size (within a few nanometers). For this purpose, Figure 6-10 shows the X-ray diffractgrams of the as-printed and heat-treated conditions as references for those taken after exposure to the in-service conditions for up to 3000h. As a guidance, the thermal cycling condition used in the present study was implemented in the Temperature-Time-Transformation (TTT) diagram of IN718 welds reported by Thompson *et al*. [139] to reveal the expected phases evolutions during the thermal exposure as shown in Figure 6-11.

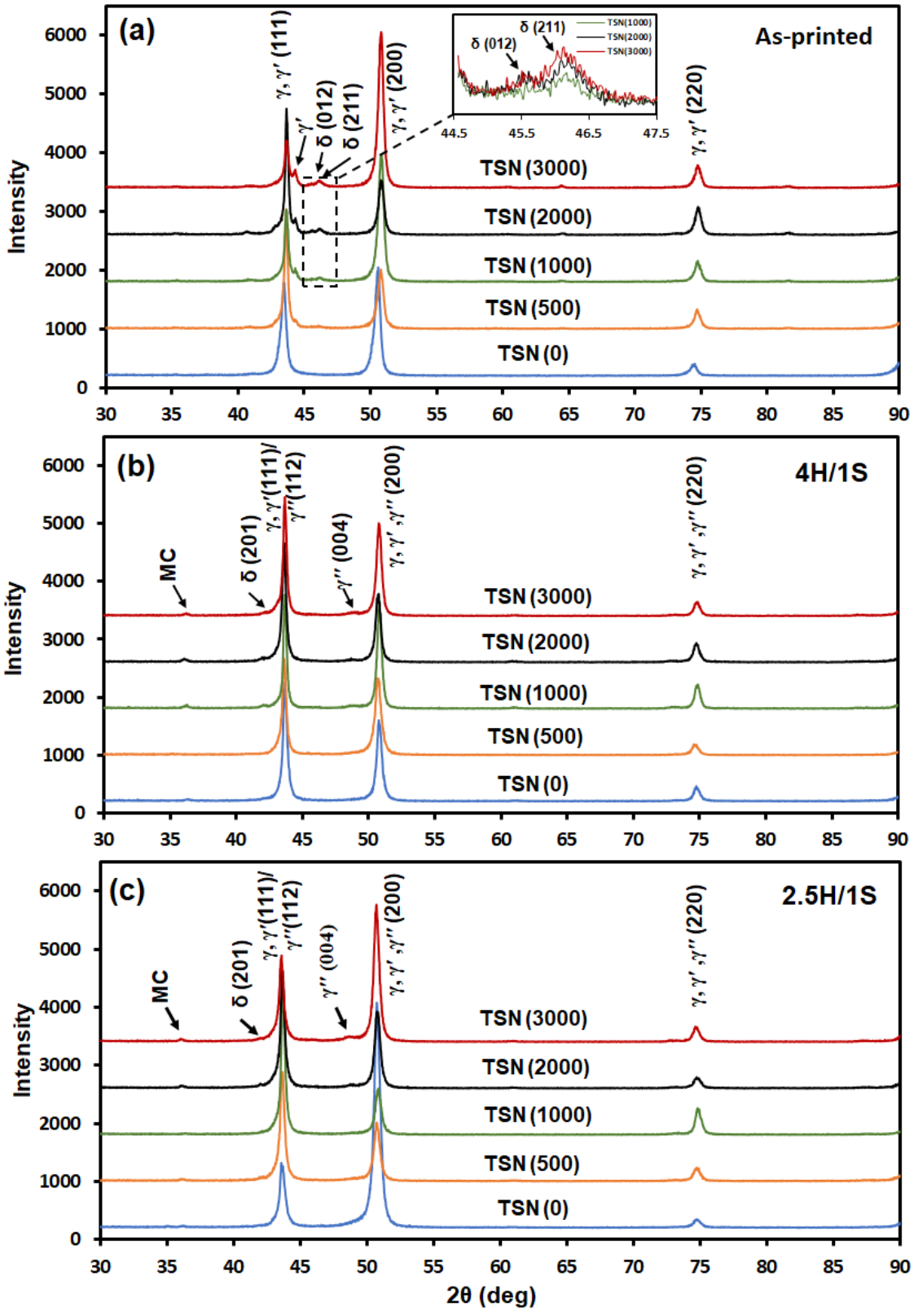

Figure 6-10: Evolution of XRD diffractograms as a function of in-service thermal exposure time of LPBF IN718 in: (a) as-printed, (b) 4H/1S and (d) 2.5H/1S.

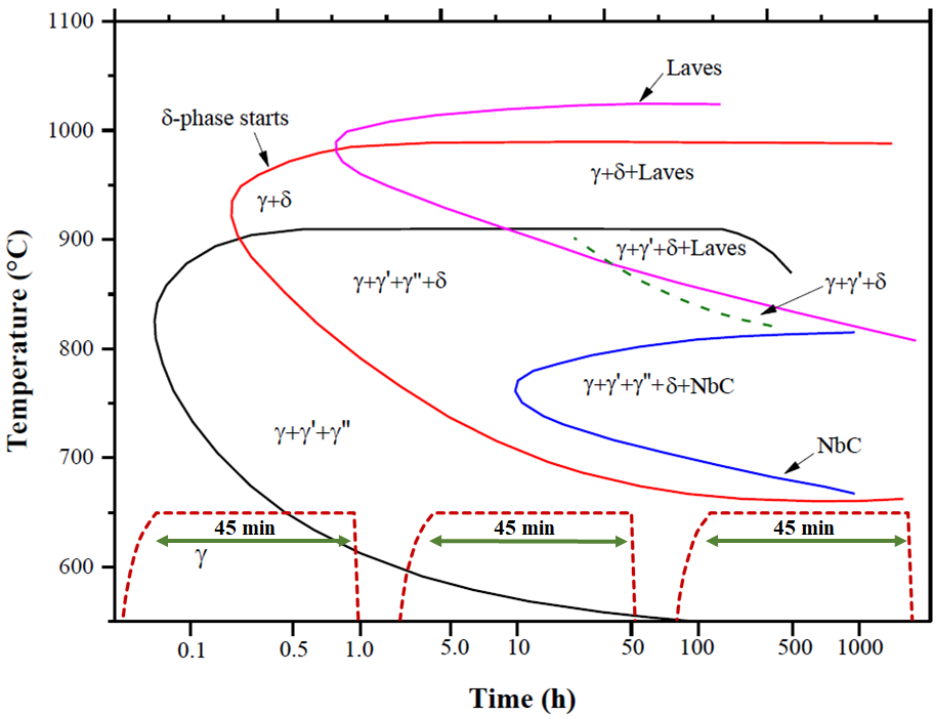

Figure 6-11: Temperature-time-transformation diagram of IN718 superalloy [139]. The thermal cycle applied in the present study is included in this diagram.

In the as-printed condition, the XRD pattern of the initial state (TSN (0)) shows the occurrence of major peaks at 43.45° (111), 50.59° (200) and 74.53° (220) which correspond to the FCC γ-matrix with no minor peaks formation as shown in Figure 6-10a. After thermal exposure, additional minor peaks of some secondary phases were detected. As can be seen from the XRD patterns acquired after 500 to 3000h in Figure 6-10a, a minor peak at 2θ = 44.2° emerged indicating the precipitation of γ′ phase. Also, it is important to note that the intensity of this peak increases with the increase of the thermal exposure period indicating that greater precipitation of γ′ phase with further exposure time. Such precipitation of the γ′ phase after thermal exposure is consistent with the TTT diagram shown in Figure 6-11 and can be explained by realizing that the thermal exposure at a temperature of 650°C acted as a second step of the standard aging treatment of the IN718 superalloy. It is well-recognized that the standard aging treatment of IN718 consists of two steps as follows: (1) holding at 720°C for

8h, followed by furnace cooling to 620°C with a cooling rate of 55°C/h, and (2) holding at 620°C for 8h followed by air cooling to room temperature after which both γ″ and γ′ phases precipitate [11,26]. However, the precipitation of the γ″ phase is not observed through the XRD patterns of the thermal cycled as-printed conditions. This could be attributable to the slower precipitation kinetics of γ″ phase as compared with that of γ′ in the as-printed condition.

The precipitation sequence of γ″ and γ′ phases is mainly dependent on the ratio of (Al + Ti)/Nb in IN718 alloy, which varies between 0.65 and 0.9, as well as the aging time and temperature [136]. Sundararaman *et al.* [140] reported that both γ″ and γ′ phases can form simultaneously when this ratio is approximately equal to ≈ 0.66 (contents expressed in at.%) at a temperature range of 550 - 660°C for a long aging time, whereas at a temperature range of 700-900°C, both can form after a short aging time. In contrast, Cozar *et al*. [141] reported that if this ratio is higher than 0.8, the precipitation of γ′ precedes the precipitation of γ″. However, a lot of discrepancies in the literature still exists concerning the sequence of formation of the γ″ and γ′ phases. In the present study, according to the EDS analysis, the as-printed IN718 presents a ratio of 0.93-1. Hence, the precipitation of γ′ before the γ″ phase is more likely to occur just after thermal exposure. Nevertheless, the XRD pattern acquired even after long exposure time did not show the precipitation of γ″. This could be attributed to the retention of a significant amount of the Nb-microsegregation at inter-dendritic regions even after the prolonged thermal exposure (see Figure 6-6b) and depleted it from the γ-matrix which is necessary for the precipitation of γ″ (Ni_3Nb), thus γ′ is expected to be the dominant strengthening phase in the thermal cycled as-printed condition.

Furthermore, for the prolonged thermal exposure (1000, 2000 and 3000h), the XRD patterns show the occurrence of additional two minor peaks at 2θ = 45.6° and 46.2° which correspond

to (012) and (211) δ-phases, respectively, as shown in the magnified inset in Figure 6-10a, and their intensities increase with the increase of the exposure period indicating that more δ-phases precipitated with longer thermal exposure. Such precipitation of the δ-phase in the as-printed condition after prolonged thermal exposure is consistent with the SEM analysis (Figure 6-5h and j). As can be noticed from Figure 6-11, the maximum temperature of the thermal cycling (650°C) is lower than the precipitation temperature of δ-phase, as its precipitation range is between 700 – 1000°C with a maximum precipitation rate at ≈ 900°C [13]. Zhang *et al*. [54] reported that the incubation period necessary for nucleation of δ-phase in the additively manufacture IN625 alloy is less than 5 min in a temperature range of 800°C to 870°C. However, in our case, the precipitation of δ-phases occurred after thermal exposure at 650°C for a period of ≥ 1000h. The precipitation of δ-phase at low temperature was also reported by Slama *et al.* [136,142], as they observed its precipitation in wrought IN718 after aging treatment (isothermal exposure) at 680°C for 100h. The incubation period is mainly dependent on the diffusion rate of the alloying elements such as Nb which are present in δ-phase (Ni_3Nb). Therefore, at low temperatures, the diffusion rate and growth kinetics are quite slow that consequently increase the nucleation barrier for δ-phase. Furthermore, as mentioned earlier, the presence of a high concentration of Nb along the inter-dendritic region after long thermal exposure (Figure 6-6b) also significantly contributed to the precipitation of δ-phase. Another reason for such discrepancies in the precipitation temperature of δ-phase is that the TTT diagram shown in Figure 6-11 is not made for the additively manufacture IN718 alloy, thus changes in the precipitation condition of some phases are expected.

Unlike the as-printed condition, according to the EDS analysis, the 4H/1S and 2.5H/1S heat-treated conditions present a relatively lower (Al + Ti)/Nb ratio of 0.66-0.75 when

compared with that of the as-printed condition. This is attributable to the applied heat treatments prior to thermal exposure (unlike the as-printed condition) which included homogenization treatment at 1080° for 4 and 2.5h, respectively, after which a significant amount of Nb was released into the γ-matrix after the back diffusion of Nb-segregates and dissolution of Laves phase of the as-printed condition. Therefore, simultaneous precipitation of γ″ and γ′ phases is expected during the subsequent aging treatment (720°C/8h + 620°C/8h) as well as thermal exposure at 650°C.

Although the microstructure of the initial state of both 4H/1S and 2.5H/1S conditions contains γ″ and γ′ phases, as a result of the aging treatment, in addition to δ-phase as observed from the microstructure analysis (Figure 6-7a and b and Figure 6-8a and b), the XRD patterns of the initial state of both conditions (see Figure 6-10b and c) did not exhibit the presence of any of these phases which can be explained by its small content to be lower than the detection limit (≈ 5 %) of the XRD. However, after thermal exposure, the XRD patterns of the 4H/1S and 2.5H/1S heat-treated conditions exhibited the precipitation of (004) γ″ peak at 2θ = 48.8° indicating that greater precipitation of γ″ occurred after prolonged thermal exposure at 650°C which acted as a continuation of the second step of the aging treatment. Furthermore, another supplementary peak at 2θ = 42° of both 4H/1S and 2.5H/1S conditions is observed that corresponds to the further precipitation of (201) δ-phase after thermal exposure (Figure 6-10b and c, respectively) which is consistent with the microstructure analysis. Also, it should be noted that the precipitation of γ′ phase is not observed even after the prolonged thermal (unlike the as-printed condition). This might be attributed to its relatively lower volume fraction in the heat-treated condition (more homogenized microstructure), as the volume fractions of γ′ and γ″ in the fully heat-treated IN718 alloy are 5% and 20 %, respectively [143]. Hence, it can be

concluded that the γ″ phase is expected to be the dominant strengthening phase for the 4H/1S and 2.5H/1S conditions even after thermal exposure.

6.4 Discussion

The evolutions of the mechanical properties of the LPBF-fabricated IN718 during the in-service exposure for up to 3000h are closely related to its microstructural characteristics. For the as-printed condition, the precipitation of γ′ phase just after thermal exposure hardened the IN718 alloy, and therefore its tensile and yield strengths significantly increased at the expense of its ductility due to the restriction of the movement of the dislocations, during the plastic deformation, by the dispersed γ′ phases in the γ-matrix. However, the coarsening of γ′ precipitates after further thermal exposure for more than 500h resulted in a gradual decrease in both tensile and yield strengths and an increase in the material ductility, in relation to those after 500h, with increasing exposure time. For quantification, the grain size of the γ′ phase in the as-printed condition after thermal cycling for 500h up to 3000h was calculated from the XRD data using Scherrer's equation as follows: $\Phi = 0.9\,\lambda/L\cos(\theta)$ [142], where Φ is the mean size of the crystalline domain, λ is the X-ray wavelength, L is the full width half maximum (FWHM) of the diffraction peak of γ′ and θ refers to the diffraction angle of γ′ (2θ = 44.2°). The FWHM is measured using the Gaussian fitting method in Origin software (OriginPro 2019b, OriginLab Corp, Northampton, MA, USA) [144].

Figure 6-12 shows the evolution of the γ′ average grain size as a function of the thermal exposure duration. It can be seen in this figure that after thermal exposure for 500h, a very fine (≈ 8 nm) γ′ grain size precipitated which significantly contributed to such improvement in the mechanical properties. When increasing the exposure duration up to 3000h, a monotonic increase in grain size from ≈ 8 to 22 nm is observed. Thus, progressive deterioration in the

mechanical strength and increase in material plasticity of the as-printed condition are observed. However, the ductility after 3000h exhibited plateau behavior, and it is expected to decrease with further thermal exposure time (>3000h). This is due to the greater precipitation of the needle-like δ-phase at the inter-dendritic regions which is well-recognized by its harmful effect on the material ductility.

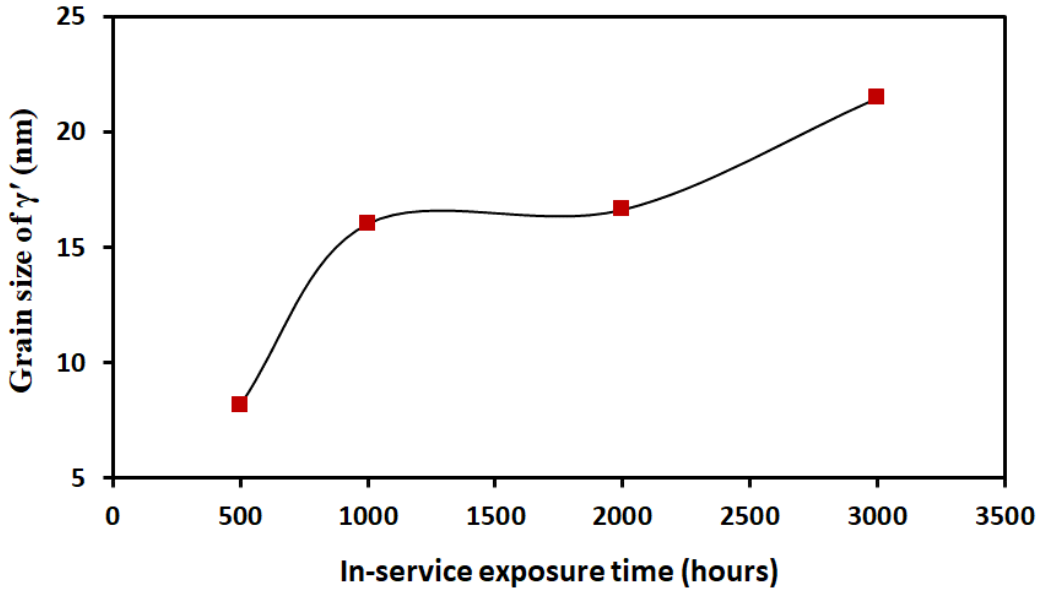

Figure 6-12: Grain size evolution of γ′ in the as-printed condition as a function of the in-service exposure time.

For the 4H/1S condition, according to the microstructure (Figure 6-7d, e, g and h) and XRD (Figure 6-10b) analyses, the initial slight increase in both tensile and yield strengths until 1000h is attributed to the combined effect of greater precipitation of γ″ in the matrix as well as the increased precipitation of δ-phase along the grain boundaries. The presence of δ-phase along the grain boundaries acts as a barrier against the dislocation motion during the plastic deformation and pins the grain boundaries sliding which in turn strengthens the material. However, its contribution to strengthen the material is much less than γ″ phases. Zhang *et al.* [24] reported that the precipitation of the appropriate amount of the inter-granular δ-phase

improves the grain boundary strength, as it impedes the grain boundary movements. After longer thermal exposure for more than 1000h, the phase transformation of γ″ into the more stable δ-phase, as indicated by the formation of the intra-granular δ-phase (see Figure 6-7j and l), led to a continuous and progressive decrease of the tensile and yield strengths. Also, the rest of γ″ phases are expected to be coarsened during such prolonged thermal exposure which consequently leads to inferior mechanical properties. It has been reported by Jouiad *et al*. [120] that the coarsening rate of the γ″ is very fast due to the large coherency of γ/γ″ strains. Further, Yu *et al*. [138] reported that the thermal exposure at 700°C for 10000h for wrought IN718 resulted in an increase in the diameter of the γ″ from approximately 50 nm to 500 nm ~1 μm in addition to the decrease of its volume fraction due to phase transformation to δ-phase which ended up with a reduction in the material strength. Moreover, such coarsening of γ″ precipitates is expected to be one of the main causes of the improvement of the material ductility with the increase of the thermal exposure time (Figure 6-4b). However, further TEM analysis is required to effectively follow the evolution of γ″ morphologies and size during thermal exposure.

Similarly, in the 2.5H/1S treated condition, the greater precipitation of inter-granular δ and γ″ phases just after thermal exposure resulted in the first improvement of both tensile and yield strength until 500h. Further exposure time results in the formation of the intra-granular δ-phase at the expense of γ″ phase which in turns deteriorated the material strength. Unlike the 4H/1S condition, the ductility of the 2.5H/1S condition exhibited a non-monotonous trend as the elongation to failure progressively increased until 2000h, then decreased with further exposure time (3000h) due to the greater precipitation of intra-granular δ-phase (Figure 6-8n to q) in relation to that precipitated in the 4H/1S condition after 3000h (Figure 6-7l).

In order to enlighten the differences in the mechanical behavior and the thermal stability between the as-printed, 4H/1S and 2.5H/1S conditions, Figure 6-13a and b shows the evolution of the tensile and yield strengths of each condition at different intervals of thermal exposure. As can be seen in this figure, the as-printed condition exhibited higher tensile strengths at all intervals of thermal exposure when compared with these of the 2.5H/1S and 4H/1S conditions. This is attributed to the combined effect of the high primary dislocation density as well as the precipitation of the strengthening phase (γ'). Due to the rapid and repetitive heating and cooling during the LPBF process, high-level thermal stresses and high density of dislocation tangles are induced in the as-printed samples which in turn contribute to the material strength. In the previous study [130], it has been reported that the microstructure of as-printed condition contains large local plastic strains and high dislocation density that was indicated by relatively higher kernel average misorientation (KAM) (0.85°) when compared with those obtained after the 2.5H/1S and 4H/1S treatment (0.75 and 0.5°, respectively). Despite the higher tensile strength of as-printed condition over the 2.5H/1S and 4H/1S conditions, the presence of such high thermal/residual stresses ends up with parts distortion and cracks formation, in some cases, which is not suitable for the industry.

Furthermore, Figure 6-13a and b helps to follow the thermal stability of each condition over the in-service exposure up to 3000h. In the present study, thermal stability is measured by assessing the loss of strength of each condition after the in-service exposure for 3000h with respect to the initial state. However, in the as-printed condition, the comparison of the thermal cycled condition after 3000h with the initial state (0h) is not representative for its thermal stability as the initial state of the as-printed condition was completely free from any strengthening phases. Therefore, it is reasonable to assess the thermal stability of the as-printed

condition by evaluating the strength loss of the thermal cycled condition for 3000h with respect to the thermal cycled condition for 500h. As can be seen in this figure, the as-printed condition exhibited relatively lower thermal stability over the long in-service exposure, compared with the heat-treated conditions, as its TS and YS decreased after thermal exposure for 3000h by 7.4 and 7.7% of its state at 500h. This is attributed to the high fraction of the δ-phase at the inter-dendritic regions (Figure 6-5i and j) as well as the retained microsegregations and Laves phase even after the prolonged thermal exposure (Figure 6-6b).

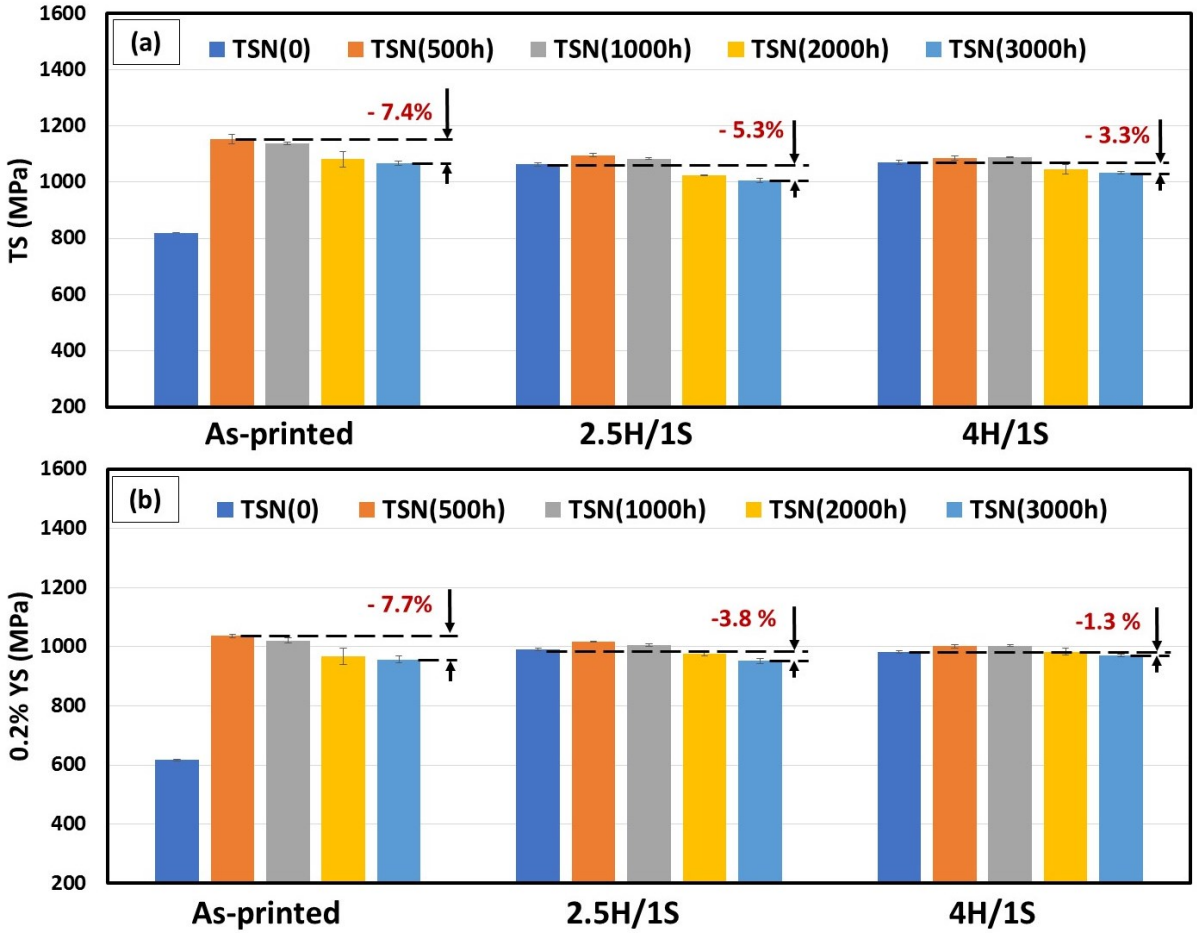

Figure 6-13: Comparison of the tensile properties at different thermal exposure intervals between the as-printed, 2.5H/1S and 4H/1S conditions: (a) TS and (b) YS.

For the heat-treated samples, the comparison between the 2.5H/1S and 4H/1S conditions reveal that the 4H/1S had a relatively higher thermal stability as its TS and YS decreased after

thermal exposure for 3000h by only 3.3 and 1.3% of the initial state, whereas in the 2.5H/1S condition, both strengths decreased by 5.3 and 3.8%. Furthermore, it is important to notice that the initial deterioration in the material strength of the 2.5H/1S condition during the thermal exposure occurred earlier when compared with the 4H/1S condition, as the strength of the 2.5H/1S condition started to decrease after an exposure time of 1000h, whereas in the 4H/1S, the material strength deteriorated after 2000h. Such earlier deterioration in the mechanical strength and lower thermal stability of the 2.5H/1S can be attributed to the faster and greater precipitation of the intra-granular δ-phase at the expense of the γ″ after prolonged thermal exposure (Figure 6-8g, h and i) which is well-known by its harmful impact [120] on the mechanical properties.

As a consequence of the aforementioned discussion, it can be concluded that the 4H/1S condition able to retain higher mechanical strength at elevated temperature for a longer exposure time at 650°C with higher thermal stability when compared to the as-printed and 2.5H/1S treated conditions. Furthermore, the 4H/1S condition exhibited a continuous improvement in the material ductility during thermal exposure even after 3000h, whereas in the 2.5H/1S condition, ductility deterioration after 3000h occurred. This indicates that using the 4H/1S condition for the post-heat treatment of IN718 components fabricated by LPBF is more reliable during the in-service conditions.

6.5 Conclusion

In the present study, the evolutions of the microstructure and elevated-temperature (650°C) mechanical properties of the LPBF-fabricated IN718 as a function of different in-service exposure periods of 500, 1000, 2000 and 3000h have been investigated. The main findings can be summarized as follows:

- The microstructure analysis of the initial state of the as-printed condition (TSN(0)) typically presents very fine cellular and columnar dendritic patterns aligned parallel to the building direction where a significant amount of Laves phase and microsegregations are embedded. After thermal exposure up to 3000h, the dendritic patterns are still present and identical to the initial state because the thermal cycling temperature is too low to dissolve Laves phase and diffuse the microsegregations back into the γ-matrix. However, the thermal cycling condition acts as an aging treatment after which the precipitation of γ′ occurs in all thermal cycled conditions. After prolonged thermal exposure (i.e. 2000 and 3000h), very fine needle-shaped δ-phases are formed within the inter-dendritic regions where Nb was enriched.
- In the 2.5H/1S and 4H/1S conditions, the microstructure analysis does not present new phases formed after thermal exposure with respect to the initial state of both conditions. However, a greater amount and size of lamellar inter-granular δ-phase is observed after thermal exposure. Furthermore, after prolonged thermal exposure, there is a phase transformation of the metastable γ″ into stable intra-granular δ-phases but still far from the complete transformation since a very limited quantity of this intra-granular δ-phase is observed.
- After thermal exposure, the tensile properties of both 2.5H/1S and 4H/1S conditions initially increase with increasing the exposure time, and then decrease with further exposure. Such a non-monotonic behavior is attributable to the greater precipitation of γ″ and inter-granular δ phases just after thermal exposure, which in turn improves the material strength, followed by coarsening of δ and γ″ along with the incomplete dissolution of γ″ via its transformation to δ that result in strength deterioration.

- The comparative analysis of the tensile results of the as-printed and heat-treated conditions indicates that the 4H/1S condition exhibits the highest thermal stability as its tensile and yield strengths after 3000h thermal exposure decrease by only 3.3 and 1.3%, respectively, of the initial state, whereas both strengths decrease by 7.4 and 7.7% in the as-printed condition and 5.3 and 3.8% in the 2.5H/1S condition.
- The 4H/1S treatment results in delaying the deterioration of the tensile and yield strengths of the LPBF IN718 to be after 2000h, while for 2.5H/1S treatment, the strength deterioration occurs after 1000h.

Chapter 7 : Conclusions, Research Contributions and Recommendations for Future Work

In this chapter, the main findings and outcomes of this thesis are concluded. Also, the main research contributions of the current study with respect to the literature are highlighted. Finally, recommendations for future research are provided.

7.1 Conclusions

This thesis presents a comprehensive investigation on the behavior/performance of the additively manufactured IN718 superalloy fabricated by the LPBF process under the conditions of as-printed, post-heat-treated and during the in-service thermal exposure. The influence of different heat treatment conditions, including a wide time range of homogenization (at 1080°C; 1 to 7h) and solution (at 980°C; 15 to 60 min) treatments, on the microstructure and mechanical properties of LPBF IN718 parts is investigated. Also, this work reports an optimization of the heat treatment conditions for the LPBF-fabricated IN718 that can fulfill the design requirements, especially in the aerospace industry. For the first time, the behavior of the optimum heat-treated LPBF-fabricated IN718 under the in-service conditions for a long time is assessed.

Investigation on the effect of the treatments time window shows that the homogenization treatment at 1080°C for 1h is not enough to change the as-printed texture, grain structure and annihilated the primary dislocations. Also, the inter-dendritic segregates and Laves phase are only partially dissolved and diffused into the γ-matrix after this treatment. However, a complete recrystallized material with stress relieved equiaxed grains and random texture is obtained after 4h at 1080°C. Further increase in the homogenization time to 7h at this temperature results in grain growth with greater and coarser carbides. For the solution treatment at 980°C, it is found

that its time plays a crucial role to control the precipitation amount of δ-phase but confers a very mild impact on the grain structure and crystallographic texture.

The effects of the treatments time window on the mechanical properties at RT and 650°C have been investigated. It is found that the 1h homogenization treatment conditions exhibit the highest mechanical properties at RT and 650°C due to the combined effect of the precipitate hardening mechanism and the preservation of the high primary dislocation density inherited from the printing process. The increase in the homogenization treatment to 4 and 7h results in a progressive decrease in the mechanical properties at RT and 650°C. This is due to the considerable annihilation of the primary dislocation tangles with the homogenization time and the precipitation of more and coarser MC carbide particles that consequently consumes a great amount of the forming elements (Nb and Ti) of the strengthening phases (γ′ and γ″). The increase in the solution treatment time is found to have an effective role in the improvement of the elevated-temperature tensile strength due to the enhancement of the grain bounder strength via the pinning effect of inter-granular δ-phase to the grain boundary movement. Finally, a post-heat treatment map is provided through which the microstructure and mechanical properties can be tailored according to the design requirements.

Based on the results obtained at different treatments time, a multi-objective optimization is employed to tune the homogenization and solution time aiming to develop the optimum heat treatment conditions of the LPBF IN718. The effects of homogenization treatment times of 2, 2.5, 3, 3.5 and 4h followed by solution treatment for 1h and standard aging treatment on the precipitates, texture, grain boundaries and morphology of LPBF IN718 are investigated. The results show that the 2.5h homogenization treatment (2.5H/1S) is the threshold after which the depletion of the solute elements (Ti and Nb) from the γ-matrix occurs, as a drop in the γ-matrix

lattice parameter after 3, 3.5 and 4h-long treatment supports this hypothesis. However, the microstructure of this condition still contains a significant number of elongated grains with a noticeable change in the crystallographic orientation (100) as compared to the as-printed condition. In contrast, nearly complete recrystallization with a significantly weakened texture along the (100) direction is obtained after the 4h homogenization treatment (4H/1S). At room temperature, both 2.5H/1S and 4H/1S treatments result in a significant improvement in the tensile properties, as compared to those of the conventionally heat-treated LPBF IN718 (AMS standards) and the wrought (AMS 5662) alloy. Also, a good balance between the strength and ductility is obtained after the 4H/1S treatment. At 650°C, both 2.5H/1S and 4H/1S treated samples exhibit higher tensile and yield strengths than, and a comparable ductility to those of the (AMS 5662) wrought IN718. The 4H/1S condition is recommended to be the post-heat treatment of LPFB IN718 components in situations where isotropic materials with homogenous mechanical properties are required.

Finally, after obtaining the optimum heat treatment conditions (2.5H/1S and 4H/1S) of the LPBF IN718, it is important to evaluate their thermal stability under the in-service environment. Thus, this study investigates the impact of the in-service thermal cycle of the aircraft turbine engine for periods of 500, 1000, 2000 and 3000h on the microstructure and the elevated-temperature (650°C) mechanical properties of the as-printed, 2.5H/1S and 4H/1S conditions. For the as-printed condition, the microstructure analysis of the initial state and the thermal cycled conditions for up to 3000h presents identical dendritic patterns due to the lower temperature (650°C) of the thermal cycling condition to dissolve Laves phase and diffuse the microsegregations back into the γ-matrix. However, a very fine needle-shaped δ-phase is formed at the inter-dendritic after prolonged thermal exposure time (i.e. 2000 and 3000h). In

the 2.5H/1S and 4H/1S conditions, after thermal exposure, a greater amount and size of lamellar inter-granular δ-phase is observed. Moreover, a phase transformation of the metastable γ″ into stable intra-granular δ-phases occurred after prolonged thermal exposure. The comparative analysis of the tensile results at 650°C shows that the 4H/1S condition possesses a relatively higher thermal stability than the as-printed and 2.5H/1S conditions. Furthermore, the 4H/1S treatment results in delaying the deterioration of the tensile and yield strengths of the LPBF IN718 to be after 2000h, while for 2.5H/1S treatment, the strength deterioration occurs after 1000h.

7.2 Contributions

Over the past few years, improving the performance of the additively manufactured IN718 components using the LPBF process has received significant attention from different industrial sectors, especially the aerospace industry. This is due to the high demand to replace the existing conventions manufacturing methods that could not cope with the fast development of advanced generations of turbine engines and limit the design freedom to manufacture complex geometrical components along with other challenges encountered during the manufacturing of IN718 components. However, the lack of information about the suitable post-heat treatment conditions of the LPBF IN718 rendered the majority of researchers in the existing literature to use the AMS standard treatments of the cast and wrought material to homogenize the as-printed microstructure and improve the mechanical properties which ended up with non-encouraged results. Besides, very limited studies are available in the literature on the evaluation of the microstructure and mechanical properties at elevated temperatures which is necessary to judge the reliability of LPBF IN718 during the in-service conditions**.** Thus, the implementation of LPBF in the real industries to manufacture IN718 components is still in its infancy.

Therefore, in the present study, an effective post-heat treatment window is introduced that helps to deeply understand the evolution of the as-printed microstructure under the theses treatment conditions and to customize the mechanical properties of the produced parts either at RT or elevated temperature based on the intended application. Furthermore, for the first time, this study provides a post-heat treatments map that contains a broad range of material properties to be suitable for a wide sector of industrial applications.

For the aerospace applications, a wrought-like structure, in terms of grain morphologies and homogeneous microstructure, and mechanical properties (high and isotropic mechanical properties) is required which is quite far from that obtained in LPBF IN718. Therefore, in the present study, the heat treatment condition that can achieve such a wrought-like microstructure with superior mechanical properties at both RT and 650°C is identified for the LPBF IN718 via multi-objective optimization for the homogenization and solution treatments time. Recognition of this condition has a significant impact on maximizing the LPBF potentials in the aerospace industry to fabricate critical IN718 components in aircraft turbine engines.

Furthermore, investigation of the impact of the long-term in-service exposure on LPBF IN718 in as-printed and heat-treated conditions has not been found in the literature yet. This might be due to the limitations of the facilities to physically simulate the in-service operation conditions of an aircraft turbine engine. For instance, applying the non-isothermal exposure (aircraft engine thermal cycling) for prolonged periods is quite difficult to be employed using the traditional furnaces. In this work, a state-of-the-art thermal cycling rig is used which is intentionally specialized for this kind of testing. In this rig, a robotic arm attached to the sample holder gives the freedom to samples to easily move inside and outside the furnace tube. This provides the accessibility to simulate such cyclic working conditions even with controlling the

heating rate as well as cooling rate via cooling fans. Hence, the evolution of the microstructure of the as-printed and heat-treated IN718 during the in-service exposure is deeply understood and correlated with the development of the elevated-temperature mechanical properties.

7.3 Recommendations for future work

Based on the work results presented herein, the need for more studies is identified as listed in the following recommendations for future research directions:

- In the present study, it has been concluded that the 4H/1S treatment condition is suitable to achieve isotropic grain structure and its effect on the elevated-temperature (650°C) tensile properties is only investigated on the vertically built samples (parallel to building direction). More studies with different printing direction are required to ensure the capability of this condition to produce isotropic mechanical properties. For instance, tensile samples with orientations of 0°, 45°, 90° and 45° × 45° in relation to the building direction are necessary to be examined at 650°C to assess the mechanical properties isotropy.
- Based on this work, it does not seem that the temperature of 1080°C is the recrystallization temperature of the LPBF IN718 since the static recrystallization process reaches completion in more than 1h (4h) during the homogenization treatment at 1080°C. For this reason, more research work is still needed to figure out the recrystallization temperature of LPBF IN718 to be applied for the homogenization treatment. This can be achieved by trying temperatures higher than 1080°C while keeping in mind that the melting temperature of IN718 is approximately 1260°C. Such a finding of the recrystallization temperature will significantly save the processing time.

- The presented work is solely experimental studies. However, there is still a need to have extensive studies using any of the thermodynamic calculation software. Combining simulations and experimental test results would provide a better understanding of the evolution of the phases during the applied heat treatment and the simulated in-service exposure. For instance, the discrepancies around the precipitation sequence of γ″ and γ′ phase during the aging treatment can be solved by simulating the chemical composition of IN718 and the treatment parameters (temperature and duration).
- In this work, after prolonged thermal exposure, the phase transformation of γ″ into stable intra-granular δ-phase occurs which adversely affect the mechanical properties. More research is required to evaluate the evolution of the volume fraction of transformed γ″ to intra-granular δ-phase as a function of the exposure time. Furthermore, such a phase transformation occurs earlier (after 1000h) in the 2.5H/1S treated condition as compared to the 4H/1S condition in which such phase transformation occurs after 2000h. Further research is necessary to recognize the main driving force for such an earlier phase transformation in the 2.5H/1S condition.
- The evolution of the size of the strengthening phases as a function of thermal exposure time is only tracked analytically in the present study using the XRD data due to its tiny size (few nanometers). Further TEM analysis is required to deeply understand the impact of thermal exposure on the morphology of these phases.
- Evaluating the creep and fatigue performance of the optimum heat-treated LPBF-fabricated IN718 is still required as some of turbine engine components are experiencing such mechanical loading.

References

[1] C. Luke Nelson, Selective laser melting of nickel superalloys for high temperature applications, Thesis for Doctor of Philosophy Degree, University of Birmingham, 2013.

[2] Y.L. Hu, Y.L. Li, S.Y. Zhang, X. Lin, Z.H. Wang, W.D. Huang, Effect of solution temperature on static recrystallization and ductility of Inconel 625 superalloy fabricated by directed energy deposition, Materials Science and Engineering: A. 772 (2020) 138711. https://doi.org/10.1016/j.msea.2019.138711.

[3] N.J. Harrison, Selective laser melting of nickel superalloys: solidification, microstructure and material response, Thesis for Doctor of Philosophy Degree, University of Sheffield, 2016. http://etheses.whiterose.ac.uk/17033/ (accessed April 22, 2020).

[4] I. Gurrappa, I.V.S. Yashwanth, I. Mounika, H. Murakami, S. Kuroda, The importance of hot corrosion and its effective prevention for enhanced efficiency of gas turbines, (2014).

[5] E. Akca, A. Gürsel, A review on superalloys and IN718 nickel-based Inconel superalloy, Periodicals of Engineering and Natural Sciences. 3 (2015) 15–27.

[6] M. Ashabul Anam, Microstructure and mechanical properties of selective laser melted superalloy Inconel 625, Thesis for Doctor of Philosophy in Industrial Engineering, University of Louisville, 2018.

[7] M.D. Sangid, T.A. Book, D. Naragani, J. Rotella, P. Ravi, P. Kenesei, J.-S. Park, H. Sharma, J. Almer, X. Xiao, Role of heat treatment and build orientation in the microstructure sensitive deformation characteristics of IN718 produced via SLM additive manufacturing, Additive Manufacturing. 22 (2018) 479–496.

[8] D.F. Paulonis, J.J. Schirra, Alloy 718 at Pratt & Whitney-Historical perspective and future challenges, Superalloys. 718 (2001) 13–23.

[9] A. Thomas, M. El-Wahabi, J. Cabrera, J. Prado, High temperature deformation of Inconel 718, Journal of Materials Processing Technology. 177 (2006) 469–472.

[10] D. Keiser, H. Brown, Review of the physical metallurgy of Alloy 718, 1976.

[11] D. Deng, Additively manufactured Inconel 718: microstructures and mechanical properties, Licentiate Thesis Degree, Linköping University, 2018.

[12] W.M. Tucho, P. Cuvillier, A. Sjolyst-Kverneland, V. Hansen, Microstructure and hardness studies of Inconel 718 manufactured by selective laser melting before and after solution heat treatment, Materials Science and Engineering: A. 689 (2017) 220–232.

[13] X. Li, J. Shi, C. Wang, G. Cao, A. Russell, Z. Zhou, C. Li, G. Chen, Effect of heat treatment on microstructure evolution of Inconel 718 alloy fabricated by selective laser melting, Journal of Alloys and Compounds. (2018).

[14] N.C. Ferreri, S.C. Vogel, M. Knezevic, Determining volume fractions of γ, γ′, γ″, δ, and MC-carbide phases in Inconel 718 as a function of its processing history using an advanced neutron diffraction procedure, Materials Science and Engineering: A. 781 (2020) 139228. https://doi.org/10.1016/j.msea.2020.139228.

[15] G. Cao, T. Sun, C. Wang, X. Li, M. Liu, Z. Zhang, P. Hu, A.M. Russell, R. Schneider, D. Gerthsen, Investigations of γ′, γ ″and δ precipitates in heat-treated Inconel 718 alloy fabricated by selective laser melting, Materials Characterization. 136 (2018) 398–406.

[16] H. Eiselstein, Metallurgy of a Columbium-Hardened Nickel-Chromium-Iron Alloy, Advances in the Technology of Stainless Steels and Related Alloys. (1965). https://doi.org/10.1520/STP43733S.

[17] Y. Desvallées, M. Bouzidi, F. Bois, N. Beaude, Delta phase in Inconel 718: mechanical properties and forging process requirements, Superalloys. 718 (1994) 281–291.

[18] H. Zhang, S. Zhang, M. Cheng, Z. Li, Deformation characteristics of δ phase in the delta-processed Inconel 718 alloy, Materials Characterization. 61 (2010) 49–53.

[19] S. Li, J. Zhuang, J. Yang, X. Xie, The effect of phase on crack propagation under creep and fatigue conditions in alloy 718, Superalloys. 718 (1994) 625–706.

[20] M.J. Donachie, S.J. Donachie, Superalloys: A Technical Guide, 2nd Edition, ASM International, 2002.

[21] M. Sundararaman, P. Mukhopadhyay, S. Banerjee, Carbide precipitation in nickel base superalloys 718 and 625 and their effect on mechanical properties, Superalloys. 718 (1997) 625–706.

[22] C.T. Sims, A contemporary view of nickel-base superalloys, The Journal of The Minerals, Metals & Materials Society. 18 (1966) 1119–1130. https://doi.org/10.1007/BF03378505.

[23] F. Zupanič, T. Bončina, A. Križman, F. Tichelaar, Structure of continuously cast Ni-based superalloy Inconel 713C, Journal of Alloys and Compounds. 329 (2001) 290–297.

[24] D. Zhang, Z. Feng, C. Wang, W. Wang, Z. Liu, W. Niu, Comparison of microstructures and mechanical properties of Inconel 718 alloy processed by selective laser melting and casting, Materials Science and Engineering: A. 724 (2018) 357–367.

[25] P. Liu, J. Hu, S. Sun, K. Feng, Y. Zhang, M. Cao, Microstructural evolution and phase transformation of Inconel 718 alloys fabricated by selective laser melting under different heat treatment, Journal of Manufacturing Processes. 39 (2019) 226–232.

[26] D. Zhang, W. Niu, X. Cao, Z. Liu, Effect of standard heat treatment on the microstructure and mechanical properties of selective laser melting manufactured Inconel 718 superalloy, Materials Science and Engineering: A. 644 (2015) 32–40.

[27] P. G.D., What Is Wrought Metal?, (n.d.). https://www.hunker.com/13412365/what-is-wrought-metal.

[28] E. Hosseini, V. Popovich, A review of mechanical properties of additively manufactured Inconel 718, Additive Manufacturing. 30 (2019) 100877.

[29] R. Seede, Microstructural analysis and mechanical properties evaluation of heat treated selective laser melted Inconel 718, Thesis for Master of Science Degree, Masdar Institute of Science and Technology, 2017.

[30] W.E. Frazier, Metal additive manufacturing: A review, Journal of Materials Engineering and Performance. 23 (2014) 1917–1928. https://doi.org/10.1007/s11665-014-0958-z.

[31] L. Yang, K. Hsu, B. Baughman, D. Godfrey, F. Medina, M. Menon, S. Wiener, Additive manufacturing of metals: the technology, materials, design and production, Springer, 2017.

[32] E.C. Santos, M. Shiomi, K. Osakada, T. Laoui, Rapid manufacturing of metal components by laser forming, International Journal of Machine Tools and Manufacture. 46 (2006) 1459–1468. https://doi.org/10.1016/j.ijmachtools.2005.09.005.

[33] S. Bremen, W. Meiners, A. Diatlov, Selective laser melting: a manufacturing technology for the future, Laser Technik Journal. 9 (2012) 33–38.

[34] J. Strößner, M. Terock, U. Glatzel, Mechanical and microstructural investigation of nickel-based superalloy IN718 manufactured by selective laser melting (SLM), Advanced Engineering Materials. 17 (2015) 1099–1105.

[35] T. Trosch, J. Strößner, R. Völkl, U. Glatzel, Microstructure and mechanical properties of selective laser melted Inconel 718 compared to forging and casting, Materials Letters. 164 (2016) 428–431.

[36] M. Monzón, Z. Ortega, A. Martínez, F. Ortega, Standardization in additive manufacturing: activities carried out by international organizations and projects, The International Journal of Advanced Manufacturing Technology. 76 (2015) 1111–1121.

[37] I. Gibson, D. Rosen, B. Stucker, Additive Manufacturing Technologies: 3D Printing, Rapid Prototyping, and Direct Digital Manufacturing, 2nd ed., Springer-Verlag, New York, 2015. https://doi.org/10.1007/978-1-4939-2113-3.

[38] Laser Additive Manufacturing (AM): Classification, Processing Philosophy, and Metallurgical Mechanisms | SpringerLink, (n.d.). https://link.springer.com/chapter/10.1007/978-3-662-46089-4_2 (accessed April 8, 2020).

[39] I. Gibson, D.W. Rosen, B. Stucker, Powder Bed Fusion Processes, in: I. Gibson, D.W. Rosen, B. Stucker (Eds.), Additive Manufacturing Technologies: Rapid Prototyping to Direct Digital Manufacturing, Springer US, Boston, MA, 2010: pp. 120–159. https://doi.org/10.1007/978-1-4419-1120-9_5.

[40] M. Brandt, Laser Additive Manufacturing: Materials, Design, Technologies, and Applications, Woodhead Publishing, 2016.

[41] J.-P. Choi, G.-H. Shin, S. Yang, D.-Y. Yang, J.-S. Lee, M. Brochu, J.-H. Yu, Densification and microstructural investigation of Inconel 718 parts fabricated by selective laser melting, Powder Technology. 310 (2017) 60–66. https://doi.org/10.1016/j.powtec.2017.01.030.

[42] C.Y. Yap, C.K. Chua, Z.L. Dong, Z.H. Liu, D.Q. Zhang, L.E. Loh, S.L. Sing, Review of selective laser melting: Materials and applications, Applied Physics Reviews. 2 (2015) 041101.

[43] K. Guan, Z. Wang, M. Gao, X. Li, X. Zeng, Effects of processing parameters on tensile properties of selective laser melted 304 stainless steel, Materials & Design. 50 (2013) 581–586. https://doi.org/10.1016/j.matdes.2013.03.056.

[44] M. Shiomi, K. Osakada, K. Nakamura, T. Yamashita, F. Abe, Residual Stress within Metallic Model Made by Selective Laser Melting Process, CIRP Annals. 53 (2004) 195–198. https://doi.org/10.1016/S0007-8506(07)60677-5.

[45] A. Mostafa, I. Picazo Rubio, V. Brailovski, M. Jahazi, M. Medraj, Structure, texture and phases in 3D printed IN718 alloy subjected to homogenization and HIP treatments, Metals. 7 (2017) 196.

[46] E. Chlebus, K. Gruber, B. Kuźnicka, J. Kurzac, T. Kurzynowski, Effect of heat treatment on the microstructure and mechanical properties of Inconel 718 processed by selective laser melting, Materials Science and Engineering: A. 639 (2015) 647–655.

[47] X. Wang, X. Gong, K. Chou, Review on powder-bed laser additive manufacturing of Inconel 718 parts, Journal of Engineering Manufacture. 231 (2017) 1890–1903.

[48] C. Li, Z. Liu, X. Fang, Y. Guo, Residual stress in metal additive manufacturing, Procedia CIRP. 71 (2018) 348–353.

[49] B.E. Carroll, T.A. Palmer, A.M. Beese, Anisotropic tensile behavior of Ti–6Al–4V components fabricated with directed energy deposition additive manufacturing, Acta Materialia. 87 (2015) 309–320.

[50] R. Seede, A. Mostafa, V. Brailovski, M. Jahazi, M. Medraj, Microstructural and microhardness evolution from homogenization and hot isostatic pressing on selective laser melted Inconel 718: structure, texture, and phases, Journal of Manufacturing and Materials Processing. 2 (2018) 30.

[51] I. Picazo Rubio, Selective laser melting of Inconel 718: Microstructure and mechanical properties, Thesis for Master of Science Degree, Masdar Institute of Science and Technology, 2016.

[52] M. Ni, C. Chen, X. Wang, P. Wang, R. Li, X. Zhang, K. Zhou, Anisotropic tensile behavior of in situ precipitation strengthened Inconel 718 fabricated by additive manufacturing, Materials Science and Engineering: A. 701 (2017) 344–351.

[53] D. Deng, R.L. Peng, H. Brodin, J. Moverare, Microstructure and mechanical properties of Inconel 718 produced by selective laser melting: Sample orientation dependence and effects of post heat treatments, Materials Science and Engineering: A. 713 (2018) 294–306.

[54] F. Zhang, L.E. Levine, A.J. Allen, M.R. Stoudt, G. Lindwall, E.A. Lass, M.E. Williams, Y. Idell, C.E. Campbell, Effect of heat treatment on the microstructural evolution of a nickel-based superalloy additive-manufactured by laser powder bed fusion, Acta Materialia. 152 (2018) 200–214.

[55] T. DebRoy, H. Wei, J. Zuback, T. Mukherjee, J. Elmer, J. Milewski, A.M. Beese, A. Wilson-Heid, A. De, W. Zhang, Additive manufacturing of metallic components–process, structure and properties, Progress in Materials Science. 92 (2018) 112–224.

[56] B. Song, X. Zhao, S. Li, C. Han, Q. Wei, S. Wen, J. Liu, Y. Shi, Differences in microstructure and properties between selective laser melting and traditional manufacturing for fabrication of metal parts: A review, Frontiers of Mechanical Engineering. 10 (2015) 111–125.

[57] Q. Jia, D. Gu, Selective laser melting additive manufacturing of Inconel 718 superalloy parts: Densification, microstructure and properties, Journal of Alloys and Compounds. 585 (2014) 713–721.

[58] J. Schneider, B. Lund, M. Fullen, Effect of heat treatment variations on the mechanical properties of Inconel 718 selective laser melted specimens, Additive Manufacturing. 21 (2018) 248–254.

[59] V. Petkov, Alloy 718 manufactured by AM Selective Laser Melting, Materials Engineering, master's level, Luleå University of Technology, 2018.

[60] A. Maamoun, Selective laser melting and post-processing for lightweight metallic optical components, Thesis for Doctor of Philosophy Degree, McMaster University, 2019. https://macsphere.mcmaster.ca/handle/11375/24032 (accessed April 15, 2020).

[61] S. Moorthy, Modeling and characterization of mechanical properties in laser powder bed fusion additive manufactured Inconel 718, Thesis for Master of Science Degree (Mechanical Engineering), Colorado School of Mines, 2018.

[62] Y. Gao, D. Zhang, M. Cao, R. Chen, Z. Feng, Effect of δ phase on high temperature mechanical performances of Inconel 718 fabricated with SLM process, Materials Science and Engineering: A. 767 (2019) 138327.

[63] J.-R. Zhao, F.-Y. Hung, T.-S. Lui, Microstructure and tensile fracture behavior of three-stage heat treated Inconel 718 alloy produced via laser powder bed fusion process, Journal of Materials Research and Technology. (2020). https://doi.org/10.1016/j.jmrt.2020.01.030.

[64] E. Yasa, Manufacturing by combining selective laser melting and selective laser erosion/laser re-melting, CIRP Annals-Manufacturing Technology. 60 (2011) 263–266.

[65] S.A.E. Aerospace, Aerospace Material Specification: AMS 5662, in: SAE International, 2009.

[66] S.A.E. Aerospace, Aerospace Material Specification: AMS 5383, in: SAE International, 2012.

[67] L. Zhou, A. Mehta, B. McWilliams, K. Cho, Y. Sohn, Microstructure, precipitates and mechanical properties of powder bed fused Inconel 718 before and after heat treatment, Journal of Materials Science & Technology. 35 (2019) 1153–1164.

[68] K. Amato, S. Gaytan, L. Murr, E. Martinez, P. Shindo, J. Hernandez, S. Collins, F. Medina, Microstructures and mechanical behavior of Inconel 718 fabricated by selective laser melting, Acta Materialia. 60 (2012) 2229–2239.

[69] M. Calandri, S. Yin, B. Aldwell, F. Calignano, R. Lupoi, D. Ugues, Texture and microstructural features at different length scales in Inconel 718 produced by selective laser melting, Materials. 12 (2019) 1293.

[70] B. Vrancken, L. Thijs, J.-P. Kruth, J. Van Humbeeck, Heat treatment of Ti6Al4V produced by selective laser melting: microstructure and mechanical properties, Journal of Alloys and Compounds. 541 (2012) 177–185.

[71] A. Riemer, S. Leuders, M. Thöne, H. Richard, T. Tröster, T. Niendorf, On the fatigue crack growth behavior in 316L stainless steel manufactured by selective laser melting, Engineering Fracture Mechanics. 120 (2014) 15–25.

[72] A. Kreitcberg, V. Brailovski, S. Turenne, Effect of heat treatment and hot isostatic pressing on the microstructure and mechanical properties of Inconel 625 alloy processed by laser powder bed fusion, Materials Science and Engineering: A. 689 (2017) 1–10.

[73] M. Saadati, A.K. Edalat Nobarzad, M. Jahazi, On the hot cracking of HSLA steel welds: Role of epitaxial growth and HAZ grain size, Journal of Manufacturing Processes. 41 (2019) 242–251. https://doi.org/10.1016/j.jmapro.2019.03.032.

[74] R. Singh, J. Hyzak, T. Howson, R. Biederman, Recrystallization behavior of cold rolled alloy 718, Superalloys. 718 (1991) 205–215.

[75] W.M. Tucho, V. Hansen, Characterization of SLM-fabricated Inconel 718 after solid solution and precipitation hardening heat treatments, Journal of Materials Science. 54 (2019) 823–839.

[76] R. Jiang, A. Mostafaei, J. Pauza, C. Kantzos, A.D. Rollett, Varied heat treatments and properties of laser powder bed printed Inconel 718, Materials Science and Engineering: A. 755 (2019) 170–180.

[77] Atomic Radius for all the elements in the Periodic Table, WOLFRAM MATHEMATICA. (2014). https://periodictable.com/Properties/A/AtomicRadius.v.html.

[78] Y. Cao, P. Bai, F. Liu, X. Hou, Y. Guo, Effect of the solution temperature on the precipitates and grain evolution of IN718 fabricated by laser additive manufacturing, Materials. 13 (2020) 340. https://doi.org/10.3390/ma13020340.

[79] H. Qi, M. Azer, A. Ritter, Studies of standard heat treatment effects on microstructure and mechanical properties of laser net shape manufactured Inconel 718, Metallurgical and Materials Transactions A. 40 (2009) 2410–2422.

[80] X. Zhao, J. Chen, X. Lin, W. Huang, Study on microstructure and mechanical properties of laser rapid forming Inconel 718, Materials Science and Engineering: A. 478 (2008) 119–124.

[81] F. Liu, X. Lin, G. Yang, M. Song, J. Chen, W. Huang, Recrystallization and its influence on microstructures and mechanical properties of laser solid formed nickel base superalloy Inconel 718, Rare Metals. 30 (2011) 433–438.

[82] P. Blackwell, The mechanical and microstructural characteristics of laser-deposited IN718, Journal of Materials Processing Technology. 170 (2005) 240–246.

[83] S. Raghavan, B. Zhang, P. Wang, C.-N. Sun, M.L.S. Nai, T. Li, J. Wei, Effect of different heat treatments on the microstructure and mechanical properties in selective laser melted Inconel 718 alloy, Materials and Manufacturing Processes. 32 (2017) 1588–1595.

[84] V. Popovich, E. Borisov, A. Popovich, V.S. Sufiiarov, D. Masaylo, L. Alzina, Functionally graded Inconel 718 processed by additive manufacturing: Crystallographic texture, anisotropy of microstructure and mechanical properties, Materials & Design. 114 (2017) 441–449.

[85] Y.-L. Kuo, S. Horikawa, K. Kakehi, The effect of interdendritic δ phase on the mechanical properties of Alloy 718 built up by additive manufacturing, Materials & Design. 116 (2017) 411–418.

[86] D. Ivanov, A. Travyanov, P. Petrovskiy, V. Cheverikin, E. Alekseeva, A. Khvan, I. Logachev, Evolution of structure and properties of the nickel-based alloy EP718 after the SLM growth and after different types of heat and mechanical treatment, Additive Manufacturing. 18 (2017) 269–275.

[87] V. Popovich, E. Borisov, A. Popovich, V.S. Sufiiarov, D. Masaylo, L. Alzina, Impact of heat treatment on mechanical behaviour of Inconel 718 processed with tailored microstructure by selective laser melting, Materials & Design. 131 (2017) 12–22.

[88] A. Kreitcberg, V. Brailovski, S. Turenne, Elevated temperature mechanical behavior of IN625 alloy processed by laser powder-bed fusion, Materials Science and Engineering: A. 700 (2017) 540–553.

[89] E. Fayed, D. Shahriari, M. Saadati, V. Brailovski, M. Jahazi, M. Medraj, Influence of homogenization and solution treatments time on the microstructure and hardness of Inconel 718 fabricated by laser powder bed fusion process, Materials. 13 (2020).

[90] A. Hilaire, E. Andrieu, X. Wu, High-temperature mechanical properties of alloy 718 produced by laser powder bed fusion with different processing parameters, Additive Manufacturing. 26 (2019) 147–160.

[91] G.E. Bean, T.D. McLouth, D.B. Witkin, S.D. Sitzman, P.M. Adams, R.J. Zaldivar, Build orientation effects on texture and mechanical properties of selective laser melting Inconel 718, Journal of Materials Engineering and Performance. 28 (2019) 1942–1949. https://doi.org/10.1007/s11665-019-03980-w.

[92] X. Li, J.J. Shi, G.H. Cao, A.M. Russell, Z.J. Zhou, C.P. Li, G.F. Chen, Improved plasticity of Inconel 718 superalloy fabricated by selective laser melting through a novel heat treatment process, Materials & Design. 180 (2019) 107915. https://doi.org/10.1016/j.matdes.2019.107915.

[93] H. Yuan, W.C. Liu, Effect of the δ phase on the hot deformation behavior of Inconel 718, Materials Science and Engineering: A. 408 (2005) 281–289. https://doi.org/10.1016/j.msea.2005.08.126.

[94] Y.C. Lin, J. Deng, Y.-Q. Jiang, D.-X. Wen, G. Liu, Hot tensile deformation behaviors and fracture characteristics of a typical Ni-based superalloy, Materials & Design. 55 (2014) 949–957. https://doi.org/10.1016/j.matdes.2013.10.071.

[95] A. Mostafa, D. Shahriari, I.P. Rubio, V. Brailovski, M. Jahazi, M. Medraj, Hot compression behavior and microstructure of selectively laser-melted IN718 alloy, The International Journal of Advanced Manufacturing Technology. 96 (2018) 371–385.

[96] Y. Wang, L. Zhen, W.Z. Shao, L. Yang, X.M. Zhang, Hot working characteristics and dynamic recrystallization of delta-processed superalloy 718, Journal of Alloys and Compounds. 474 (2009) 341–346. https://doi.org/10.1016/j.jallcom.2008.06.079.

[97] S.-H. Zhang, H.-Y. Zhang, M. Cheng, Tensile deformation and fracture characteristics of delta-processed Inconel 718 alloy at elevated temperature, Materials Science and Engineering: A. 528 (2011) 6253–6258.

[98] G. Varela-Castro, J.-M. Cabrera, J.-M. Prado, Critical strain for dynamic recrystallisation. The particular case of steels, Metals. 10 (2020) 135. https://doi.org/10.3390/met10010135.

[99] GE Reports Staff, 5 Ways GE is Changing the World with 3D Printing, (2017). https://www.ge.com/news/reports/5-ways-ge-changing-world-3d-printing.

[100] D.A. Lesyk, S. Martinez, B.N. Mordyuk, V.V. Dzhemelinskyi, A. Lamikiz, G.I. Prokopenko, Post-processing of the Inconel 718 alloy parts fabricated by selective laser melting: Effects of mechanical surface treatments on surface topography, porosity, hardness and residual stress, Surface and Coatings Technology. 381 (2020) 125136. https://doi.org/10.1016/j.surfcoat.2019.125136.

[101] D. Newell, Solution anneal heat treatments to enhance mechanical performance of additively manufactured Inconel 718, Thesis for Doctor of Philosophy Degree, Air Force Institute of Technology, 2020. https://scholar.afit.edu/etd/3210.

[102] W. Huang, J. Yang, H. Yang, G. Jing, Z. Wang, X. Zeng, Heat treatment of Inconel 718 produced by selective laser melting: Microstructure and mechanical properties, Materials Science and Engineering: A. 750 (2019) 98–107.

[103] R. Shi, S.A. Khairallah, T.T. Roehling, T.W. Heo, J.T. McKeown, M.J. Matthews, Microstructural control in metal laser powder bed fusion additive manufacturing using laser beam shaping strategy, Acta Materialia. 184 (2020) 284–305. https://doi.org/10.1016/j.actamat.2019.11.053.

[104] N. Raghavan, S. Simunovic, R. Dehoff, A. Plotkowski, J. Turner, M. Kirka, S. Babu, Localized melt-scan strategy for site specific control of grain size and primary dendrite arm spacing in electron beam additive manufacturing, Acta Materialia. 140 (2017) 375–387. https://doi.org/10.1016/j.actamat.2017.08.038.

[105] T.T. Roehling, S.S.Q. Wu, S.A. Khairallah, J.D. Roehling, S.S. Soezeri, M.F. Crumb, M.J. Matthews, Modulating laser intensity profile ellipticity for microstructural control during metal additive manufacturing, Acta Materialia. 128 (2017) 197–206. https://doi.org/10.1016/j.actamat.2017.02.025.

[106] T. Vilaro, C. Colin, J.D. Bartout, L. Nazé, M. Sennour, Microstructural and mechanical approaches of the selective laser melting process applied to a nickel-base superalloy, Materials Science and Engineering: A. 534 (2012) 446–451. https://doi.org/10.1016/j.msea.2011.11.092.

[107] Y.-L. Kuo, S. Horikawa, K. Kakehi, Effects of build direction and heat treatment on creep properties of Ni-base superalloy built up by additive manufacturing, Scripta Materialia. 129 (2017) 74–78. https://doi.org/10.1016/j.scriptamat.2016.10.035.

[108] B. Diepold, N. Vorlaufer, S. Neumeier, T. Gartner, M. Göken, Optimization of the heat treatment of additively manufactured Ni-base superalloy IN718, International Journal of Minerals, Metallurgy and Materials. 27 (2020) 640–648. https://doi.org/10.1007/s12613-020-1991-6.

[109] C.S. Pande, B.B. Rath, M.A. Imam, Effect of annealing twins on Hall–Petch relation in polycrystalline materials, Materials Science and Engineering: A. 367 (2004) 171–175. https://doi.org/10.1016/j.msea.2003.09.100.

[110] Y. Yuan, Y. Gu, C. Cui, T. Osada, T. Yokokawa, H. Harada, A Novel Strategy for the Design of Advanced Engineering Alloys—Strengthening Turbine Disk Superalloys via Twinning Structures, Advanced Engineering Materials. 13 (2011) 296–300. https://doi.org/10.1002/adem.201000232.

[111] E. Fayed, D. Shahriari, M. Saadati, V. Brailovski, M. Jahazi, M. Medraj, Effect of Homogenization and Solution Treatments Time on the Elevated-Temperature Mechanical Behavior of Inconel 718 Fabricated by Laser Powder Bed Fusion, Manuscript Submitted for Publication. (2020).

[112] Design Expert software, Stat-Ease, Inc., Minneapolis, MN, 2019.

[113] B. Beausir, J.-J. Fundenberger, Analysis tools for electron and X-ray diffraction, Université de Lorraine, Metz, 2017. www.atex-software.eu.

[114] Quantax Esprit software, Bruker Nano GmbH, Berlin, Germany, 2015.

[115] H. Zhang, D. Gu, C. Ma, M. Guo, J. Yang, R. Wang, Effect of post heat treatment on microstructure and mechanical properties of Ni-based composites by selective laser melting, Materials Science and Engineering: A. (2019) 138294.

[116] D. Connétable, B. Ter-Ovanessian, É. Andrieu, Diffusion and segregation of niobium in fcc-nickel, Journal of Physics: Condensed Matter. 24 (2012) 095010. https://doi.org/10.1088/0953-8984/24/9/095010.

[117] L. Johnson, M. Mahmoudi, B. Zhang, R. Seede, X. Huang, J.T. Maier, H.J. Maier, I. Karaman, A. Elwany, R. Arróyave, Assessing printability maps in additive manufacturing of metal alloys, Acta Materialia. 176 (2019) 199–210. https://doi.org/10.1016/j.actamat.2019.07.005.

[118] Dave VanAken, Engineering concepts: formation of annealing twins, Industrial Heating. (2000). https://www.industrialheating.com/articles/86154-engineering-concepts-formation-of-annealing-twins.

[119] T. Watanabe, An approach to grain boundary design for strong and ductile polycrystals, Res Mechanica. 11 (1984) 47–84.

[120] M. Jouiad, E.Marin, R. Devarapali, J. Cormier, F. Ravaux, C. Gall, J.-M. Franchet, Microstructure andmechanical properties evolutions of alloy 718 during isothermal and thermal cycling over-aging, Materials and Design. 102 (2016) 284–296. https://doi.org/10.1016/j.matdes.2016.04.048.

[121] S.J. Hong, W.P. CHEN,, T.W. WANG, A diffraction study of the γ″ phase in Inconel 718 superalloy, Metallurgical and Materials Transactions A. 32A (2001).

[122] X.S. Xie, J.X. Dong, M.C. Zhang, Research and Development of Inconel 718 Type Superalloy, Materials Science Forum. 539–543 (2007) 262–269. https://doi.org/10.4028/www.scientific.net/MSF.539-543.262.

[123] Y. Han, P. Deb, M.C. Chaturvedi, Coarsening behaviour of γ″- and γ′-particles in Inconel alloy 718, Metal Science. 16 (1982) 555–562. https://doi.org/10.1179/030634582790427118.

[124] A. Agnoli, C. Le Gall, J. Thebault, E. Marin, J. Cormier, Mechanical properties evolution of γ′/γ″ nickel-base superalloys during long-term thermal over-aging, Metallurgical and Materials Transactions A. 49 (2018) 4290–4300. https://doi.org/10.1007/s11661-018-4778-x.

[125] A. Volek, R.F. Singer, R. Buergel, J. Grossmann, Y. Wang, Influence of topologically closed packed phase formation on creep rupture life of directionally solidified nickel-base superalloys, Metallurgical and Materials Transactions A. 37 (2006) 405–410. https://doi.org/10.1007/s11661-006-0011-4.

[126] H. Monajati, A.K. Taheri, M. Jahazi, S. Yue, Deformation characteristics of isothermally forged UDIMET 720 nickel-base superalloy, Metallurgical and Materials Transactions A. 36 (2005) 895–905. https://doi.org/10.1007/s11661-005-0284-z.

[127] M. Dehmas, J. Lacaze, A. Niang, B. Viguier, TEM Study of High-Temperature Precipitation of Delta Phase in Inconel 718 Alloy, Advances in Materials Science and Engineering. 2011 (2011) e940634. https://doi.org/10.1155/2011/940634.

[128] M. Balbaa, S. Mekhiel, M. Elbestawi, J. McIsaac, On selective laser melting of Inconel 718: Densification, surface roughness, and residual stresses, Materials & Design. 193 (2020) 108818. https://doi.org/10.1016/j.matdes.2020.108818.

[129] X. Yu, X. Lin, F. Liu, L. Wang, Y. Tang, J. Li, S. Zhang, W. Huang, Influence of post-heat-treatment on the microstructure and fracture toughness properties of Inconel 718 fabricated with laser directed energy deposition additive manufacturing, Materials

Science and Engineering: A. (2020) 140092. https://doi.org/10.1016/j.msea.2020.140092.

[130] E. Fayed, M. Saadati, D. Shahriari, V. Brailovski, M. Jahazi, M. Medraj, Optimization of the post-process heat treatment of additively manufactured Inconel 718 superalloy using laser powder bed fusion process, Manuscript Submitted for Publication. (2020).

[131] A.C. Karaoglanli, K. Ogawa, A. Türk, I. Ozdemir, Thermal shock and cycling behavior of thermal barrier coatings (TBCs) used in gas turbines, in: Progress in Gas Turbine Performance, IntechOpen, 2013.

[132] D.-H. Jeong, M.-J. Choi, M. Goto, H.-C. Lee, S. Kim, Effect of service exposure on fatigue crack propagation of Inconel 718 turbine disc material at elevated temperatures, Materials Characterization. 95 (2014) 232–244.

[133] Z. Wang, K. Guan, M. Gao, X. Li, X. Chen, X. Zeng, The microstructure and mechanical properties of deposited-IN718 by selective laser melting, Journal of Alloys and Compounds. 513 (2012) 518–523.

[134] J.F. Radavich, The physical metallurgy of cast and wrought alloy 718, in: Superalloys 718 Metallurgy and Applications (1989), TMS, 2004: pp. 229–240. https://doi.org/10.7449/1989/Superalloys_1989_229_240.

[135] Y. Idell, L.E. Levine, A.J. Allen, F. Zhang, C.E. Campbell, G.B. Olson, J. Gong, D.R. Snyder, H.Z. Deutchman, Unexpected δ-phase formation in additive-manufactured Ni-based superalloy, JOM. 68 (2016) 950–959. https://doi.org/10.1007/s11837-015-1772-2.

[136] C. Slama, C. Servant, G. Cizeron, Aging of the Inconel 718 alloy between 500 and 750 °C, Journal of Materials Research. 12 (1997) 2298–2316. https://doi.org/10.1557/JMR.1997.0306.

[137] L.M. Suave, J. Cormier, P. Villechaise, A. Soula, Z. Hervier, D. Bertheau, J. Laigo, Microstructural evolutions during thermal aging of alloy 625: Impact of temperature and forming process, Metallurgical and Materials Transactions A. 45 (2014) 2963–2982. https://doi.org/10.1007/s11661-014-2256-7.

[138] Z.S. Yu, J.X. Zhang, Y. Yuan, R.C. Zhou, H.J. Zhang, H.Z. Wang, Microstructural evolution and mechanical properties of Inconel 718 after thermal exposure, Materials Science and Engineering: A. 634 (2015) 55–63. https://doi.org/10.1016/j.msea.2015.03.004.

[139] R. Thompson, J. Dobbs, D. Mayo, The effect of heat treatment on microfissuring in alloy 718, Weld.J. 65 (1986) 299.

[140] M. Sundararaman, P. Mukhopadhyay, S. Banerjee, Precipitation of the δ-Ni3Nb phase in two nickel base superalloys, Metallurgical Transactions A. 19 (1988) 453–465. https://doi.org/10.1007/BF02649259.

[141] R. Cozar, A. Pineau, Morphology of γ’ and γ" precipitates and thermal stability of Inconel 718 type alloys, Metallurgical Transactions. 4 (1973) 47–59. https://doi.org/10.1007/BF02649604.

[142] C. Slama, M. Abdellaoui, Structural characterization of the aged Inconel 718, Journal of Alloys and Compounds. 306 (2000) 277–284. https://doi.org/10.1016/S0925-8388(00)00789-1.

[143] A. Chamanfar, L. Sarrat, M. Jahazi, M. Asadi, A. Weck, A.K. Koul, Microstructural characteristics of forged and heat treated Inconel-718 disks, Materials & Design (1980-2015). 52 (2013) 791–800. https://doi.org/10.1016/j.matdes.2013.06.004.

[144] OriginPro, OriginLab Corporation, Northampton, MA, USA, 2019.